Examination into Structural Behaviour of High Strength S690 and S960 Welded Sections through Advanced Numerical Simulation

MENGFEI ZHU

PhD

The Hong Kong Polytechnic University

2024

The Hong Kong Polytechnic University

Department of Civil and Environmental Engineering

Examination into Structural Behaviour of High Strength S690 and S960 Welded Sections through Advanced Numerical Simulation

MENGFEI ZHU

A thesis submitted in partial fulfilment of the requirements for the degree of Doctor of Philosophy

August 2023

CERTIFICATE OF ORIGINALITY

I hereby declare that this thesis is my own work and that, to the best of my knowledge and belief, it reproduces no material previously published or written nor material that has been accepted for the award of any other degree or diploma, except where due acknowledgement has been made in the text.

____________(Signed)

Mengfei ZHU (Name of student)

LIST OF SYMBOLS

A	Cross-section area of the welded section
A, B	Stress relief coefficients of hole drilling method
A_{c1}	Temperature of austenite transformation start
A_{c3}	Temperature of austenite transformation end
A_{ij}	The quantity of phase *i* transformed to phase *j* per time unit
a_f, a_r, b and c	Coefficients of the double ellipsoidal heat source model
a	Reduction factors of yield strength
α	The coefficient related to the martensitic transformation rate
B	Outer diameter of the box section
b_1	Dimension of upper flange of the H-section
b_2	Dimension of lower flange of the H-section
c_p	Specific Heat Capacity
E	Young's modulus
$\varepsilon_1, \varepsilon_2, \varepsilon_3$	Measured relieved strains of rosette in three directions
ε_u	Elongation at ultimate strength
ε_y	Elongation at yield strength
ε_f	Elongation at fracture
λ, λ_a	Thermal conductivity
f_M	The martensite fraction
f_y	Yield strength of steel
f_u	Ultimate strength of steel
h	Dimension of flange of the H-section and the box section
H	Height of the stocky column
h_c	Convection heat transfer coefficient
I	Welding current
M_s	The theoretical martensite start temperature

$N_{c,Rd}$	Design resistance of the welded section
$N_{c,Rt}$	Measured resistances of the welded section
$N(\theta)$	Exponent illustrating the reaction rate
P	Metallurgical phase proportion
$\bar{P}$	Interpreted as the equilibrium value
ρ	The density of material
q, q_{arc}	Heat input energy of welding seam
q_c	Convective heat transfer between steel and air
q_r	Radiative heat transfer between steel and air
σ_r	The Stefan-Boltzmann coefficient
T	Temperature
t_{f1}	Plate thickness of upper flange of the H-section
t_{f2}	Plate thickness of lower flange of the H-section
t_w	Plate thickness of web of the H-section
TR	Equivalent to a “time delay” associated with the reaction
U	Welding voltage
v	Speed of welding arc move
v	Poisson’s ratio
∇	Laplace-operaattori factor

ABBREVIATION

AC	Alternating Current
CCT	Continuously Cooling Transformation
CGHAZ	Coarse-Grain Heat-Affected Zone
CSLM	Confocal Scanning Laser Microscope
DC	Direct Current
EC3	Eurocode 3
FEM	Finite Element Method
GMAW	Gas Metal Arc Welding
HAZ	Heat-affected Zone
HSS	High Strength Steel
LVDT	Linear variable differential transformer
NDT	Non-destructive Testing
MAG	Metal Active Gas Arc Welding
MIG	Melt Inert-gas Welding
pWPS	Pre-Welding Procedure Specification
Q&T	Quenching and Tempering
RF	Reference Point
SAW	Submerged Arc Welding
SEM	Scanning Electron Microscope
SMAW	Shielded Metal Arc Welding
TMCP	Thermo-Mechanical Control Process
TTT	Time Temperature-Transformation
UHSS	Ultra-High Strength Steel
WPS	Welding Procedure Specification

ABSTRACT

Owing to advances in metallurgical development in recent years, high strength S690 and S960 steel have been produced in an industrial scale in many parts of the world. These high strength steel are highly engineered steel products which strengths are readily achieved through carefully controlled heat treatments to achieve specific microstructures during steel production. However, many researchers consider that the microstructures of these high strength steel are readily affected during welding, resulting in significant reductions in various mechanical properties in the heat-affected zones of their welded sections. It should be noted that while such reductions are found in many tests reported in the literature, the plate thicknesses of these high strength steel are typically smaller than 1 mm for applications in the automobile industry. Hence, it is highly desirable to examine and quantify such effects in high strength S690 and S960 steel plates of practical dimensions in construction, i.e., 10 to 30 mm thick.

This thesis presents a comprehensive examination into structural behaviour of these high strength S690 and S960 welded sections under axial loads, and both experimental and numerical investigations have been conducted to provide scientific data for development of structural understanding. **It should be noted that the effects of welding onto these S690 and S960 steel have been studied systematically while metallurgical changes within the heat-affected zones of these welded sections is simulated** through **coupled thermomechanical-metallurgical analyses using an advanced numerical simulation package SYSWELD**. In this study, the welding process is simulated with the following analyses:

i) **a thermal analysis** to determine *thermal responses* of the steel plates, i.e. transient temperature distribution history;
ii) **a metallurgical analysis** to determine *highly localized phase transformation* within the heat affected zones of the steel plates under the transient temperature distribution history; and
iii) **a thermomechanical analysis** to determine *mechanical responses* of the welded sections of the steel plates under the transient temperature distribution history, i.e. locked-in stresses and strains, and distortion.

All these numerical results are incorporated into structural models with consistent element types and mesh configurations in a general finite element package **Abaqus** so that structural analyses are performed to determine *structural responses* of these sections, i.e., stresses and strains, displacements and deformations. **Hence, a generalized thermal-metallurgical-mechanical-structural finite element simulation approach, i.e., TMMS approach**, is established for these high strength steel welded sections, and the effects of welding onto the structural behaviour of these welded sections are readily examined in a direct manner.

Key research findings are:

- Continuous cooling temperature curves

  By systematic dilatometry tests and SEM observations conducted on the S690 and the S960 coupons, a set of *continuous cooling temperature curves* (CCT curves) *for various phases of the steel* over a practical range of cooling rates commonly encountered in welding have been obtained for both steels. These curves are parts of the essential data for simulating phase transformations in the heat-affected zones of these steels during welding.

- Microstructural transformations within heat affected zones

  With the use of SYSWELD, finite element models of these steel plates with uniform metallurgical properties (**homogeneous microstructures) are transformed** under a direct exposure to transient temperature distribution history according to *the maximum temperatures and the amount of heat input energy experienced during welding*. Hence, finite element meshes with non-uniform metallurgical properties (**heterogeneous microstructures)** are obtained. As a result, the mechanical properties of the heat affected zones of the welded sections are determined directly according to the predicted volumetric fractions of various steel phases.

- Calibration against experimental data: temperatures and residual stresses

  Transient temperature distribution history of four S960 welded sections during welding have been carefully recorded using thermocouples. Surface residual stresses of these sections were also measured with the use of the hole-drilling method. These data were employed to calibrate these finite element models, and good comparisons on both the temperatures and the residual stresses were achieved. In general, the effects of these residual stresses are found to be proportionally less pronounced when compared with those of S355 welded sections.

- Calibration against experimental data: structural behaviour of welded sections under compression

  A comprehensive experimental investigation was carried out to examine the structural behaviour of 39 stocky columns of S690 and S960 welded H- and Box sections under axial compression. The thicknesses of the S690 steel plates are 10, 16 and 30 mm while those of the S960 steel plates are 15 mm. The heat input energy for welding range from 1.0 to 3.0 kJ/mm. With a proper control on the butt-welding at mid-height of these sections, it was demonstrated that the effects of welding onto these sections have been successfully eliminated. Hence, the cross-section resistances of all of these columns are fully mobilized.

More importantly, the structural behaviour of these stocky columns with welded splices was also successfully simulated with the proposed TMMS approach, and good comparisons among the predicted and the measured deformation characteristics of these columns over the entire deformation ranges were successfully achieved.

In short, this thesis presents an investigation into ***"welding – microstructural transformations - mechanical properties - structural behaviour"*** of the high strength S690 and S960 welded sections. The proposed TMMS approach has been successfully validated to simulate the structural performance of both the S690 and the S960 steel welded sections of practical dimensions in construction.

PUNLICATIONS

Conference Papers

- M. F. Zhu, K. F. Chung, and H. C. Ho (2023). Experimental investigation into the compression resistance of S690 and S960 box sections under a controlled welding process. The 13th Pacific Structural Steel Conference (PSSC'22), 27^{th}~30^{th} October, Chengdu

Journal Papers

- M. F. Zhu, Y. F. Hu, Y. W. Han, K. F. Chung, and David A. Nethercot. Investigation into structural behaviour of high strength S690 and S960 welded H-sections under compression. *Engineering Structures* (Under Review).
- M. F. Zhu, K. F. Chung, Y. F. Hu, H. Jin, T. Y. Xiao. Thermo-metallurgical-mechanical-structural simulation approach on stocky columns of high strength S960 steel welded box sections under compression. *Engineering Structures* (Under Review)
- M. F. Zhu, K. F. Chung, Y. F. Hu, H. Jin and Y.W. Han. Advanced numerical simulation on effects of welding onto high strength S690 and S960 steel welded H-sections (under preparation)

ACKNOWLEDGEMENTS

First and foremost, I want to express my heartfelt gratitude to my supervisor, Prof. K. F. CHUNG, for his unwavering support, illuminating guidance, and enthusiastic motivation throughout my research endeavour. During these five years study project, he always provided me with a clear direction and powerful supports. His profound and insightful knowledge in academic and engineering domains, his genuine attitude, and his research fervour have been a great encouragement for me. I believe I will benefit from this experience for a lifetime.

I also wish to express my profound appreciation to Dr. H. C. HO, Dr. Y. F. HU, and Dr. M XIAO for their valuable insights and assistance throughout the past years. Their extensive experience and warm support have helped me a lot during these years.

I would also like to express my thanks to the technicians from Laboratory Y001, including Mr. M. C. NG, Mr. K. L. CHEUNG, Mr. C. F. CHEUNG and Mr. K. H. WONG. The successful completion of the experimental investigation is attributable to the invaluable assistance of the laboratory team, whose friendly demeanour and expertise were instrumental in facilitating the project's execution.

Grateful thanks are extended to members in the research group CNERC, including Mr. H JIN, Ms. Y. B. GUO, Mr. W CHEN, Ms. M. F. LI and Mr. Y. W. HAN, for their positive and optimistic work attitude, and for the help they provide me during all these years. Assistances provided by seniors Dr. X LIU, Dr. K WANG, and Dr. X. M. LIN are also greatly appreciated. Special thanks for Mr. Y. C. WANG and Ms. T. Y. XIAO on help of metallurgy science and SEM tests, I have derived significant benefits from their extensive experience in the field of material engineering.

The financial supports from the Hong Kong Polytechnic University and the Chinese National Engineering Research Centre for Steel Construction (Hong Kong Branch) of are also acknowledged.

Last but not the least, I would like to extend my appreciation to my parents, Mr. X. K. ZHU and Mrs. W. C. CHEN, thank you for your encouragement and support on my dream of becoming a Doctor of Philosophy. I also want to say thank you to my boyfriend Mr. C. H. HSIEH, for your kind companionship and help throughout my academic pursuits.

CONTENTS

LIST OF FIGURES

LIST OF TABLES

CHAPTER ONE

INTRODUCTION

1.1. Research background

According to Eurocode, a high strength steel is a low carbon steel with a yield strength equal to at least 460 N/mm^2 and up to 700 N/mm^2. An ultra-high strength steel is a low carbon steel with a yield strength up to 1100N/mm^2(CEN 2007). Compared with common structural steel widely employed in construction, such as the S275 and the S355 steel, the high strength steel and the ultra-high strength steel exhibit considerably superior yield strengths that are two to three times of those of the normal strength steel. The high strength steel provide a cost-effective means of achieving significant savings not only in material cost, but also in various stages of fabrication, handling, transportation, and site assembly. The advantages offered by these high strength steel are readily translated into a substantial reduction in the overall carbon footprint associated with the construction industry. The benefits of adopting both the high strength and the ultra-high strength steel in design of structural systems also contribute to establishment of improved practice for sustainable construction, which are important for mitigating environmental impacts of construction activities (Amraei *et al*. 2019). Table 1-1 provides several examples of the high strength steel produced in various countries and regions. While these steel may vary in terms of their chemical compositions and mechanical properties, they are typically categorized as low carbon steel that display exceptional strength and hardness as well as good formability and weldability. The superior mechanical properties of these steel are achieved through a deliberated selection of chemical compositions and heat treatment, which work in concert to optimize their microstructure, and enhance their performance.

Table 1-1 Examples of high strength steel produced in different countries and regions

Country (region)	Standard	High Strength Steel	Quality level
China	GB/T 1591-2008	Q460, Q500, Q550, Q690	A, B, C, D, E
Europe	BS EN10025-6	S460, S500, S550, S690, S890, S960	Q, QL, QL1
America	ASTM	A992/992M, A913/913M, A514/514M	-
Japan	JISG 3106-2004	BHS500, BHS700, HT590, HT780, SA440	-
Australia	AS-NZS 36578-2011	AS3678, OPTIM 700	-

High strength steel are highly effective to be adopted as compression members, in particular, when buckling does not control, such as heavily loaded stocky columns. In contrary to those steel adopted in mechanical engineering, automotive engineering, and aerospace engineering, both the high strength and the ultra-high strength steel have not been extensively used in the construction industry. This can be attributed to a lack of sufficient scientific understanding to the effects of welding onto both mechanical properties and structural behaviour of their welded sections. In general, welding in normal strength steel such as S275 and S355 steel does not cause any significant strength reduction on the welded sections, as their microstructure does not undergo significant phase transformation after welding (Chung *et al.* 2020). Currently, the welding parameters for most high strength steel are determined primarily through experience of welders, as well as trial welding. However, there is only limited research on the metallurgical and the mechanical properties of the welded sections of the high strength steel. This knowledge gap underscores the need for a comprehensive and systematic study to investigate both the mechanical properties and the structural behaviour of those welded sections. Meanwhile, few design guidance for the high strength steel, especially for the ultra-high strength steel with a yield strength up to 960MPa, are provided in design standards. Therefore, a thorough investigation into the effects of welding onto these high strength steel is urgently needed to acquire the scientific understanding to the effects of welding onto the structural behaviour of these high strength steel, and to propose supplementary design methods for engineering applications in construction.

It should be noted that the traditional "thermal-mechanical" finite element modelling technique does not fully account for the effects of phase transformation that occurs during welding in the high strength steel. In comparison with other low carbon steel, various heat treatments and rolling processes are used to make these high strength steel with plastic deformations within the stable austenite temperature range (Rikken *et al*. 2018). The processes of welding often induce phase transformations in these steel, which may cause significant reduction in the mechanical properties in their heat-affected zones of the welded sections. During heating, the basic phase of the high strength steel undergoes a transformation to austenite, and upon cooling, it returns to its original state (Avrami 1941). These heating and cooling cycles often introduce significant microstructural changes in the heat-affected zones of the welded sections, as well as residual stresses and strains.

After an extensive search in the literature, research on the effects of welding onto the S690 and the S960 steel considering phase transformation is found to be very limited. There is an urgent need for detailed metallographic and thermodynamic experiments to obtain essential data for use in thermo-mechanical finite element models. Such experimental data are needed as input data for calibration and validation for these models which are aimed to simulate the post-welding thermo-mechanical and metallurgical responses in the high strength steel under practical welding conditions. Consequently, a new "thermo-metallurgical-mechanical-structural" finite element modelling approach is developed, which is able to simulate the effects of phase transformation after welding. After a careful calibration, the proposed approach will facilitate accurate prediction of metallurgical and mechanical responses of these high strength steel due to welding.

1.2. Research objectives and scope of works

The key objectives of this research are:

1. To obtain the continuous cooling transformation (CCT) curves of the S690 and the S960 steel, together with various critical transformation temperature, to identify specific state of phase transformations of these steel.
2. To develop a "thermo-metallurgical-mechanical-structural" numerical simulation approach for accurate simulation of the structural performance of the high strength steel welded sections considering phase transformation.
3. To measure the welding-induced residual stress on surfaces of S960 welded H-sections and box sections, and to verify consistency between the predicted and the measured data.
4. To analyse structural behaviour of the S690 and the S960 welded sections under compression.

To achieve the proposed objectives, a list of research tasks is presented as follows:

1. To conduct a total of 40 monotonic tensile tests on S690 and S960 cylindrical coupons, to measure the mechanical properties of the S690 and the S960 steel on both the steel plates and the welded sections.
2. To carry out dilatometry tests on both the S690 and the S960 steel, to obtain the CCT curves over a practical range of cooling rates, thus identify the metallurgical changes of the S690 and the S960 steel during welding process.
3. To fabricate a total of 39 S690 and S960 spliced H- and box sections according to established welding procedure specification (WPS). The section resistances, the load-shortening curves, and the failure modes of these sections are obtained using a 25,000kN electro-hydraulic servo-controlled compression test system.
4. To measure transient temperature history and residual stresses of a total of four S960 welded H-sections and box sections for calibration of the proposed simulation approach.
5. To develop a finite element modelling approach considering phase transformation

of the S690 and the S960 steel during welding, and to calibrate these models against measured temperature history and residual stresses.

6. To simulate structural performance of the S690 and S960 welded sections under compression, and to verify accuracy of the proposed models against measured data.

1.3. Methodology

Both experimental and numerical methods are used in this project, and details are:

- *Task 1: Experimental and numerical investigations into phase transformation of high strength S690 and S960 steel during welding*

In this task, the microstructure of both the S690 and the S960 steel were observed using a scanning electron microscope. Through dilatometry tests, CCT curves were obtained, and they were analysed to provide various material data on both thermo-mechanical and thermo-metallurgical properties of these steel. These material data were then integrated with a heat source model to accurately simulate welding processes of the S690 and the S960 steel using an advanced finite element package SYSWELD. After exporting numerical results of the welding simulation into another finite element simulation package Abaqus, the structural behaviour of the S690 and the S960 welded sections under compression are obtained. This approach was referred as the "thermal-metallurgical-mechanical-structural (TMMS)" finite element simulation approach, which is illustrated in Figure 1.1.

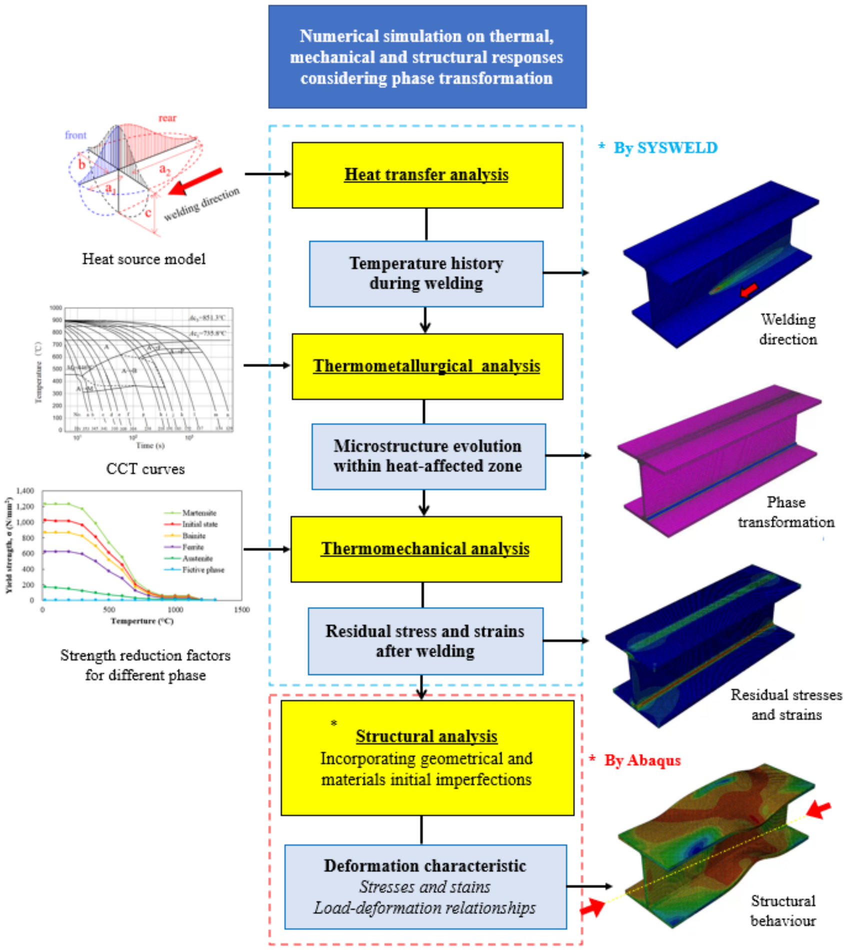

Figure 1.1 The thermal-metallurgical-mechanical-structural finite element simulation approach

- *Task 2: Full scale structural tests of S690 and S960 stocky columns under compression*

In this task, a total of twenty S690 and a total of nineteen S960 stocky columns were fabricated. Compression tests were then conducted to obtain the structural behaviour of these stocky columns. The experimental results were then compared with the numerical results of the finite element models for calibration of the proposed "thermal-metallurgical-mechanical-structural" simulation approach.

- *Task 3: Temperature and residual stress measurements on S960 stocky columns*

For the same purpose of calibrating the proposed simulation approach, transient temperature history during welding of a total of four S960 stocky columns were measured with thermocouples. Additionally, the welding-induced surface residual stresses of these S960 stocky columns were also measured with the hole drilling method. These experimental results were compared with the numerical results to demonstrate the accuracy of the proposed simulation approach.

1.4. Outline of the thesis

This thesis consists of a total of eight chapters, with each main chapter addressing a specific topic related to various examinations into structural behaviour of both the S690 and the S960 stocky columns through advanced numerical simulation. The outline of each chapter is presented as follows:

- *Chapter 1: Introduction*

  This chapter provides an introduction to the research background of this thesis. The key objectives together with the research methodology are also presented.

- *Chapter 2: Literature review*

  This chapter presents an extensive review on key research topics of high strength steel, include the welding technology of high strength steel, the numerical thermo-mechanical simulation of welding, various residual stress measurements on the S690 and S960 welded sections, and the structural behaviour of high strength steel sections under compression.

- *Chapter 3: Material properties and microstructures of S690 and S960 steel*

  This chapter presents an extensive experimental investigation into material properties of both the S690 and the S960 steel. This includes: i) characterization of both yield and tensile strengths, and ductility at room temperature obtained from monotonic tensile tests, and ii) CCT curves and related thermal properties obtained from dilatometry tests.

- *Chapter 4: Section resistances of S690 and S960 stocky columns under compression*

  This chapter presents an experimental investigation into a total of 39 S690 and S960 stocky columns under compression. It should be noted that in many of these stocky columns, there are welded splices at their mid-heights. The test results of these stocky columns were employed to demonstrate that with a proper control of welding, there is no reduction in the mechanical properties of the heat-affected zone. In addition, these measured section resistances are also employed to validate the proposed design rules for section classification which were consistent to those given in EN 1993-1-1(CEN 2005).

- *Chapter 5: Investigation into residual stresses of S960 stocky columns*

  This chapter presents an extensive programme to measure both transient temperature history and welding-induced residual stresses of a total of four S960 welded H-sections and box sections. With the use of the hole drilling method, these four sections with different plate thicknesses were examined to provide data for subsequence calibration of the proposed numerical models.

- *Chapter 6: Numerical simulation on welding of the S960 sections considering phase transformation*

  This chapter presents a series of numerical simulations on the effects of welding on the S960 welded sections considering phase transformation. Using the finite element package SYSWELD, the coupled "thermo-mechanical-metallurgical" models were developed. The simulation results including transient temperature history, welding-induced residual stresses, and post-welding phase transformation were then compared with experimental results to demonstrate on accuracy of the simulations.

- *Chapter 7: Numerical modelling on structural behaviour of S690 and S960 stocky columns under compression*

  This chapter presents an advanced numerical simulation of on the structural behaviour of the S690 and the S960 welded H-sections under compression. Based on the proposed numerical simulations described in Chapter 6, all the results of the numerical simulations of welding were imported as initial conditions into the general finite element package Abaqus to examine their structural behaviour under compression. Good comparison between the measured and predicted results of these stocky columns are successfully achieved. In addition, the numerical results without considering the phase transformation is also introduced, to demonstrate the advantage of proposed simulation approach.

- Chapter 8: Conclusions and Future Work

  This chapter summarizes key findings of the project together with and their academic merits. A plan for future work is also presented.

CHAPTER TWO

LITERATURE REVIEW

2.1. Introduction

In this chapter, a literature review of current research on the welding of high strength steel has been presented, consisting of five key parts. In each part, the literature including both experimental and numerical investigations were summarized as:

1）The gradual progress of understanding on the high strength steel and the ultra-high strength steel, especially on heat treatments and metallurgy filed. Material properties of these material and their applications on civil construction were also introduced.

2）The welding technology of both the S690 and the S960 steel, including the comparison of welding methods, research on how to develop a welding procedure specification (WPS) document, and the optimization of welding electrodes and welding parameters.

3）The numerical simulation of welding on high strength steel, including the heat source models, the thermo-mechanical approach, and some recent investigation in the thermo-metallurgical-mechanical approach using a finite element simulation package SYSWELD.

4）The investigation of welding-induced residual stress of high strength steel welded H- and box sections. Different measurement methods have been presented, and typical simplified distribution models for those H- and box sections are also introduced.

5）Finally, some recent research on the structural behaviour of high strength steel stocky columns under compression are summarized.

2.2. High strength steel and ultra-high strength steel

2.2.1. Overview

During the last fifty years, with the development of the metallurgy industry and the efficiency use of resource, the energy used to produce a ton of steel has been reduced by around 60% (Worldsteel association 2022). Figure 2.1 presents the trend of total crude steel production from 1950 to 2021. The data encompasses 64 countries and regions all over the world. In addition to the general uptrend, the growth of steel production has become more obvious since 2000. In 2021, the worldwide production of crude steel production reached 1,951 million tons, and the high strength steel takes up a significant part in it. The huge production capacity of high strength steel have allowed it to be used in a variety of engineering applications, including pipelines, machinery, mining, automotive, and more recently, construction.

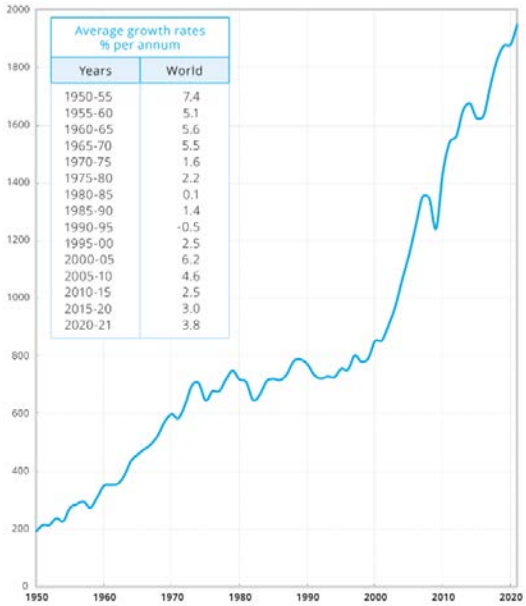

Figure 2.1 World crude steel production 1950 to 2021

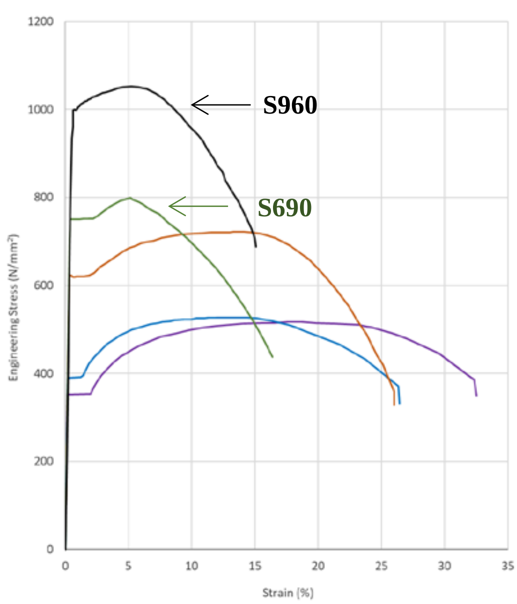

Figure 2.2 Stress-strain curves of different steel grades used in civil construction

Among the different types of steel, high strength steel is a kind of multi-phase steel that contain various phases at room temperature, such as ferrite, bainite, martensite, pearlite, retained austenite, and tempered martensite. The proportion of these phases are designed to obtain the functional characteristics of the steel. Compared to the normal strength steel, the high strength and the ultra-high strength steel have higher strength value but are usually reduced in ductility (Willms 2009). Figure 2.2 illustrates the engineering stress-strain curves of some low carbon steel used in civil construction. Compared to the normally used steel such as the S275 and the S355 steel, high strength S690 and S960 steel have higher yield and tensile strengths but exhibit comparatively reduced ductility and Y-T ratio.

Currently, commonly used high strength steel are primarily manufactured using two methods: 1) Quenching and Tempering (Q&T); or 2) Thermo-Mechanical Controlled Processing (TMCP). In these two methods, the Q&T steel undergoes a high temperature austenitization process, succeeded by rapid cooling, resulting in the formation of martensitic microstructures that significantly augment the strength. Meanwhile, TMCP is a steelmaking technique involving controlled heating, cooling, and mechanical deformation during heat treatment to optimize mechanical properties of the steel.

To compare mechanical properties of the S690 and the S960 steel, Table 2-1 and Table 2-2 summarized some measured data of the S690 and the S960 steel available in literatures obtained from experimental investigations. As shown in these tables, it is evident that the mechanical properties of the S690 steel, with thicknesses from 5 to 30 mm, and of the S960 steel, with thicknesses from 5 to 15 mm, are fairly consistent.

Table 2-1 Mechanical properties of S690 steel

Steel	Author	Plate thickness (mm)	E (kN/mm)	f_y (N/mm^2)	f_u (N/mm^2)	f_u/f_y	ε_u	δ/%
S690	Usami *et.al*	6	216	732	888	1.21	0.06	10.7
	Rasmussen *et al.*	5	210	670	775	1.16	0.09	11.2
	K. F. Chung *et al.*	6	219	782	836	1.07	0.062	17.2
		10	212	787	843	1.07	0.064	17.4
		16	212	822	867	1.05	0.068	16.9
		30	215	808	860	1.06	0.067	16.1

	J. Y. Xue *et.al*	12	211	727	814	1.12	0.065	18.2
	G Shi *et.al*	10	206	799	854	1.07	0.061	16.5

Table 2-2 Mechanical properties of S960 steel

Steel	Author	Plate thickness (mm)	E (kN/mm)	f_y (N/mm^2)	f_u (N/mm^2)	f_u/f_y	ε_u	δ/%
S960	K. F. Chung *et al.*	5	202	935	1029	1.10	0.061	15.8
		10	213	1028	1110	1.08	0.058	18.2
		15	214	1027	1102	1.07	0.058	17.4
	G Shi *et.al*	6	206	1020	1096	1.07	0.057	18.1
		8	206	963	1050	1.09	0.059	13.5
		10	206	996	1081	1.09	0.055	10.7
	H. Y. Ban	14	208	973	1052	1.08	0.049	12.5
	S. Y. Ye *et.al*	12	210	986	1032	1.05	0.045	16.6

Figure 2.3 illustrates the comparison of the f_u/f_y values and the elongation at fracture of S690 and S960. It is shown that for both the S690 and the S960 steel in the literature have an elongation at fracture of more than 10%, while some of the *fu/fy* values of the S690 steel are higher than those of the S960 steel. For both kinds of steel, this ratio is generally above 1.05.

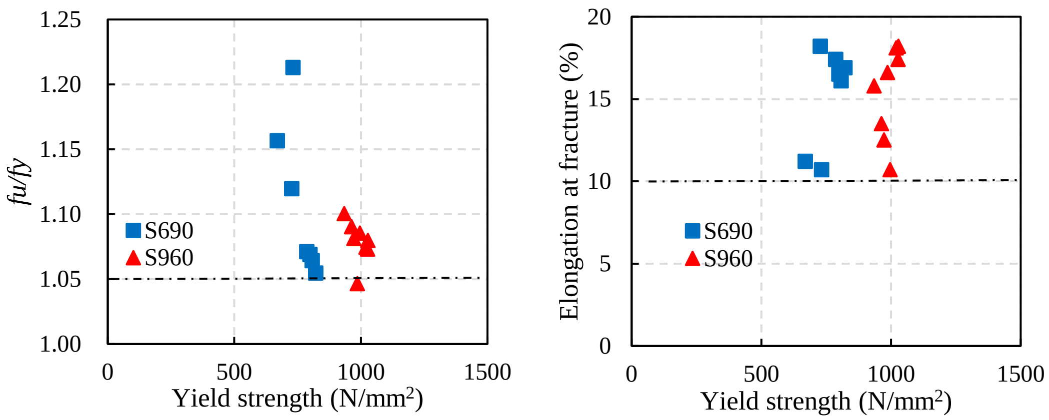

Figure 2.3 Comparison of S690 and S960: f_u/f_y and elongation at fracture

In recent years, with the application of high strength steel in construction projects, high strength steel up to 460MPa grade have become more common and has been involved into the steel standard of many countries and regions. Additionally, there has been an extensions of high strength S690 and S960 steel, in various engineering applications. In 2005, the Latitude Mansion in Australia used Bisplate 80 (with a yield strength equal to 690MPa) steel plates in its basement columns, and the roof trusses were reinforced with 650-690 MPa steel plates. Incorporating HSS in this manner resulted in reduced column sizes and excavation expenses, thereby increasing the available floor area of the building. The use of the S690 steel also important in the design of the Sony Centre in Berlin, as it allowed the designers to achieve the weight reduction, thereby reducing the number of supports required and creating a visually lightweight structure, as shown in Figure 2.4 b). Furthermore, the high strength steel allowed the roof to be suspended several stories above the building, thus minimizing additional loading on the underlying structure.

a) Latitude mansion **b) Sony Centre**

Figure 2.4 Typical building structures use high strength steel S690

In response to its characteristics of light self-weight and high bearing capacity, high strength steel has also been gradually used in bridge engineering. The Seto Ohashi Bridge in Japan used large quantities of high strength steel, including HSS with grade 600MPa, 690MPa, and 800MPa in its box-section beams and connecting members. In

2021, the Cross Bay Link bridge in Hong Kong utilized S690 steel on its box arch. This implementation not only resulted in a sleek and lighter architectural design, but also contributed to a reduced carbon footprint during the fabrication and construction phases. The adoption of S690 steel with thinner cross-sections led to reduced welding area and a shorter construction period. Consequently, the Cross Bay Link bridge now stands as the largest-span steel arch bridge in Hong Kong.

a) Seto Ohashi Bridge

b) Cross Bay Link

Figure 2.5 Typical bridge structures used high strength steel S690

The Fast Bridge 48 in Sweden is another example of the application of UHSS. It is a 48 m single-span bridge for loads up to Military Class 70 (approximately 64 metric tons). This bridge was made by UHSS S960 and S1100 as shown in Figure 2.6 (Johansson and Collin 2010). This project is a notable example of the use of UHSS in bridge construction, and the success of the project has inspired further investment in modular construction techniques around the world.

a) Load-bearing of bridge

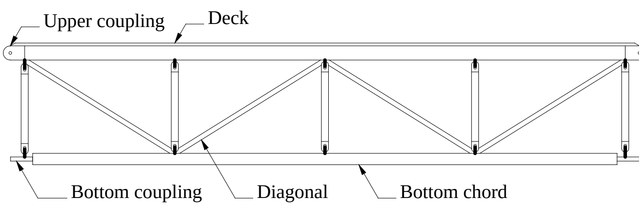

b) Schematic diagram of the truss structure

Figure 2.6 Typical bridge structures use high strength steel S960

2.2.2. Microstructure of S690 and S960

According to the interaction mechanism between dislocations and microstructures in steel materials, the mechanism of various dislocation slips has been investigated in the metallurgical industry, and various essential strengthening methods of steel can be obtained (Rheingans and Mittemeijer 2013). In summary, steel strength can be enhanced through solid solution strengthening, dislocation strengthening, substructure strengthening at product boundaries, and second phase strengthening. These methods involve incorporating solute chemical compositions, increasing crystal dislocation density, grain refinement, and the addition of a second phase, etc. (Perez 2020). Carbon interstitial solid solution strengthening stands as the most economical and efficient method to strengthen steel during the smelting process. For most HSS, martensite structures are acquired through quenching, resulting in elevated strength and hardness. The primary means of strengthening lies in the interstitial solid solution of supersaturated atoms within the martensite (Cui *et al*. 2023). With the development of metallurgical industry, the smelting of high strength steel has gradually evolved from the single Q&T (Quenching and Tempering process) method to multiple methods. All these require steel companies and scientific researchers to accurately control the chemical composition, preparation equipment, and smelting technology of steel. The production of high strength steel requires multiple smelting processes tailored to the specific steel specifications and intended usage, to meet the required material properties. The thermo- mechanically controlled processed (TMCP), direct quenching (DQ) and quenching and tempering (Q&T) process are common preparation processes (Jiang *et al*. 2019).

To ensure the strength increasing after smelting, high strength S690 and S960 steel used in this investigation are manufactured through the Q&T process. After quenching, the martensite are formed accordingly, and then turns into steady-state tempered martensite during tempering. Figure 2.7 illustrates the allotropes of austenite (γ-Fe) and ferrite (α-Fe). Similar to ferrite, austenite exhibits ductility and softness; however, its face-centered cubic structure enables it to accommodate higher carbon content compared to other steel crystal structures. As a result, austenite serves as a solid solution, frequently incorporating iron with various alloying elements. Austenitization refers to the thermal process by which steel is elevated to a temperature that induces a crystallographic transformation from initial state such as ferrite to austenite. Ferrite persists within the temperature range encompassing room temperature up to approximately A_{c1}, in a state of thermodynamic equilibrium, it initiates its transition towards austenite. Usually, carbon steel will be completely transformed to austenite at about A_{c3}. Alloying elements like Titanium, Vanadium, and Niobium hinder the growth of austenitic grains, while chemical elements such as Manganese, Phosphorus, and Sulfur accelerate the diffusion of iron atoms, leading to the expansion of austenitic grains.

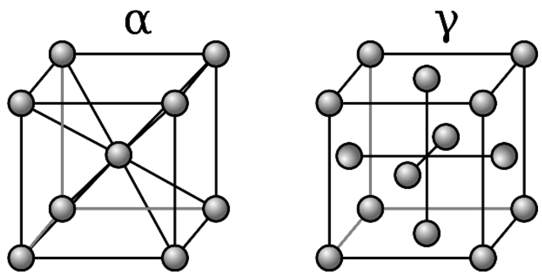

Figure 2.7 Allotropes of iron: alpha iron (Ferrite) and gamma iron (Austenite)

For carbon steel, austenite can form from pearlite in a very short time, but in HSS the time may increase a lot since the alloying elements and carbides require more time for diffusion to occur. As shown in Figure 2.8, martensite is formed by rapid cooling of austenite under conditions that inhibit its diffusive decomposition. The structure of high strength quenched steel is mainly martensite, sometimes bainite or a mixture of martensite and bainite, in addition to a small amount of retained austenite and undissolved second phase (Hsu and Xu 2007). If the steel is quenched rapidly enough from the austenitic field, the temporal constraints on diffusion-controlled compositional phenomena hinder their manifestation. Consequently, the cooling rate of steel holds paramount significance as it dictates the formation proportions of ferrite, pearlite, martensite, and other distinct phases. The relative ratios of these diverse allotropes substantiate the hardness, strength, and other essential mechanical properties of HSS.

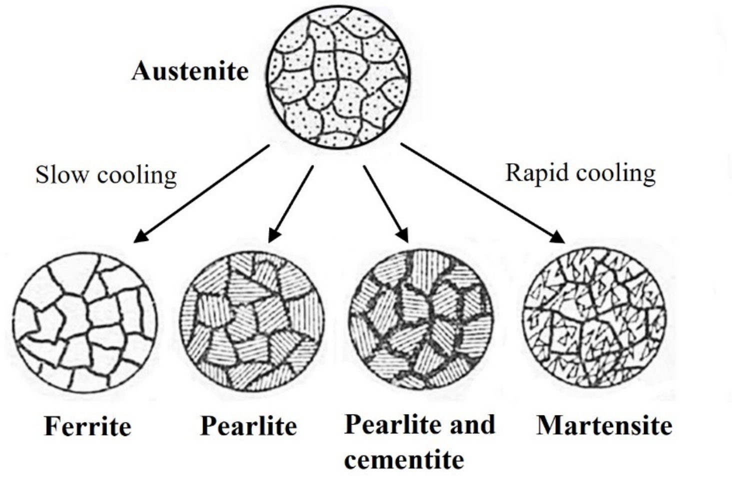

Figure 2.8 Retransformation of the austenite structure

2.2.3. Phase transformation of HSS during welding

The solid-state phase transformation during welding of high strength steel is markedly dissimilar from that of normal strength steel, owing to the impact of alloying elements and the smelting process. Some researchers have investigated the microstructural features of welded joints in HSS to infer metal phase transformations under different heat input energy, which also considered as the heating/cooling rates.

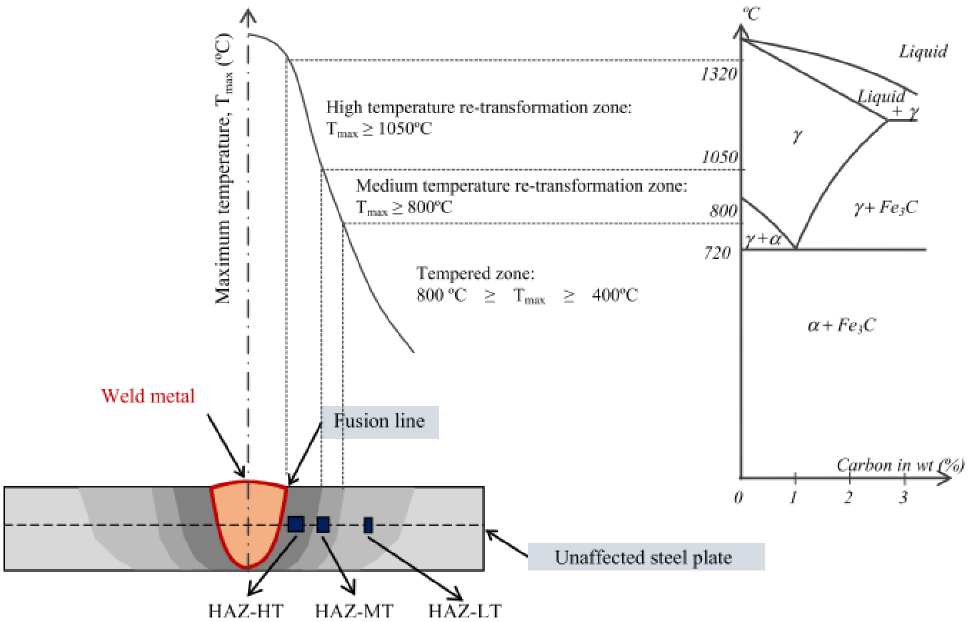

Figure 2.9 Heat-affected zones in S690 welded sections after a single pass welding

Chung *et al*. investigated into 18 S690 coupons including welded section and electrode, with varying heat input energy utilized during welding, to evaluate their mechanical properties under tension. As shown in Figure 2.9, depending on the distance from the heat source, the grains in the heat-affected zone of the S690 could have different compositions. In the S690 steel welded sections, martensite with high strengths is formed in the vicinity of the fusion line of welding, a weak zone always exists within the HAZ which controls the overall mechanical properties of the welded sections (Chung *et al*. 2020). Celin *et.al.* analysed the effect of cooling rate on the CGHAZ microstructure of S690 steel welded joints. The impact of cooling rate on the microstructure of the CGHAZ of S690 steel welded joints was compared and summarized. SEM observations revealed that martensite, formed at the highest cooling rate, was replaced by bainite at the lowest cooling rate within the CGHAZ(Celin and Burja 2018). Table 2-3 listed the influence of cooling rates on microstructure and mechanical properties of the CGHAZ. This consequence also applies to the S690 and the S960.

Table 2-3 Effect of cooling rate on microstructure and mechanical properties of CGHAZ

Cooling rate	Microstructure	Mechanical properties
High Speed	Martensite	High hardness, low toughness
Relatively high speed	Martensite + Ferrite	Strength slightly decreased; toughness increased
Medium speed	Martensite + Ferrite + Bainite	Optimum strength and toughness
Relatively Low speed	Ferrite + Bainite	Strength and toughness decrease
Low speed	Bainite	Minimum strength and toughness

In recent years, the confocal scanning laser microscope (CSLM) provide a dynamic vision of phase transformation during welding and heat treatment process, while observe the dissolution and growth behaviour of inclusions of steel. In 2020, Shen *et al.* used CSLM to investigate phase transformations and microstructural evolution of

P91 steel. It is found that γ-austenite initiates from *δ*-ferrite grain boundaries, and eventually from grain interiors (Shen, Chen, and Wang 2020). The investigation focuses on the underlying mechanism of phase transformation in high strength S690 and S960 steel, thereby furnishing a theoretical basis to facilitate the design of welding procedures for such materials. Taljat *et al.* investigated the effect of volume change due to austenitic-martensitic transformation on residual stresses, and proved that the effect of this process on the overall residual stress is not negligible (Taljat, Radhakrishnan, and Zacharia 1998). Deng and Murakawa found that the phase transformation start temperature has a significant influence on the residual stresses. For low carbon steel, the impact of phase transformation on welding deformation and residual stress will be changed due to the carbon content (Deng and Murakawa 2006). Many studies on phase transformation of low-alloy steel demonstrate that a suitable metal phase transformation kinetic model needs to be introduced, to accurately simulate post-weld deformation and residual stress after welding, therefore precise simulation of the impact of welding on HSS.

2.3. Welding of S690 and S960 steel

2.3.1. Welding technology

Welding is a process of joining by metal melting, which inevitably leads to thermal stress, residual stress, and deformation on base metal. Welded sections frequently represent the weakest points in complex structures, and the quality of the weld directly influences the structural integrity (Shome and Tumuluru 2015). In contrast to conventional structural steel, high strength steel exhibits distinct material properties that necessitate meticulous technical deliberation, particularly in relation to weldability. With the application of such metal materials, the research work on corresponding welding technology is also gradually improved. In civil engineering construction field, many welding methods are employed to cater to the diverse construction conditions and demands, ranging from submerged arc welding, gas-shielded welding, electric arc welding, etc.

First developed in the 1940s, the Gas Metal Arc Welding (GMAW) is currently the most widely employed industrial welding process, favoured for its versatility, rapidity, and simplicity of integration with robotic automation. The power source of GMAW may comprise Direct Current (DC), Alternating Current (AC), or Pulse Power Source.

As shown in Figure 2.10, the GMAW torch nozzle incorporates a specialized shielding gas diffuser for dispensing the stored shielding gas from the gas cylinder, which would cause fusion defects, porosity, and weld metal embrittlement if they encounter the electrode, the arc, or the welding metal (Gaspar and Balogh 2013). Typically, the composition of the shielding gas is determined based on the base metal and the welding process. A mixture of Ar + He is commonly utilized for non-ferrous metal welding, while CO_2 is typically utilized for steel welding. Furthermore, the welding heat and energy are enhanced by a higher CO_2 content. Therefore, a combination of Ar+CO_2 is frequently employed for welding of high strength steel.

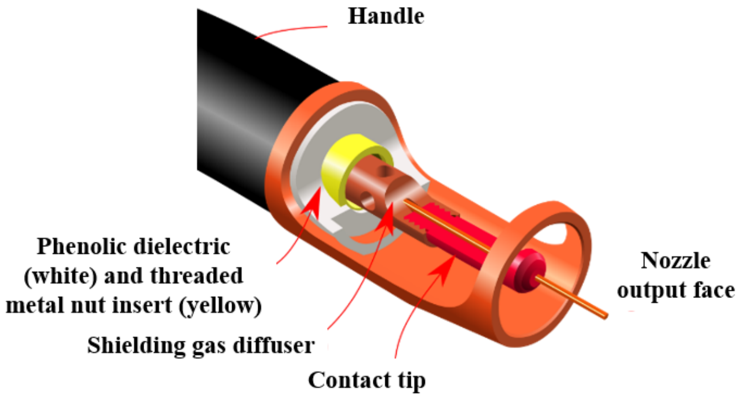

Figure 2.10 GMAW torch nozzle cutaway

Assuming that the welding current is I, the voltage between the electrode and the welding part is U, and the moving speed of the welding head is v, where η is the thermal efficiency, in welding mechanics, it reflects the heat loss caused by radiation and convection transferred to the air during welding. The heat input per unit length of the welding part, Q, can be calculated by the following formula:

$$Q = \frac{\eta IU}{v} \tag{2.1}$$

Besides, when the welding materials and weld conditions are not properly selected, cracks may also occur around weld section. The residual stresses, deformations and cracks are the main reasons for the strength reduction of structures with welding. Hence, it is critical to anticipate and mitigate these phenomena to ensure optimal structural integrity and safety.

Extensive literature and technical manuals suggest that the temporal duration of cooling between 800°C and 500°C subsequent to GMAW holds significance in delineating the weld quality of HSS. Specifically, the $t_{8/5}$ value tends to rise with higher preheating temperatures and heat inputs while decreasing with a thinner plate thickness. With a longer $t_{8/5}$ duration, the hardness and strength of the weld section and heat-affected zone will decrease accordingly (Mi *et al*. 2020). Therefore, it is significant to control the $t_{8/5}$ during welding process of high strength S690 and S960 steel. According to BS EN 1011-2(Standard 2001), the $t_{8/5}$ is calculated as:

$$t_{8/5} = (4300 - 4.3T_0) \times 105 \times \frac{Q^2}{d^2} \times [\left(\frac{1}{500 - T_0}\right)^2 - \left(\frac{1}{800 - T_0}\right)^2] \times F_2 \qquad (2.2)$$

where T_0 is the preheat or ambient temperature (normal temperature as 20℃);

Q is the welding heat input;

F_2 is the shape factor for the two-dimensional heat flow (0.9 for butt welds).

Stoschka *et al*. investigated the impact of restraint condition and clamping distance on the distribution of residual stress and distortion for welding. It shows that the application of external restraints can effectively mitigate the transverse plastic strain distribution-induced angular bending distortion, and the clamping condition of the welded structure can be quantitatively characterized by the intensity of restraint in FEM(Stoschka, Loose, and Barsoum 2016). In 2017, LIU *et al*. studied on the weld joint crack sensitivity of the Q960E by oblique Y-shaped groove welding crack test. They investigated the effect of welding process on the properties and microstructure of welded joints. The Q960E high strength steel with a thickness of 25 mm was welded under $\varphi(\mathrm{Ar})80\% + \varphi(\mathrm{CO_2})20\%$ shielded gas welding. This research study demonstrated that preheating the steel above 180°C is effective in preventing cold cracks during welding (Liu, Zhang, and Chen 2017). Analysis of the microstructure through metallographic microscopy revealed the presence of strip martensite and lower bainite microstructures typically located at the center of the weld seam, while the heat-affected zone exhibited strip martensite and granular bainite microstructures. Under same welding conditions, comparison of QT S960 and TMCP S960 was carried out by Schaupp *et al*. Utilizing the experimental results, the critical stress for crack initiation and the embrittlement index are ascertained (Schaupp *et al*. 2020). The microstructures identified in the S960 welded joint were observed to improve its strength and toughness. These studies have contributed to advancing the understanding of the underlying theories and practical applications of high strength steel welding, aiming to achieve a balance between heat input energy, welding efficiency, and weld quality.

Meanwhile, submerged arc welding (SAW) is a commonly used welding process for high strength steel structures. In this process, a protective gas shield and a slag, which may include alloying elements, are generated by a layer of powdered flux. This technique is particularly useful in controlling welding quality in the presence of thick steel plates and high heat input energy (Sharma *et al*. 2019). In recent years, in response to the challenge of decreasing the strength of welded joints, novel welding techniques have been employed in high strength steel welding applications, including gas tungsten arc welding, spot welding, electron beam welding, laser beam welding, etc. Considering the actual processing conditions and economy, in the experimental section of this thesis, GMAW with $\varphi(\mathrm{Ar})80\% + \varphi(\mathrm{CO_2})20\%$ as shielding gases was used as the welding method, to complement the steel plates with thicknesses from10mm to 30mm that employed.

To ensure the tensile strength and yield strength, high strength S690 and S960 steel used in this study is manufactured through a Q&T process. This process will cause the weld section is rendered vulnerable to cold cracking, which commonly exhibits a substantial latency period. To prevent cold cracking in welding, it is important to employ appropriate welding parameters and preheating techniques, which can reduce the vulnerability of the weld section and minimize the risk of welding joint failure. Chapter 4 of this thesis details the advancement of welding parameters with 150-200℃ preheating, which effectively mitigates the generation of cold cracks in high strength S690 and S960 steel.

2.3.2. The welding procedure specification

The welding procedure specification (WPS) is an important document that offers comprehensive instructions for welding that conform to relevant code requirements and production standards. It typically contains information that welders need to consider during welding, including the welding method, shielding gas, preheating temperature, gas flow rate, welding parameters, voltage and current, welding speed, and cooling regulations. The WPS is an essential tool to ensure consistent quality in welding and to ensure that welded components perform safely and effectively in their intended applications. The process for creating a WPS is standardized, e.g., according to ISO 15607:2019 (Standard 2019), the first step in the welding process is the development of a preliminary welding procedure specification (pWPS) by the steelworks manufacturer, which outlines general welding parameters. After conducting trial welds, the manufacturer and testing institution will perform a qualification process that results in a Welding Procedure Qualification Record (WPQR). The final WPS is then developed based on the WPQR. During the welding process, it must follow the parameters specified in the WPS, and control the heat input within the designated range (Zrilic *et al*. 2007). Upon completion of the welding, non-destructive testing (NDT) can immediately identify any welding defects and ensure overall construction quality. The quality process of WPS is shown in Figure 2.11.

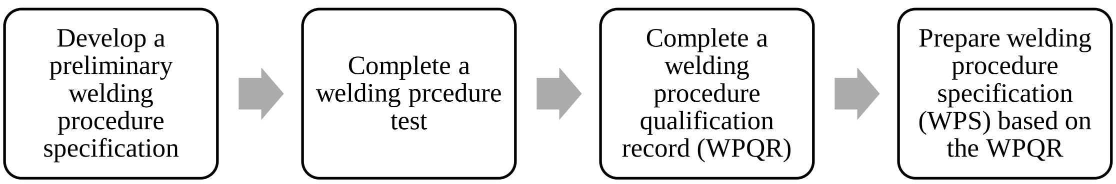

Figure 2.11 Method of qualifying welding procedures

As in the field of civil engineering, the primary aim of creating a WPS is to ensure high-quality welding while keeping the cost affordable. Therefore, in the process of developing a WPS, the selection of electrodes must be carefully evaluated to ensure both quality and cost-effectiveness.

2.4. Thermo-mechanical-metallurgical simulation of welding process

With the improvement of computer computing capability and the development of finite element technology, welding thermo-elasticity numerical simulation not only provides accurate and comprehensive residual stress filed data, but also significantly reduces the cost in experimental measurements. Consequently, the finite element method based on thermo-elasticity mechanics is gradually becoming an important method in calculating residual stresses of welded structures. The welding process results in different cooling rates and complex phase transformation in the welded sections, which conventional material models in heat transfer simulation find challenging to describe. Therefore, alternative approaches are needed to accurately simulate the multiphase transformation and mixed properties.

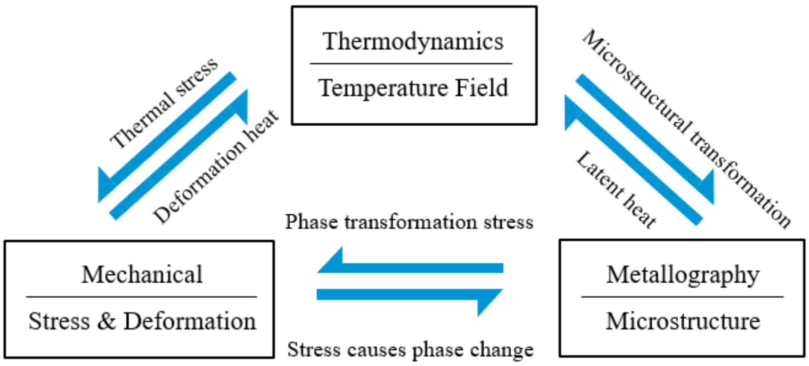

Figure 2.12 The relationship of coupling in thermo-mechanical-metallurgical welding simulation

Figure 2.12 illustrates the relationship of coupling in the thermo-mechanical-metallurgical welding simulation. The three couplings are interdependent, meaning that changes in one will affect the others. For example, high thermal input during welding may cause excessive plastic deformation and residual stresses in the material, which can lead to changes in the material's microstructure and affect its properties. The precision of numerical simulations is contingent upon the accurate depiction and characterization of the relationships between the various fields in the coupled model. During the simulation coupling process, the selection of the heat source model and phase transformation kinetic model is of paramount importance.

2.4.1. Heat source model

In the numerical simulation of welding, the selection and verification of the heat source model is a crucial step as it can differ based on the welding conditions such as electric arc welding, submerged arc welding, gas shielded welding, and others. This part of literature review provides a reference for the selection and determination of heat source models for numerical simulation of welding process in Chapter 6 of this thesis.

In 1960s, the Gaussian heat sources model were first applied in finite element calculations of welding, which approximates the heat flow density distribution of the welding arc with a Gaussian mathematical model, and the distribution function can be written as:

$$q(r) = q_m \exp\left(-\frac{3r^2}{R^2}\right) = q(x,y,t) = q_m \exp\left[-\frac{3(\xi^2+y^2)}{R^2}\right] \tag{2.3}$$

where $q(m) = \frac{3Q}{\pi R^2}$, $Q = \eta UI$, $\xi = -vt$

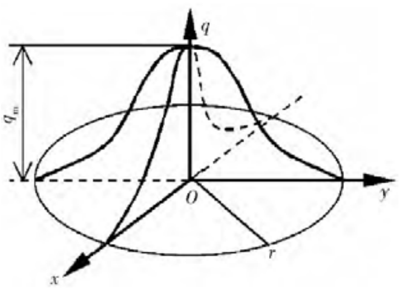

Figure 2.13 Gauss surface heat source model

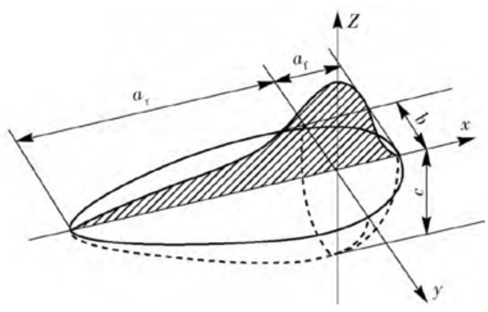

Figure 2.14 Double ellipsoid volume heat source model

As shown in Figure 2.13, The Gauss surface heat source is a circular surface heat source with radius r where the surface heat flow density $q(r)(W \cdot m^{-2})$. This surface heat source model involves fewer parameters, but only the heat flow distribution in the x and y directions are considered, while the heat flow in the thickness direction of the melt pool is neglected. In the actual welding process, the front and rear of the heat source shows asymmetry. If the Gaussian surface heat source model with front-to-back symmetry is used at this time, it will generate obvious errors (Zuo *et al*. 2020). Considering the penetration of the heat energy in the thickness of welding workpiece, based on the Gaussian surface heat source, Goldak *et al.* (Goldak, Chakravarti, and Bibby 1984) proposed a body heat source model with function of:

$$q(x,y,z,t) = \frac{6\sqrt{3}Q}{\pi R^3\sqrt{\pi}} \exp\left[\frac{-3(\xi^2+y^2+z^2)}{R^2}\right] \tag{2.4}$$

Indeed, the instantaneous welding pool is not symmetrical along the y-axis, but the front half of the temperature gradient is steeper, and the rear half of the temperature gradient is slower. Considering this factor, the semi-ellipsoidal heat source model was further improved (Lundbäck 2003), as shown in Equation 2.5, the front ellipsoid can be expressed as:

$$q(x,y,z,t) = \frac{6\sqrt{3}f_f Q}{\pi a_f bc\sqrt{\pi}} \exp\left[\frac{-3\xi^2}{a_f^2}+\frac{-3y^2}{b^2}+\frac{-3z^2}{c^2}\right] \tag{2.5}$$

The rear ellipsoid can be expressed as:

$$q(x,y,z,t) = \frac{6\sqrt{3}f_r Q}{\pi a_r bc\sqrt{\pi}} \exp\left[\frac{-3\xi^2}{a_f^2}+\frac{-3y^2}{b^2}+\frac{-3z^2}{c^2}\right] \tag{2.6}$$

where a_f and a_r are the length of front and rear semi-ellipsoid;

f_f and f_r are the energy fractions of the front and rear semi-ellipsoid, while $f_f + f_r = 2$.

The double ellipsoidal heat source model accurately describes the actual welding heat flow distribution and melt pool shape. According to Amin *et al*., the parameters a_f, a_r, b, and c could be determined based on the dimensions of melt width and melt depth of the single-pass arc weld respectively, as shown in Figure 2.15 (Azar and Akselsen 2012). Li and Lu analysed the sensitivity of those parameter in SAW, compared with residual stress results tested by hole drilling method, double ellipsoidal heat source model with calibrated parameters can provide good simulation results with an error of 3% or less (Li and Lu 2011). Jia *et al.* summarized different heat source model parameters on GMAW numerical models (Jia *et al*. 2014). Ma then investigated the influence of efficiency and heat flux distribution parameter of double ellipsoidal heat source model in automatic multiple regression analysis (Ma 2015). In contrast to C. Tsai who took f_f and f_r as 0.67 and 1.32, these two values were verified to be 0.6 and 1.4 (Tsai, Han, andJung 2006).

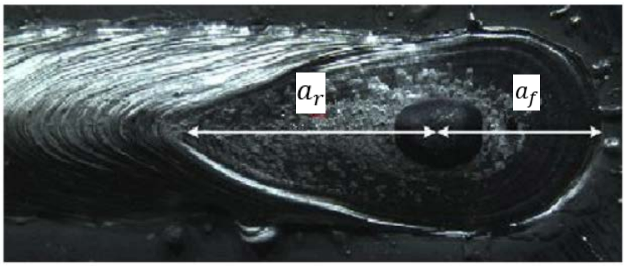

Figure 2.15 The location of a_f and a_r parameters of double ellipsoidal models

For the shielded metal arc welding (SMAW) and gas tungsten arc welding (GTAW), M. Slovácek *et al.* modified the double ellipsoidal heat source model to better match the actual temperature field test results(Slováček *et al*. 2006). In general, for both GMAW and SAW, the optimized Goldak double ellipsoid heat source model provides a good simulation of the heat transfer from heat source to metal. In the finite element modelling part of this investigation, this heat source model is selected, and specific parameters are determined by experimental measurements and heat source calibrations.

2.4.2. Thermodynamic simulation considering phase transformation

Microstructure determines material properties. When solid state phase transformation happens, the change in density generates phase plasticity, which affects the stress distribution; meanwhile, the material properties of the new phase and the parent phase are different, which also leads to changes in the stress state of the structure. The investigation of numerical simulation on stress redistribution with temperature changes is an important topic in heat treatment, quenching and tempering methods, and welding.

In 1971, Ueda and Yamakawa from Japan proposed a thermal elastic-plastic method by finite element. Considering the mechanical properties changes with temperature, they assume the temperature analysis is carried out independently before the stress analysis, and in each step of calculation, the material is influenced by the results of previous stage (Ueda and Yamakawa 1971). This approach of sequential coupling influenced the subsequent thermodynamic finite element simulation investigations. In 1974, Tatsuo and Kikuaki further developed the finite element formulation of the thermal elastic-plastic stress analysis. By introducing the coefficient of thermal expansion, a stress-strain increment relationship was involved which can be used to derive the equilibrium equation (Inoue and Tanaka 1975). Toyoda *et al.* conducted experimental and numerical works for the coupling of microstructure, material properties and temperature in the welding process, and they found that whether the model considers phase transformation has a significant impact on the stress behaviour during heating and cooling, especially when consider the martensitic phase transformation (Toyoda and Mochizuki 2004). Leblond proposed a proprietary model for diffusion-type phase transformations. The model assumes that the material's microstructure is composed of a set of discrete regions that can undergo phase transformations (Leblond 2000). This assumption results in a system of differential equations that can be used to forecast phase transformations along any thermal path.

During this stage, the understanding of thermo-stresses was still at a hypothetical and simplified level. As research into welding residual stress in such materials has progressed, it has become apparent that the traditional "thermo-mechanical" finite element modelling method is relatively inaccurate, with a significant discrepancy between simulated and measured values. For instance, if only considered the elastic modulus, yield strength, Poisson's ratio, and coefficient of thermal expansion of welded components were taken according to value of room temperature (20°C), the result of the welding simulation is not accurate enough. If the phase transformation kinetic model can accurately describe the interrelationship between the new phase and the parent phase, with temperature and time, it can predict the stress-strain relationship during welding process more accurately, as well as the effect of phase transformation on the mechanical properties of material.

The conventional methodology for delineating kinetics, as manifested in transformation curves and elucidated through modes of nucleation, growth, and impingement (Avrami 1939). Typically, the examination of nucleation rate and the analysis of TTT diagrams adequately serve the investigation of kinetic phenomena in solid-state phase transformations, with consideration an isokinetic analysis (constant velocity) for determining the volume fraction of the solid phase (f_i) isothermally using the Johnson-Mehl-Avrami equations as the transformation kinetics model (Fanfoni and Tomellini 1998).

$$\xi_A = 1 - \exp\left[-b(t - t_s)^n\right] \tag{2.7}$$

$$n = \frac{ln\left[\frac{ln(1-\xi_1)}{ln(1-\xi_2)}\right]}{ln\left(\frac{t_1}{t_2}\right)} \tag{2.8}$$

$$b = \frac{ln(1-\xi_1)}{t_1^n} \tag{2.9}$$

where t is cooling time; t_1 and t_2 are the isothermal time for the corresponding temperature;

ξ_1 and ξ_2 are the volume fraction of the generated phase at the corresponding temperature;

b, n, t_s should be determined through experiments.

For non-diffusion phase transformation (martensite transformation), the most widely used model is the Koistinen-Marburger equation proposed by D. Koistinen and R. Marburger in 1959(Koistinen and Marburger 1959).

$$\xi_M = 1 - \exp\left[-\alpha(M_s - T)\right] \tag{2.10}$$

where ξ_M is the volume fraction of martensite;

T is temperature;

M_s is the martensitic transformation start temperature; for low carbon steel, the value of $\alpha = 1.1 \times 10^{-2}(K^{-1})$.

To calibrate this model, Olson *et al.* optimized the K-M equation from the perspective of considering the probability of martensite nucleation (Olson, Tsuzaki, and Cohen 1987). Due to the influence of alloying elements in carbon steel, Jung *et al.* considered the cooling rate based on thermodynamics and proposed a model which introduced new material-related constants (Jung, Kang, and Lee 2012). Deshpande *et al.* aimed to compare the predicted results obtained from both SYSWELD and Abaqus for a combined butt joint welding and post weld heat treatment. It can be inferred that utilization of Abaqus necessitates the development of user-defined subroutines to facilitate the analysis, a task that can become notably complex in scenarios involving complex geometries and complex weld paths. Meanwhile, SYSWELD seems to need lower time for process modelling and can be considered as an alternative to Abaqus (Deshpande *et al*. 2011). Fisher *et al.* applied a recently developed Python script to transpose SYSWELD outcomes, subsequently incorporating the results into Abaqus. This integration is demonstrated through an illustrative example analysis involving a butt welding plate (Fisher and Nahshon 2015).Through this method, residual stress and distortion of welding process can be taken into account in the calculations. Specifically, this method uses the SYSWELD code to simulate the welding process and converts the results into a format that can be processed by Abaqus. Then, when performing finite element analysis in Abaqus, these results are considered as input data. Therefore, this method can more accurately predict the mechanical behaviour of welded structures and improve design efficiency. Tian *et al.* discussed FEM by Abaqus and SYSWELD used to investigate the effects of metallurgical phase transformation on welding residual stress induced by MIG butt-welding (Tian *et al*. 2017). In terms of temperature-dependent mechanical properties, it should be noted that Abaqus simulations rely only on the properties of Phase 1, whereas SYSWELD simulations utilize the properties of all three phases. The influence of metallurgical phase transformation on longitudinal residual stresses is evident in the substantial disparity in peak value and shape between the fusion zone and heat-affected zone. Moradi and Pasternak used software Abaqus and SYSWELD for the thermo-mechanical simulation of the welding process (Moradi Eshkafti 2017), followed by a compressive test. The force-displacement behaviour was plotted and analysed. Differences in transverse stresses were observed when comparing the results of both software. These discrepancies may be attributed to differences in temperature iso-surfaces and the absence of a suitable heat source model in Abaqus. Marques *et al.* provided a detailed comparison of finite element methods used in fusion welding processes(Marques, Silva, and Pereira 2020). As shown in Table 2-4, the accuracy of simplified mechanical models and thermo-mechanical models in Abaqus needed to be improved.

Table 2-4 Comparison between FEA models

Model	Material Data	Computation Time	Applicability	Quality
Thermo-mechanical-metallurgical models	Temperature dependent material data, Young's modulus, yield stress	Very high	Research	Certain—If the material data is available. Uncertain- if the material data is not available and is calculated by extrapolation.
Thermo-mechanical models	No need of temperature dependent material data	High	Research and Industry	Effective deformation prediction. Only the average stress level can be evaluated.
Simplified mechanical models	No need of temperature dependent material data	Low	Research and Industry	Effective deformation prediction.

Despite some previous research in welding engineering, current finite element simulations of welding for S690 and S960 high strength steel in structural engineering are still limited to the "thermo-mechanical" simulation level, it is essential to explore the influence of phase transformation on welding deformation and residual stresses in these materials. Hence, the selection of a suitable phase transformation kinetic model is essential for the efficient and accurate prediction of the welding effects on high-strength S690 and S960 steel.

2.5. Residual stress on high strength steel

2.5.1. Residual stress measurement techniques

Residual stresses are the stresses that remain in a component after processing, mechanical fabrication, or welding. They are a crucial factor in the structural behaviour of steel members, particularly when considering the impact of welding heat input. Tensile residual stress can have an adverse effect on material performance or component life, whereas compressive residual stress may enhance material fatigue strength (Guo *et al*. 2021). The measurement and investigation of residual stress started at the beginning of 1920s, and since then a variety of measurement methods have been developed, This classification encompasses three primary categories: non-destructive techniques, semi-destructive techniques, and destructive techniques. Table 2-5 list several measurement methods that have been summarized by Rossini *et al.*, with the measurement technique, advantages and disadvantages of each method(Rossini *et al*. 2012).

Table 2-5 Comparison of residual stress measurement methods

Categories	Measurement method	Advantage	Disadvantage
Destructive method	Sectioning	Wide range of material, economy, hand-held	Interpretation of data, limited strain resolution
Semi-destructive method	Hole drilling	Fast, easy used, generally available, hand-held, wide range of material	Interpretation of data, limited strain sensitivity
	Deep hole drilling	Deep interior stresses measurement, thick section components, wide range of material	Interpretation of data, limited strain sensitivity and resolution
Non-destructive method	X-ray diffraction	Ductile, generally available, wide range of material	Lad-based system, small components, only basic measurements
	Neutron diffraction	Macro and Micro RS, optimal penetration and resolution, 3D maps	Only specialist facility, lab-based system

Barkhausen noise	Very quick, wide sensitive to microstructure effects especially in welds	Only ferromagnetic materials, need to divide the microstructure signal from that due to stress
Ultrasonic	Generally available, very quick, low cost, hand-held	Limited resolution, bulk measurements over whole volume
Synchrotron	Improved penetration and resolution of X rays, depth profiling, fast, macro and micro-RS	Only specialist facility, lab-based systems

Depending on the measurement scale, these measurement methods are respectively aimed towards macroscopic and microscopic residual stresses, i.e., residual stresses developed in the member of structures and residual stresses existing inside the grains. In the structural engineering, most of the macroscopic steel residual stresses are still measured by hole drilling method because it's simple in operation and the result is usually stable. The mechanism of this measurement method is to drill a small hole on the surface of the component, measure the released strain through strain gauges and calculate the residual stress based on the stress-strain relationship. This method was first proposed by Mathar (Mathar 1934) in 1934, Socte and Vancormburgge then improved the measurement accuracy with employed electrical strain gauges (Socte and Vancormburgge 1950). In the following decades, some researchers have studied the stress release coefficients continuously, and try to reduce the interference of mechanical drilling on the residual stress values. In 1981, ASTM E837 initially published in the United States and has undergone subsequent revisions (Standard 2008). As illustrates in Figure 2.16, the typical hole-drilling apparatus with microscope could help to control the hole aligned concentric and depth.

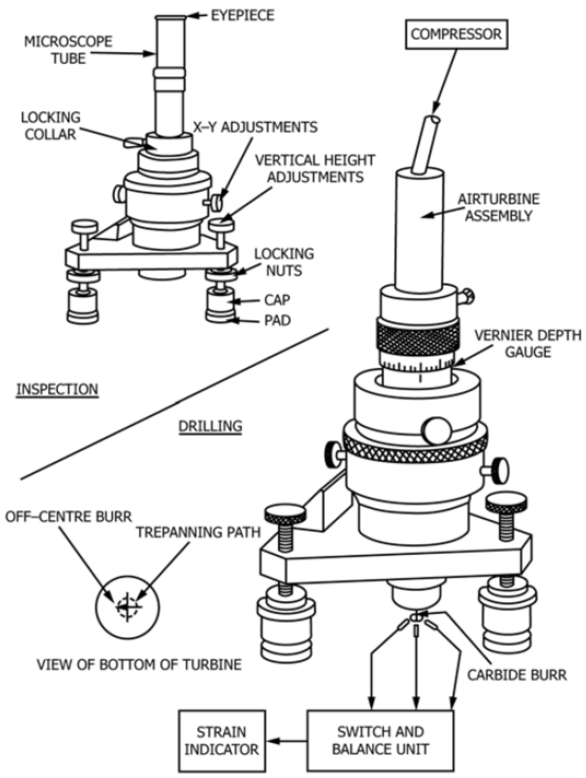

Figure 2.16 A typical hole-drilling apparatus, (a) optical device for cantering the tool holder, (b) hole-drilling tool (Owens 1993)

With the development of measurement technology, combined with optical technology, sophisticated drilling, finite element simulation and other research, the accuracy and intelligence of hole drilling method has been significantly improved in recent years. Schajer *et al* determined the optimum level of regularization that strikes a balance between the conflicting requirements of noise reduction and stress solution distortion during the process of drilling (Schajer 2007). Abraham introduced Electronic Speckle Pattern Interferometry (ESPI) into the measurements and found that hole drilling method can obtain the residual stresses along the plate thickness direction stably in medium-thick plates (Abraham 2011).Liu measured the residual stress of S690 welded H-section with reference to the ASTM, while summarized the simplified residual stress pattern of webs and flanges for single-pass welding (Liu 2017). Halabuk *et al* investigated the impact of cylindrical surfaces on the assessment of residual stresses. Despite certain errors, the hole drilling method remains viable for cylindrical structures featuring a substantial radius, with surface curvature standing out as the most significant influencing factor (Halabuk and Návrat 2022). Considering the economy, reliability, and accuracy of the experiment, in the residual stress measurement test section of Chapter 5, the investigation was carried out using hole drilling method with reference to GB/T 31310-2014 (Standard 2014).

2.5.2. Simplified distribution pattern of residual stress on high strength steel sections

Residual stresses that persist in welded components can significantly affect their structural performance. The cooling process following welding frequently results in varying cooling rates between the flange-web junctions and other sections of H-sections or box sections, resulting in localized tensile stresses in the former and compressive stresses in the latter. The heterogeneous stress field produced by these residual stresses can significantly influence the loading capacity of the component. In recent years, scholars have extensively investigated the distribution of residual stresses in welded structures made by S690 and S960 steel, outlining the impact of factors such as material properties, plate thickness, and welding procedures on residual stress values and distribution. Table 2-6 summarized some research on residual stress distribution of S690 and S960 welded H-section.

Table 2-6 Summary of research on residual stress of S690 and S960 welded H-section

Year	Steel grade	Author	Research method	Plate thickness	Conclusion
1994	690MPa	Rasmussen *et al.*(Rasmussen and Hancock 1995).	Sectioning method FEM	5mm, 8mm	Residual stress data was obtained
1996	690MPa	Beg *et al.*(Beg and Hladnik 1996)	Sectioning method	10mm, 12mm	Residual stress data (flange) was obtained
					Comparison with

					normal strength steel
2014	690MPa 960MPa	H. Y. Ban *et al.*(Ban, Shi, and Shi 2014)	Sectioning method FEM Parameter study	14mm	Residual stress data was obtained A simplified residual stress model is proposed
2018	690MPa 960MPa	L. W. Tong *et al.*(Tong, Jie, and Li 2018)	Sectioning method	10mm, 20mm	Residual stress data was obtained Comparison with normal strength steel
2018	690MPa	G. Q. Li *et al.*(Li, Li, and Wang 2018)	Sectioning method FEM Parameter study	16mm	Residual stress data was obtained A simplified residual stress model is proposed
2018	690MPa	X Liu (Liu 2017)	Sectioning method FEM Parameter study	6mm, 10mm, 16mm	Residual stress data was obtained A simplified residual stress model is proposed
2020	690MPa	W Wang *et al.*(Wang, Juan, and Yang 2020)	Sectioning method FEM	14mm	Residual stress data was obtained An equation for residual stress reduction factors at elevated

					temperatures is proposed.

Similarly, Table 2-7 summarized some research on residual stress distribution of S690 and S960 welded box section. It should be noted that the examples chosen here are all experiments where the welding seams are not located on the corners of the box, namely the selected examples only involve welding at the intersection of two flanges and two webs of the box section.

Table 2-7 Summary of research on residual stress of S690 and S960 welded box section

Year	Steel grade	Author	Research method	Plate thickness	Conclusion
1982	690MPa	Usami *et al.*(Usami, Fukumoto, and Aoki 1982)	Sectioning method	6mm	Residual stress data was obtained
1994	690MPa	Rasmussen *et al.*(Rasmussen and Hancock 1995)	Sectioning method FEM	5mm	Residual stress data was obtained
2013	960MPa	H. Y. Ban *et al.* (Ban, Shi, and Shi 2013)	Sectioning method FEM Parameter study	14mm	Residual stress data was obtained A simplified residual stress model is proposed
2016	690MPa	Khan *et al.*(Khan et al. 2016)	Neutron diffraction method	5mm,16mm	Residual stress data was obtained A simplified residual stress model is proposed
2017	690MPa	G. Q. Li *et al.*(Li, Li, and Wang 2017)	Sectioning method FEM	16mm	Residual stress data was obtained A simplified residual stress

			Parameter study		model is proposed
2017	690MPa	J. Jiang *et al.*(Jiang *et al.* 2017)	Hole drilling method FEM	16mm	Residual stress data was obtained Analysis the impact of welding process on the residual stress

From Table 2-6 and Table 2-7, previous studies have mainly focused on the range of plate thickness from 5 to 16mm. Within this range, high strength steel plates could be considered as thin plates, which means that ignoring the different distribution of residual stress in the direction of plate thickness. After obtaining the residual stresses by hole drilling method and sectioning method, some researchers summarized the simplified distribution models of welding residual stresses on high strength steel H-section and box section. Distribution patterns illustrated in Table 2-8 and Table 2-9 all for the components with non-flame cut edges. That is because the high temperature during flame cutting would leave a certain amount of stress on the edge of steel plates. In consideration of space, the specific formulae for the values of each unified model are not listed here.

Table 2-8 Distribution patterns of residual stress on high strength steel H-sections

Steel grade	Author	Residual stress pattern
1996	Prawel *et al.*	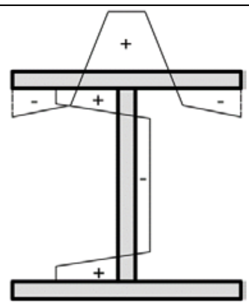

2006	ECCS	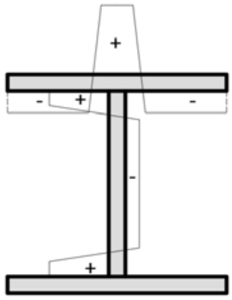
2017	GB50017	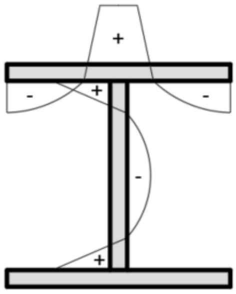
2020	Wang *et al.*	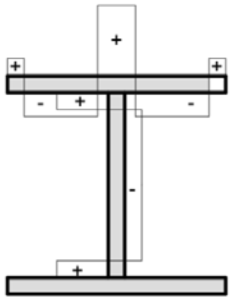

Various pattens have also been employed by scholars to describe the residual stress distributions in welded box sections. Similar to H-sections, box sections tend to have larger residual stresses concentrated at the weld joints, although the residual stresses in welded box sections exhibit a certain degree of symmetry. Table 2-9 present some investigations about the distribution patterns of residual stress on high strength steel box sections. All these residual stress distribution patterns can be used in simulations of structural performance.

Table 2-9 Distribution patterns of residual stress on high strength steel box sections

Steel grade	Author	Residual stress pattern

1976	ECCS	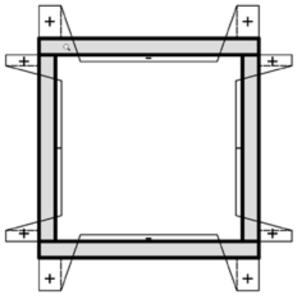
2013	Ban *et al.*	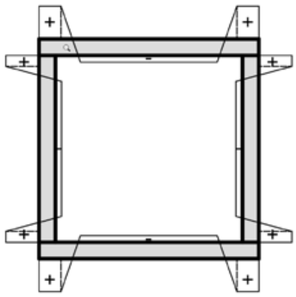
2017	GB50017	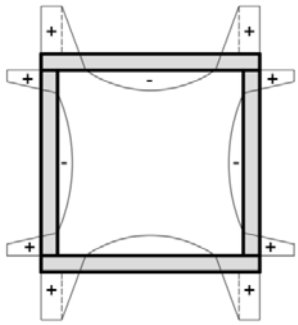
2020	Wang *et al.*	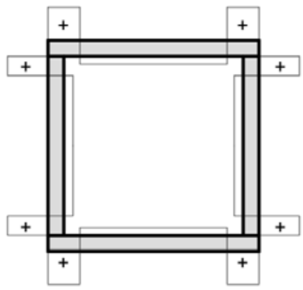

However, the simplified unified model of residual stresses used in calculating high strength steel welded sections is limited as it fails to capture the complexity of residual stress forms and disregarding the changes in value along the plate thickness. Additionally, the use of such models may result in deviations in the strength and stability of welded components, particularly when different welding processes are employed. In Chapter 5, some residual stress patterns mentioned here are compared with measured data on S960 welded sections. To simulate the residual stresses induced by welding more accurately, a new thermo-mechanical-metallurgical coupled approach is introduced in Chapter 6 of this thesis.

2.6. Local buckling of S690 and S960 welded sections

Local buckling is a phenomenon that occurs in plate elements such as flanges or webs of H-sections, when they are subjected to compression. To address this issue, conventional approaches involve designing sections to be more compact. However, high strength steel offers the potential for more economical solutions through the adoption of thinner, lighter, and longer sections. In these components, plate elements tend to be thinner and wider than those in normal strength steel members. Nevertheless, this can also result in local buckling becoming the primary design criterion instead of ultimate bearing capacity.

In this section of the literature review, recent research on axial compression tests of high strength S690 and S960 steel stocky columns is summarized. While current European and Chinese steel codes have expanded the range of steel yield strength up to 700 MPa, it is important to note that specific compression test results for high-strength steel stocky columns, particularly S960 steel, are still limited. In these codes, the column curves for axial compression are based on relevant tests and theoretical studies of columns made by steel in a lower strength.

Table 2-10 and Table 2-11 present some of the current experimental investigations on high strength steel stocky columns under axial compression.

Table 2-10 Experimental investigations of high strength steel stocky columns H-sections

Year	Steel grade	Plate thickness (mm)		Author	Number of specimens	Research method
		t_f	t_w			
1992	690MPa	8	5	Rasmussen *et al.* (Rasmussen andHancock 1992)	6	Compression test
2012	960MPa	14	14	C.C. Lin (Lin 2012)	4	Compression test FEM
2021	960MPa	12	12	X Li (Li 2021)	2	Compression test FEM

Table 2-11 Experimental investigations of high strength steel stocky columns box sections

Year	Steel grade	Plate thickness (mm)	Author	Number of specimens	Research method
2009	690MPa	6	Nishino *et al.*(Nishino, Ueda, and Tall 2009)	6	Compression test
1982	690MPa	6	Usami *et al.*(Usami, Fukumoto, and Aoki 1982)	7	Compression test
1992	690MPa	5	Rasmussen *et al*(Rasmussen and Hancock 1992).	13	Compression test
2012	960MPa	14	C .C Lin (Lin 2012)	4	Compression test FEM

Currently, the axial compression test data for S960 stocky columns are relatively scarce, and the cross-section classification is still unclear. Meanwhile, the study of welded spliced shorty columns of high strength steel is still relatively imperfect, and the effect of different heat input energy of welding on residual stress and loading capacity is still unclear. This study will fill the gap in this area of experimental investigation, and in Chapter 4, a total of 39 S690 and S960 stocky columns were tested under axial compression.

CHAPTER THREE

EXPERIMENTAL INVESTIGATION: MATERIAL PROPERTIES AND MICROSTRUCTURES OF S690 AND S960 STEEL

3.1. Introduction

This chapter concerns the experimental investigation of material properties and microstructural performance of high strength S690 and S960 steel. The monotonic tensile tests were conducted on various parent metals and weld sections of S690 and S960 to determine Young's modulus, yield strength, ultimate strength, and elongation at fracture. Furthermore, dilatometry tests and electron microscopic observations were performed to obtain the continuous cooling transformation (CCT) phase diagram and metallographic photos of these materials. These results provide insights into the unique properties of high strength S690 and S960 steel and the challenges that arise during welding, as well as offers particular evidence to facilitate the subsequent welding simulations discussed in Chapter 6.

Therefore, a total of 75 specimens and coupons were tested in this chapter, including:

- 5 specimens for microstructure observations;
- 40 coupons for monotonic tensile tests;

  (Includes 15 parent metal coupons, 4 welding electrode coupons, and 21 welded section coupons)
- 30 coupons for dilatometry tests and subsequent hardness tests.

In 2009, EN 10025-6(Standard 2009) has already defined the minimum yield strength (f_y), the tensile strength (f_u), and the minimum elongation at fracture (ε_u) of high strength steel plates with different thicknesses. The minimum impact energy (K) requirements at different temperatures are also provided, and some related data of the S690 and the S960 steel are shown in Table 3-1.

Table 3-1 Material properties requirements of high strength steel S690 and S960

Steel grade	f_y (N/mm²)			f_u (N/mm²)			ε_u	K at -
	3<t≤50	50<t≤100	100<t≤150	3<t≤50	50<t≤100	100<t≤150	(%)	20°C(J)
S690	≥690	≥650	≥630	770-940	760-930	710-900	14	≥40
S960	≥960	-	-	980-1150	-	-	10	≥40

In construction, the basic mechanical properties of high strength steel that needed to be considered include yield strength, ultimate strength, Y-T ratio, and elongation at fracture. Most of the high strength steel undergo a complex smelting and heat treatment process to achieve the required strength and ductility properties. Before a systematic investigation into welding, it is necessary to understand the production process of the high strength S690 and S960 steel involved in this study.

3.1.1. Chemical composition of high strength S690 and S960 steel

High strength steel used in civil construction require high yield strength and ductility, as well as good weldability and fatigue performance. In the metallurgical industry, different steel specifications necessitate sophisticated smelting processes to meet diverse material property requirements. The thermo-mechanically controlled process (TMCP), direct quenching (DQ), and quenching and tempering (Q&T) are some common processes in steelmaking.

The thermo-mechanically controlled process (TMCP) has been widely adopted for the production of low-alloy high strength steel in Japan and Europe. Nevertheless, the traditional quenching and tempering (Q&T) process is still indispensable for manufacturing thick steel plates that demand high strength and stability. This is due to an economic accessibility of the martensitic structure which enhances both strength and hardness of the steel. In this study, both the S690 and the S960 steel plates were produced using the Q&T process by Nanjing Iron and Steel United Co., Ltd. in Nanjing, China. Table 3-2 lists the chemical composition of the steel plates with different thicknesses. Based on the material certificates, the supplier incorporates various chemical elements such as Manganese, Cobalt, and Niobium to improve the mechanical properties of the steel. Moreover, the compositions of the metal elements in both the S690 and the S960 steel with the same grades but different plate thicknesses are essentially identical. In the S690 steel with a plate thickness of 30 mm, only the compositions of Chromium and Molybdenum are notably higher than those of other thicknesses.

Table 3-2 Chemical composition of employed S690 and S960 steel

Steel name	Plate thickness (mm)	C $\times10^3$	Si $\times10^2$	Mn $\times10^2$	P $\times10^3$	S $\times10^3$	Nb $\times10^3$	Cr $\times10^3$	Ti $\times10^4$	Mo $\times10^3$	B $\times10^4$	Cu $\times10^2$	Ceq $\times10^2$
		Chemical composition (wt%)											
Q690E	10	130	26	139	11	1	27	270	150	140	17	-	45
Q690E	16	130	25	140	15	1	27	280	150	170	17	-	46
Q690E	30	140	26	137	9	1	25	370	160	240	15	-	49
SC960E	10	160	23	102	7	1	-	439	-	557	14	3	54
SC960E	15	170	25	103	10	2	-	430	-	579	15	1	55

Among the aforementioned steel, product names and composition requirements of rare metal follow GB/T 16270-2009(Standard 2009). But according to the strength requirements of relative specifications mentioned in Chapter 1, they can all be classified as S690 and S960 steel. According to the material certificate provided by the manufacturer, these steel plates are all processed with quenching and tempering process. Typical quenching and tempering processes for high strength S690 and S960 steel are illustrated in Figures 3.1 and 3.2, respectively.

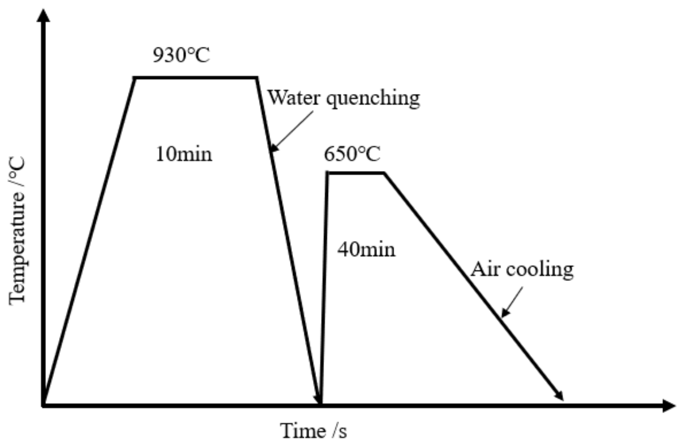

Figure 3.1 Quench and temper process of S690.

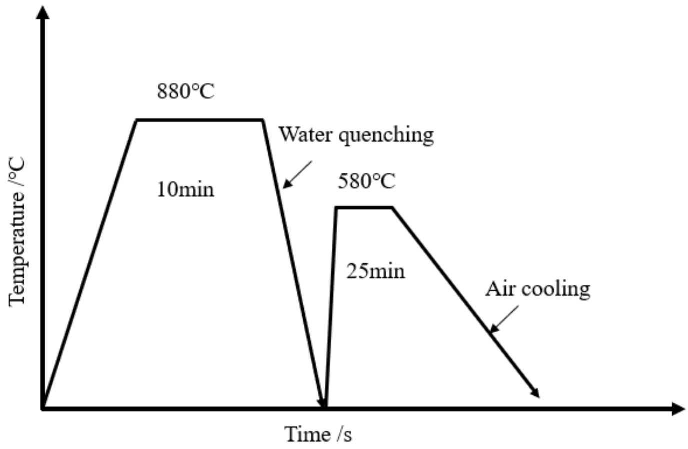

Figure 3.2 Quench and temper process of S960.

According to the manufacturer, the specific quenching and tempering operation factors such as quenching temperature, tempering temperature, holding time, etc., are confidential. Typical quenching temperature for S690 steel available in the literature is approximately 930°C, with a holding time of approximately 10 minutes, followed by tempering at 650°C for 40 minutes. For the S960 steel, the quenching temperature is typically as high as 880°C, followed by a 10-minute holding period and tempering at 580°C for 25 minutes. Generally, after the steel billet is heated and rolled, it is cooled to a specific temperature and then subjected to off-line heat treatment. During this off-line heat treatment, a roller quenching machine is employed to achieve the precise quenching temperature. Then the steel was gradually heated to just below the critical temperature. Once the required temperature has been reached, the high strength steel plate is held for a certain period. The heat relieves the internal stresses in the steel, after which the steel undergoes cooling in the air.

3.1.2. Microstructures of the S690 and the S960 steel

To determine the stable microstructure of S690 and S960 steel achieved after the specific smelting process, a series of surface etching and microscopic observations were performed to examine their microstructure. Following the needs of investigations, specimens were cut from those high strength steel plates with different plate thicknesses involved in this investigation. For each specimen, it was cut into a cuboid with a cross-sectional size of 1cm^2 (as shown in Figure 3.3). The specimen was polished with a diamond polishing agent and a nylon polishing cloth, and then put into 4% nitric acid alcohol solution to corrode for 10 seconds. Finally, the specimen was coated with a conductive gel, then observed with a tungsten thermionic emission (SEM) system as shown in Figure 3.4.

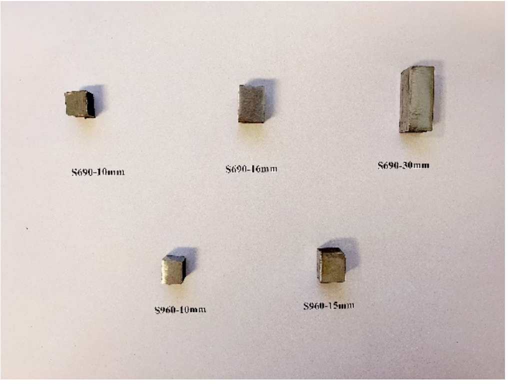

Figure 3.3 Microstructure specimens

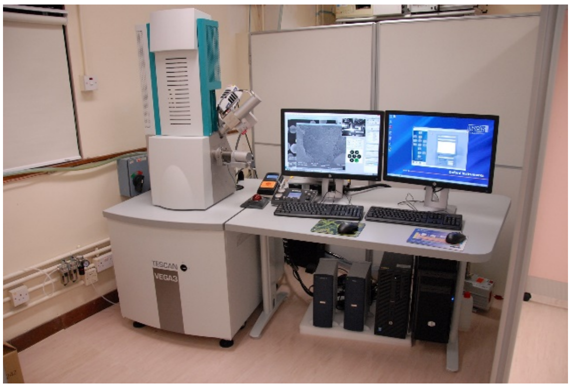

Figure 3.4 Scanning electron microscope (SEM) system

Considering the influence of rolling along the plate thickness, three positions for each specimen were observed, as shown in Figure 3.5.

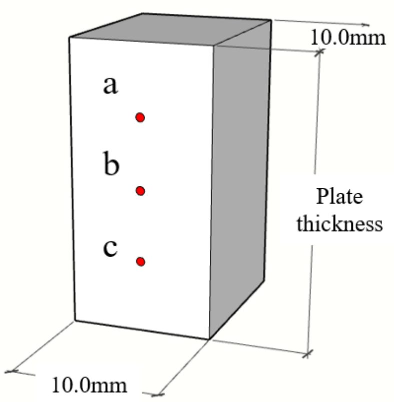

Figure 3.5 Illustration of the three observation positions on the specimen

a) the microstructure at a position 1/4 from the upper surface of the steel plate,

b) the microstructure at a position 1/2 from the upper surface,

c) the microstructure at a position 3/4 from the upper surface.

The microstructure photos of the steel plates along the thickness direction are illustrated in Figures 3.6 and 3.7. The magnification of the electron microscope is 10 μm.

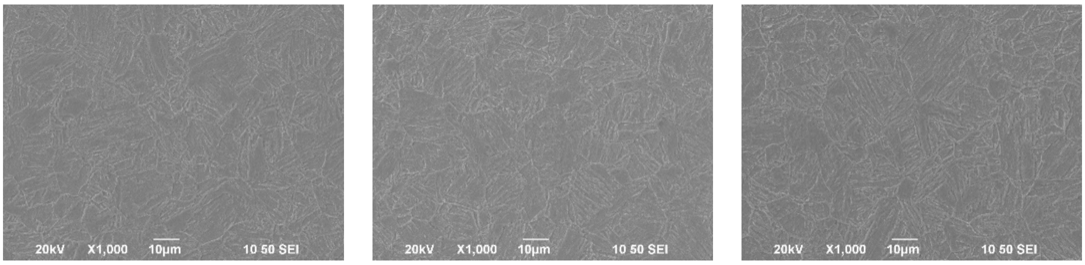

(a) (b) (c)

S690-10mm

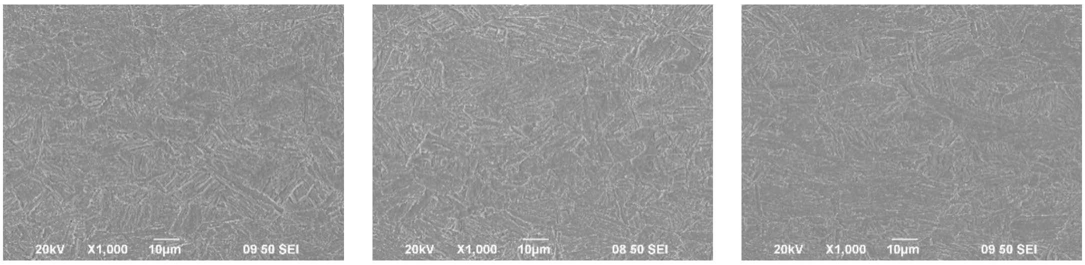

(a) (b) (c)

S690-16mm

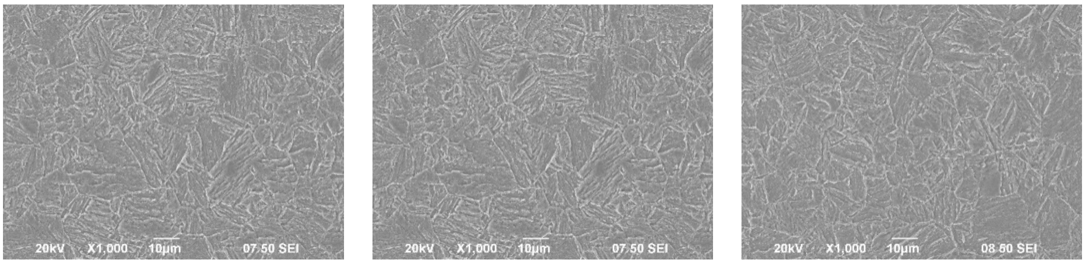

(a) (b) (c)

S690-30mm

Figure 3.6 Microstructure of S690

From the microstructure characteristics of the steel plate under the scanning electron microscope, it can be found that the high strength S690 steel under quenching and tempering has a fairly uniform and fine crystal lattice structure, and the main microstructure of the steel plate at room temperature are tempered martensite and bainite. Notably, the grain sizes of the 30mm S690 steel plate are comparatively larger than those of the S690 steel of other plates, which may be attributable to the difficulty in temperature control during the rolling process.

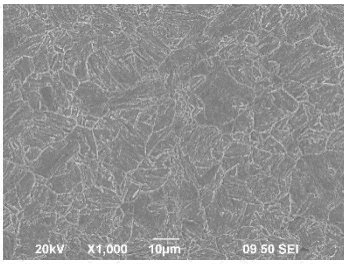

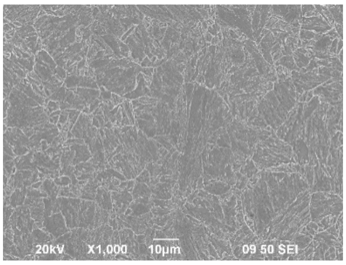

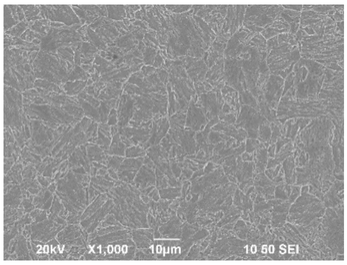

(a) (b) (c)

S960-10mm

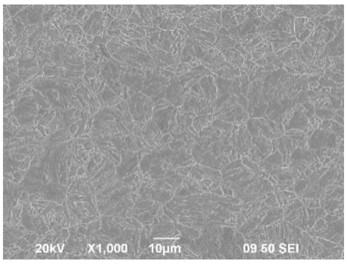

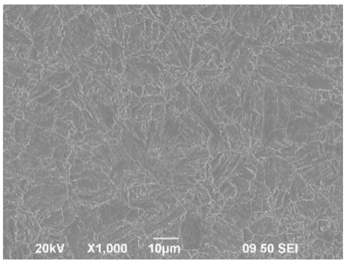

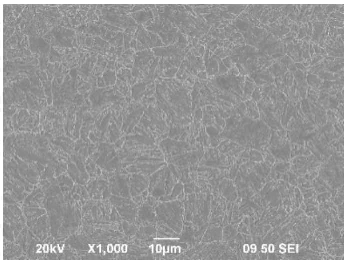

(a) (b) (c)

S960-15mm

Figure 3.7 Microstructure of S960

The microstructure analysis of S960 steel reveals that the quenching and tempering process produces a predominantly tempered martensite microstructure after cooling to room temperature, irrespective of the plate thickness at 10mm or 15mm. These observations are basically consistent with the material certificates provided by the steel supplier, and proved that the heat treatment process of Q&T steel is stable and dependable.

3.2. Monotonic tensile tests

3.2.1. Test programme

In order to characterize the mechanical properties, monotonic tensile tests are commonly utilized to obtain the engineering stress-strain curves. For a thorough understanding of the mechanical behaviour of the S690 and the S960 steel, it is important to conduct monotonic tensile tests on both the base metal and welded sections, with various levels of heat input energy.

According to Liu (Liu 2017), a total of 16 cylindrical coupons of the S690 parent metal and their welded sections as well as weld metal with different heat input energy were tested. The steel plates used in that test were the same batch as those used in this chapter, and the test programme is shown in Table 3-3. In particular, the submerged arc welding (SAW) was used due to the high processing requirements imposed by the heat input of 5.0 kJ/mm on these S690 steel plates.

Table 3-3 Test programme of S690-QT monotonic tensile tests

Coupon	Steel grade	Welding method	Welding electrode	Heat input energy, q(kJ/mm)
PM	S690-QT	-	-	-
WS-1.0		GMAW	Lincoln 121K3C-H	1.0
WS-1.5				1.5
WS-2.0				2.0
WS-5.0		SAW	Lincoln LAC-690	5.0

Note: PM denotes coupons made from parent metal plates, and WS denotes coupons made from welded sections.

Meanwhile, to investigate the mechanical properties of the S960 welded section, and to obtain specific tensile strengths of the S960 steel plates and their welded section (with heat input energy at 1.0, 1.5 and 2.0 kJ/mm), a test programme of the tensile tests on the coupons of the S960 parent metals and welded sections have been carried out, too. The test programme of the S960 steel is shown in Table 3-4.

Table 3-4 Test programme of S960-QT monotonic tensile test

Coupon	Steel grade	Welding method	Welding material	Heat input energy, q(kJ/mm)
PM	S960-QT	-	-	-
WS-1.0		GMAW	Lincoln GM120	1.0
WS-1.5				1.5
WS-2.0				2.0

Note: PM denotes coupons made from parent metal plates, and WS denotes coupons made from welded sections.

Details of coupon dimensions, fabrication process, test procedures, and test results are described as follows.

3.2.2. Specimen preparation

For the S690 and the S960 monotonic tensile tests, geometrical dimensions of the coupons were designed according to BS EN ISO-6892-1(Standard 2009). Due to different testing time and batches, the exact dimensions of these coupons also vary. The gauge lengths of the standard coupons were determined according to Equation 3.1 given in BS EN ISO-6892-1:

$$L_0 = 5.65\sqrt{A_0} \tag{3.1}$$

where A_0 is the original cross-sectional area along the parallel portion of cylindrical coupons.

For the S690 and the S960 parent plates with different thicknesses, the dimensions of PM coupons are shown in Figure 3.8. The gauge length is 25 mm.

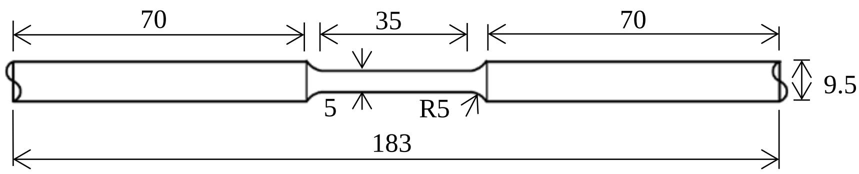

Figure 3.8 Dimensions of coupons of S690-PM and S960-PM

For the S690 welded sections, the coupons were cut from 16mm thick S690 steel plates. The dimensions of the S690 welded steel coupons is shown in Figure 3.9. The gauge length is 30mm.

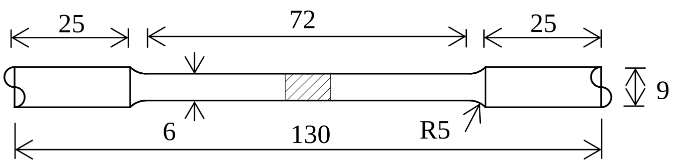

Figure 3.9 Dimensions of coupons of S690-WS

For the S960 welded sections, all the coupons were cut from 15mm thick S960 steel plates. The dimensions of the S960 welded coupons are shown Figure 3.10 and Figure 3.11. The gauge length is 25 mm. To observe the microstructure of the heat-affected zone after fracture, the weld seam was placed in an off-centre position during the manufacturing of coupons of both S960-1.5 and 2.0 series.

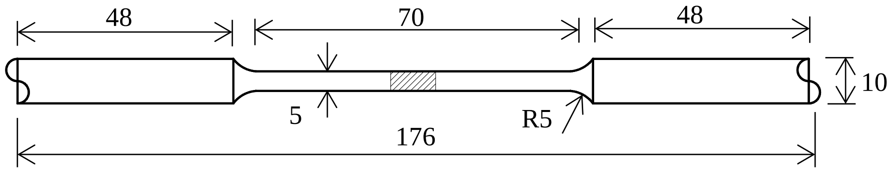

Figure 3.10 Dimensions of coupons of S960-1.0

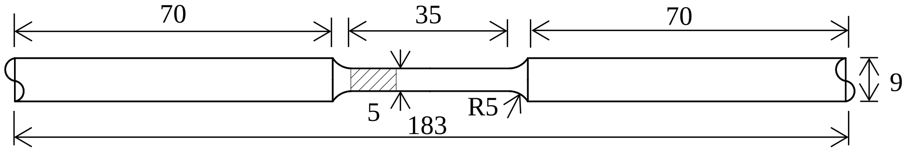

Figure 3.11 Dimensions of coupons of S960-1.5&2.0

Except for those coupons of the S690-5.0 series which were fabricated with submerged arc welding, all the coupons of welded section were fabricated with GMAW butt welded using an in-house robotic welding system. The electrode, the welding parameters and the shielding gas were specified after a number of trials. The welding parameters for the S690 steel plates are summarized in Table 3-5, and V-shaped bevels were used in all welded sections, as shown in Figure 3.12.

Table 3-5 Welding parameters for S690 welded sections

Welding type	Heat input energy, q (kJ/mm)	Voltage, U(V)	Current, I(A)	Welding speed, v (mm/s)	Efficiency μ	No. of passes	Computed heat input energy, q (kJ/mm)
GMAW	1.0	28.0	195	4.8	0.85	4	0.97
	1.5	25.9	228	3.3		3	1.52
	2.0	25.9	230	2.5		2	2.03
SAW	5.0	33.0	630	4.0	0.95	1	4.94

Note: Heat input energy $q = \mu U I v$.

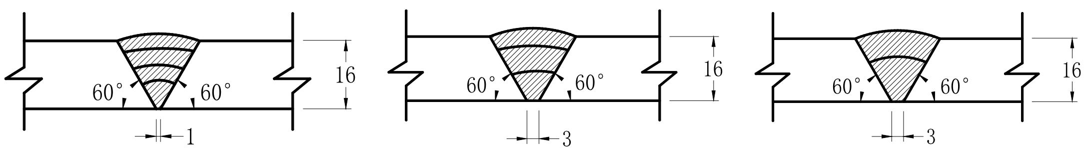

S690-1.0 S690-1.5 S690-2.0

q=1.0 kJ/mm q=1.5 kJ/mm q=2.0 kJ/mm

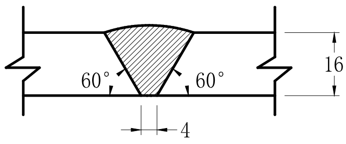

S690-5.0

q=5.0 kJ/mm

Figure 3.12 Joint details of welded sections for the S690 steel plates

Similarly, the welding parameters of the S960 steel plates are shown in Table 3-6. Being different from S690, vertical bevels were used in all the welded sections, as shown in Figure 3.13. The different welding groves design (double V shape and vertical shape) are due to the processing of different batches of coupons.

Table 3-6 Welding parameter of S960 steel plates

Welding type	Heat input energy, q (kJ/mm)	Voltage, U(V)	Current, I(A)	Welding speed, v (mm/s)	Efficiency μ	No. of passes	Computed heat input energy, q (kJ/mm)
GMAW	1.0	28.9	215	5.3	0.85	4	0.99
	1.5	28.0	207	3.3		4	1.49
	2.0	28.0	212	2.5		3	2.01

Note: Heat input energy $q = \mu UIv$.

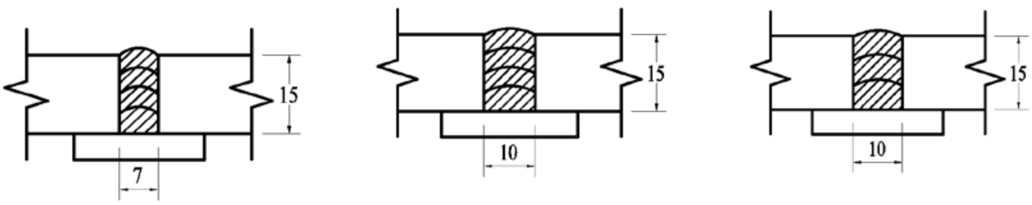

Weld section of S960-1.0 Weld section of S960-1.5 Weld section of S960-2.0

Figure 3.13 Joint details of welded sections for the S960 steel plates

All these coupons were machined with a high precision CNC system. Smoothness of the surface and parallelism of gauge length of the coupons were carefully controlled to meet the requirements given in GB/T 2975-2018 (Standard 2018). Therefore, the effect of potential high temperature on the steel was minimized during fabrication.

3.2.3. Test set-up and instrumentation

In this experimental investigation, an INSTRON 8803 Servo-hydraulic Testing System was employed to measure stress-strain curves of the S690 and the S960 coupons. The basic test set up is shown in Figure 3.14.

Figure 3.14 Test setup of monotonic tensile test

Photographs were taken during the tensile tests at 30-second intervals to capture deformation of the coupons. Two LED lights were utilized to enhance the photo brightness. Throughout the tests, a high-frequency TML AWS-50C data logger was used to record the applied load and strain values.

3.2.4. Test results

The measured material properties, including yield strengths, ultimate strengths, and the elongation at fracture of the S690 and the S960 parent metal coupons are summarized in Table 3-7. The stress-strain curves of selected coupons of each plate thickness are plotted in Figure 3.15.

Table 3-7 Mechanical properties of S690 and S960 parent metal

Coupon	E (kN/mm^2)	f_y (N/mm^2)	f_u (N/mm^2)	f_u/f_y	ε_u (%)
S690-10-1	210	774	826	1.07	16.95
S690-10-2	211	786	847	1.08	18.93
S690-10-3	214	802	857	1.07	19.35
S690-16-1	207	805	855	1.05	16.36
S690-16-2	211	819	869	1.06	16.37
S690-16-3	220	812	878	1.06	17.87
S690-30-1	211	791	841	1.06	16.60
S690-30-2	218	822	874	1.06	17.63
S690-30-3	215	813	866	1.07	15.28
S960-10-1	214	1027	1109	1.08	17.50
S960-10-2	219	1025	1107	1.08	16.03
S960-10-3	224	1032	1113	1.08	18.25
S960-15-1	219	1025	1102	1.07	17.61
S960-15-2	217	1018	1091	1.07	15.30
S960-15-3	222	1040	1114	1.07	17.35

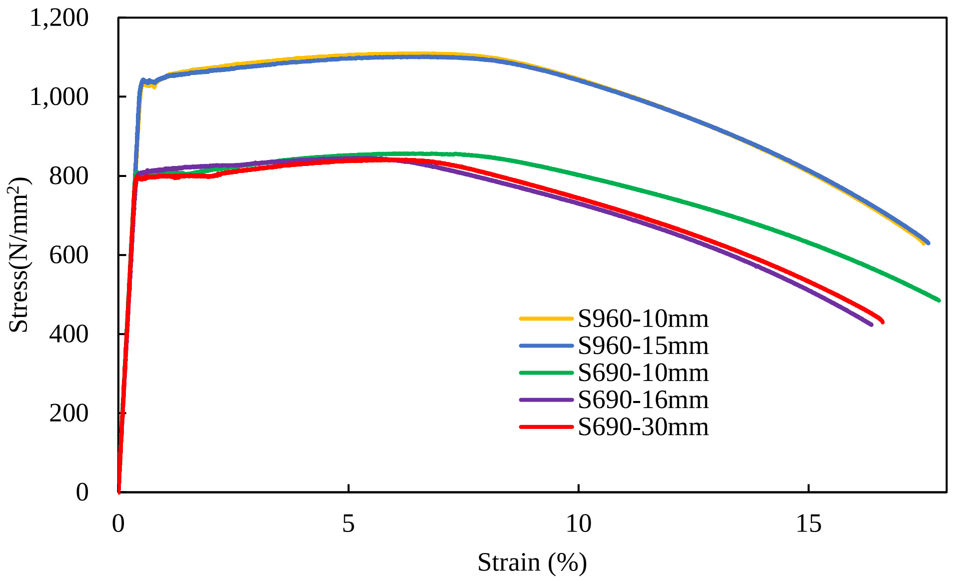

Figure 3.15 Stress-strain curves of selected S690 and S960 parent metal

It should be noted that in EN 1993-1-12(Standard 2007), the mechanical properties of S690 should meet the following requirements:

i) f_u/f_y >1.05, ii) $\varepsilon_u \geqslant 15 f_y/E$, and iii) $\varepsilon_f \geqslant 10\%$

where f_u and f_y are the ultimate strength and the yield strength of the steel, respectively;

ε_u is the elongation at tensile strength;

ε_f is the elongation at fracture.

From the test results of the parent metal, the stress-strain curves of both the S690-QT and the S960-QT materials shows a clear yield platform. The average yield strengths of the 10mm, the 16mm and the 30mm thick S690 steel plates are found to be 787 N/mm^2, 822 N/mm^2, and 809 N/mm^2 respectively. The average yield strengths of the 10mm and the 15mm thick S960 steel plates are both found to be 1028 N/mm^2. The elongation at fracture of all the S690 and the S960 coupons exceed 15%. Assuming the above requirements are applicable to the steel yield strengths greater than 700 MPa, all the S690 and the S960 parent metal investigated in this study are found to meet these requirements.

Figure 3.16 illustrates a comparison of f_u/f_y value and elongation at fracture of tested parent metal coupons. It is shown that for both the S690 and the S960 steel, elongation at fracture is more than 10%, while the f_u/f_y values are higher than 1.05. Despite the difference in yield strength, these two values are quite close for coupons made from the S690 and the S960 steel.

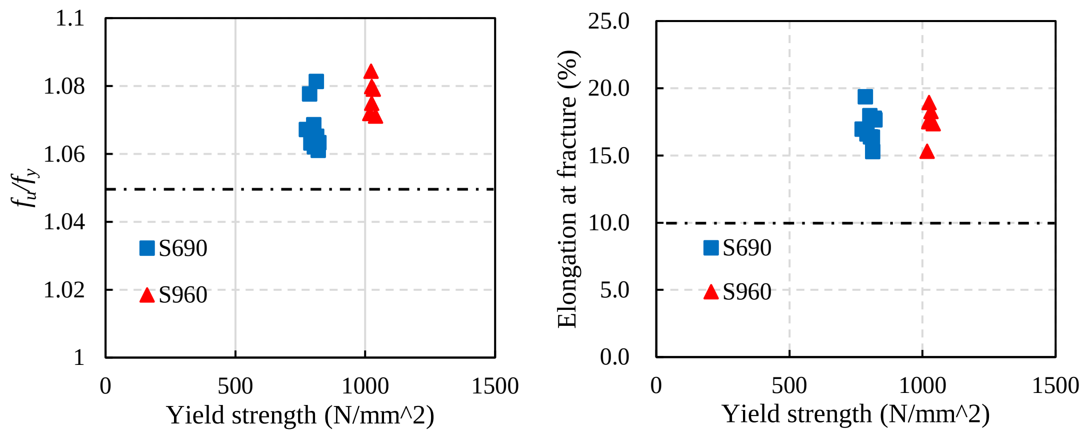

Figure 3.16 Comparison of S690 and S960: f_u/f_y and elongation at fracture

Moreover, the mechanical properties of the S690-QT welded sections with various heat input energy have been well examined. The test results of the S690 welded sections(Liu 2017) are presented in Table 3-8.

Table 3-8 Mechanical properties of S690 welded coupons

Coupons	Heat input energy (kJ/mm)	E (kN/mm^2)	f_y (N/mm^2)	f_u (N/mm^2)	f_u/f_y	ε_u (%)
690-1.0-1	1.0	207	622	723	1.16	18.0
690-1.0-2		210	611	723	1.18	18.2
690-1.0-3		211	620	720	1.16	17.3
690-1.5-1	1.5	212	693	795	1.15	10.4
690-1.5-2		211	688	784	1.14	10.0
690-1.5-3		209	677	772	1.14	10.4
690-2.0-1	2.0	205	659	744	1.13	10.0
690-2.0-2		211	661	748	1.13	9.3
690-2.0-3		206	652	745	1.14	8.9
690-5.0-1	5.0	213	810	835	1.03	17.2
690-5.0-2		210	809	857	1.06	17.0
690-5.0-3		215	808	858	1.06	18.2
Weld metal	-	210	700	820	1.17	18.0

The representative stress-strain curves of the S690 PM, WS and WM are plotted in Figure 3.17. As shown in this figure, the mechanical properties of the S690 welded sections have different reduction levels. For those welded sections with a heat input energy of 1.0 kJ/mm, the reduced yield strength is found to be 748 N/mm^2, which is very close to the yield strength of the parent metal at 761 N/mm^2. The tensile strengths of the parent metal and welded section also fairly similar. For welded sections with higher heat input energy up to 5.0kJ/mm, there is a significant reduction in both yield and tensile strengths. Table 3-9 summarizes various mechanical properties of these S690 steel welded sections.

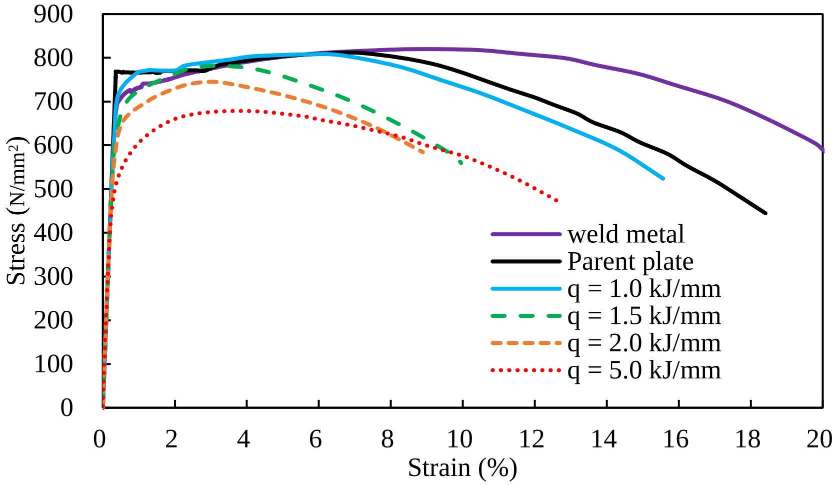

Figure 3.17 Stress-strain curves of S690 welded sections with different heat input energy.

Table 3-9 Summary of tensile test results of S690 welded sections

Coupons	Heat input energy, q (kJ/mm)	E (kN/mm²)	f_y (N/mm²)	f_u (N/mm²)	f_u/f_y	ε_u (%)
S690-1.0	1.0	209	748	808	1.08	14.2
S690-1.5	1.5	211	686	784	1.14	10.3
S690-2.0	2.0	207	657	746	1.13	9.4
S690-5.0	5.0	203	533	670	1.25	12.5
S690-PM	-	208	761	819	1.08	18.9
S690-WM	-	210	700	820	1.20	18.0

The average values of the reduction factors for various mechanical properties of the S690 welded sections are presented in Table 3-10. It is apparent that as the welding heat input increases, the mechanical properties of the welded sections are readily reduced, the most significant reduction is found in the welded section with q=5.0 kJ/mm, and a reduction in the yield strength at 30% is attained.

Table 3-10 Reduction factors to mechanical properties of S690 welded sections

Heat input energy, q (kJ/mm)	Reduction factors, α		
	Yield strength f_y	Tensile strength f_u	Elongation at fracture ε_u
1.0	0.98	1.00	0.78
1.5	0.90	0.97	0.56
2.0	0.86	0.92	0.51
5.0	0.70	0.83	0.68

Note: Yield strength ratio= f_y/f_{y_PM}, tensile strength ratio= f_u/f_{u_PM}, Elongation at fracture ratio= $\varepsilon_u/\varepsilon_{u\_PM}$.

After testing, significant necking was observed in all the coupons, as shown in Figure 3.18. It should be noted that necking occurred within the heat-affected zones of the welded sections in all tested coupons, which is also found to be typical as in literatures.

a) Overall view b) Detailed

- - - - Boundary of the weld metal
WM Weld metal
HAZ Heat affected zone
UB Unaffected base material

Figure 3.18 Deformed coupons of S690 welded sections

Similarly, tensile tests were also conducted on the S960 coupons to assess the mechanical properties of welded sections with different heat input energy. The test results of the S690 welded sections are presented in Table 3-11.

Table 3-11 Mechanical properties of S960 welded sections

Coupons	heat input energy (kJ/mm)	E (kN/mm^2)	f_y (N/mm^2)	f_u (N/mm^2)	f_u/f_y	ε_u (%)
960-1.0-1	1.0	182	947	1050	1.11	9.4
960-1.0-2		212	969	1046	1.07	10.2
960-1.5-1	1.5	206	952	1021	1.07	15.7
960-1.5-2		198	936	1006	1.07	16.6
960-2.0-1	2.0	213	955	1028	1.08	12.7
960-2.0-2		209	932	1017	1.09	16.6
Weld metal	-	199	996	1052	1.06	14.8

Test results of the S960 parent metal, weld metal, and welded sections with different heat input energy q are compared, and the stress-strain curves of these coupons are shown in Figure 3.19.

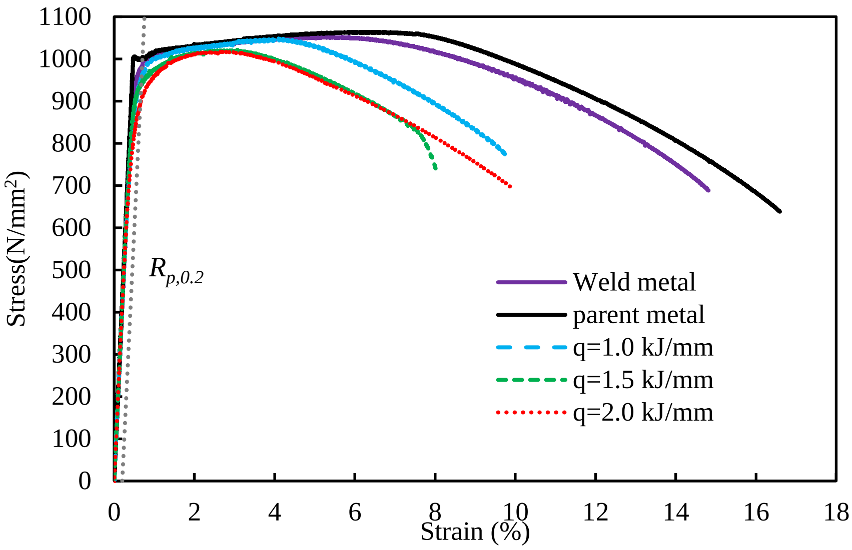

Figure 3.19 Stress-strain curves of S960 welded sections with different heat input energy

Table 3-12 summarizes various mechanical properties of these coupons, and it is shown that the mechanical properties of these welded section are reduced significantly when the heat input energy q is increased. The engineering stress-strain curves of these welded sections are plotted onto the same graph in Figure 3.19 for direct comparison. Reduction factors for various mechanical properties of these S960 welded sections are presented in Table 3-13.

Table 3-12 Summary of tensile test results of S960 welded sections

Coupons	Heat input energy (kJ/mm)	E (kN/mm^2)	f_y (N/mm^2)	f_u (N/mm^2)	f_u/f_y	ε_u (%)
S960-1.0	1.0	197	958	1048	1.09	9.8
S960-1.5	1.5	202	941	1021	1.07	16.2
S960-2.0	2.0	199	893	1017	10.9	14.7
S960-PM	-	211	1000	1063	1.06	16.6
S960-WM	-	199	996	1052	1.06	14.8

In all these S960 coupons, necking was observed to occur within the gauge length of the coupons, and the critical cross-sections were found to be fractured. Additionally, after testing, the coupons of selected welded sections were etched with a 5% nitric acid alcohol solution, and the resulting etching marks on six of these coupons are shown in Figure 3.20.

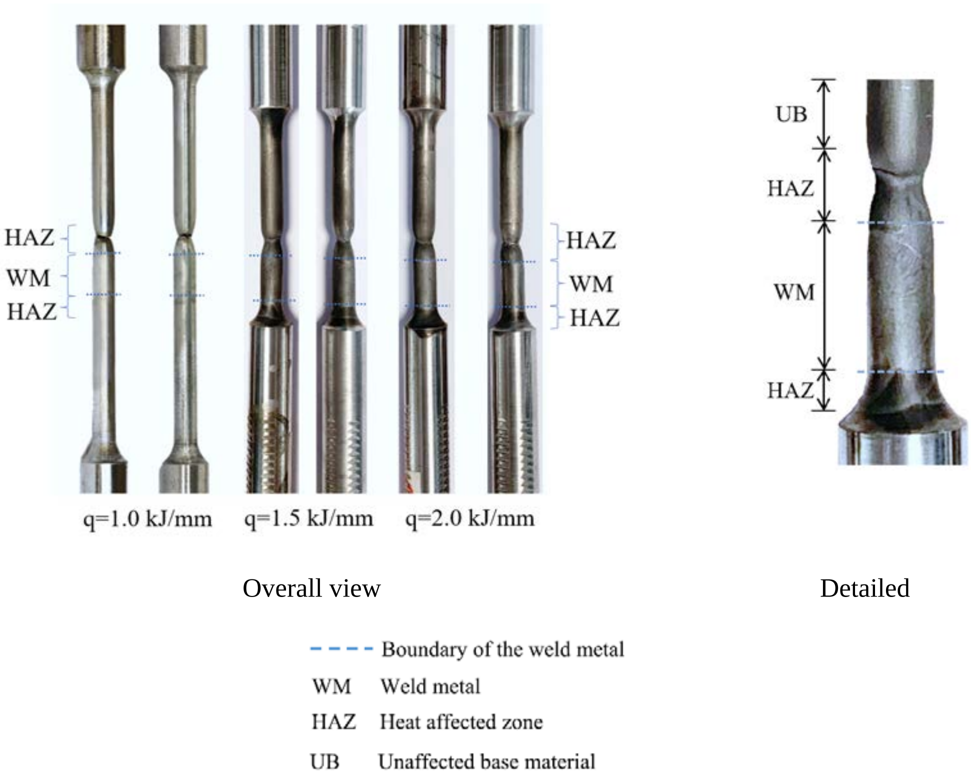

Figure 3.20 Deformed coupons of S960 welded sections

The fracture occurred within the heat-affected zones of the welded sections in all of these coupons, and no fracture was found in neither the weld sections nor the parent metal. These results suggest that the welded sections of the S960 steel plates under investigation are susceptible to fracture within the heat-affected zones. It seems to be appropriate to draw attention to engineers about this possible failure mode.

Table 3-13 Reduction factors for S960 welded sections

Heat input energy, q (kJ/mm)	Reduction factors, α		
	Yield strength f_y	Tensile strength f_u	Elongation at fracture ε_u
1.0	0.96	0.99	0.59
1.5	0.94	0.96	0.48
2.0	0.89	0.96	0.60

Notes: Reductor ratio= f_y/f_{y_PM} for yield strength, reductor ratio= f_u/f_{u_PM} for tensile strength, reductor ratio= $\varepsilon_u/\varepsilon_{u\_PM}$ for elongation at fracture.

It should be noted that the reduction factors for yield strengths (at 0.2% proof strains) of the welded sections with q=1.0, 1.5, and 2.0 kJ/mm are found to be 0.96, 0.94 and 0.89, respectively; the reduction factors for tensile strengths of the welded sections with q=1.0, 1.5, and 2.0kJ/mm are found to be 0.99, 0.96 and 0.96, respectively. In short, after controlling the heat input energy, the strength reduction of the welded sections on the S960 steel is found to be in an acceptable range. According to the given welding parameters, when the welding heat input energy lies within the range of 1.0 kJ/mm to 2.0 kJ/mm, a reasonable control is readily achieved for both the S690 and the S960 steel. The results obtained in this part will be used in subsequent developments of welding procedure specifications and the finite element models.

3.3. Dilatometry tests

3.3.1. Test programme

The continuous cooling transformation (CCT) phase diagram is often used in heat treatment and welding process of structure steel. It illustrates various phases of the steel when it is cooled at different rate(Avrami 1941). Generally, CCT curves describe the extent of phase transformation of the steel as a function of time for a continuously decreasing temperature. In other words, a sample of the steel is first austenitised, then cooled at a predetermined rate, and the degree of phase transformation is measured. A series of dilatometry tests were carried out, to measure the phase transformation of the steel during welding, and to obtain data for phase transformations. Table 3-14 presents the test programme of the S690 and the S960 dilatometry tests.

Table 3-14 Test programme of the S690 and the S960 dilatometry tests

Steel grade	Cooling rate (°C/s)	Total nos. of coupons
S690	70	14
	50	
	30	
	20	
	15	
	10	
	5	
	2.5	
	2	
	1.5	
	1	
	0.6	
	0.25	
	0.15	
S960	100	16
	70	
	50	
	30	
	20	
	10	
	5	
	3	
	2	
	1	
	0.5	
	0.3	
	0.15	
	0.1	
	0.05	
	0.025	

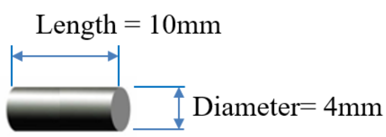

Figure 3.21 Typical dimension of dilatometry test coupons

The test programme was basically designed with reference to a literature(Grajcar *et al*. 2014). For both the S690 and the S960 steel, coupons were heated to a temperature of 900°C at a constant rate of 1°C/s and held at that temperature for a duration of five minutes. Following this, the coupons were cooled at different rates as shown in Figure 3.22. After complete cooling, the coupons were etched with a 4% nitric acid alcohol solution for 10 seconds, and then washed with ethanol to remove any surface residue. The coupons were then air-dried for subsequent microscopic observations. Since only the grain size and phase distribution were required, without the need for observing the microstructural details such as dislocations on the coupons, an optical microscope was employed for the observation.

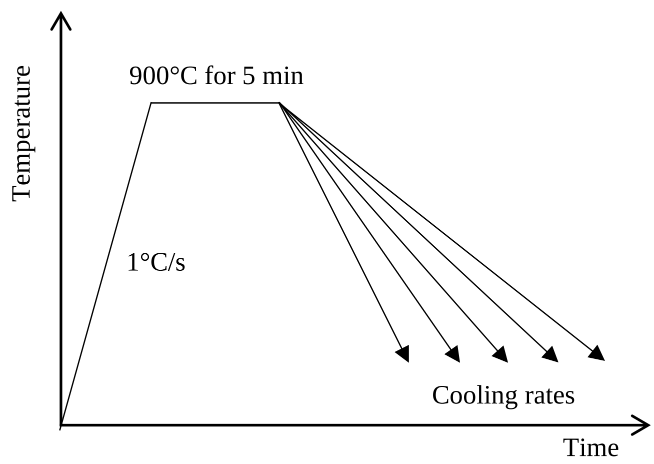

Figure 3.22 Schematic illustration of the schedule for dilatometer tests

According a reference paper(Wang *et al*. 2014), a total of 14 different cooling rates from 70°C/s to 0.15°C/s were applied onto the S690 coupons, while a total of 16 different cooling rates from 100°C/s to 0.025°C/s were applied onto the S960 coupons. For all the coupons after the thermal expansion measurements, hardness tests were also carried out to determine the effect of cooling rates on hardness. The equipment together with a schematic diagram on hardness tests are shown in Figure 3.23.

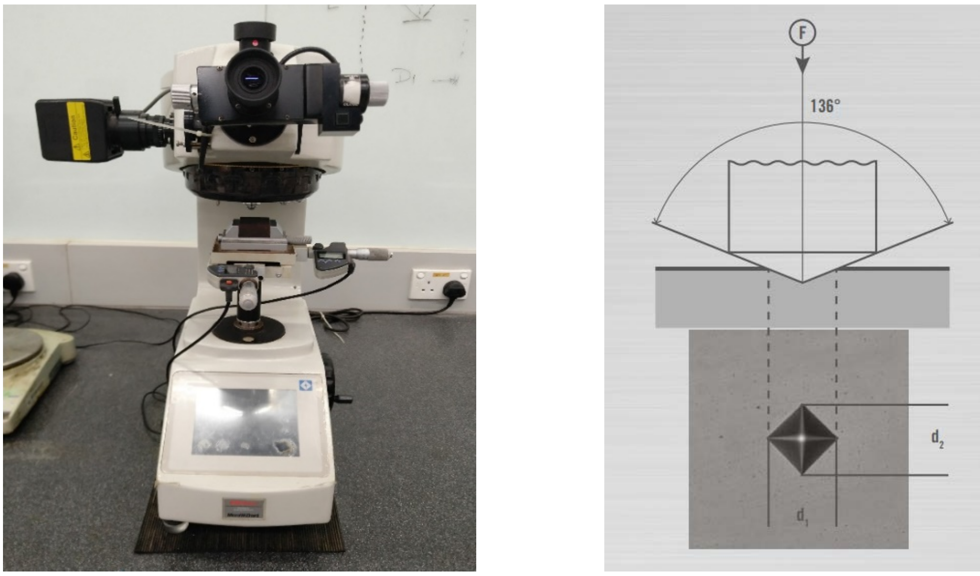

a) Overall setups b) Schematic diagram of hardness tests

Figure 3.23 Equipment and schematic diagram on hardness tests

3.3.2. Test set-up and instrumentation

Both the S690 and the S960 specimens were machined from 16mm and 15mm thick steel plates, respectively. The chemical composition of the S690 and the S960 steel plates used for dilatometry test coupon are shown in Tables 3 15 and 3 16.

Table 3-15 Chemical composition of S690 coupons

Steel	Chemical composition (wt%)										
	C	Si	Mn	P	S	Nb	Cr	Ti	Mo	B	Ceq
	$\times 10^3$	$\times 10^2$	$\times 10^2$	$\times 10^3$	$\times 10^3$	$\times 10^3$	$\times 10^3$	$\times 10^4$	$\times 10^3$	$\times 10^4$	$\times 10^2$
S690-QT	130	25	140	15	1	27	280	150	170	17	46

Table 3-16 Chemical composition of S960 coupons

Steel	Chemical composition (wt%)									
	C	Si	Mn	P	S	Cr	Mo	B	Cu	Ceq
	$\times 10^3$	$\times 10^2$	$\times 10^2$	$\times 10^3$	$\times 10^3$	$\times 10^3$	$\times 10^3$	$\times 10^4$	$\times 10^2$	$\times 10^2$
S960-QT	170	25	103	10	2	430	579	15	1	55

The test coupons were machined into small cylinders with a diameter of 4 mm, and a height of 10 mm, as shown in Figure 3.24. The test was carried out in a L78-RITA quenching and deformation dilatometer at the department of Mechanical Engineering in the University of Hong Kong.

Figure 3.24   Typical coupons for dilatometry tests

During the dilatometry test, the coupon was placed securely onto a sample holder with one end in contact with a pushrod, and then placed inside a furnace where it was subjected to a predefined temperature profile of heating and cooling. A highly precise displacement sensing system was employed during the test to measure the linear dimensional changes of the coupon, i.e., undergoing either expansion or contraction. After the test, the coupon was then examined with an optical microscope to assess its finial microstructure phase, as shown in Figure 3.25.

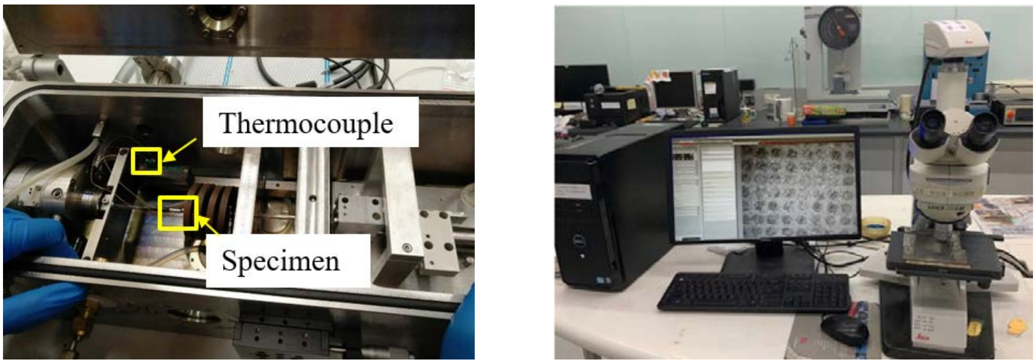

Figure 3.25   Thermal Dilatometer and optical microscope used in dilatometry tests

3.3.3. Test results

The dilatometric curves were obtained after data analysis on the measurements of thermal expansion tests. Hence, the phase transformation temperatures of the S690 and the S960 steel are estimated after analysing various inflexions of the curves, the critical temperature, namely, A_{c1}, A_{c3} and M_s are then determined simultaneously. Figure 3.26 illustrated the dilatometric curves of S690 steel coupons under different cooling rate. Cooling rates from 70°C/s to 0.15°C/s are marked at the lower right corner of each image.

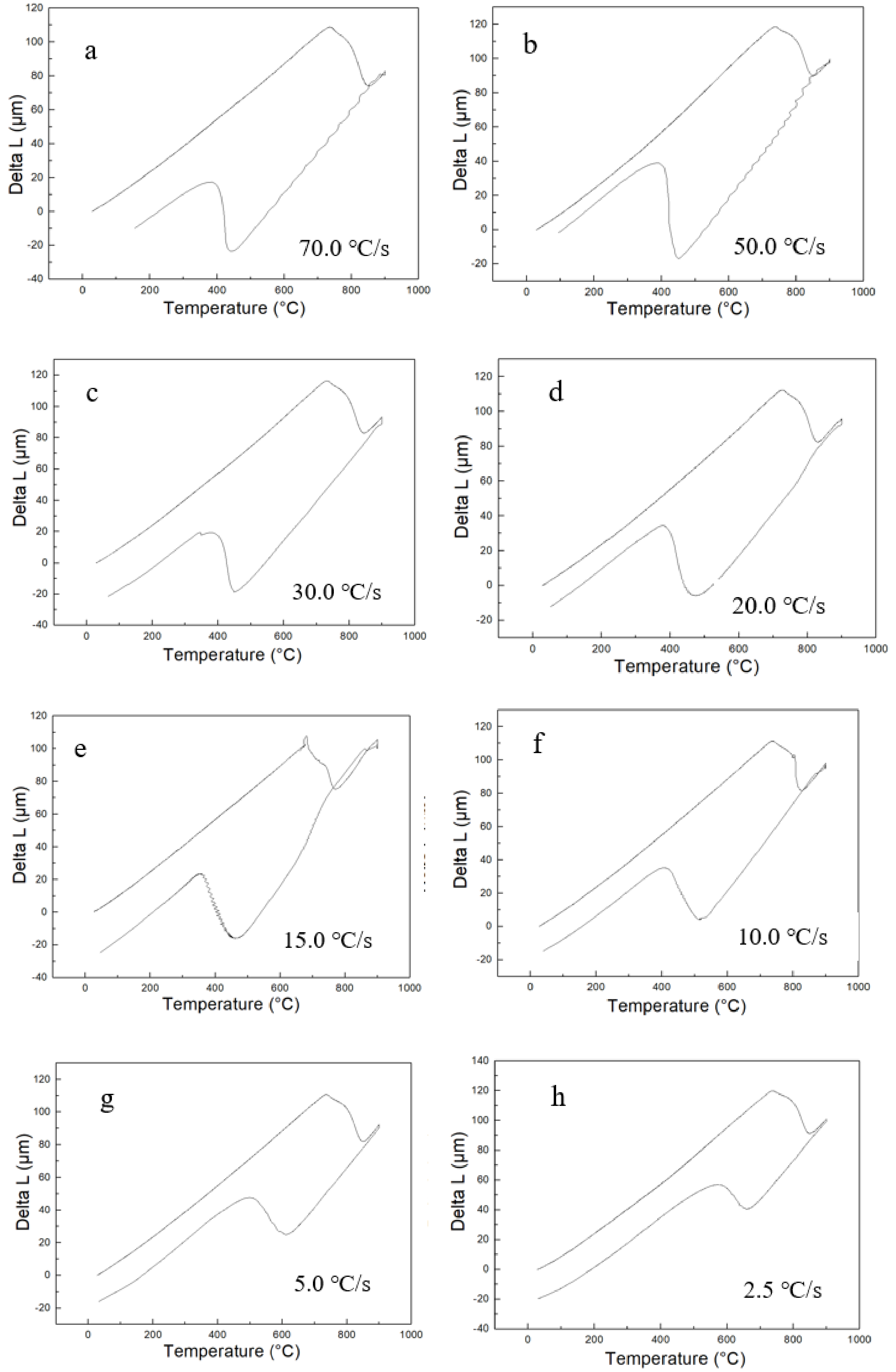
a
70.0 °C/s
b
50.0 °C/s
c
30.0 °C/s
d
20.0 °C/s
e
15.0 °C/s
f
10.0 °C/s
g
5.0 °C/s
h
2.5 °C/s
Delta L (μm)
Temperature (°C)

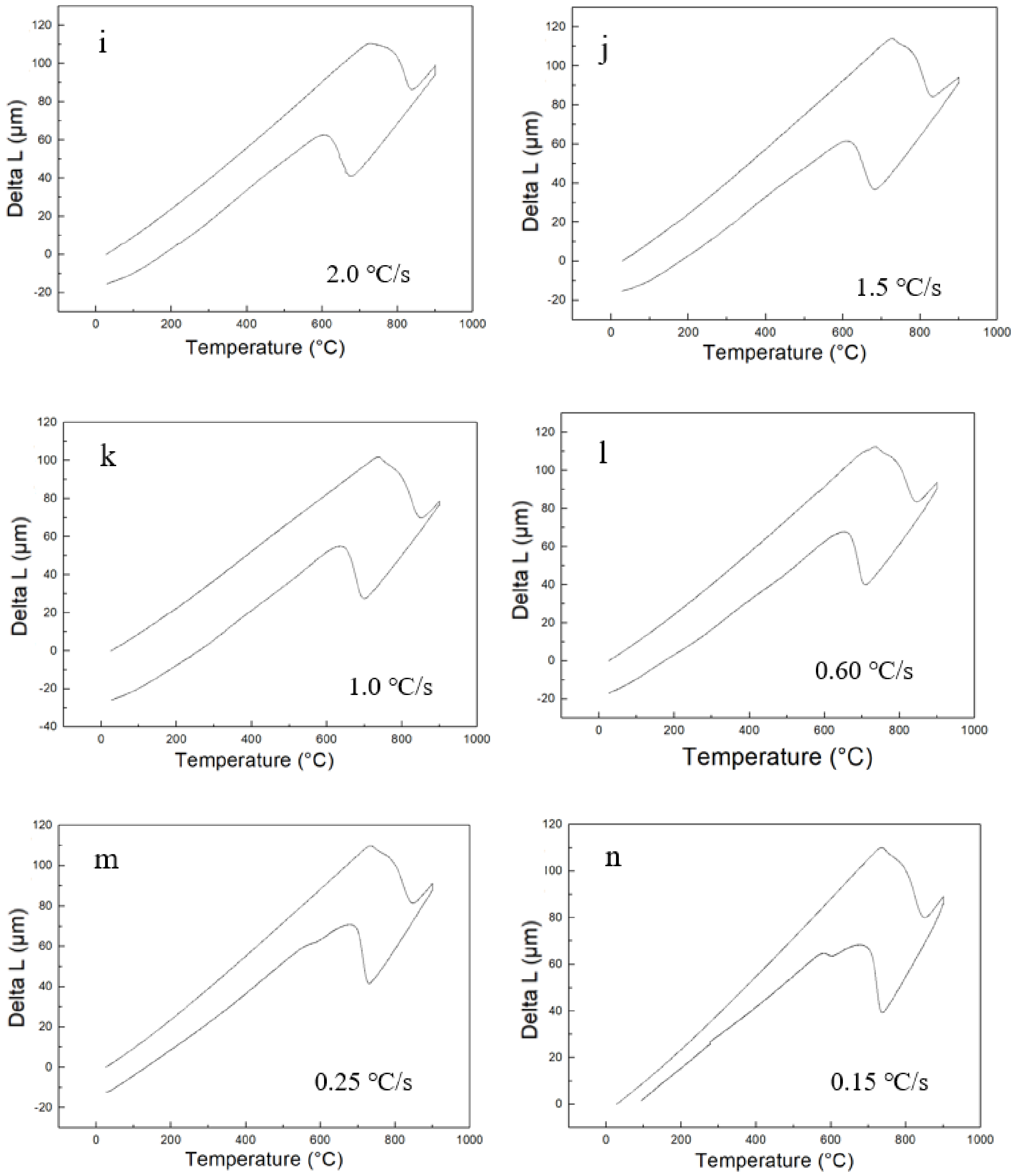

Figure 3.26 Dilatation curves of S690 steel obtained from different cooling rates

The metallographic results of the S690 steel have been successfully obtained through electron microscope observations on the coupons after surface etching. Figure 3.27 illustrates all the SEM images of the S690 coupons after thermal expansion tests. As shown in Image. b of Figure 3.27, at a cooling rate of 50°C/s, the main phase of S690 specimen is martensite. When the cooling rate is 10°C/s (Image. f), minor bainite appears. At a cooling rate of 2°C/s (Image. i), the main phase becomes ferrite, bainite and pearlite. For the slowest cooling rate 0.15°C/s, in Image. n, only bainite and ferrite were observed.

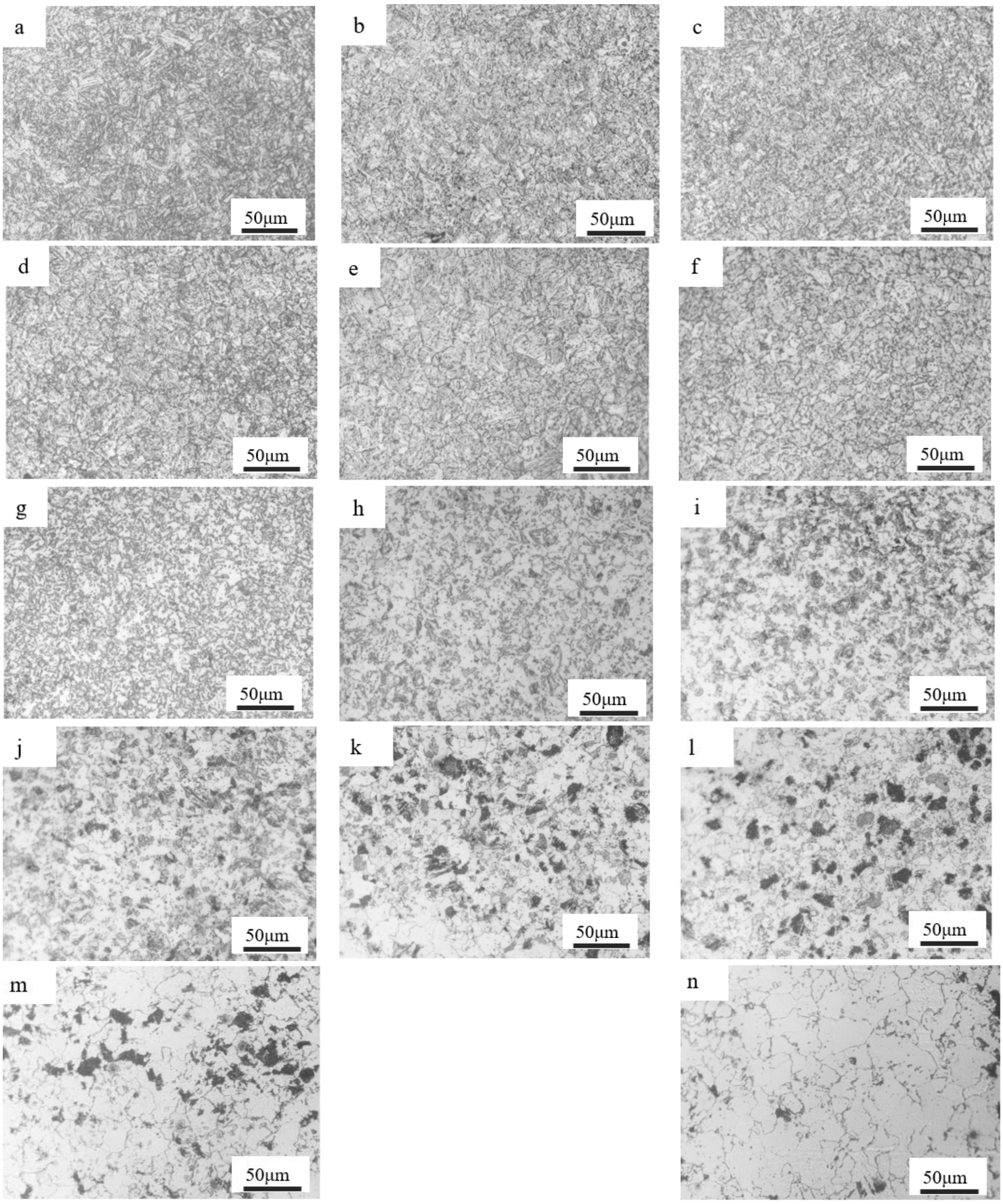

Figure 3.27 Metallography test results of the S690 steel

According to the dilatometric curves illustrated in Figure 3.26, and the microstructure images illustrated in Figure 3.27, the continuous cooling transformation curves of the S690 steel are plotted in Figure 3.28. The A_{c1} and A_{c3} temperatures for the S690 steel are then determined to be 735.8°C and 851.3°C, respectively. These temperatures are critical in the phase transformation of austenite from ferrite, where A_{c1} indicates the initiation of the transformation process while A_{c3} represents the completion of the transformation. Understanding these critical temperatures is important for predicting the microstructure of the S690 steel, as well as for determining appropriate heat treatment processes and welding conditions, for example, determining a reasonable range of inter-layer and pre-heating temperatures.

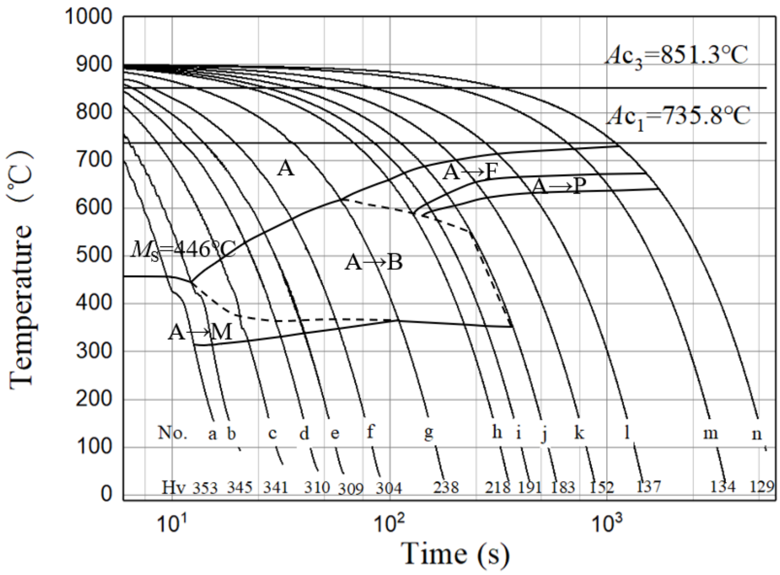

Figure 3.28 CCT curves of the S690 steel

Table 3-17 summarized the critical cooling time $t_{8/5}$, cooling rates and the phase composition of each of these CCT curves.

Table 3-17 Data of S690 CCT curves

No.	$t_{8/5}$ (s)	Cooling rates (°C/s)	Phase composition
a	4	70.0	M100
b	6	50.0	M100
c	10	30.0	B10+M90
d	15	20.0	B50+M50
e	20	15.0	B55+M45
f	30	10.0	B70+M30
g	60	5.0	B100
h	120	2.5	F30+B70
i	150	2.0	F35+P5+B60
j	200	1.5	F40+P7+B53
k	300	1.0	F72+P28
l	900	0.6	F79+P21
m	1200	0.25	F82+P18
n	2000	0.15	F85+P15

The hardness test results of all the coupons were shown in Figure 3.29 and Table 3-18. It is shown that, the hardness of these coupons is gradually reduced when the cooling rates are decreased correspondingly.

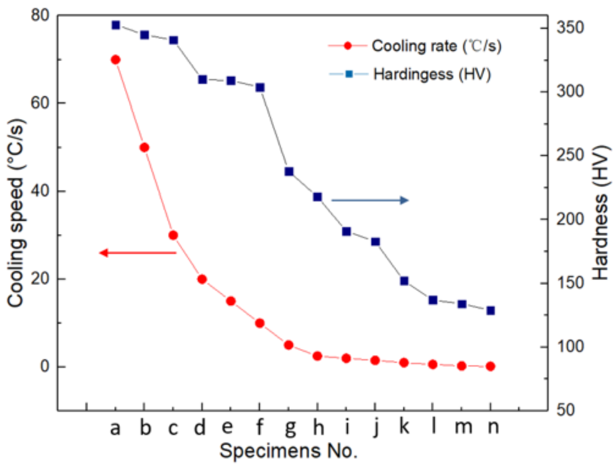

Figure 3.29 Hardness test results of the S690 steel under 14 cooling rates

Table 3-18 Hardness values of the S690 steel under 14 cooling rates

No.	Cooling rates (°C/s)	Hardness (HV)
a	70.0	353
b	50.0	345
c	30.0	341
d	20.0	310
e	15.0	309
f	10.0	304
g	5.0	238
h	2.5	218
i	2.0	191
j	1.5	183
k	1.0	152
l	0.6	137
m	0.25	134
n	0.15	129

Using the same analytical method, the metallographic results of the S960 steel have also been successfully obtained by the electron microscope examination onto the coupons after thermal expansion tests. Figure 3.30 illustrated the dilatometric curves of S960 steel coupons under different cooling rate. Cooling rates from 100°C/s to 0.025°C/s are marked at the lower right corner of each image.

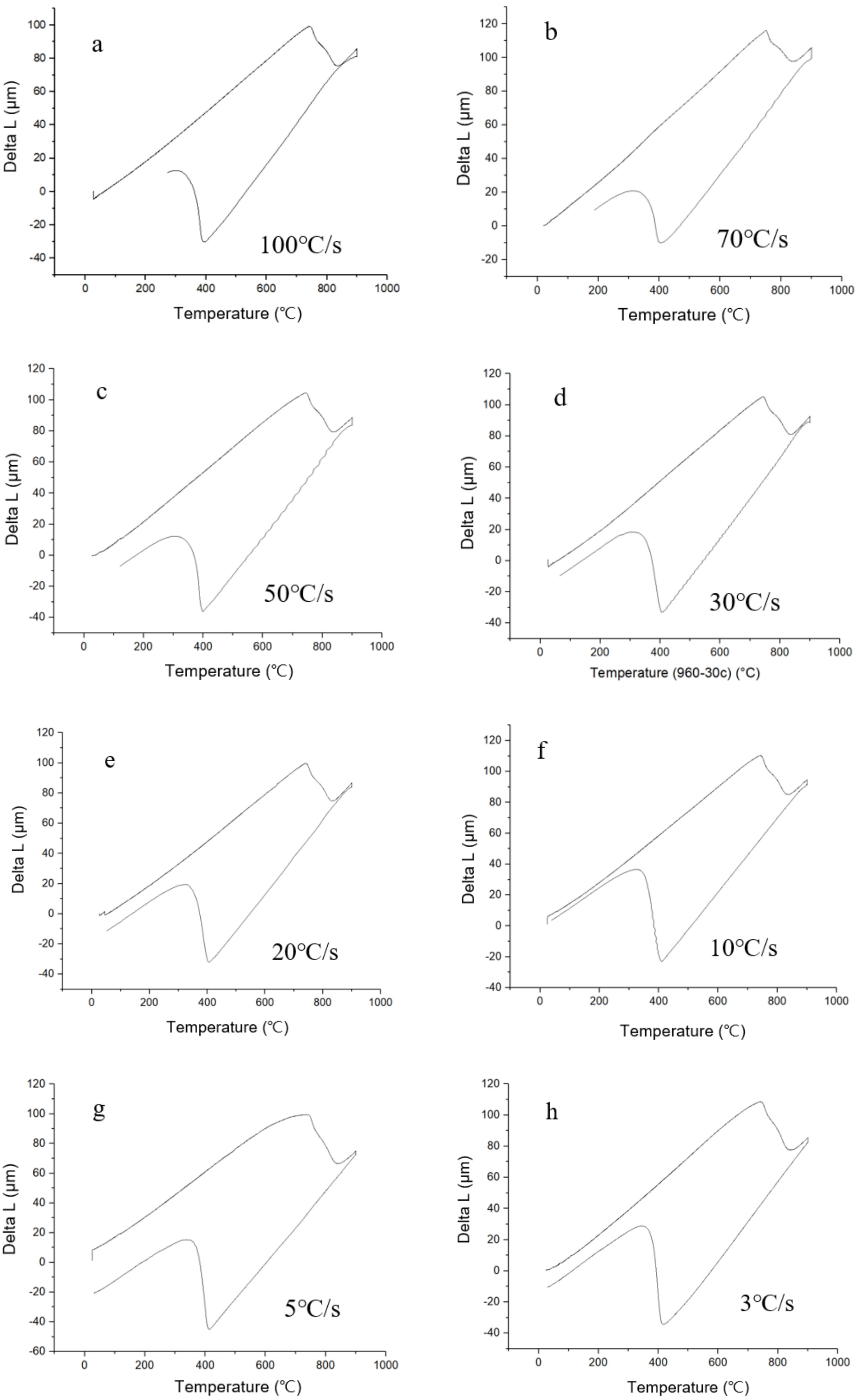
a
100°C/s
b
70°C/s
c
50°C/s
d
30°C/s
e
20°C/s
f
10°C/s
g
5°C/s
h
3°C/s
Delta L (μm)
Temperature (℃)
Temperature (960-30c) (°C)

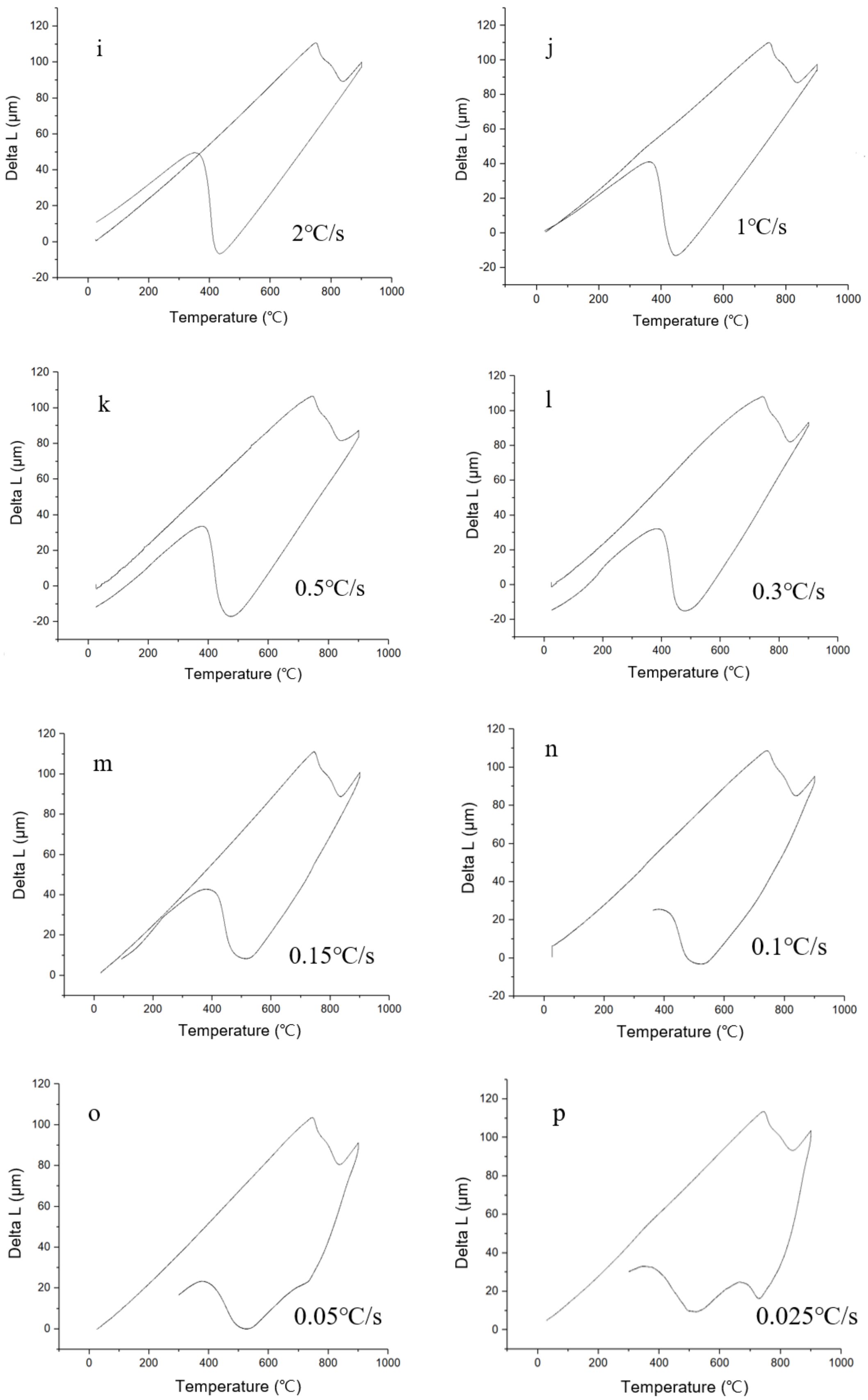

Figure 3.30 Dilatation curves of S960 steel obtained from different cooling rates

The microstructural evolution of the S960 coupons under different cooling rates was examined with an optical microscopy, and the results are illustrated in Image. a to m of Figure 3.31. When the maximum cooling rate of 100°C/s was applied, the microstructure of the S960 coupon was primarily martensite, as illustrated in Image. a. With decreasing cooling rates, bainite gradually formed, which can be observed in Image. g to Image. m. At the slowest cooling rate of 0.025°C/s, the microstructure of the S960 coupon was predominantly ferrite and bainite. The findings from this investigation provide important insights into the effect of cooling rate on the microstructural characteristics of high strength steel.

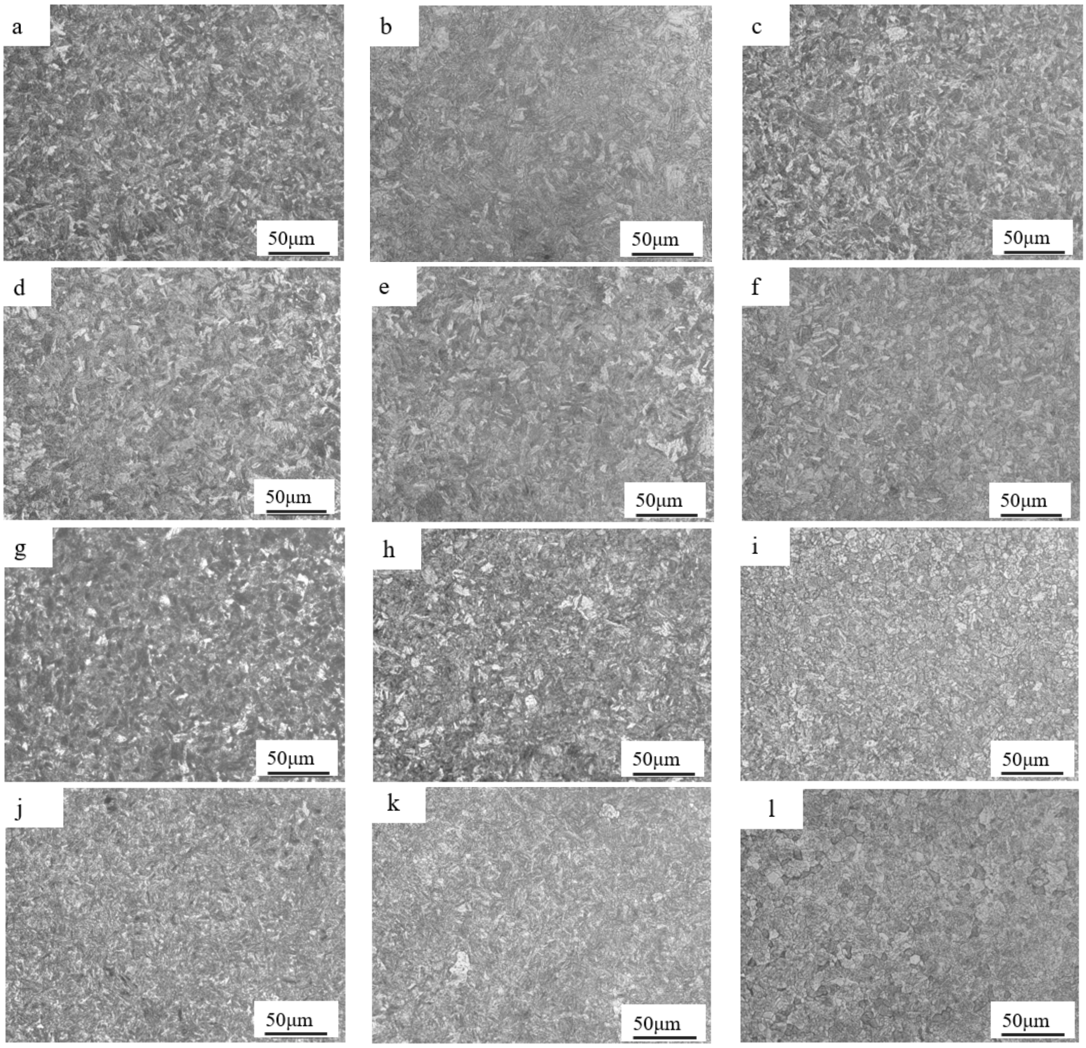

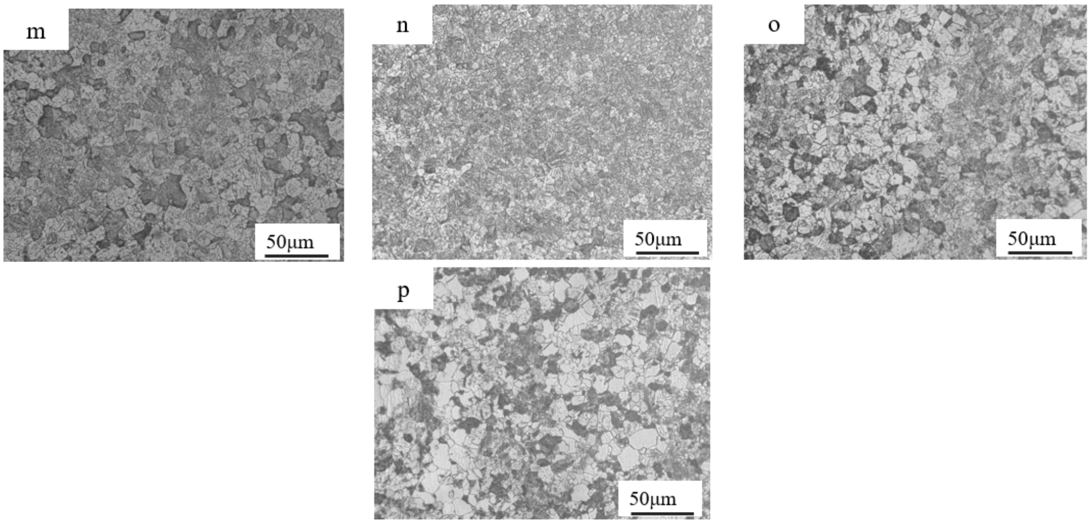

Figure 3.31 Metallography test results of S960

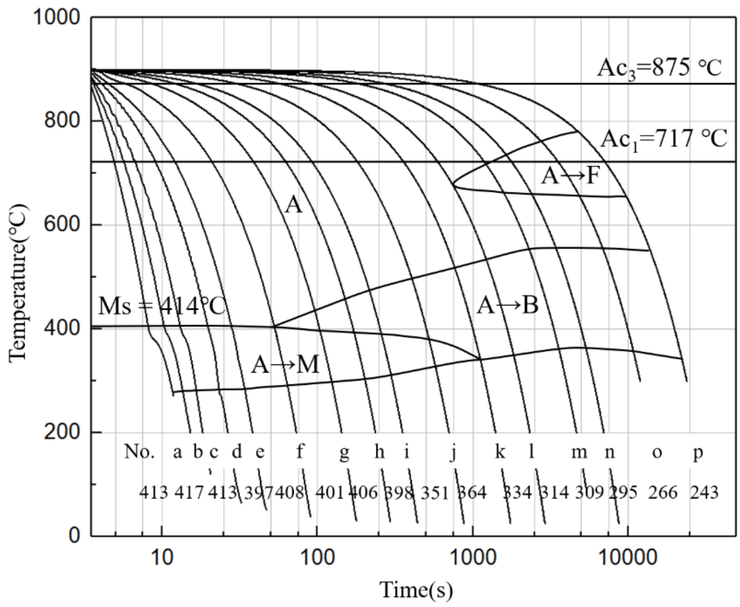

Figure 3.32 CCT curves of the S960 steel

The summarized CCT curves of the S960 are shown in Figure 3.32. Corresponding A_{c1} and A_{c3} temperatures are determined to be 717°C and 875°C, respectively.

Table 3-19 Data of S960 CCT curves

No.	$t_{8/5}$ (s)	Cooling rate (°C/s)	Phase composition (%)
a	3	100	M100
b	4	70	M100
c	6	50	M100
d	10	30	M100
e	15	20	M100
f	30	10	M100
g	60	5	B10+M90
h	100	3	B20+M80
i	150	2	B70+M30
j	300	1	B80+M20
k	600	0.5	B100
l	1000	0.3	B100
m	2000	0.15	F10+B90
n	3000	0.1	F20+B80
o	6000	0.05	F40+B60
p	12000	0.025	F55+B45

The hardness test results of the S960 thermal expansion coupons are present in Figure 3.33 and Table 3-20.

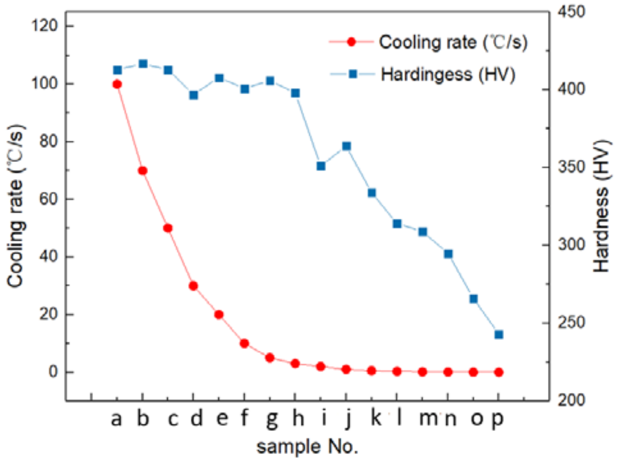

Figure 3.33 Hardness test results of the S960 steel under 16 cooling rates

It is shown that with an increase in cooling rate, the hardness of the coupon gradually decreases. Nevertheless, due to the high intrinsic hardness of the S960 steel, the hardness remains relatively high, even at the slowest cooling rate of 0.025°C/s, with a value of 243 Hv. It is suggesting that an increase in the volume fraction of martensite can significantly enhance the hardening properties of the steel.

Table 3-20 Hardness values of the S960 steel under 16 cooling rates

No.	Cooling rate (°C/s)	Hardness (Hv)
a	100	413
b	70	417
c	50	413
d	30	397
e	20	408
f	10	401
g	5	406
h	3	398
i	2	351
j	1	364
k	0.5	334
l	0.3	314
m	0.15	309
n	0.1	295
o	0.05	266
p	0.025	243

In conclusion, this chapter presented detailed examinations of the mechanical properties of the S690 and the S960 steel, both on parent metal and welded sections. The development of continuous cooling transformation (CCT) curves, and the hardness values of coupons subjected to different cooling rates for the S690 and the S960 steel are also introduced. Findings of all these investigations offer a comprehensive understanding of the thermal and mechanical behaviour of high strength S690 and S960 steel. In Chapter 6, these metallographic and mechanical properties obtained from these experimental investigations will be integrated in the definition of the S690 and the S960 steel, includes CCT curves, metal phase transformations, and other thermo-mechanical properties under numerical simulation.

CHAPTER FOUR

EXPERIMENTAL INVESTIGATION: SECTION RESISTANCES OF S690 AND S960 STOCKY COLUMNS UNDER COMPRESSION

4.1. Introduction

This chapter presents a comprehensive experimental investigation into the structural behaviour of the S690 and the S960 welded stocky columns with various heat input energy applied to the spliced butt welding. The primary objective of this investigation is to quantify the section resistance of welded stocky columns made by high strength S690 and S960 steel under axial compression. In addition, it aims to determine if a proven welding procedure specification is able to prevent any reduction in the section resistances of these S690 and S960 steel after welding.

Therefore, this chapter presents the compression tests of spliced stocky columns of high strength S690 and S960 steel which are fabricated under a carefully controlled welding process, together with the structural responses of these columns of welded H-sections with various section classifications. The welding procedure specification was developed systematically to determine various welding parameters, namely current, voltage, welding speed, and preheating temperature. These parameters were meticulously determined and then applied to fabrication of the S690 and the S960 stocky columns.

A total of 39 columns were tested in this experimental investigation, and they were:

- 12 stocky columns of S690 welded H-sections;
- 11 stocky columns of S960 welded H-sections;
- 8 stocky columns of S690 welded box sections; and
- 8 stocky columns of S960 welded box sections.

In these stocky columns, full penetrations were provided at the mid-heights of both the flanges and the webs of these columns. Typical cross-sectional dimensions of the S690 and S960 stocky columns are shown in Figure 4.1 to Figure 4.5.

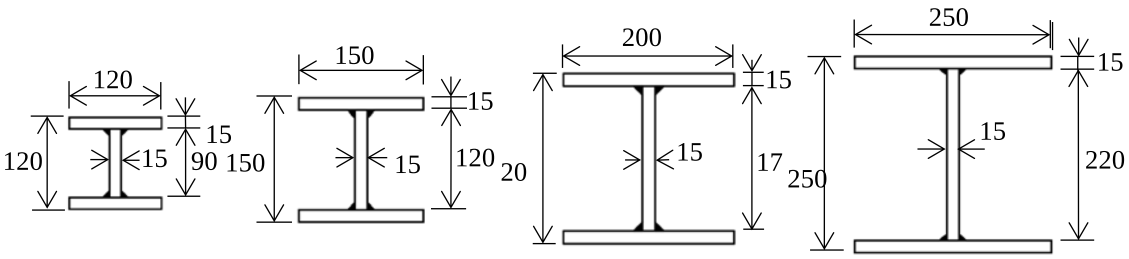

Section 960-H1 **Section 960-H2** **Section 960-H3** **Section 960-H4**

Figure 4.1 Cross-sectional dimensions of S960 welded H-sections

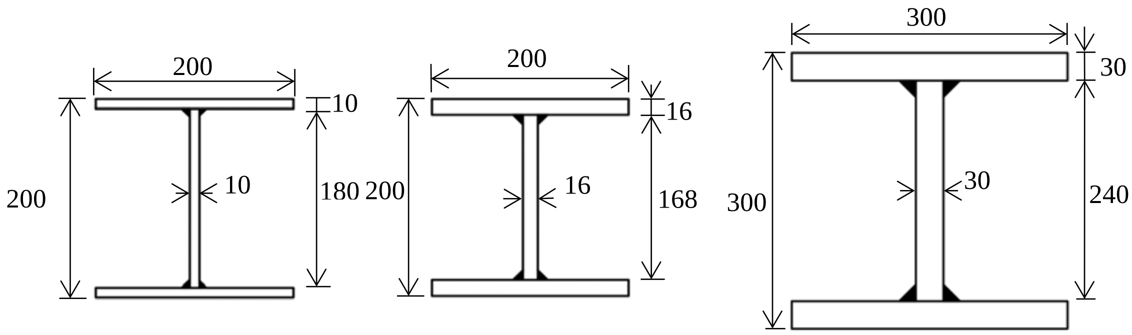

Section 690-H1 **Section 690-H2** **Section 690-H3**

Figure 4.2 Cross-sectional dimensions of S690 welded H-sections

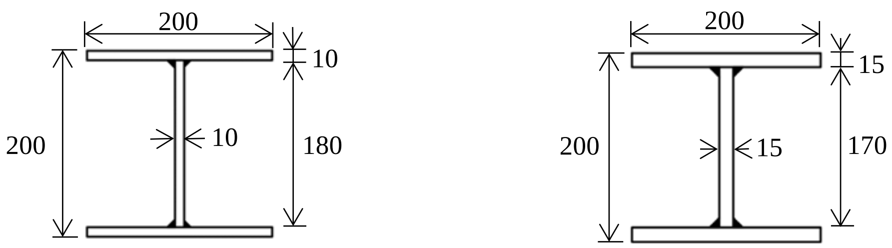

Section 960-H1 **Section 960-H2**

Figure 4.3 Cross-sectional dimensions of the S960 welded H-sections

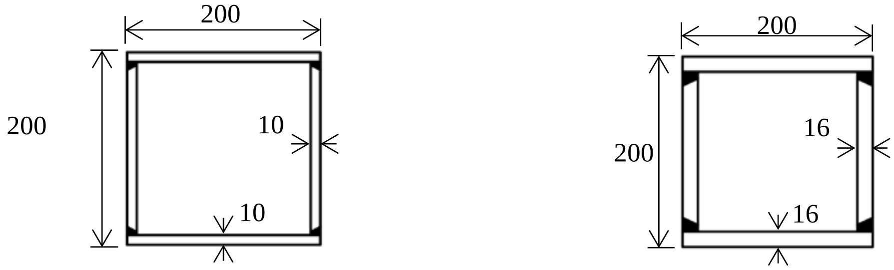

Section 690-B1 **Section 690-B2**

Figure 4.4 Cross-sectional dimensions of the S690 welded box sections

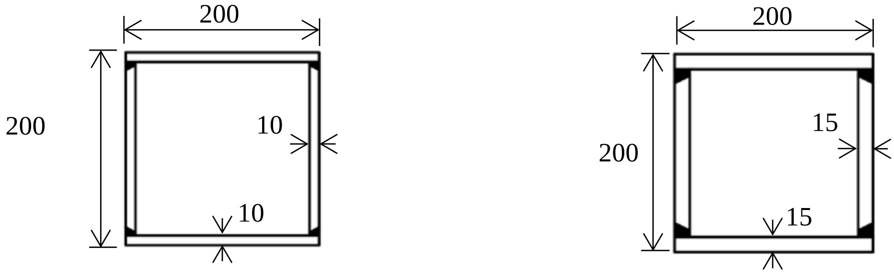

960-B1 **960-B2**

Figure 4.5 Cross-sectional dimensions of the S960 welded box sections

The specimens are labelled according to the "steel grade-section type (H-section or box section)-type number-heat input energy of butt weld". The test results including final deformation shapes, failure modes, measured resistances, and load-shortening curves are presented and discussed in subsequent sections. Both the fabrication process and the test programme are thoroughly explained.

4.2. WPS of S690 and S960 steel

As discussed in the literature review, the welding procedure specification (WPS) outlines all necessary requirements for welders, materials, and equipment involved in the welding process. Through the implementation of a WPS, welding quality can be assured, and the welding process can be standardized the manufacturing process.

According to EN ISO 15607-2(Standard 2018), the WPS must be pertinent to the fabrication project, to meet the production requirements, consider the largest coverage as much as possible. In general, the welding parameters of WPS are determined through experience of welders and trial tests, and these include welding voltage, current, welding speed, preheating requirements, and post-weld heat treatment. In general, a vertical very complicated because it is more difficult than a horizontal welding, and it requires welders to possess a higher level of skill. For the same reasons, the welding evaluation results of butt welds are readily adopted to cover those of fillet welds. Therefore, in the development of the WPS, butt welding is often chosen.

In order to formulate the WPS of the S690 and the S960 steel, the welding process for those welded sections need to be verified, to ensure that the welding process is reasonable, safe, and the structural performance of these welded sections are representative. In this project, PROVA, an accredited welding inspection agency in Hong Kong, and Pristine Metal Structure Co., Ltd., an established steel fabrication factory in China were consulted to establish a reliable WPS dataset. A total of four different WPS were collected, i.e., welding of 16mm thick S690 steel with q=1.0 and 2.0 kJ/mm, and the welding of 15mm thick S960 steel with q=1.0 and 2.0 kJ/mm. The WPS development and the responsibilities of all parties during this process are shown in Figure 4.6.

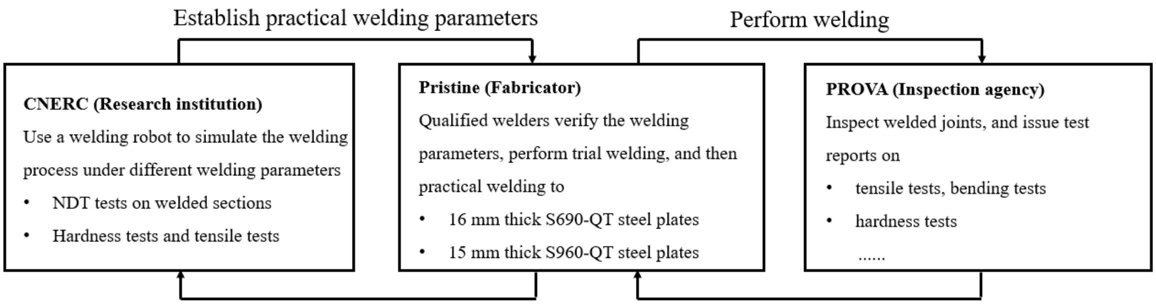

Figure 4.6 Design and implementation of a WPS for high strength steel

In this study, GMAW was adopted as the welding process. In the selection of the electrode, as stipulated in BS EN ISO 16834(Standard 2012), an even-match or an over-match welding is typically selected. This implies that the electrode needs to have a yield strength that is approximately the same or even higher than the parent metal. Due to the limited space, this chapter presents the development of only two WPS that of the S960 steel plates. As shown in Figure 4.7, these two WPS are applicable for heat input energy q=1.0 kJ/mm and q=2.0 kJ/mm, and the number of welding runs in a V-shaped groove on the 15mm thick S960 steel plate is seven and four, respectively.

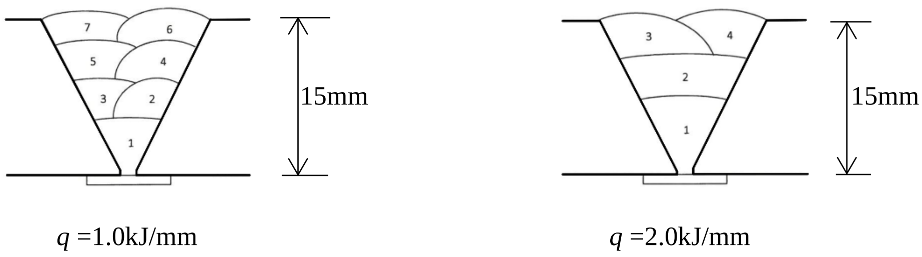

Figure 4.7 Run sequences of WPS for 15mm thick S960 steel

Based on the results of the tensile tests presented in Chapter 3, for the S960 steel welded sections, the yield strength reductions with heat input energy *q*=1.0 kJ/mm and *q*=2.0 kJ/mm were found to be 0.96 and 0.89, which are considered to be acceptable. Therefore, these welding parameters used in Chapter 3 were selected for the development of the WPS for the S960 steel. The preheating temperature of the S960 steel is set to range between 120°C and 150°C before welding.

The welding process also employs a shielding gas mixture of inert gases, including Ar and CO_2 at a flow rate of 20 to 25L/min. It should be noted that during welding, the current and the voltage of the welding machine may fluctuate. As an example, the energy recorded during welding of three passes with different heat input energy are shown in Figure 4.8. Upon comparison of the recorded data at heat input energy of 1.0 and 2.0 kJ/mm, it is observed that the heat input energy for each weld pass fluctuates ±10%, and this is considered to be acceptable. To maintain consistent heat input energy (*q*) during subsequent investigations of the WPS and fabrication of the welded sections, it is recommended to monitor both the current and the voltage closely, in order to achieve the target heat input value, and to keep the travel speed of the welding constant.

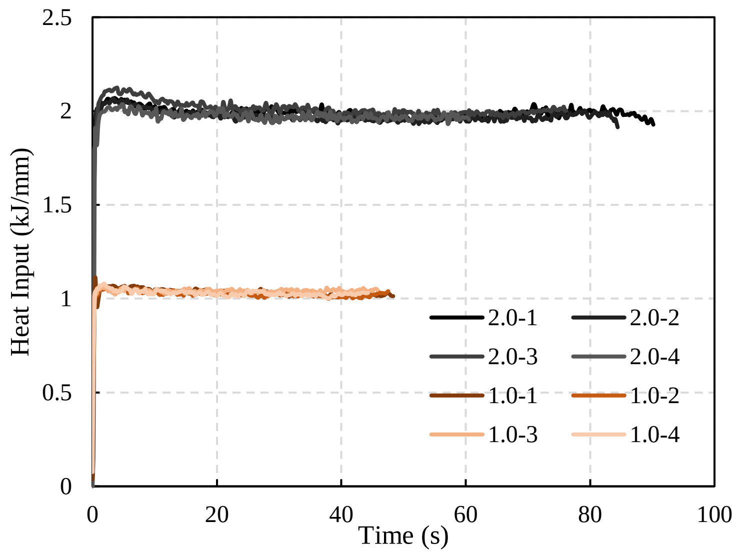

Figure 4.8 Measured heat input energy during welding process (q=1.0/2.0 kJ/mm)

After cooling down to the room temperature, a number of non-destructive tests (NDT) are carried out to detect whether there is any no internal crack or defect in the weld sections. After stablishing these operation welding parameters, qualified welders might modify these parameters for efficiency with welding on the S960 steel plates, as illustrated in Figure 4.9. The current, the voltage, the welding speed, the preheating temperature and the inter-pass temperatures of each welding seam were all carefully recorded.

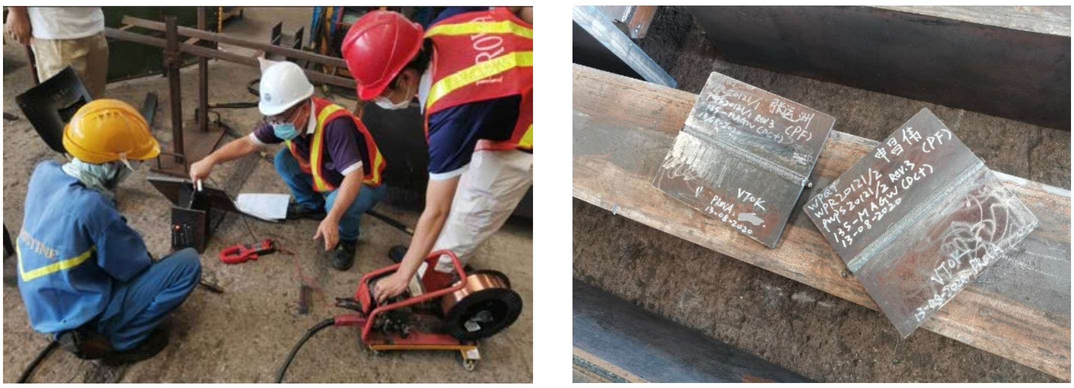

Figure 4.9 Developing WPS in Pristine Metal Structure Co., Ltd

After completing the welding process, the welded sections underwent various other detection methods, including monotonic tensile tests, bending tests, and hardness tests at an accredited laboratory, PROVA, under the HOKLAS scheme operated by the Hong Kong Accreditation Service. Results of these tests demonstrate effectiveness of the employed welding parameters in the WPS document. An example of the key information of the WPS of the S960 steel with a heat input energy *q*=1.0kJ/mm is shown in Figure 4.10. In general, for fabrication of the S690 and the S960 welded sections, a strict adherence to all these parameters defined in the WPS is essential.

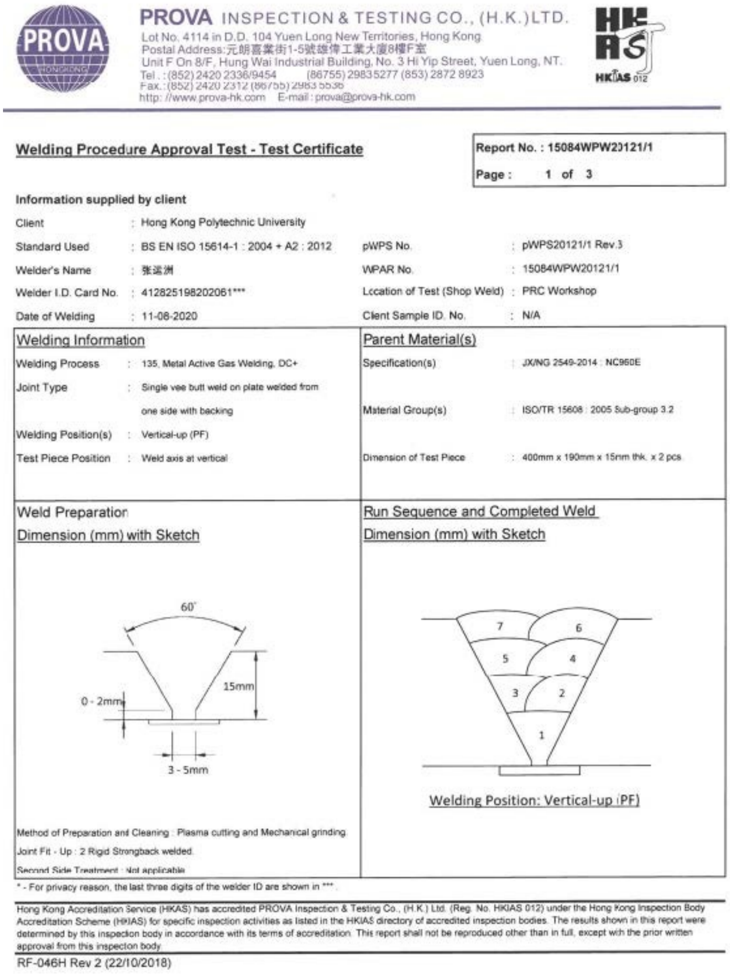

PROVA INSPECTION & TESTING CO., (H.K.)LTD.
Lot No. 4114 in D.D. 104 Yuen Long New Territories, Hong Kong
Postal Address:元朗喜業街1-5號雄偉工業大廈8樓F室
Unit F On 8/F, Hung Wai Industrial Building, No. 3 Hi Yip Street, Yuen Long, NT.
Tel.:(852) 2420 2336/9454 (86755) 29835277 (853) 2872 8923
Fax.:(852) 2420 2312 (86755) 2983 5536
http://www.prova-hk.com E-mail: prova@prova-hk.com

Welding Procedure Approval Test - Test Certificate

Report No.: 15084WPW20121/1
Page: 1 of 3

Information supplied by client

Client	: Hong Kong Polytechnic University		
Standard Used	: BS EN ISO 15614-1 : 2004 + A2 : 2012	pWPS No.	: pWPS20121/1 Rev.3
Welder's Name	: 张遥洲	WPAR No.	: 15084WPW20121/1
Welder I.D. Card No.	: 412825198202061***	Location of Test (Shop Weld)	: PRC Workshop
Date of Welding	: 11-08-2020	Client Sample ID. No.	: N/A

Welding Information		Parent Material(s)	
Welding Process	: 135, Metal Active Gas Welding, DC+	Specification(s)	: JX/NG 2549-2014 : NC960E
Joint Type	: Single vee butt weld on plate welded from one side with backing	Material Group(s)	: ISO/TR 15608 : 2005 Sub-group 3.2
Welding Position(s)	: Vertical-up (PF)		
Test Piece Position	: Weld axis at vertical	Dimension of Test Piece	: 400mm x 190mm x 15mm thk. x 2 pcs

Weld Preparation Dimension (mm) with Sketch

60°
15mm
0 - 2mm
3 - 5mm

Method of Preparation and Cleaning : Plasma cutting and Mechanical grinding
Joint Fit - Up : 2 Rigid Strongback welded
Second Side Treatment : Not applicable

Run Sequence and Completed Weld Dimension (mm) with Sketch

7 6 5 4 3 2 1

Welding Position: Vertical-up (PF)

* - For privacy reason, the last three digits of the welder ID are shown in ***.

Hong Kong Accreditation Service (HKAS) has accredited PROVA Inspection & Testing Co., (H.K.) Ltd. (Reg. No. HKIAS 012) under the Hong Kong Inspection Body Accreditation Scheme (HKIAS) for specific inspection activities as listed in the HKIAS directory of accredited inspection bodies. The results shown in this report were determined by this inspection body in accordance with its terms of accreditation. This report shall not be reproduced other than in full, except with the prior written approval from this inspection body.

RF-046H Rev 2 (22/10/2018)

Figure 4.10 WPS of the S960 steel with a heat input energy *q*=1.0kJ/mm

4.3. Fabrication process of welded sections

To start, all the S690 and the S960 steel plates underwent a pre-cutting process using an underwater plasma-cutting machine, in order to minimize any negative effect of heating onto the cutting edge of the plates. For 30mm thick steel plates, flame cutting was utilized instead due to limitation of the equipment. It should be noted that the welding processes were carefully controlled and monitored during fabrication, and the voltages, the currents, and the welding speeds for each welding run were controlled by experienced welders and welding operators, in a strict compliance to the WPS. Moreover, the fabrication process of these welded H-section with welded splices is shown in Figure 4.11. Butt welding was performed on a pair of steel plates, and these steel plates were assembled steel plates into a stocky column of H-section or box section. In addition, two S355 30mm thick steel plates were welded onto the welded section to ensure a uniform load distribution during testing.

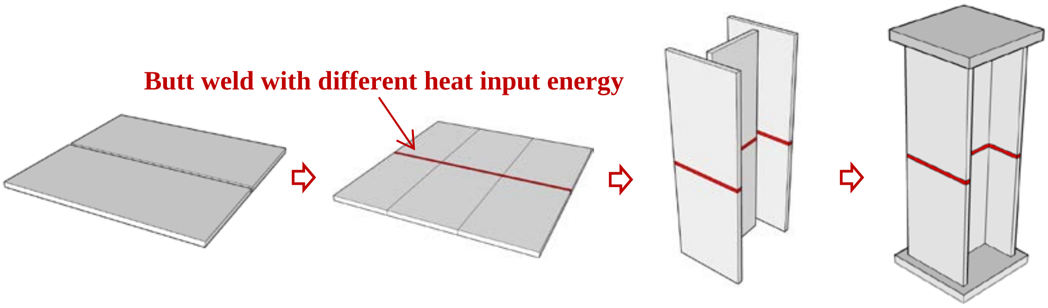

Figure 4.11 Fabrication of a stocky column of welded H-section

The fabrication processes of these stocky columns are illustrated in Figure 4.12, and this includes a) preheating before welding, b) longitudinal welding performed by a qualified welder using GMAW method, c) welded steel plates cut by plasma, and d) welded H-sections and box sections.

a) Preheating

b) GMAW using automatic welding machine

c) Welded steel plates cut ready for assembly

d) Assembled stocky columns

Figure 4.12 Fabrication processes of S690 and S960 stocky columns

Since the WPS was developed using the 16mm thick S690 steel plate, it is considered to be applicable to steel plates with thickness ranging from 8mm to 32mm, i.e., 0.5*t* to 2.0*t*, where *t* is the plate thick used in the WPS. In the case of 30mm thick S690 steel plates, large amount of heat during welding may result in significant deformation in the welded section. To mitigate these deformations, an X-shaped groove was employed, and a total of 20 weld runs were provided sequentially as illustrated in Figure 4.13. This type of bevelling conforms to standard practice of welding thick steel plates in construction.

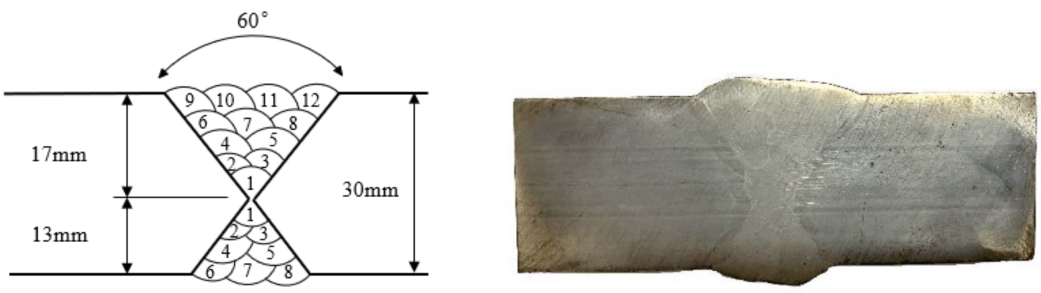

a) Welding's sequence b) Etched section after welding

Figure 4.13 Multi-pass welding of 30mm thick S690 steel

To compare the effects of different heat input energy *q* onto the structural behaviour of welded sections, the following *q* values were adopted, as presented in Table 4-1. All specimens were fabricated according to the given requirements, the current and the voltage were carefully recorded to ensure the heat input energy. After welding, no cracks were observed on the surface of all the fillet weld or butt weld sections.

Table 4-1 Heat input energy of different sections

Steel grade	Plate thickness *t*, (mm)	Heat input energy *q*, (kJ/mm)
S690	10	1.0, 1.5, 2.0
	16	1.0, 1.5, 2.0
	30	1.0, 1.8, 3.0
S960	10	1.0, 1.5, 2.0
	15	1.0, 1.5, 2.0

4.4. Test programme

Considering the objectives of this experimental investigation, a total of three tasks were included in the section, namely a) investigation of the section classification to EN 1993-1-1 for H-sections, b) evaluation of the absence of reduction under controlled welding of H-sections, and c) evaluation of the absence of reduction under controlled welding of box sections. The test programme and dimensions of the test specimens obtained through measurements for each task are detailed below.

Task I: Section classification to EN 1993-1-1

According to previous investigation, a total of 12 compression tests on the S690 stocky columns have been carried out, and these four welded H-sections with different cross-sectional dimensions, and the flange and the web with different thicknesses, i.e., 6, 10 and 16 mm(Chung *et al*. 2020). A representative column is selected from each of the four different sections, namely, H-120×10, H-150×10, H-200×16, and H-250×16. The section classification rules in EN 1993-1-1(Standard 2005), indicate that H-120×10 is Class 1 section, H-200×16 is Class 2 section, while H-150×10 and H-250×16 are Class 3 sections. The test programme of these four sections and nominal cross section dimensions of welded H-sections are presented in Figure 4.14 and Table 4-2.

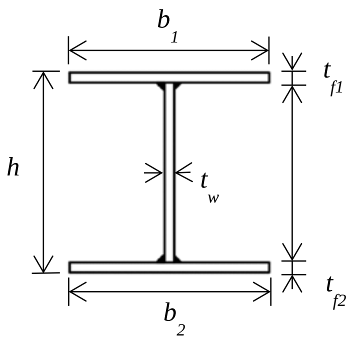

Figure 4.14 Nominal cross section dimensions of welded H-sections

Table 4-2 Test programme of S690 welded H-sections

Section	Section classification	Measured dimensions H (mm)	h (mm)	b_1 (mm)	b_2 (mm)	t_{f1} (mm)	t_{f2} (mm)	t_w (mm)	A (mm^2)
H-120×10	Class 1	460	137.3	119.6	119.6	9.95	9.95	6.0	3,084
H-150×10	Class 3	460	166.7	149.3	149.3	9.95	9.95	6.0	3,852
H-200×16	Class 2	610	228.3	199.5	199.5	16.02	16.02	10.0	8,349
H-250×16	Class 3	760	283.2	249.9	249.9	16.03	16.03	10.0	10,516

Except for these S690 sections, four typical cross-sections of the S960 stocky columns were also fabricated to examine the member resistances and deformation capacities with different section classifications, namely H–120×15, H–150×15, H–200×15, and H–250×15 correspond to Class1, 2, 3, and 4. Table 4-3 presents the test programme and measured dimensions.

Table 4-3 Test programme of S960 welded H-sections

Section	Section classification	Measured dimensions H (mm)	h (mm)	b_1 (mm)	b_2 (mm)	t_{f1} (mm)	t_{f2} (mm)	t_w (mm)	A (mm^2)
H–120×15	Class 1	360	118.9	119.0	118.9	14.90	14.97	14.9	4,883
H–150×15	Class 2	448	149.0	148.9	148.7	14.53	14.60	14.6	6,081
H–200×15	Class 3	598	198.1	200.4	200.3	15.01	15.13	15.1	8,570
H–250×15	Class 4	751	247.4	246.7	248.0	14.87	14.87	14.9	9,843

Task II: No reduction under controlled welding of H-sections

Understanding the behaviour of high strength steel welded members can lead to the development of improved welding procedures, which can be used to optimize the design and construction of structures made by high strength steel. Therefore, a total of twenty H-sections were fabricated and tested. The test programme and the measured geometric

dimensions of these H-sections are presented in Table 4-4 and

Table 4-5.

Table 4-4 Test programme and measured dimensions of the S690 spliced H-sections

Section	Section classification	Heat input energy q (kJ/mm)	Measured dimensions: H (mm)	h (mm)	b_1 (mm)	b_2 (mm)	t_{f1} (mm)	t_{f2} (mm)	t_w (mm)	A (mm^2)
H-200×10	Class 4	-	598	199.1	199.2	199.3	9.53	9.43	9.48	5,487
H-200×10a		1.0	589	200.3	199.3	199.3	9.33	9.57	9.45	5,481
H-200×10b		1.5	590	200.3	201.5	199.5	9.70	9.71	9.70	5,644
H-200×10c		2.0	590	200.4	199.2	199.0	9.87	9.70	9.78	5,665
H-200×16	Class 3	-	587	197.8	197.3	197.5	16.30	16.00	16.15	9,050
H-200×16a		1.0	597	198.7	197.5	198.0	16.30	16.37	16.33	9,171
H-200×16b		1.5	588	199.8	196.4	196.5	16.63	16.07	16.35	9,156
H-200×16c		2.0	599	202.3	197.8	196.3	16.17	16.40	16.28	9,183
H-300×30	Class 1	-	898	299.5	299.5	299.4	30.02	30.03	30.00	25152
H-300×30a		1.0	900	300.1	299.5	299.5	29.31	30.24	29.75	24978
H-300×30b		1.8	899	300.9	300.5	300.7	30.21	30.04	30.10	25341
H-300×30c		3.0	900	301.3	300.3	300.4	30.32	30.20	30.25	25455

Table 4-5 Test programme and measured dimensions of the S960 spliced H-sections

Section	Section classification	Heat input energy q (kJ/mm)	Measured dimensions H (mm)	h (mm)	b_1 (mm)	b_2 (mm)	t_{f1} (mm)	t_{f2} (mm)	t_w (mm)	A (mm^2)
H-200×10	Class 4	-	600	198.3	197.9	197.6	9.98	9.89	9.94	5,702
H-200×10a		1.0	599	201.0	197.9	199.4	9.83	9.75	9.79	5,666
H-200×10b		1.5	600	201.2	198.1	197.8	9.95	9.78	9.87	5,696
H-200×10c		2.0	599	200.4	198.2	198.2	9.72	9.72	9.92	5,648
H-200×15	Class 3	-	598	198.1	200.4	200.3	15.01	15.13	15.10	8,570
H-200×15a		1.0	594	200.1	197.4	198.2	15.16	15.21	15.18	8,584
H-200×15b		1.5	601	200.2	196.8	196.8	15.44	15.24	15.34	8,639
H-200×15c		2.0	599	200.9	197.5	197.7	15.20	15.00	15.10	8,545

Task III: No reduction under controlled welding of box sections

For the S690 and the S960 box sections, similar plate thicknesses were used. A total of 8 S690 box sections and 8 S960 box sections with two different cross-sections were devised in this test programme. The measured geometric dimensions of these box sections are summarized in Table 4-6 and Table 4-7.

Table 4-6 Test programme and measured dimensions of the S690 box sections

Section	Section classification	Heat input energy q (kJ/mm)	Measured dimensions						A (mm^2)
			H (mm)	b_1 (mm)	b_2 (mm)	b_3 (mm)	b_4 (mm)	d (mm)	
B-200×10	Class 1	-	589.9	198.5	198.7	197.5	199.5	9.6	7258
B-200×10a		1.0	598.9	199.2	197.7	199.6	197.3	9.6	7255
B-200×10b		1.5	603.2	197.4	199.8	196.7	200.0	9.6	7256
B-200×10c		2.0	597.3	198.3	198.5	199.3	199.5	9.6	7272
B-200×16	Class 1	-	598.2	197.0	200.3	197.7	200.0	16.3	11882
B-200×16a		1.0	597.5	199.2	197.7	199.6	197.3	16.3	11862
B-200×16b		1.5	600.2	196.9	200.0	197.3	200.0	16.3	11869
B-200×16c		2.0	600.5	198.1	199.7	198.2	200.2	16.3	11900

Table 4-7 Test programme and measured dimensions of the S960 box sections

Section	Section classification	Heat input energy q (kJ/mm)	Measured dimensions						A (mm^2)
			H (mm)	b_1 (mm)	b_2 (mm)	b_3 (mm)	b_4 (mm)	d (mm)	
B-200×10	Class 2	-	597.3	199.0	200.1	200.0	198.2	9.4	7141
B-200×10a		1.0	589.9	199.1	198.8	197.8	199.7	9.4	7123
B-200×10b		1.5	589.2	199.7	198.9	199.7	199.6	9.4	7147
B-200×10c		2.0	600.5	197.9	196.1	197.6	196.1	9.4	7051
B-200×15	Class 1	-	601.2	199.1	198.9	198.4	199.3	15.2	11169
B-200×15a		1.0	592.1	198.0	200.6	197.7	200.0	15.2	11178
B-200×15b		1.5	589.7	197.5	199.2	197.4	198.9	15.2	11128
B-200×15c		2.0	600.1	197.7	198.8	198.1	198.1	15.2	11130

It should be noted that since the plate thickness of the webs of both these H-sections and these box sections could not be measured directly using a vernier caliper, an ultrasonic distance measuring instrument is employed to measure the thickness of these steel plates.

4.5. Test setup

All compression tests of the S690 and the S960 stocky columns were performed in the Structural Engineering Research Laboratory of the Hong Kong Polytechnic University. As shown in Figure 4.15, a 25,000kN electro-hydraulic servo-controlled compression test system is employed in this test, and the maximum compression loading of this system is 25000 kN while the maximum travel is about 500 mm. Typical instrumentation of compression tests on H-sections and box sections are illustrated in Figure 4.16 and Figure 4.17. In order to record the strain development of each specimen during compression tests, four strain gauges were attached to the mid-height of the flanges. In those welded sections of the spliced stocky columns, it was necessary to attach the strain gauges 5 mm below the welding seam. In addition, four displacement transducers (LVDTs) were installed at the top and the bottom ends of each H-section to accurately measure the direct shortenings of the stocky columns.

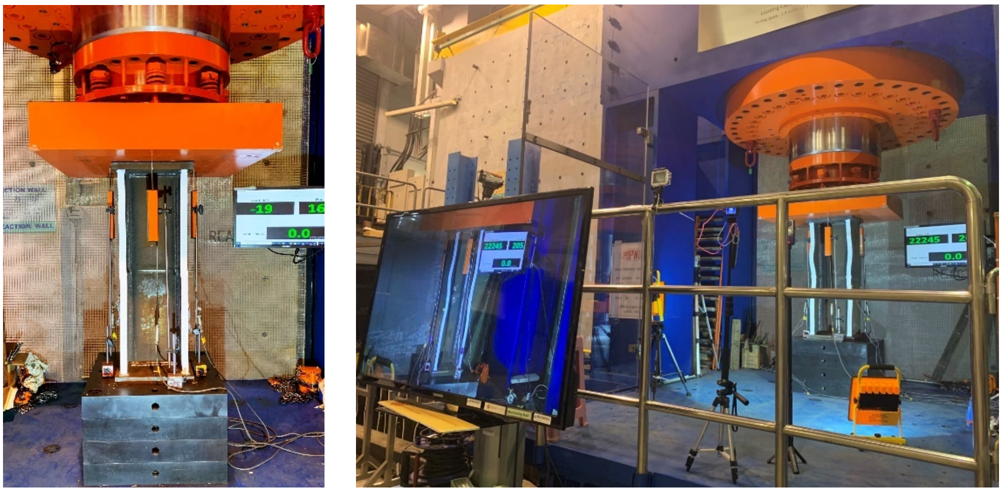

Figure 4.15 The electro-hydraulic servo-controlled compression test system

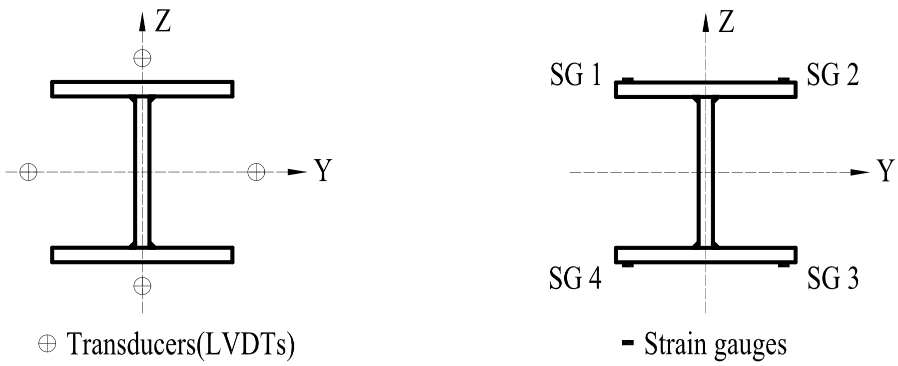

a) Arrangement of LVDTs

b) Attachment of strain gauges

Figure 4.16 Typical instrumentation of welded H-sections

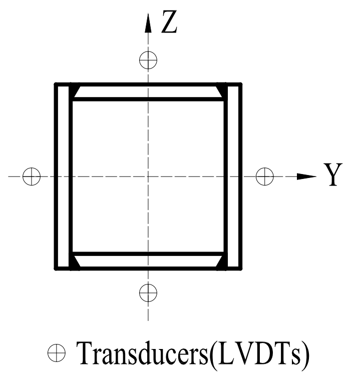

a) Arrangement of LVDTs

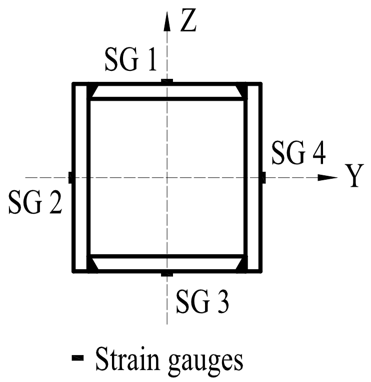

b) Locations of strain gauges

Figure 4.17 Typical instrumentation of welded box sections

In order to obtain the full range deformation characteristic of these welded sections, in particular, the unloading range, the displacement control is selected as the loading scheme. Before the test start, a preloading process was performed. With the help of laser detectors, each specimen was meticulously positioned to ensure that it was cantered precisely on the loading platform to avoid any influence of eccentricity on the test results. All specimens were loaded to 30% of the design resistance, $N_{c.Rd}$, and then drop to zero at a displacement rate of 0.5mm/min. This process was performed for three times, so that it can minimized the unintended effects of eccentricities and loading system by carefully re-alignment on the test specimens.

After preloading, the test officially began. All specimens were loaded in two stages: a) Loading state 1: from 0 to 70% of $N_{c.Rd}$, and b) Loading state 2: from 70% of $N_{c.Rd}$ to the real peak force, then dropped to 80% of the real peak force. Due to the high loads involved in the test, the loading rate was controlled at 0.3mm/min in Loading state 1 and increased to 0.5mm/min in Loading state 2. After the test was terminated, the loading was then drop monotonically from 80% of real peak force to 0 with a rate of 1.0mm/min. The deformed shape of the specimen was photographed extensively for record.

4.6. Test results

4.6.1. Failure modes

Task I: Section classification to EN 1993-1-1

Similar to the experimental results by previous researches(Liu 2017 and Chung *et al*. 2020), deformed shapes of the S690 H-sections are shown in Figure 4.18, while deformed shapes of the S960 H-sections are shown in Figure 4.19. In all cases, no cracks were found on any fillet welds. Symmetrical local buckling appears along the outstands of the flanges of these welded H-sections, while complementary local buckling is also found in their web plates. It should be noted that local deformation of the web and flange gradually increases after the maximum resistance is attained. At the end of testing, all the specimens failed in plastic local plate buckling, and the maximum out of flange deformations of these specimens are typically located at the mid-heights.

H-120×10	H-150×10	H-200×16	H-250×16
(Class 1)	(Class 3)	(Class 2)	(Class 3)

Figure 4.18 Deformed shapes of S690 H-sections under axial compression

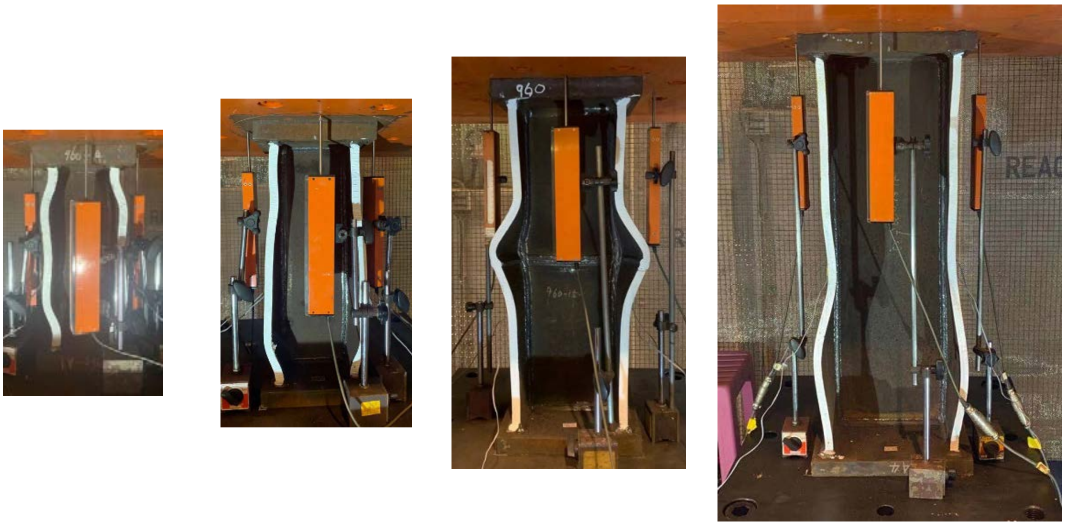

H-120×15	H-150×15	H-200×15	H-250×15
(Class 1)	(Class 2)	(Class 3)	(Class 4)

Figure 4.19 Deformed shapes of the S960 H-sections under axial compression

Task II: No reduction under controlled welding of H-sections

For the S690 and the S960 spliced welded H-sections, all the tests were also conducted successfully. Deformed shapes of all these columns after testing are illustrated together with the corresponding reference columns in Figure 4.20 and Figure 4.21. For the S690 and the S960 spliced welded H-sections with plate thickness within 10~16mm, in most cases, symmetrical local buckling appears at the flanges of these welded H-sections, while complementary local buckling is also found in their web plates. In some cases, like S690-H-200×16a, the deformation of the flange is asymmetric, but basically the outward bulges are observed at the same height of two flanges. For the S690 spliced H-sections with plate thickness 30mm, with the loading increases, the top end plate was observed an inclination, and the local buckling appears on flanges were not completely symmetrical (as illustrated in Figure 4.20-c). This phenomenon may be attributed to the initial imperfection caused by the increase in thickness of the steel plates, as well as the difficulty in aligning on the loading system due to the substantial weight of the specimens. Moreover, no fracture happened on weld sections was found in any of those spliced H-sections.

H-200×10 H-200×10a H-200×10b H-200×10c

a) Series 690-H-200×10

H-200×16 H-200×16a H-200×16b H-200×16c

b) Series 690-H-200×16

H-300×30

H-300×30a

H-300×30b

H-300×30c

c) Series H-300×30

Figure 4.20 Deformed shapes of S690 spliced H-sections under axial compression

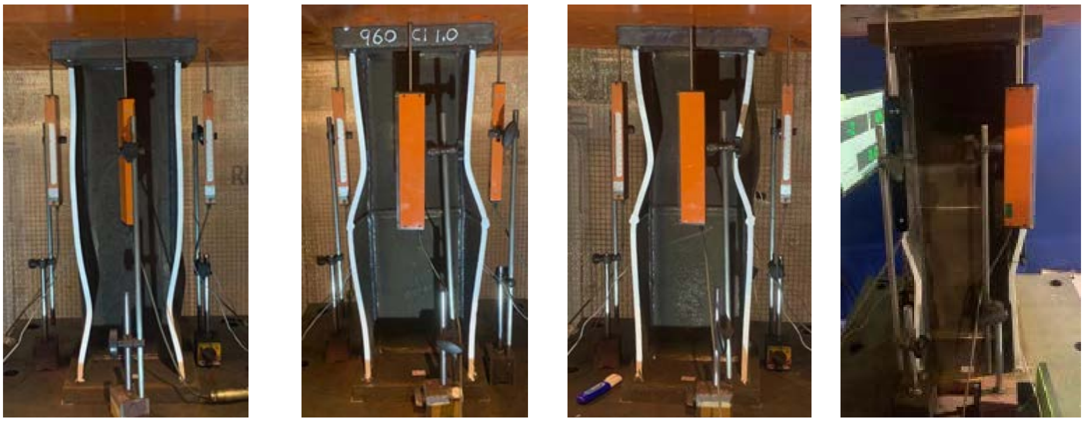

H-200×10 H-200×10a H-200×10b H-200×10c

(d) Series 960-H-200×10

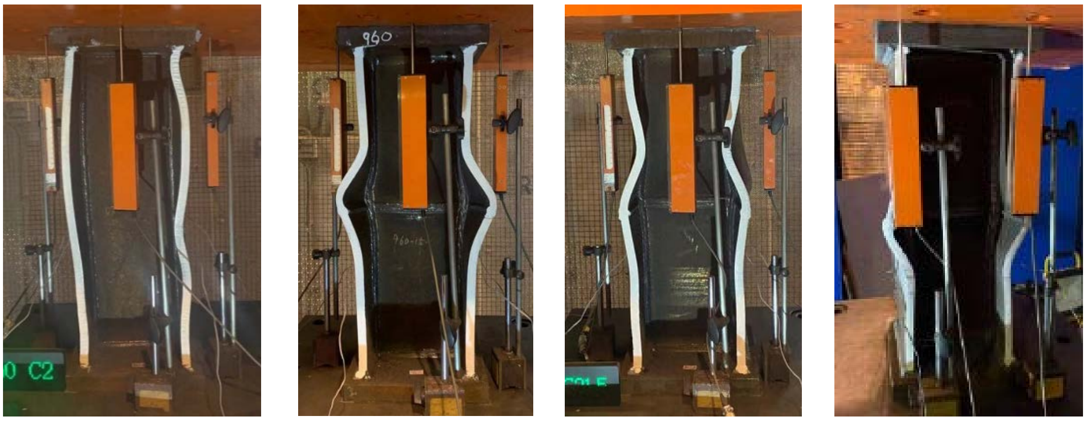

H-200×15 H-200×15a H-200×15b H-200×15c

(e) Series 960-H-200×15

Figure 4.21 Deformed shapes of S960 spliced H-sections under axial compression

Task III: No reduction under controlled welding of box sections

For the S690 and the S960 welded box sections, all the tests were conducted successfully. Deformed shapes after testing of spliced columns and reference columns are illustrated together in Figure 4.22 and Figure 4.23.

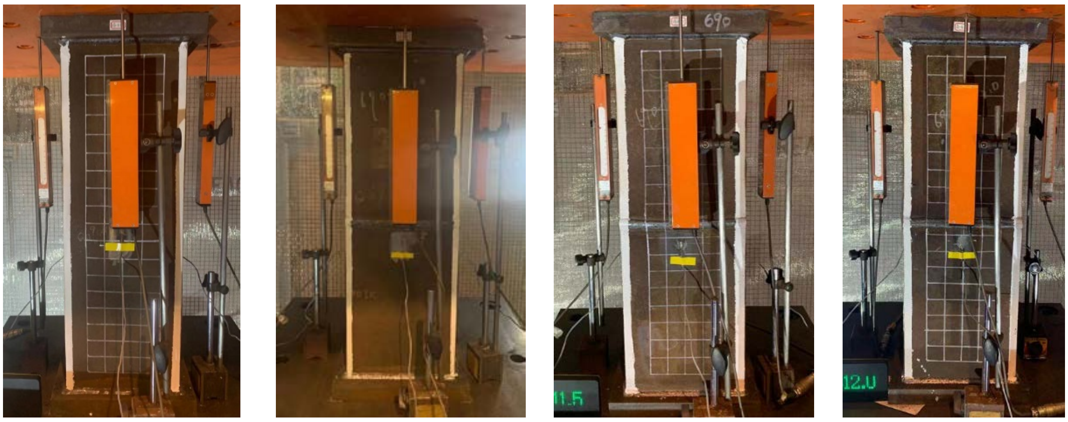

B-200×10 B-200×10a B-200×10b B-200×10c

(a) Series 690-B-200×10

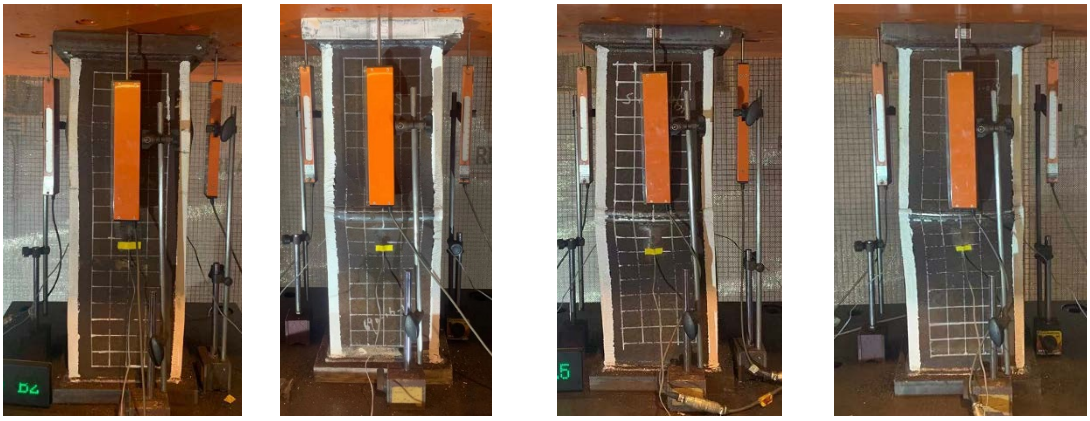

B-200×16 B-200×16a B-200×16b B-200×16c

(b) Series 690-B-200×16

Figure 4.22 Deformed shapes of S690 spliced box sections under axial compression

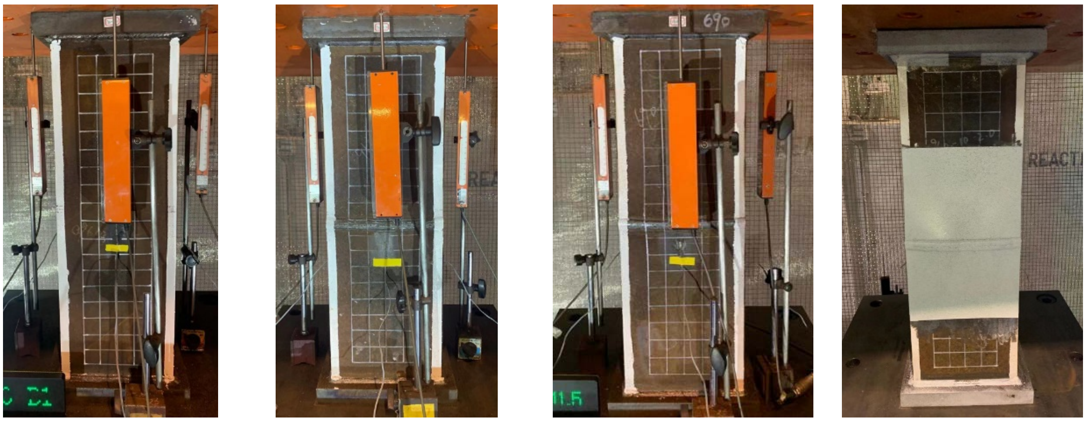

B-200×10 B-200×10a B-200×10b B-200×10c

(a) Series 960-B-200×10

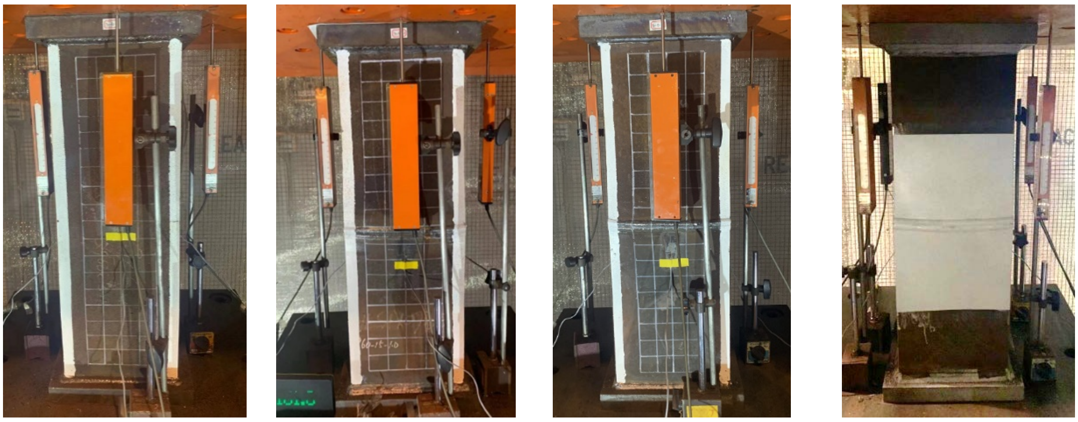

B-200×16 B-200×16a B-200×16b B-200×16c

(b) Series 960-B-200×16

Figure 4.23 Deformed shapes of S960 spliced box sections under axial compression

For the specimens 960-B-200×10c and 960-B-200×16c, since the DIC method was used to measure the strain variations during loading stage, white paint was sprayed on the surface of these two specimens. In all these cases, symmetrical local buckling appears on flanges and web of these welded box sections. The maximum deformation of almost all columns is at the half height, and this kind of outward bulge deformations are symmetrical on the two opposing flanges or web plates. Hence, plastic local plate buckling occurred on those S690 and S960 box sections, too.

4.6.2. Load-deformation relationships

Task I: Section classification to EN 1993-1-1

EN 1993-1-1(CEN, 2005) provides cross-section classification rules for steel with yield strengths up to 460 N/mm^2. For welded H-sections, the geometrical limits for Class 1 to 4 sections are:

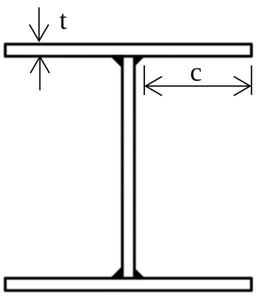

Class 1: $c\ /\ t_f \leq 9\sqrt{\frac{235}{f_y}}$

Class 2: $c\ /\ t_f \leq 10\sqrt{\frac{235}{f_y}}$

Class 3: $c\ /\ t_f \leq 14\sqrt{\frac{235}{f_y}}$

Class 4: $c\ /\ t_f > 14\sqrt{\frac{235}{f_y}}$

Figure 4.24 Cross-section classification rules for welded H-sections in EN1993-1-1

For the welded box sections, the standard specifies the geometrical limits in EN 1993-1-1 for Class 1 to 4 sections are:

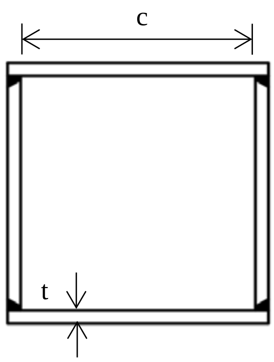

Class 1: $c \,/\, t_f \leq 33\sqrt{\frac{235}{f_y}}$

Class 2: $c \,/\, t_f \leq 38\sqrt{\frac{235}{f_y}}$

Class 3: $c \,/\, t_f \leq 42\sqrt{\frac{235}{f_y}}$

Class 4: $c \,/\, t_f > 42\sqrt{\frac{235}{f_y}}$

Figure 4.25 Cross-section classification rules for welded box sections in EN1993-1-1

Assuming that the current design rules in EN 1993-1-1 are applicable to the steel with yield strength higher than 700 MPa, Table 4-8 and Table 4-9 present the measured resistances of the S690 and the S960 H-sections, $N_{c,Rt}$, together with the design resistances, $N_{c,Rd}$, which predicted with the measured yield strength of flange and web as:

$$N_{c,Rd} = 2f_{y,f} \cdot bt_f + f_{y,w} \cdot dt_w \qquad \text{for H-sections}$$

$$N_{c,Rd} = 2f_y \cdot db_f + 2f_y \cdot db_w \qquad \text{for box-sections}$$

where $f_{y,f}$——the measured yield strengths of the flange on the welded H-section;

$f_{y,w}$——the measured yield strengths of the web on the welded H-section;

b——the measured width of the flange plate;

d——the measured overall depth of the web plate;

t_f——the measured thickness of the flange plate;

t_w——the measured thickness of the web plate of the welded H-sections;

f_y——the measured yield strengths of the welded box section;

b_f——the measured width of box section flange plate;

b_w——the measured width of box section web plate;

d——the measured thickness of box section

Table 4-8 Section resistances of S690 welded H-sections under compression

Test specimens	Section classification	Design Resistance	Measured resistance	$N_{c,Rt}/N_{c,Rd}$
		$N_{c,Rd}$ (kN)	$N_{c,Rt}$ (kN)	
H-120×10	Class 1	2,330	2,515	1.08
H-150×10	Class 3	2,912	2,998	1.03
H-200×16	Class 2	6,585	7,055	1.07
H-250×16	Class 3	8,297	8,384	1.01

Table 4-9 Section resistances of S960 welded H-sections under compression

Test specimens	Section classification	Design Resistance	Measured resistance	$N_{c,Rt}/N_{c,Rd}$
		$N_{c,Rd}$ (kN)	$N_{c,Rt}$ (kN)	
H–120×15	Class 1	5,018	5,894	1.17
H–150×15	Class 2	6,249	7,183	1.15
H–200×15	Class 3	8,822	9,537	1.08
H–250×15	Class 4	10,883	11,601	1.07

It is shown that the measured resistances are always higher than the design resistances, and hence, the current design rules given in EN 1993-1-1 can predict compressive resistances of S690 and S960 welded H-sections of different section classifications successfully. According to EN-1993-1-5(CEN, 2006), the effective area A_{eff} should be determined assuming that the cross section is subject only to stresses due to the uniform axial compression. For the Class 4 section H–250×15, when consider the effective widths to make the necessary allowances for reductions in resistance due to the effects of local buckling, the design resistance will become 10115kN, and ratio of $N_{c,Rt}$ /$N_{c,Rd}$ will become 1.15. This phenomenon shows that the current definition of the Class 4 section in Eurocode for is too conservative for high strength S960 steel.

Table 4-10 Section resistances of S690 and S960 welded box sections under compression

Test specimens	Section classification	Design Resistance	Measured resistance	$N_{c,Rt}/N_{c,Rd}$
		$N_{c,Rd}$ (kN)	$N_{c,Rt}$ (kN)	
690-B200×10	Class 1	5,717	5,824	1.02
690-B200×16	Class 1	9,767	10,616	1.09

960-B200×10	Class 2	7,334	7,813	1.07
960-B200×15	Class 1	11,482	12,281	1.07

The measured resistances are always higher than the design resistances. Consequently, the current design rules given in EN 1993-1-1 can predict compressive resistances of the S690 and the S960 welded box sections of Class 1 and Class 2 successfully.

The load-shortening curves of these 8 H-sections are plotted in Figure 4.26 for directly comparison. The axial shortenings are taken as the average values of four displacement transducers. All load-shortening curves obtained from the experiments extend above the respective design section resistances $N_{c,Rd}$ of these sections. For the S690 H-sections, all sections exhibit significant deformation ductility under compression. It is shown that S690 H-sections of Class 1 and 2 possess good deformation capacities, while Class 3 sections have little. These responses are found to be consistent with structural behaviour implied in the section classifications of stocky columns. For S960 H-sections, H-sections of Class 1, 2, and 3 possess good deformation capacities. When the Class 4 H-section reached its section resistances, the material's strength was fully utilized, and limited ductility was achieved. These responses are found to be consistent with structural behaviour implied in the section classifications. Consequently, these results agree with the section classification obtained by the current classification rules for welded cross-sections given in EN 1993-1-1.

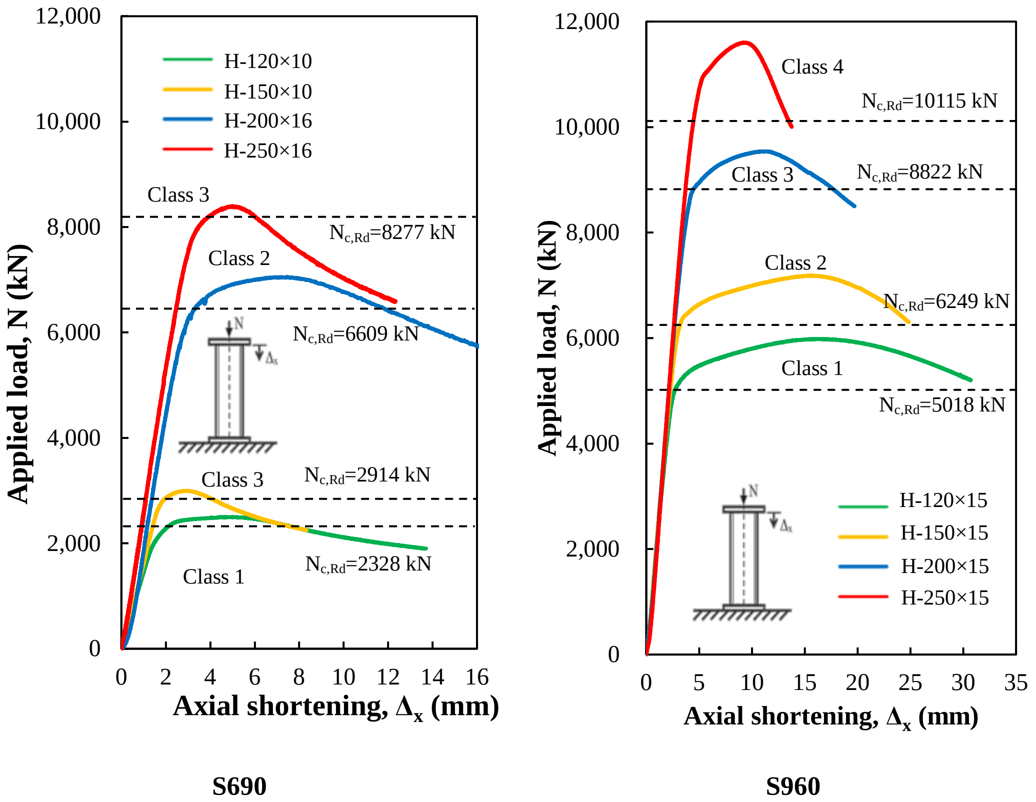

Figure 4.26 Load-shortening curves of S690 and S960 referenced welded H-sections

Local buckling on those stocky columns could be obtained after the ultimate loads were reached. Therefore, the compressive resistances have been fully mobilized before plastic local buckling happened on the flange and web plates. Moreover, EN 1993-1-1 and EN 1993-1-12 have only covered steel grade up to S700 on codified design rules. Hence, it is necessary to determine an appropriate section classification for the design of the S960 columns.

The load-shortening curves of 4 box section stocky columns are plotted in Figure 4.27 for comparison. The S690-B2 and the S960-B2 sections exhibit significant deformation ductility under compression. Considering the load-shortening curves of S690-B1 and S960-B1, although these two sections are regarded as Class 1 and Class 2 according to existing rules given in EN 1993-1-1, it is more reasonable to categorize them into Class 3 due to their low degree of ductility.

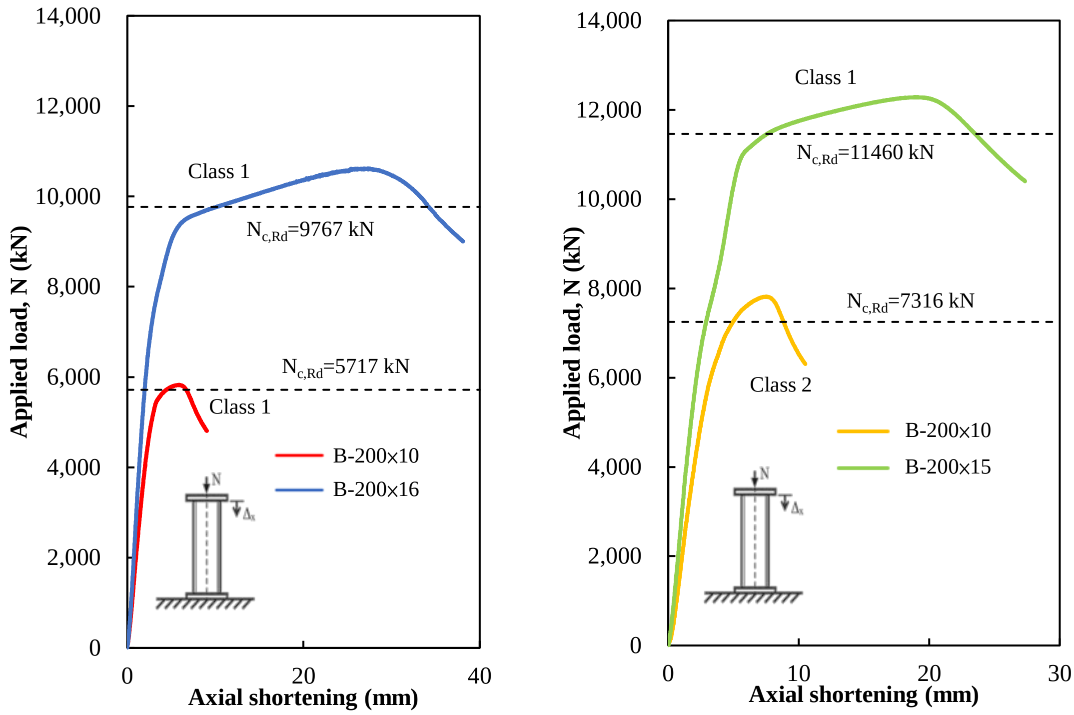

S690 S960

Figure 4.27 Load-shortening curves of S690 and S960 referenced welded box sections

Task II: No reduction under controlled welding of H-sections

Table 4-11 and Table 4-12 present the measured resistances of the S690 and the S960 spliced H-sections, $N_{c,Rt}$, together with the design resistances, $N_{c,Rd.}$ with different heat input energy on butt weld. The design resistances were predicted with measured dimensions and the yield strength measured in Chapter 3.

Table 4-11 Section resistances of S690 spliced welded H-sections under compression

Test specimens	Section classification	Heat input energy (kJ/mm)	Design Resistance $N_{c,Rd}$ (kN)	Measured resistance $N_{c,Rt}$ (kN)	$N_{c,Rt}/N_{c,Rd}$
H-200×10	Class 4	-	4,039	4,659	1.15
H-200×10a		1.0	3,884	4,505	1.04
H-200×10b		1.5	4,013	4,513	1.02
H-200×10c		2.0	4,029	4,589	1.03
H-200×16	Class3	-	7,441	7,766	1.04
H-200×16a		1.0	7,541	7,543	1.00

H-200×16b		1.5	7,528	7,605	1.01
H-200×16c		2.0	7,550	7,737	1.02
H-200×30	Class 1	-	20,336	22,975	1.13
H-200×30a		1.0	20,196	22,112	1.09
H-200×30b		1.8	20,489	22,323	1.09
H-200×30c		3.0	20,581	22,725	1.10

Table 4-12 Section resistances of S960 spliced welded H-sections under compression

Test specimens	Section classification	Heat input energy (kJ/mm)	Design Resistance $N_{c,Rd}$ (kN)	Measured resistance $N_{c,Rt}$ (kN)	$N_{c,Rt}/N_{c,Rd}$
H-200×10	Class 4	-	4,971	6,004	1.21
H-200×10a		1.0	4,934	5,825	1.18
H-200×10b		1.5	4,966	5,886	1.19
H-200×10c		2.0	4,916	5,809	1.18
H-200×15	Class 3	-	8,807	9,537	1.08
H-200×15a		1.0	8,821	9,314	1.06
H-200×15b		1.5	8,878	9,291	1.05
H-200×15c		2.0	8,781	9,356	1.07

The effective area of two series of Class 4 cross-sections were considered in accordance with EN-1993-1-5 in above tables. For the S960 H-sections, even if the effective area is not considered, all the measured resistances still higher than the design value. It shows that the current definition of the Class 4 section in Eurocode is too conservative for the S960 H-sections.

Moreover, the load-shortening curves of all S690 and S960 H-sections are plotted in Figure 4.28 for directly comparison. The $N_{c.Rd}$ in each figure is the average value of the design resistance of four columns in its series. Deformations occurred during the load-descending stage of those stocky columns, regardless of whether there are butt welds on the columns. For four 690-H3 series columns, compression test unload at around 99.5% of the maximum resistance, to avoid the safety problem caused by approaching the critical value of the test system. 690-H3 series columns still showed sufficient ductility when unloaded.

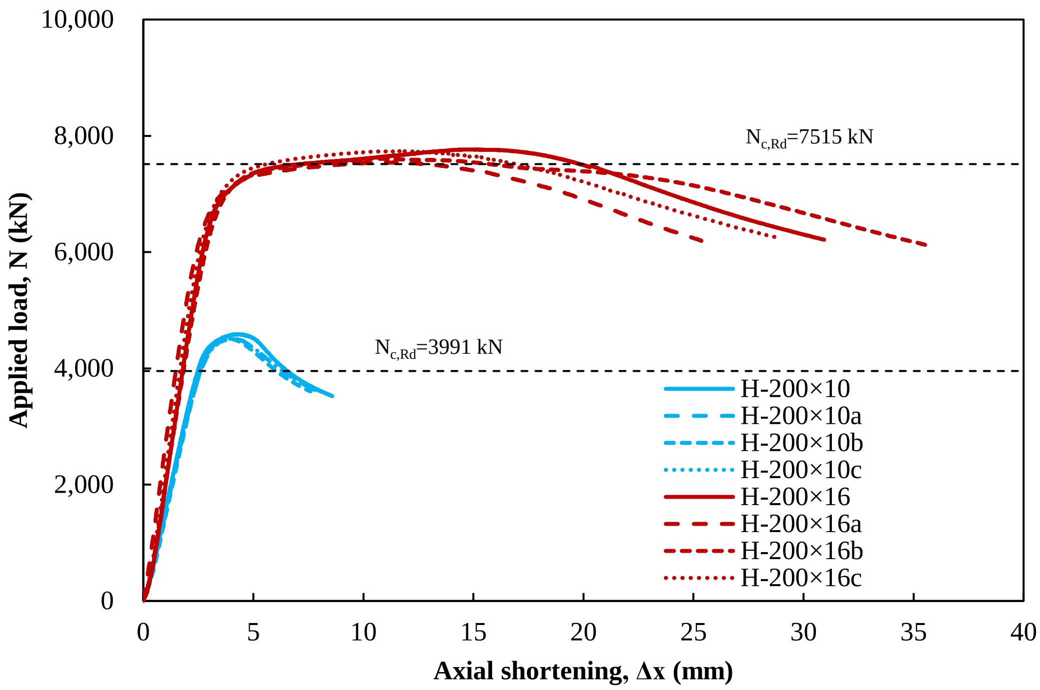

S690 H-sections: H-200×10 and H-200×16 series

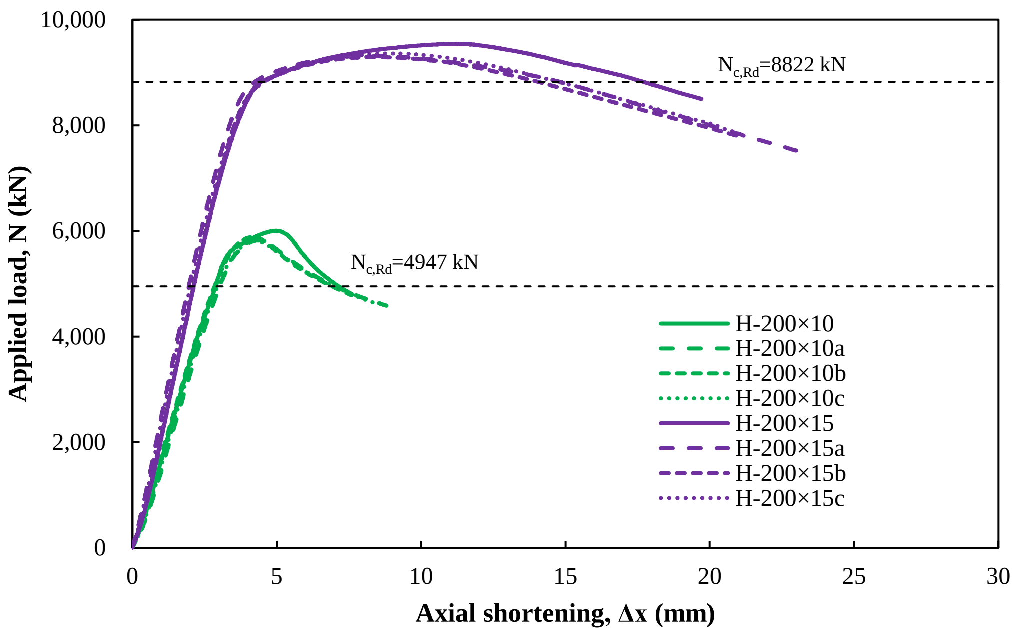

S960 H-sections: H-200×10 and H-200×15 series

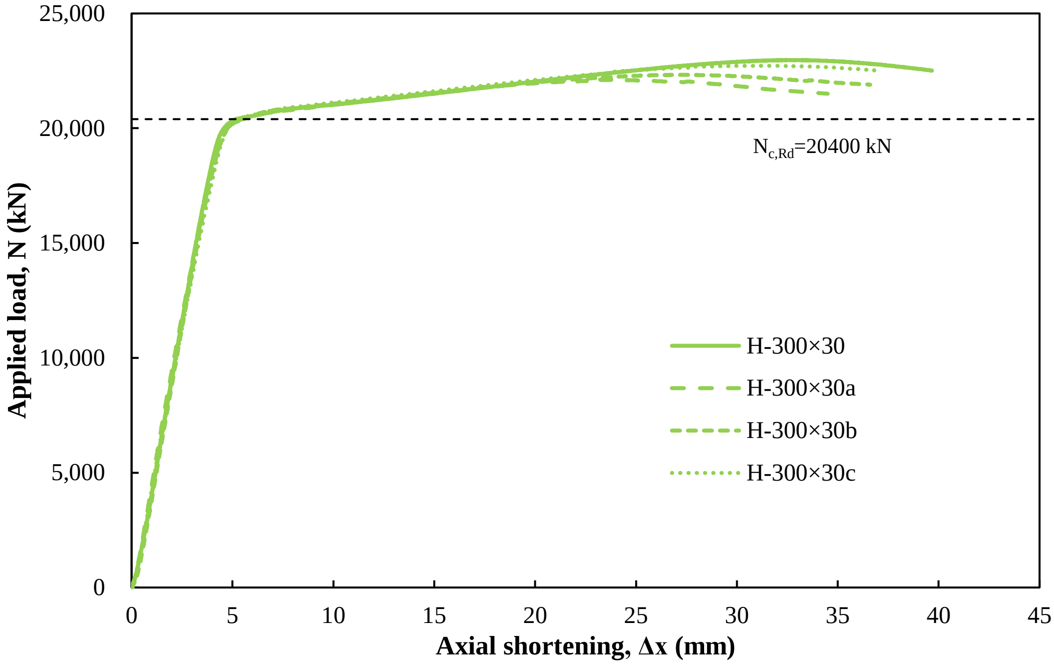

S690 H-sections: H-300×30 series

Figure 4.28 Load-shortening curves of S690 and S960 spliced welded H-sections

In each series, the reference column and the other three spliced columns have the same trend in load-shortening curves. For the S690 and the S960 columns with plate thickness 10mm, 15mm, and 16mm, the heat input energy of butt welding has no obvious influence on the resistance of the column. Taken S960-H1 and S960-H2 series as examples, the measured resistance of H1-1.0 is higher than H-1-2.0, while the measured resistance of H2-1.0 is lower than H2-2.0. For the S690 columns with plate thickness 30mm, this phenomenon also exists. Hence, by a proper control of welding processes according to given WPS, the effects on the section resistances of these S690 and S960 welded H-sections are rather minimized.

Task III: No reduction under controlled welding of box sections

Table 4-13 and Table 4-14 presents the measured resistances, $N_{c,Rt}$, together with the design resistances, $N_{c,Rd.}$ with different heat input energy on butt weld of the S690 and the S960 spliced box sections.

Table 4-13 Section resistances of S690 spliced welded box sections under compression

Specimens	Section classification	Design Resistance	Measured resistance	$N_{c,Rt}/N_{c,Rd}$

			$N_{c,Rd}$ (kN)	$N_{c,Rt}$ (kN)	
S690	B-200×10	Class 1	5,715	5,824	1.02
	B-200×10a		5,712	5,741	1.01
	B-200×10b		5,713	5,762	1.01
	B-200×10c		5,726	5,770	1.01
	B-200×16	Class 1	9,770	10,616	1.09
	B-200×16a		9,753	9,986	1.02
	B-200×16b		9,759	10,165	1.04
	B-200×16c		9,785	10,087	1.03

Table 4-14 Section resistances of S960 spliced welded box sections under compression

Specimens		Section classification	Design Resistance	Measured resistance	$N_{c,Rt}$ /$N_{c,Rd}$
			$N_{c,Rd}$ (kN)	$N_{c,Rt}$ (kN)	
S960	B-200×10	Class 2	7,342	7,813	1.06
	B-200×10a		7,323	7,421	1.01
	B-200×10b		7,348	7,423	1.01
	B-200×10c		7,249	7,315	1.01
	B-200×15	Class 1	11,478	12,281	1.07
	B-200×15a		11,487	11,774	1.02
	B-200×15b		11,436	11,771	1.03
	B-200×15c		11,437	11,727	1.03

It is found that the measured compressive resistances of all stocky columns (with or without butt weld) are higher than the predicted values according to the design rules given in EN 1993-1-1. For the S690 sections, the measured compressive resistances are about 1%~6% higher than the predicted values, for the S960 sections, this value is up to 2%~7%. Hence, by a proper control of welding processes according to the given WPS, the effects on the section resistances of these S690 and S960 welded box sections are rather minimized.

The load-shortening curves of those S690 and S960 box sections are plotted in Figure 4.29 for directly comparison. The axial shortening data is taken as the average value of four LVDTs.

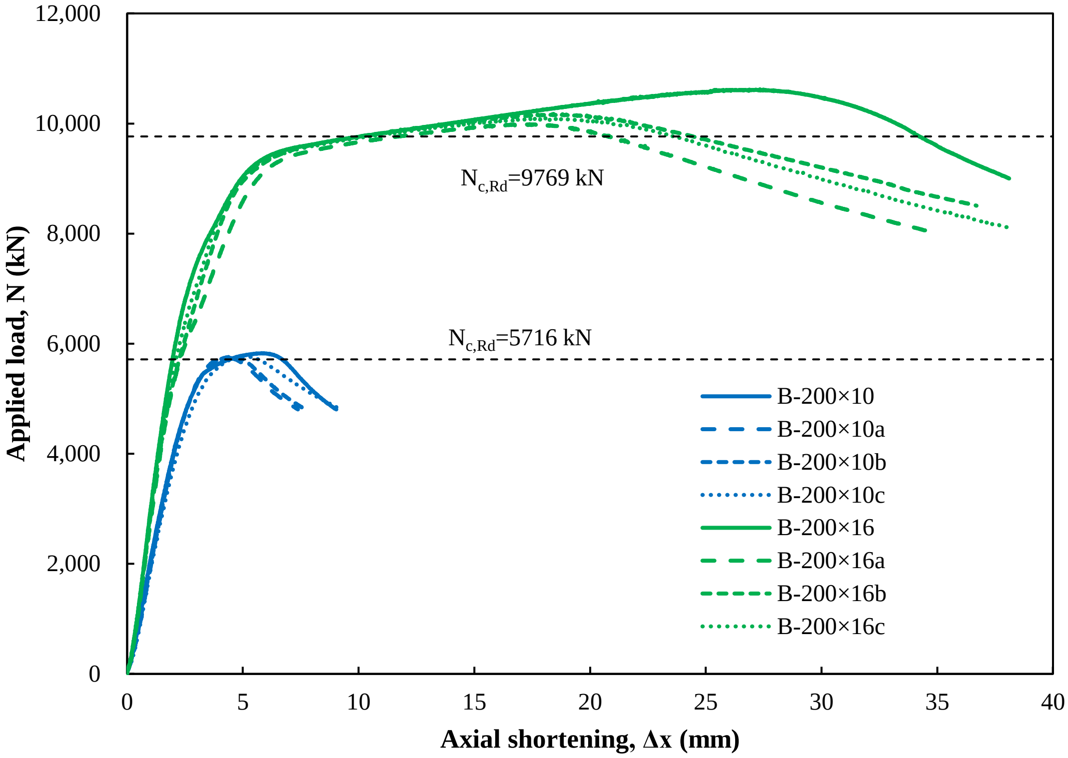

S690 box sections: B-200×10 and B-200×16 series

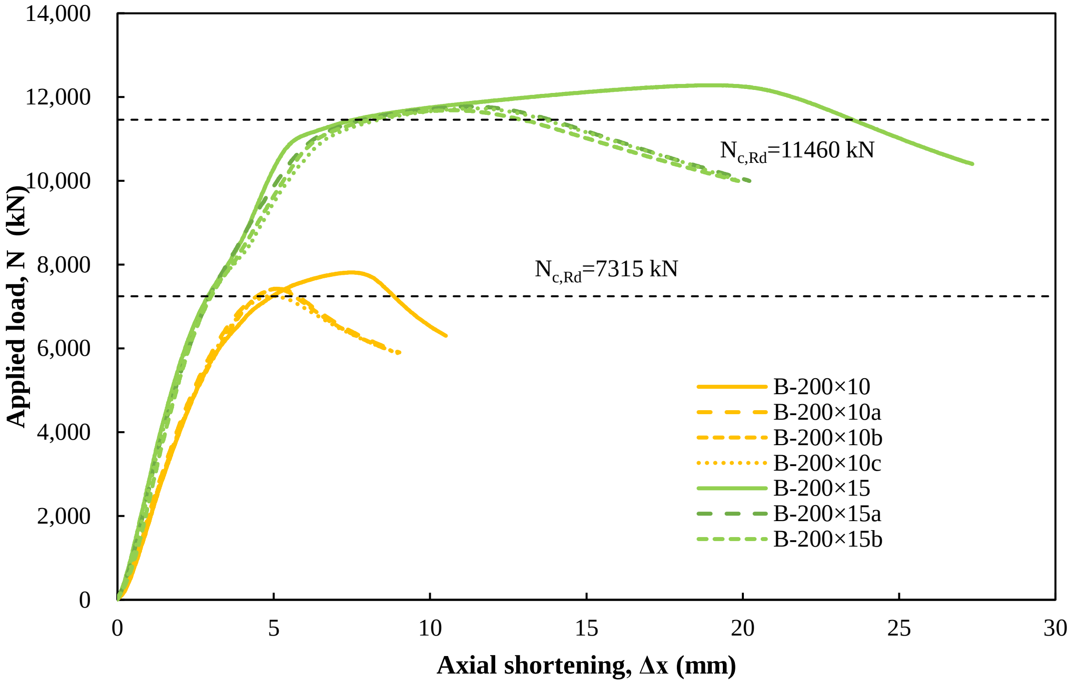

S960 box sections: B-200×10 and B-200×15 series

Figure 4.29 Load-shortening curves of S690 and S960 spliced welded box sections

For all columns, the applied load increases linearly up to about 80% of the design section resistances. Then, the slopes of the load-shortening curves begin to reduce gradually, when the applied loads continue to increase. For reference column (box sections without butt weld) like S690-B1, -B2, and S960-B1, -B2, this stage stays longer than sections with butt weld. This might attribute to the presence of residual stresses which are induced during butt welding. Since the updated EN 1993-1-12 will be finalized after sufficient experience and data have been gained, with a focus on high strength steels up to grade S960 (Kuhlmann *et al*. 2021), this study will provide valuable information for the new EC3 standard.

4.7. Conclusion

Through tensile tests on the S690 and the S960 welded coupons in Chapter 3, reliable welding procedure specifications of different heat input energy on the S690 and the S960 steel have been formulated. A series of compression tests on 39 welded stocky columns were successfully conducted and present in this chapter. All these H-sections and box sections, include 16 reference columns and 23 spliced columns were found to be failed in plastic local buckling and attained full compressive section resistances. Based on the test results, the following key findings are obtained:

- No cracks were found in any fillet weld or butt weld on those stocky columns after testing. It demonstrates that welding assembly strictly performed in accordance with the WPS is reliable.
- The S690 and the S960 sections with or without butt welded splices have the same failure modes.
- The measured compressive resistances of all these 39 sections are larger than the design values according to EN 1993-1-1.
- For the S960 H-sections of Class 1, 2, 3 and 4, full section resistances with a range of deformation capacities are achieved. For the S960 box sections of Class 1 and 2, current section classification rules are found to be conservative.

- The controlled welding process causes little impact on the cross-sectional resistances against compression of S690 and S960 spliced H-sections and box sections.

CHAPTER FIVE

EXPERIMENTAL INVESTIGATION: RESIDUAL STRESSES OF S960 STOCKY COLUMNS

5.1. Introduction

This chapter provides an in-depth investigation into the effects of welding onto the residual stresses of high strength S960 H-sections and box sections. Fabrication of these four S960 sections employed validated welding parameters according to the welding procedure specifications developed in Chapter 4. The transient temperature history during welding were measured with thermocouples. A comprehensive series of hole drilling measurements on these S960 welded sections was conducted to obtain the surface residual stresses of these sections. These experimental results will be used for subsequent calibration of finite element models.

5.2. Temperature measurements on S960 welded sections

5.2.1. Measurement programme

In this part of experimental investigation, a total of four S960 welded sections were fabricated in the Pristine Metal Structure Co., Ltd. using validated welding parameters according to the welding procedure specification, just as presented in Chapter 4. During the fabrication process, temperature history due to welding were recorded using thermocouples.

The typical section dimensions of these four S960 welded sections are shown in Figure 5.1 and Table 5-1. All the welding on these sections were adopted using gas metal arc welding (GMAW), and the welding parameters including current, voltage, and welding speed were recorded simultaneously. To prevent the electrodes from melting and flowing underneath, a pad iron with a thickness of only 1.5mm was provided at the back of the weld groove with spot welding. It was found that the pad iron fused with the section after welding, but its contribution to the resistances of these welded section is considered to be negligible.

a) H-section b) Box section

Figure 5.1 Typical sections of S960 welded sections

Table 5-1 Cross-sectional dimensions of S960 welded sections

Number	Steel Grade	Cross-section Type	Specimens Label	B (mm)	t (mm)	L (mm)
1	S960	H section	S960-H1-R	200	10	650
2			S960-H2-R	200	15	650
3		Box section	S960-B1-R	200	10	650
4			S960-B2-R	200	15	650

The mechanical properties of the S960 steel plates used in this investigation were fully reported in Chapter 3. The fabrication procedures adopted in these welded sections were consistent with those for the welded H-sections reported in Chapter 4 to ensure that both the distributions and the magnitudes of residual stresses of all these welded sections were consistent.

5.2.2. Measurement and instrumentation

These four sections were fabricated by two experienced welders from the Pristine Metal Structure Co., Ltd. in strict accordance with the welding procedure specifications reported in Chapter 4. As shown in Figure 5.2, small pieces of S355 steel plates were used for temporary fixing to prevent distortion during welding. For Section S960-B1-R and S960-B2-R shown in Figure 5.21-b), four 1.5mm thick S355 steel plates were employed as protective pads to prevent any loss of molten electrode material during the welding process of the butt weld joints.

a) H-sections b) Box sections

Figure 5.2 Temporary fix of S960 welded sections

For each welded section, a total of six thermocouples were designed to measure the surface temperatures during welding. Before welding, the surface of these measurement points underwent a meticulous polishing process to ensure an absence of surface rust. Six thermocouples were then spot welded onto the measurement points using a soldering iron. The experimental setup is shown in Figure 5.3. The experimental investigation utilized a Type-K thermocouple WWI0100, which operates within a temperature range of 0°C to 1200°C. To minimize the effects of heat convection and radiation, the exposed surfaces of the thermocouples and the measurement points were covered with ETL HT Putty, a white mud material, as shown in Figure 5.4 and Figure 5.5. During the welding process, surface temperature changes on the measurement points were monitored by capturing electrical signals, which were subsequently converted to Celsius degrees. A high-precision TML AWS-50C data logger was used to record these measured data for subsequent analysis.

Figure 5.3 Test setup for temperature measurement

It should be noted that the selection of appropriate measurement points is important, since the temperatures within the welded sections can potentially exceed the melting temperature of the steel, which also exceeds the highest temperature that can be measured with the thermocouple. Conversely, any location situated too far from the welded sections exhibit may diminished sensitivity to temperature change induced by welding. Therefore, a careful consideration should be given in choosing optimal measurement points in order to accurately capture the transient temperature history during welding. Hence, for the two S960 welded H-sections, the measurement points were marked to be directly above the webs on the flange surfaces. For the two S960 welded box sections, the measurement points were marked to be positioned 10 mm away from the welding groove. These locations of the measurement points ensured that the measured temperatures were sufficiently sensitive to the temperature changes during welding while they remained to be within the measurement range of the thermocouples.

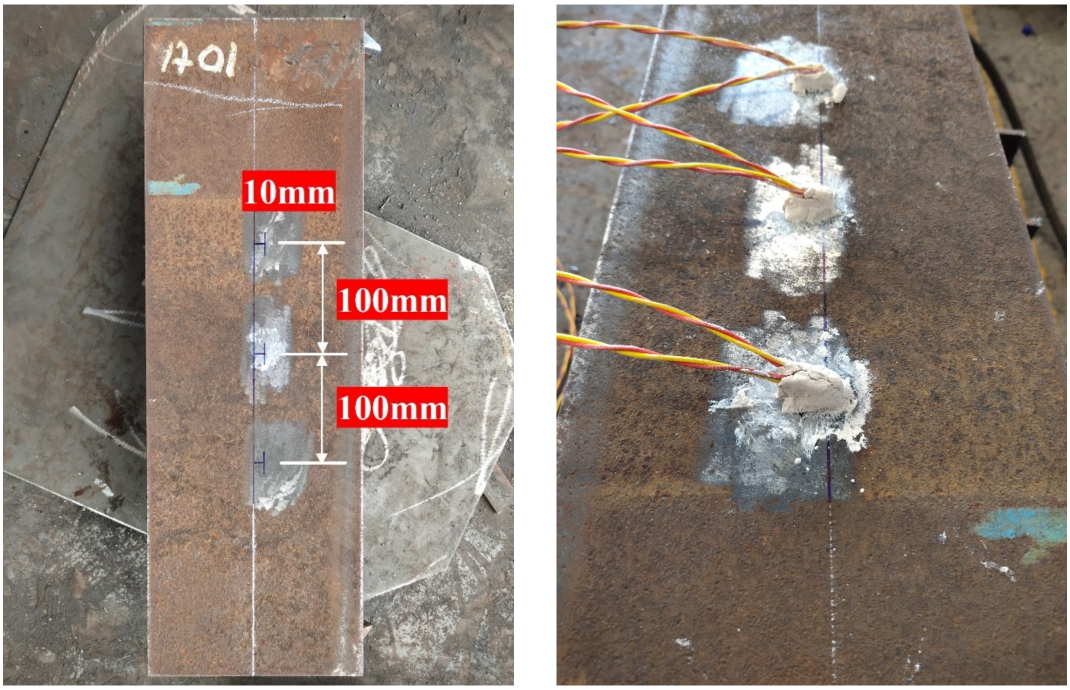

Figure 5.4 Arrangement of thermocouple of a S960 H-section

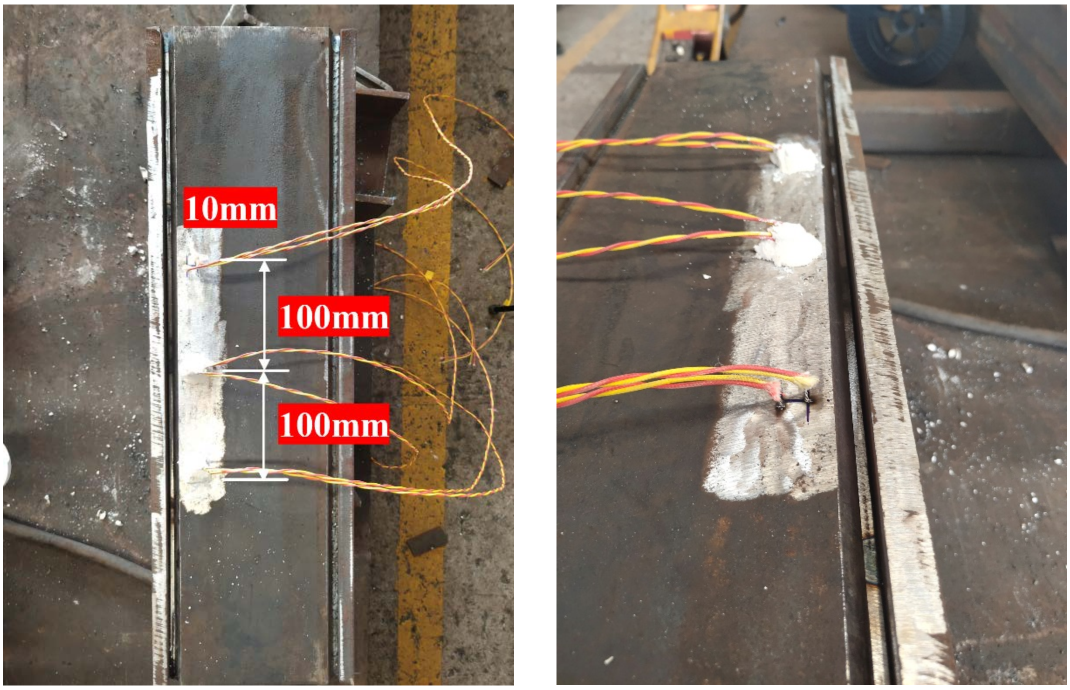

Figure 5.5 Arrangement of thermocouple of a S960 box sections

In order to prevent cold cracking on these sections, they were preheated using a flame torch over a short period of time so that the surface temperatures of the welding grooves were increased to a temperature range of 100°C to 200°C, according to the WPS reported in Chapter 4. The preheating temperature of each welding groove was also recorded before welding, as shown in Figure 5.6.

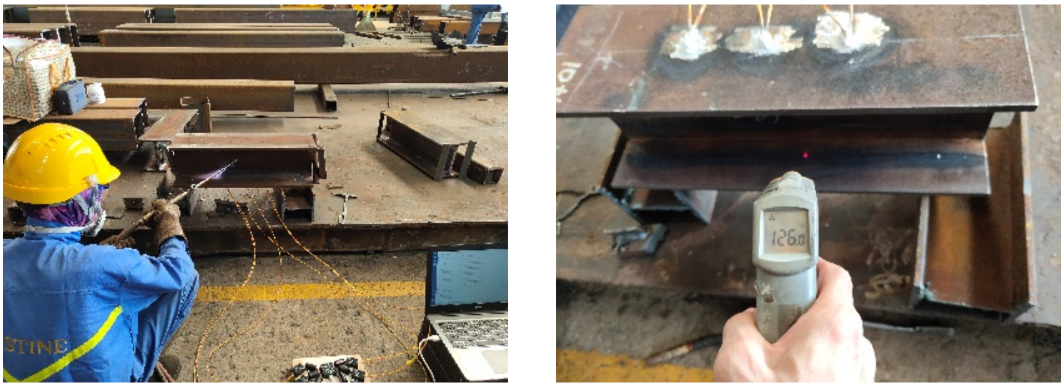

Figure 5.6 Preheating before welding of S960 welded section

5.2.3. Measured results

Collection of the preheating temperature, the welding parameters, and the temperature data for these four welded sections were successfully completed. For the two welded H-sections, in order to minimize post-welding distortion, the welders adopted a forward and reverse sequence welding. This approach involved alternating between the two welding directions during the welding process. It should be noted that the welding direction, whether from Point A to Point B or from Point B to Point A, as shown in Figure 5.7, were recorded for subsequent numerical simulations.

From each welding pass, the heat input energy q, is given by:

$$q = \eta \frac{U \cdot I}{v} \tag{5.1}$$

where U is the voltage;

I is the current;

η is the welding efficiency, and it is taken as 0.85 for GMAW;

v is the welding speed.

During the welding process, both the voltage and the current values are subject to a significant variation within a given time period. To calculate the heat input energy, an average value of all these parameters recorded is often found to be sufficient.

1. Section S960-H1-R

The thermocouple arrangement, the welding sequence and the dimensions of each weld pass of Section S960-H1-R are shown in Figure 5.7. A total of six measurement points were arranged symmetrically along the central axis of the top flange, and four fillet welds were applied between each of the two flanges and the web according to the welding pass sequence. Typical weld throat was measured to be 8.0 mm.

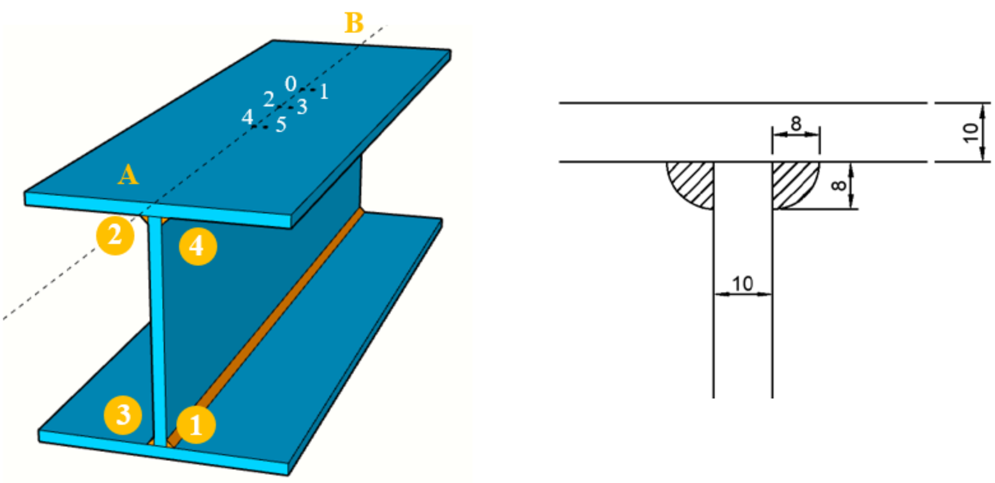

Figure 5.7 Schematic diagram of measurement set-up for Section S960-H1-R

The welding parameters for Section S960-H1-R are recorded in Table 5-2. In order to minimize weld distortion, various welding directions sequences were employed to counterbalance any thermal deformation caused by welding. Given that the welding speed was not readily measured during welding, it was calculated as the total length of the weld run divided by the time taken to complete the welding.

Table 5-2 Welding parameters for Section S960-H1-R

Section	Pass	Direction	Voltage U (V)	Current I (A)	Weld speed v (mm/s)	Heat input energy q (kJ/mm)
960-H1-R (10mm)	1	A-B	24.2-24.6	206-217	4.38	1.00
	2	A-B	24.2-24.6	206-217	4.38	1.00
	3	B-A	24.2-24.6	202-210	4.92	0.87
	4	B-A	24.2-24.6	202-210	4.92	0.87

The measured transient temperature history during welding passes No. 2 and 4 are plotted in Figure 5.8.

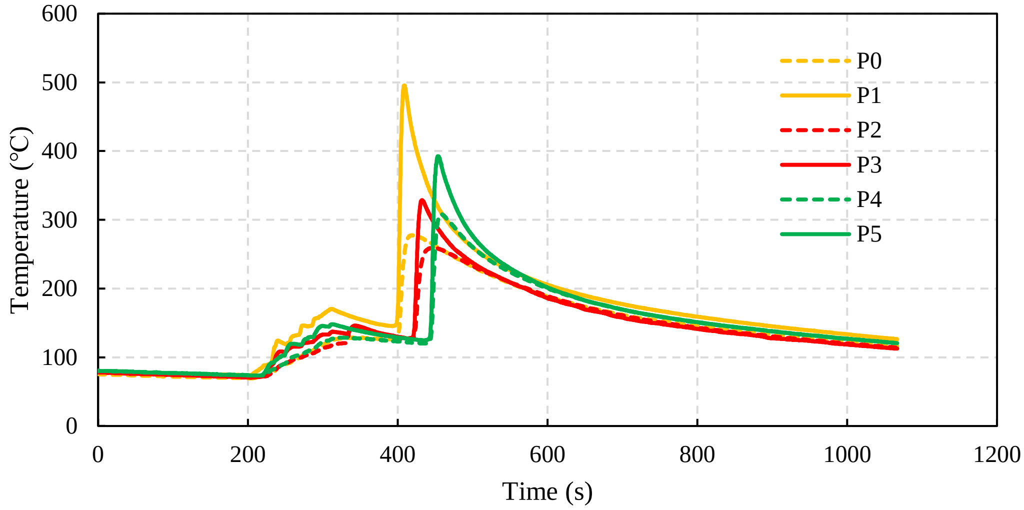

a) Welding pass: No.2

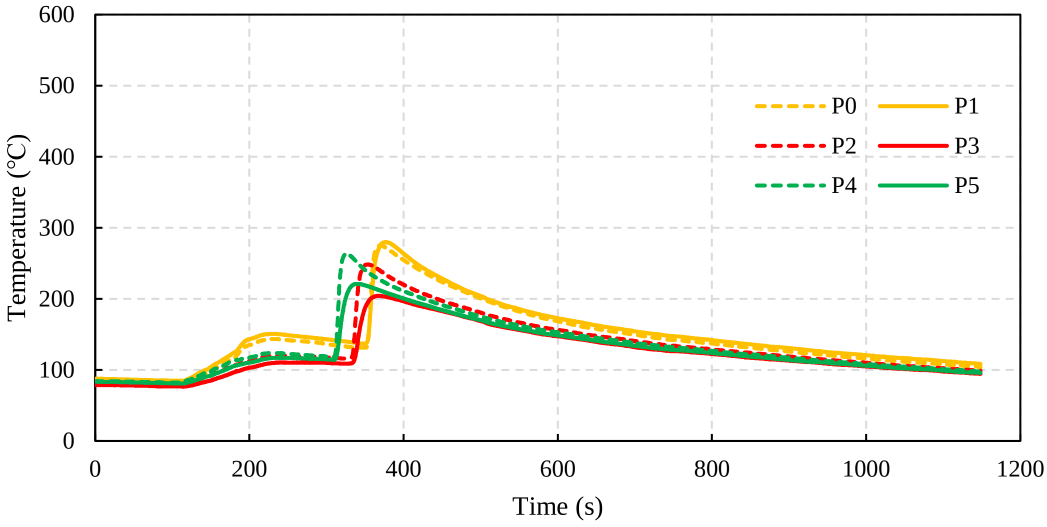

b) Welding pass: No.4

Figure 5.8 Transient temperature history of Section S960-H1-R

As shown Figure 5.8, for welding pass No. 2, a preheating temperature with a maximum value at 170°C was applied before welding. The peak temperatures during welding were obtained with Thermocouples 1, 3, and 5 along the central line of the flange. For welding pass No.4, a preheating temperature of a maximum value at 150°C was applied before welding. The peak temperatures during welding were obtained with Thermocouples 0, 2, and 4 which were located 10mm away from the central line of the flange.

2. Section S960-H2-R

Similarly, a total four passes of fillet welding were applied to Section S960-H2-R. The thermocouple arrangement, the welding sequences and the dimensions of each weld pass of Section S960-H2-R are shown in Figure 5.9. Due to an increased thickness of the steel plates, typical weld throat was measured to be 12.0 mm.

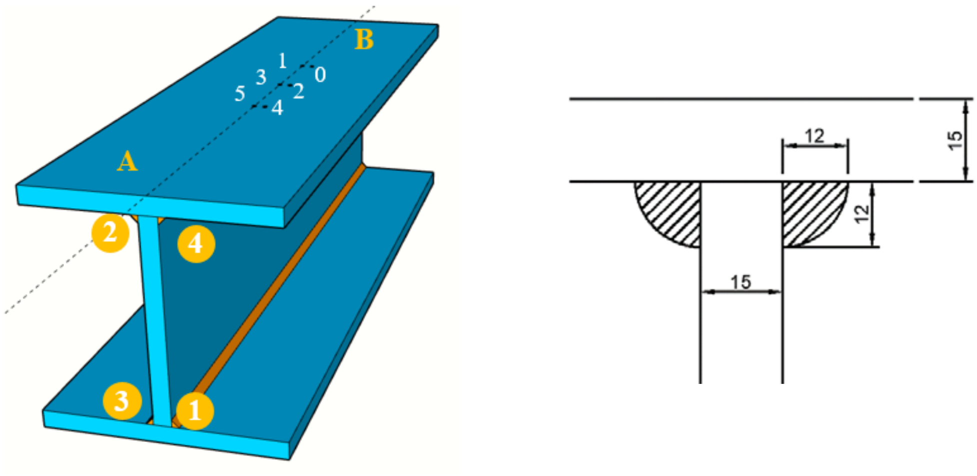

Figure 5.9 Schematic diagram of measurement set-up for Section S960-H2-R

Table 5-3 Welding parameters for Section S960-H2-R

Section	Pass	Direction	Voltage U (V)	Current I (A)	Weld speed v (mm/s)	Heat input energy q (kJ/mm)
960-H2-R (15mm)	1	A-B	29.4-29.8	288-292	4.17	1.75
	2	A-B	29.4-29.8	280-286	5.00	1.43
	3	B-A	29.4-29.8	288-296	5.00	1.43
	4	B-A	29.4-29.8	286-292	5.00	1.43

The measured transient temperature history of welding passes No. 2 and No. 4 r are plotted in Figure 5.10. As the welding direction and sequence of Section S960-H2-R are the same as those for Section S960-H1-R, for weld pass No.2, a preheating temperature at a maximum value at 100°C was applied before welding. The peak temperatures during welding were obtained with Thermocouples 1, 3, and 5 along the central line of the flange. In the case of welding pass No. 4, a preheating temperature with a maximum value at 200°C was applied before welding. The peak temperatures during welding were obtained with Thermocouples 0, 2, and 4 which were located positioned at 10mm from the central line of the flange.

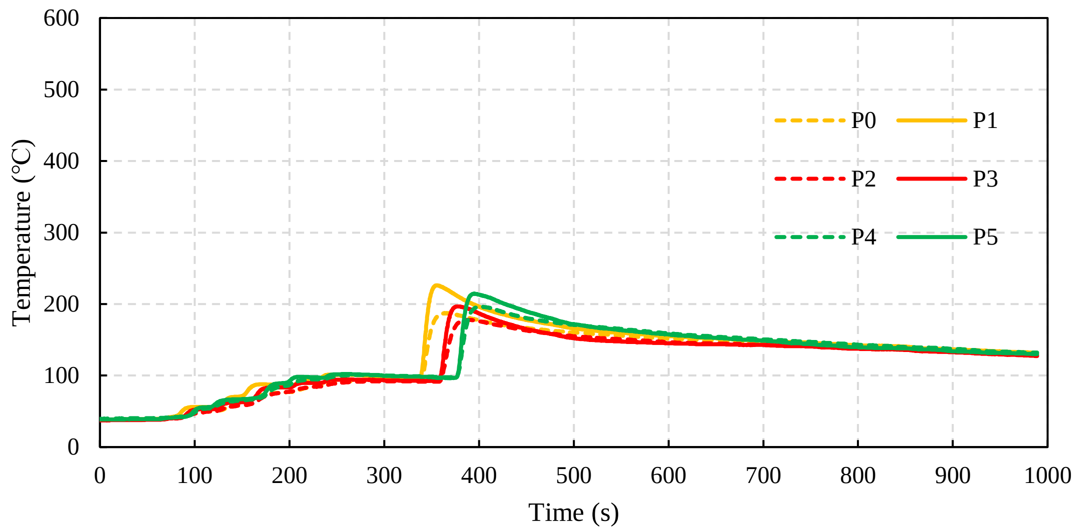

a) Welding pass: No.2

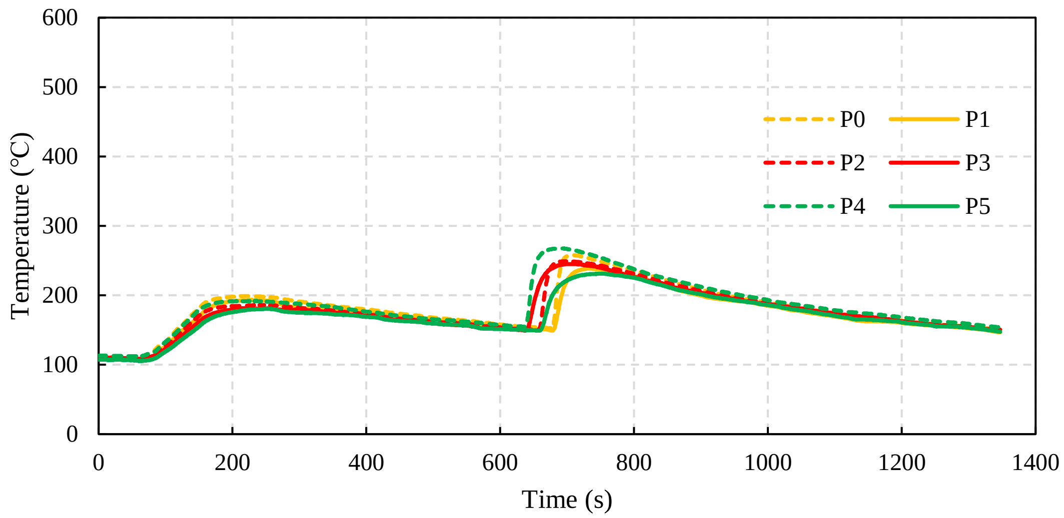

b) Welding pass: No.4

Figure 5.10 Transient temperature history of Section S960-H2-R

3. Section S960-B1-R

For the two S960 welded box sections, considering the configuration of the section corners, full penetration butt welding was used. Typical measured dimensions of the weld joint details are shown in Figure 5.11. A total of six measurement points on the surface of the section corners were located at 10 and 20 mm from the edge of the weld groove.

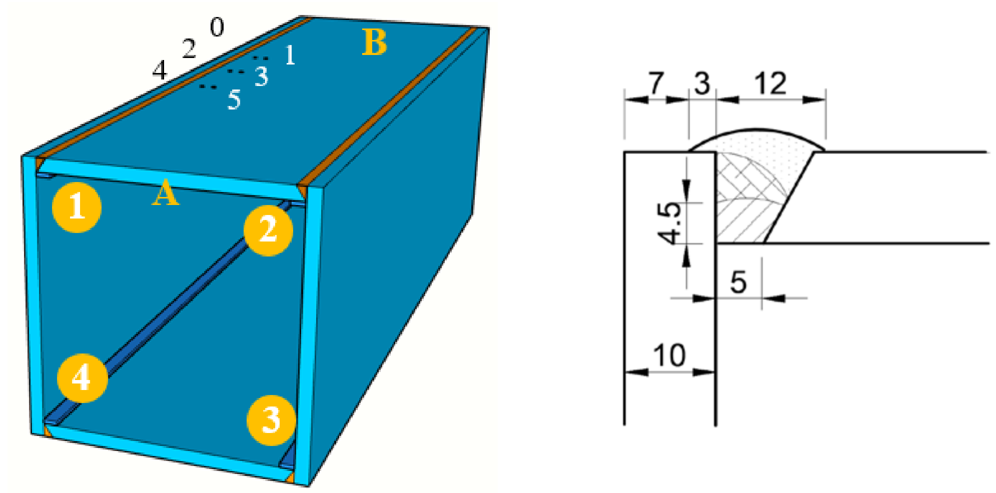

Figure 5.11 Schematic diagram of measurement set-up for Section S960-B1-R

The welding parameters for Section 960-B1-R are shown in Table 5-4. It is shown that the measured values of heat input energy for all weld passes were successfully maintained approximately at 1.00 kJ/mm with a maximum value of 1.13 kJ/mm. It should be noted that these values align with the heat input energy adopted for the fabrication of these S960 welded sections reported in Chapter 4.

Table 5-4 Welding parameters for Section S960-B1-R

Section	Pass	Direction	Voltage U (V)	Current I (A)	Weld speed v (mm/s)	Heat input energy q (kJ/mm)
960-B1-R (10mm)	1-1	A-B	24.4-24.6	198-202	4.51	0.88
	2-1	A-B	24.4-24.6	201-205	4.74	0.85
	3-1	A-B	24.4-24.8	200-205	4.58	0.89
	3-2	A-B	26.8-27.4	230-233	4.52	1.13
	3-3	A-B	26.9-27.1	208-212	4.39	1.05
	4-1	A-B	24.4-24.8	200-205	4.58	0.89
	4-2	A-B	26.8-27.4	230-233	4.52	1.13
	4-3	A-B	26.9-27.1	208-212	4.39	1.05
	1-2	A-B	26.0-26.6	220-225	4.74	1.01
	1-3	A-B	26.0-26.6	213-216	4.92	0.93
	2-2	A-B	26.0-26.6	220-225	4.64	1.03
	2-3	A-B	26.0-26.6	213-216	4.45	1.03

* Pass *i-j* denotes "Corner *i* – Welding pass *j* "

The transient temperature history of Corner No.4 during welding are presented in Figure 5.12. It should be noted that the first peak temperature at about 350°C was applied during the pre-heating. This preheating temperature exceeded the maximum scheduled value by mistake. However, as it did not reach the critical phase transformation temperature A_{c1} of the S960 steel, this mistake did not have any impact on the quality of welding.

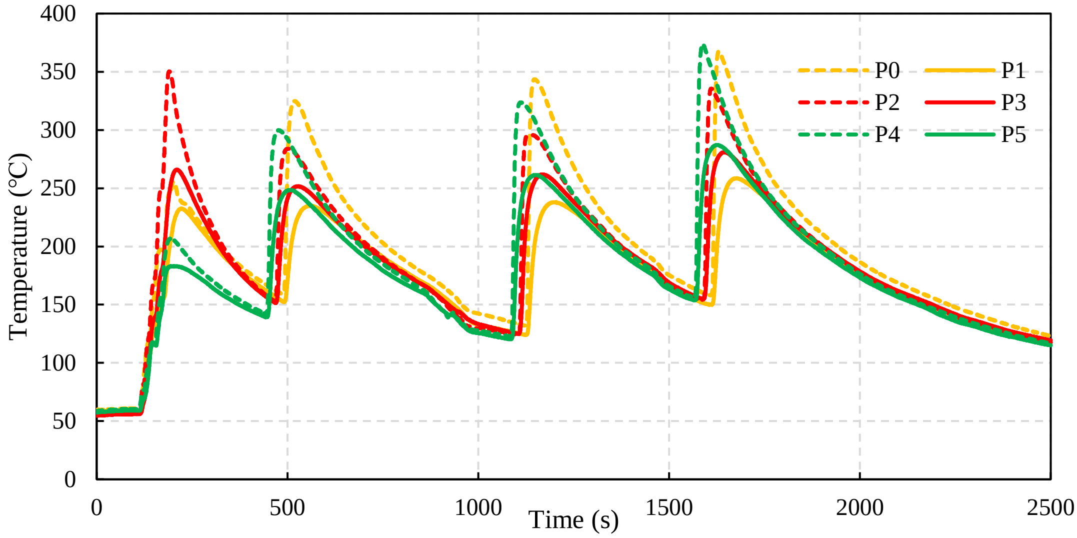

Figure 5.12 Transient temperature history of Section S960-B1-R

During welding of passes No. 4-1, 4-2, and 4-3, the maximum temperatures were obtained with Thermocouple 0, 2, and 4 along the same longitudinal line which were located 10 mm away from the welding groove.

4. Section S960-B2-R

As the plate thickness of Section S960-B2-R was 15mm, a total of four welding passes was requited for each of the welding groove. The welding sequence, measurement points, and typical measured dimensions of the welded sections are presented in Figure 5.13.

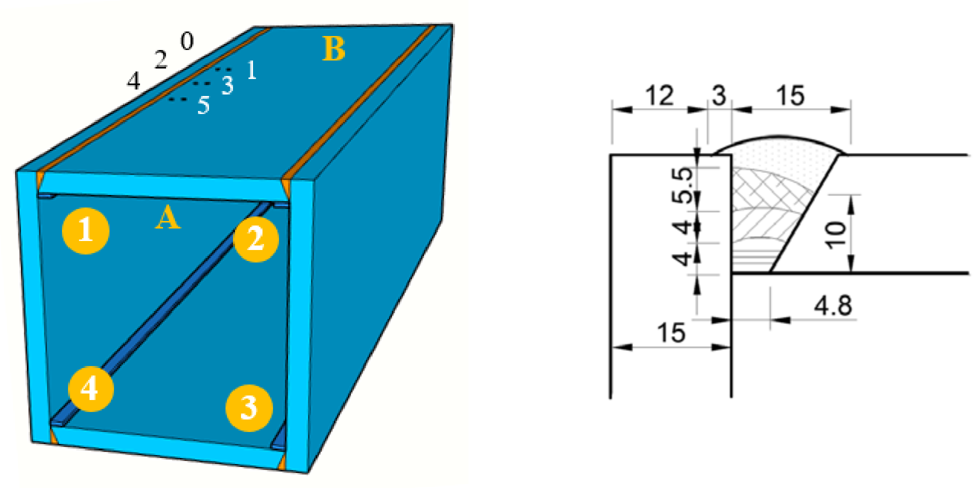

Figure 5.13 Schematic diagram of measurement set-up for Section S960-B2-R

The welding parameters of all weld passes are presented in Table 5-5. It is shown that the heat input energy for all weld passes were approximately at 1.00 kJ/mm with a maximum value of 1.19 kJ/mm. It should be noted that these values align with the heat input energy adopted for the fabrication of these S960 welded sections reported in Chapter 4.

Table 5-5 Welding parameters for Section of S960-B2-R

Section	Pass	Direction	Voltage U (V)	Current I (A)	Weld speed v (mm/s)	Heat input energy q (kJ/mm)
960-B2-R (15mm)	1-1	A-B	26.1-26.5	223-226	5.00	0.94
	2-1	A-B	26.1-26.5	223-226	4.96	0.95
	4-1	A-B	26.0-26.6	215-218	4.97	0.91
	3-1	A-B	26.0-26.6	222-225	4.74	0.99
	3-2	A-B	26.0-26.6	226-230	4.68	1.06
	3-3	A-B	27.0-27.6	230-236	4.27	1.19
	3-4	A-B	27.0-27.6	230-236	4.27	1.19
	4-2	A-B	26.0-26.6	215-218	4.78	0.11
	4-3	A-B	26.0-26.6	215-218	4.70	0.96
	4-4	A-B	26.0-26.6	215-218	4.70	0.96
	1-2	A-B	28.0-28.6	237-244	4.85	1.13
	1-3	A-B	28.0-28.6	248-253	4.77	1.19
	1-4	A-B	28.0-28.6	248-253	4.77	1.19
	2-2	A-B	28.0-28.6	237-244	4.93	1.11
	2-3	A-B	28.0-28.6	248-253	4.87	1.16
	2-4	A-B	28.0-28.6	248-253	4.87	1.16

* Pass *i-j* denotes "Corner *i* – Welding pass *j* "

The transient temperature history of Corner No.3 during welding are presented in

Figure 5.14. It should be noted that a preheating temperature at a maximum value at 180°C was applied before each welding pass.

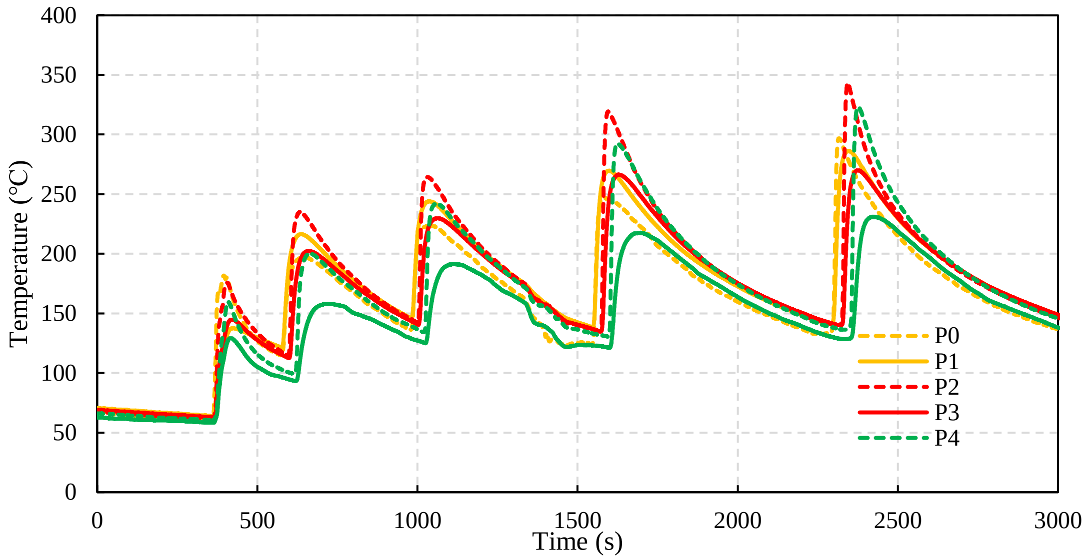

Figure 5.14 Transient temperature history of Section S960-B2-R

The peak temperatures of Section S960-B2-R during welding were obtained with thermocouples 0, 2, and 4, and it was shown that these peak temperatures progressively increased over these four welding passes. These measured temperature data were used in subsequent numerical simulations for calibration of the proposed numerical simulation models.

5.3. Residual stress measurement on S960 welded sections

5.3.1. Measurement programme

After the temperature measurements during welding, residual stress measurements were performed on these four S960 welded sections. The hole drilling method was adopted according to GB/T 31300, and a JHZK drilling device was employed. As reported in literature review presented in Chapter 2, the proposed hole drilling method has notable advantages over alternative techniques in measuring residual stress, such as being fast and easy to use, in addition not to cause any significant effect on the integrity of the steel sections. For the two H-sections S960-H1-R and S960-H2-R, the location of the measurement points on both the top flange and the web are demonstrated in

Figure 5.15. Due to the limited space available for operation of the residual stress drilling device, the number of measurement points on the web plate is restricted to seven. The spacing between the rosettes is set to be 12.5mm.

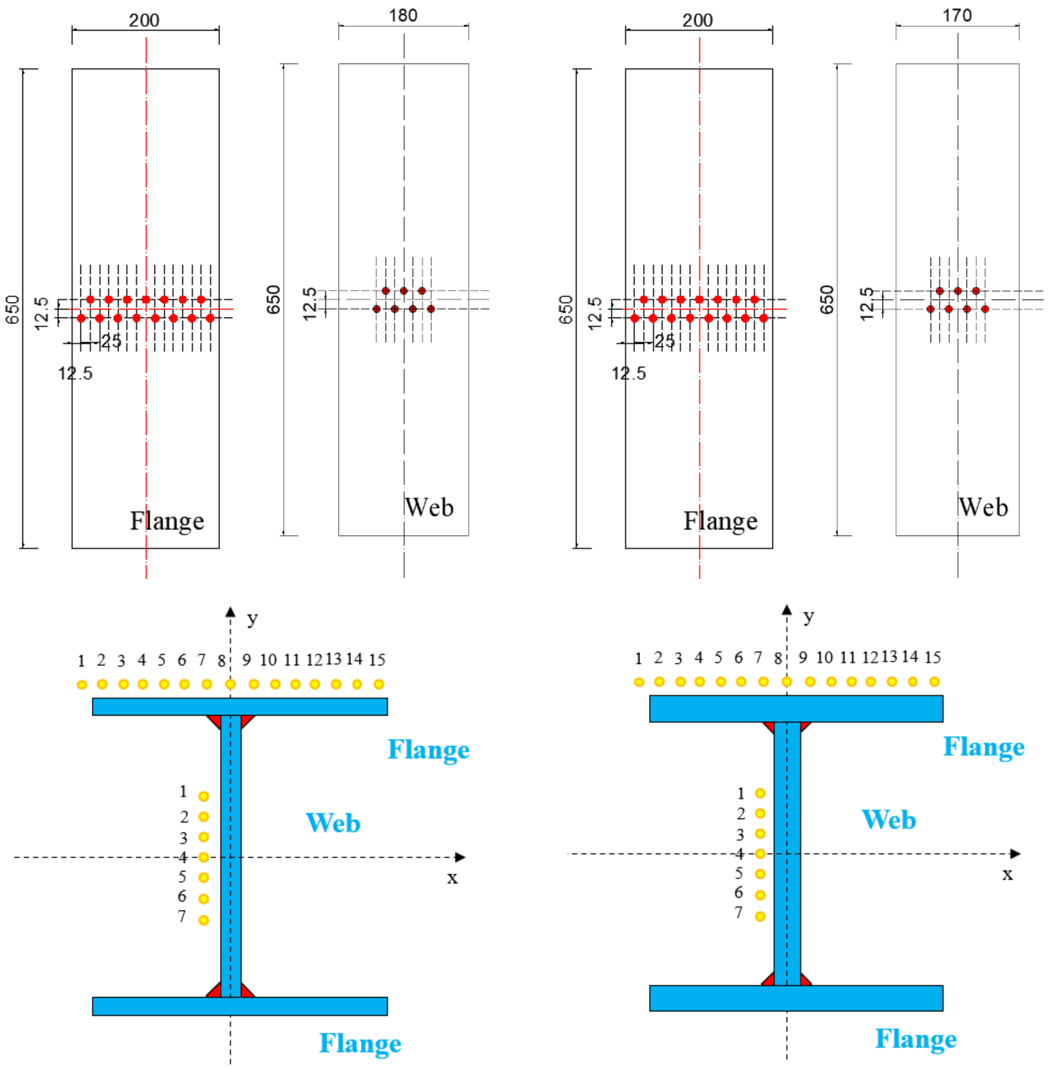

Section S960-H1-R

Section S960-H2-R

Figure 5.15 Locations of measurement points in S960 H-sections

Meanwhile, Figure 5.16 illustrates the locations of the measurement points of Section 960-B1-R and Section 960-B2-R. A total of 15 measurement points were selected on both the top flange and the web plate. The spacing between the rosettes is set to be 12.5mm. It should be noted that the surface of the top flange was properly grinded over the weldment to provide a flat surface for easy attachment of the rosettes.

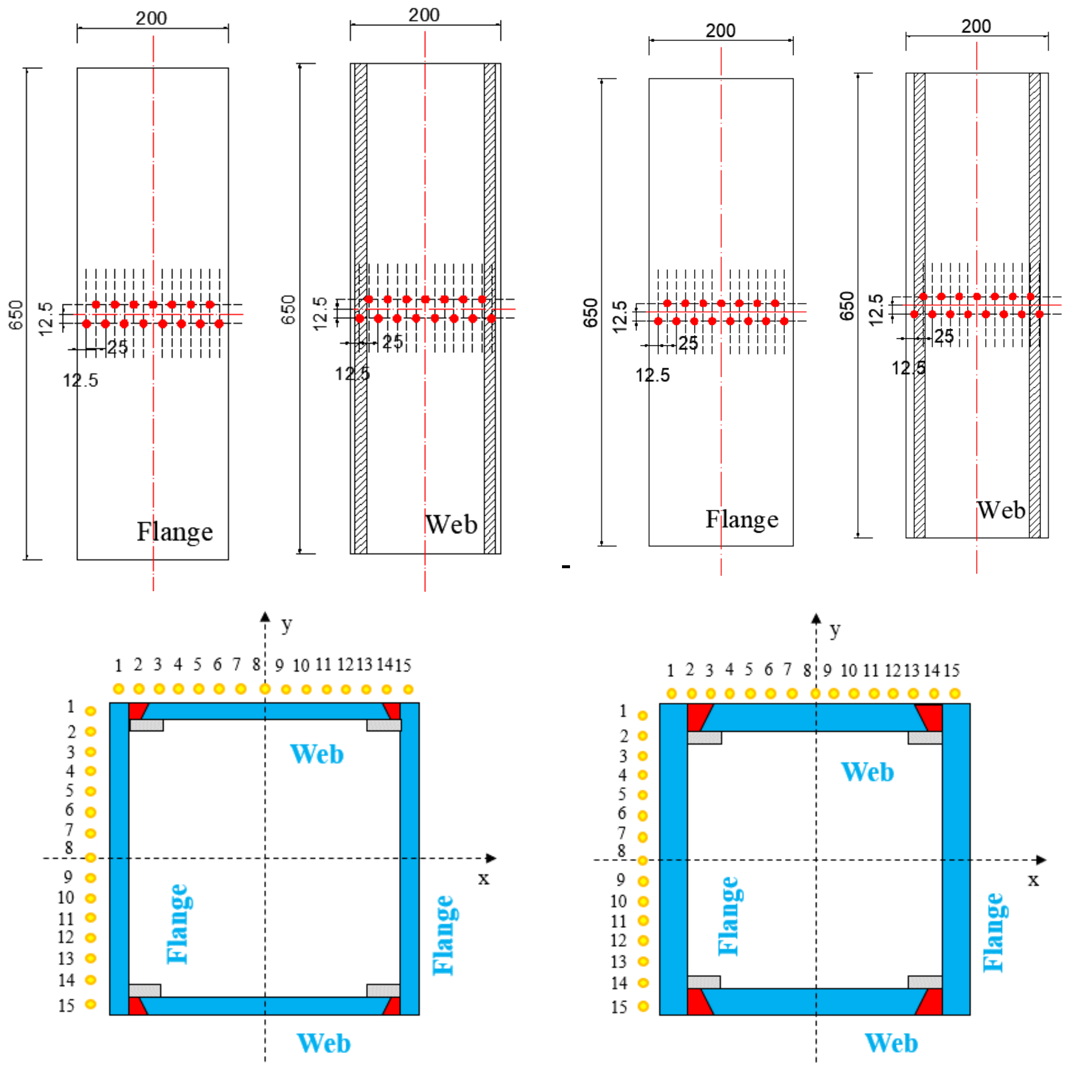

Section S960-B1-R

Section S960-B2-R

Figure 5.16 Locations of measurement points in S960 box sections

5.3.2. Measurement and instrumentation

Typical measurement set-up for residual stress measurement of S960 welded sections is shown in Figure 5.17. According to GB/T 31300, a high strength drill bit with a diameter of 1.5mm was employed, and the drilling depth was limited to 1.8mm. A JHZK residual stress drilling tool was positioned at the centre of the strain gauge rosette, and the precision of the alignment was kept within a range of ±0.004*D*. Key technical indicators of this drilling tool are presented in Table 5-6. To ensure accuracy of alignment, a specially designed microscope was employed.

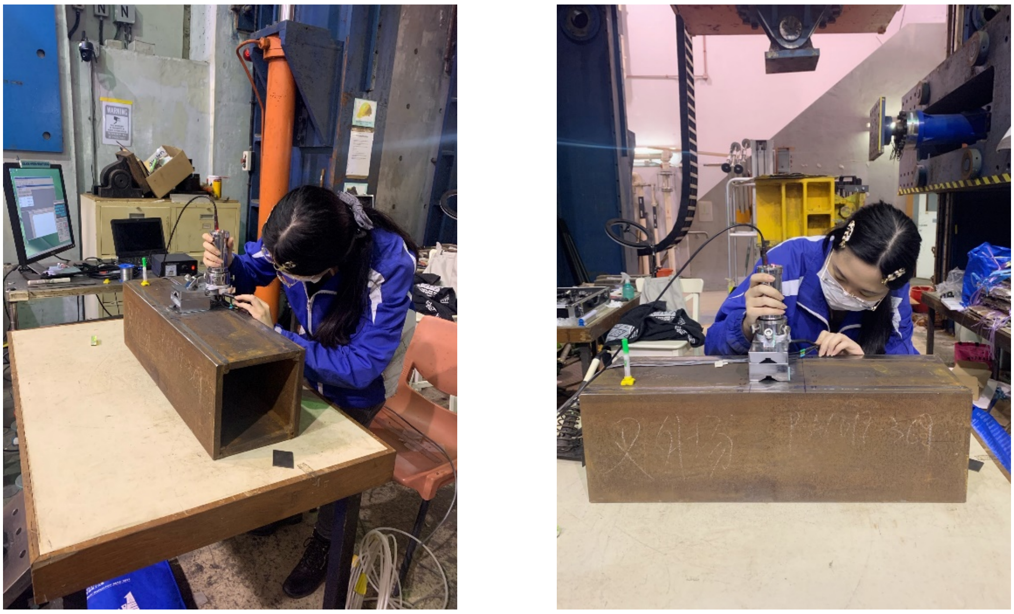

Figure 5.17 Typical set-up for residual stress measurement of the S960 welded sections

Table 5-6 Key technical indicators of a JHZK residual stress drilling tool

Drilling alignment accuracy	≤0.025mm	Optical alignment accuracy	0.01mm
Concentricity	0.005mm	Drilling verticality	≤0.01mm
Drilling diameter	0-3mm	Drilling depth	0-3mm
Speed range	3000-12000	Supply voltage	220V/50Hz
Hardness range material		≤HRC48	

Basic steps for the hole drilling on the S960 welded sections are presented as follows:

1. Polish the surface of the welded section to ensure a high level of smoothness, then wipe the surface with a 70% alcohol solution.
2. Attach rosettes onto the polished surface.
3. Connect the rosettes with wires of the strain data logger using a soldering iron.
4. Install the residual stress drilling tool at the centre of the rosette. Use the microscope to achieve alignment.
5. Set zero to the reading of the data logger, and drill a hole up to a depth of 1.8 mm as required.
6. Record the measured strain data continuously during drilling.
7. Calculate the residual stresses from the measured data with calibrated coefficients.

It should be noted that the voltage provided to the drilling tool should be regulated within the range of approximately 11-13V during drilling. Figure 5.18 illustrates an attached rosette before and after drilling, and it is shown that the deviation of alignment is within the specification requirements.

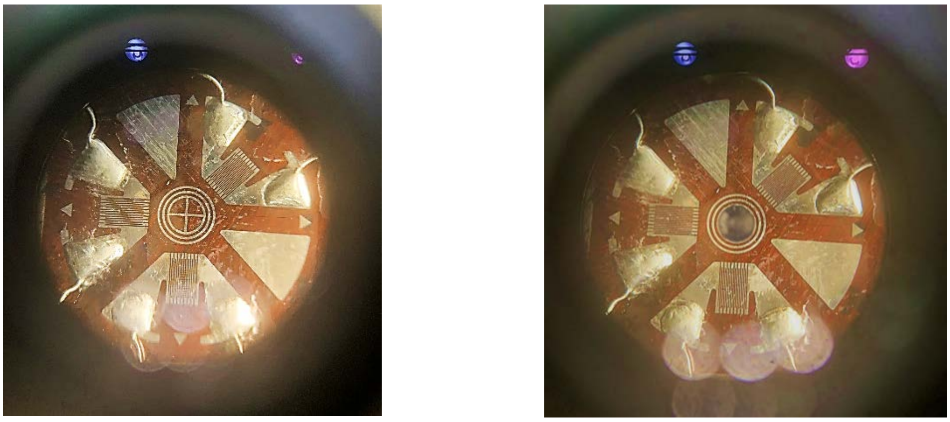

a) Rosette before drilling   b) Rosette after drilling

Figure 5.18 An attached rosette before and after drilling

For each section, the relieved strains in three different directions of each measurement point were measured. Hence, the residual stresses in both the longitudinal and the transverse directions at all the measurement points of these four S960 welded sections are calculated for further analyses.

5.3.3. Calibration coefficients for calculation of residual stresses

There are two main sources of errors in the residual stress measurement using the hole-drilling method: 1) the plastic deformations caused by stress concentration at the edge of a drilled hole, and 2) the machining-induced strains generated during drilling (GB/T 31300, 2013). Therefore, a carefully conducted calibration exercise was conducted to obtain the calibration coefficients for calculation of the residual stresses.

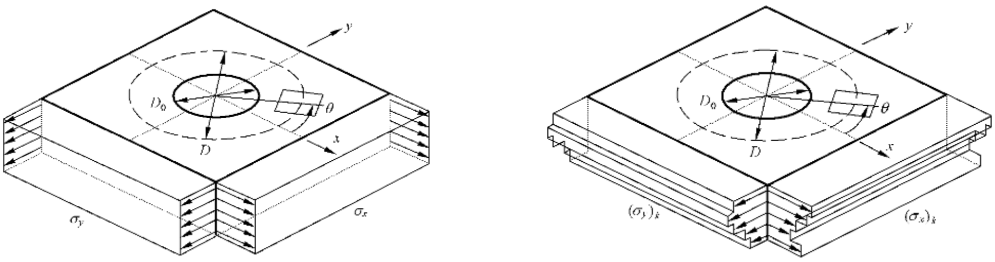

a) uniform stresses (top)   b) non-uniform stresses (bottom)

Figure 5.19 Residual stresses distributions in the vicinity of the drilled hole

As shown in Figure 5.19-a), the residual stresses within the specimen are uniform along the hole depth direction of the drilled hole, and these stresses in the x-y plane are σ_x, σ_y and τ_{xy}. As shown in Figure 5.19-b), these residual stresses within the specimen exhibits variation along the depth direction of the drilled hole. Since the plate thicknesses of four S960 welded sections are 10mm and 15mm, they are classified as thick plates according to the definition in GB/T 31310.

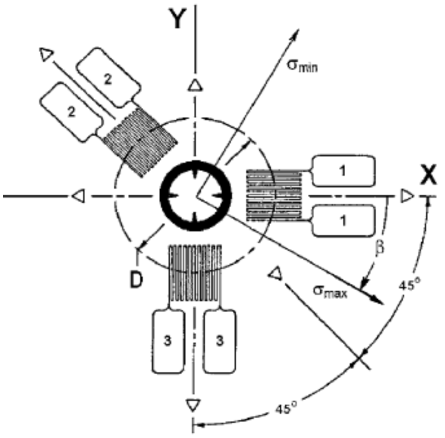

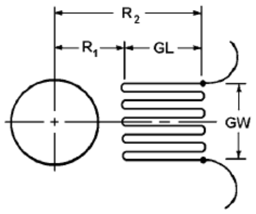

Figure 5.20 General layout and dimensions of typical rosette

General layout and dimensions of typical rosette named TJ120-1.5-φ1.5 are illustrated in Figure 5.20. Basic dimensions of the strain gauge rosette are presented in Table 5-7.

Table 5-7 Dimensions of rosette TJ120-1.5-φ1.5

D	GL	GW	R_1	R_2
5.13 mm	1.59 mm	1.59 mm	1.77 mm	3.36 mm

According to GB/T 31300, the surface strains after hole drilling is calculated by:

$$\varepsilon = \frac{1+\upsilon}{E} \times \bar{a} \times \frac{\sigma_x + \sigma_y}{2} + \frac{1}{E} \times \bar{b} \times \frac{\sigma_x - \sigma_y}{2} \cos 2\theta + \frac{1}{E} \times \bar{b} \times \tau_{xy} \sin 2\theta \tag{5.2}$$

Using the measured surface released strains ε_1, ε_2 and ε_3, the principal stress σ_1 and σ_3 are calculated by:

$$\begin{aligned} \sigma_1 &= C_1(\boldsymbol{\Delta}\varepsilon_1 + C_2\boldsymbol{\Delta}\varepsilon_3) \\ \sigma_3 &= C_1(\boldsymbol{\Delta}\varepsilon_3 + C_2\boldsymbol{\Delta}\varepsilon_1) \end{aligned} \tag{5.3}$$

where $C_1 = (A + B) / 4AB$, $C_2 = (B - A) / (A + B)$, and A, and B are the calibration coefficients.

In order to obtain the calibration coefficients, two speedily designed S960 calibration coupons were fabricated and tested under tension. The location of these rosette on the calibration coupons are illustrated in Figure 5.21. These calibration coupons were machined from 10mm and 15mm thick S960 steel plates to cover for different thicknesses encountered in the residual stress measurements. Two normal strain gauges were also attached at the centre of the coupon, to obtain data for direct comparison with those obtained from the rosettes. It should be noted that during tensile tests, any difference in the measured values of the regular strain gauges should not exceed 5%. Both of these two coupons were CNC machined to avoid any effect of residual stresses during fabrication.

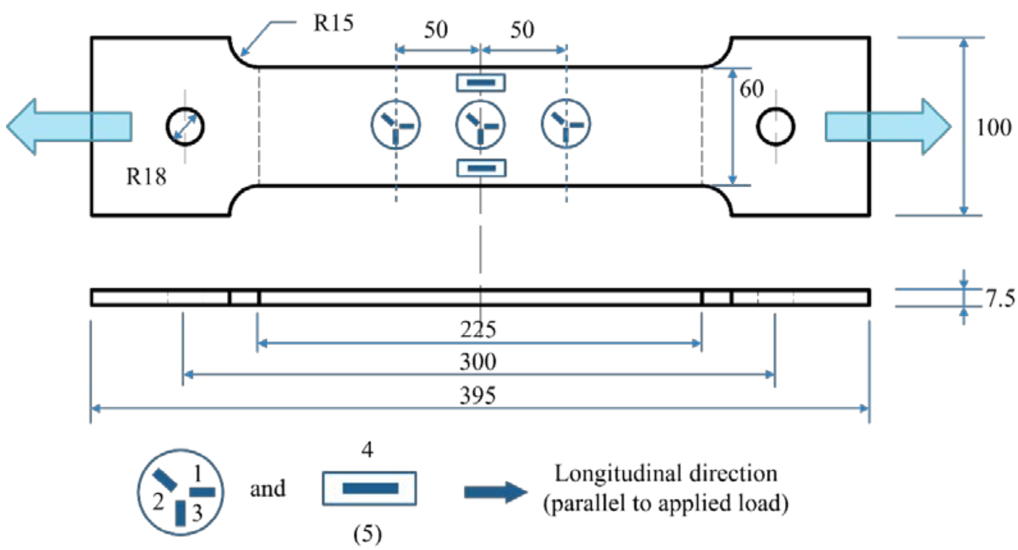

Figure 5.21 General arrangement of calibration coupons

Key steps of the calibration exercise are presented as follows:

1. Install the coupon on a tensile test machine and connect all the tensile strain gauges and rosettes to the data logger, then set zero all readings.

2. Apply loading up to a stress equal to $0.5f_y$ of the coupon, then unload. Repeat this process to check for consistency of the real-time strain data.

3. If the data are found to be consistent and the strain values are found to be zero after unloading, then start the tensile test to apply loading up to a stress equal to $0.3f_y$, and

record the strain values in direction 1 and 3, i.e., ε_1 and ε_3.

4. Then drill a hole at the centre of rosettes with the same parameters of the residual stress measurement test, then record each of the strain values after drilling.

5. Repeat Steps 3-4 twice, with increased loadings up to stresses equal to $0.7f_y$ and $0.9f_y$.

Typical measurement setup of the calibration exercise is shown in Figure 5.22. The stress-strain curves of calibration exercise before and after hole drilling are presented in Figure 5.23 to Figure 5.26.

Figure 5.22 Calibration test setup and hole drilling on coupon

Two S960 calibration coupons, namely Coupon S960-10c and S960-15c, were measured successfully. For Coupon S960-10c, the stress-strain curves before and after drilling are plotted in Figure 5.23 and Figure 5.24 for comparison, and a significant difference in the strain value after drilling is readily observed. It should be noted that for some unknown reasons, the measured values from only two rosettes were successfully recorded.

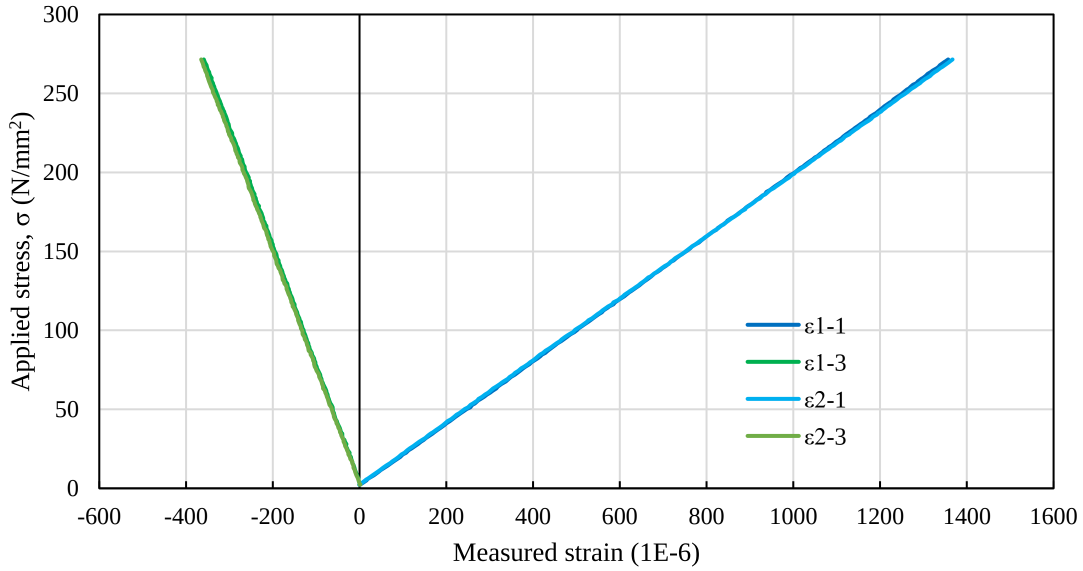

Figure 5.23 Stress-strain curves of Coupon S960-10c before drilling

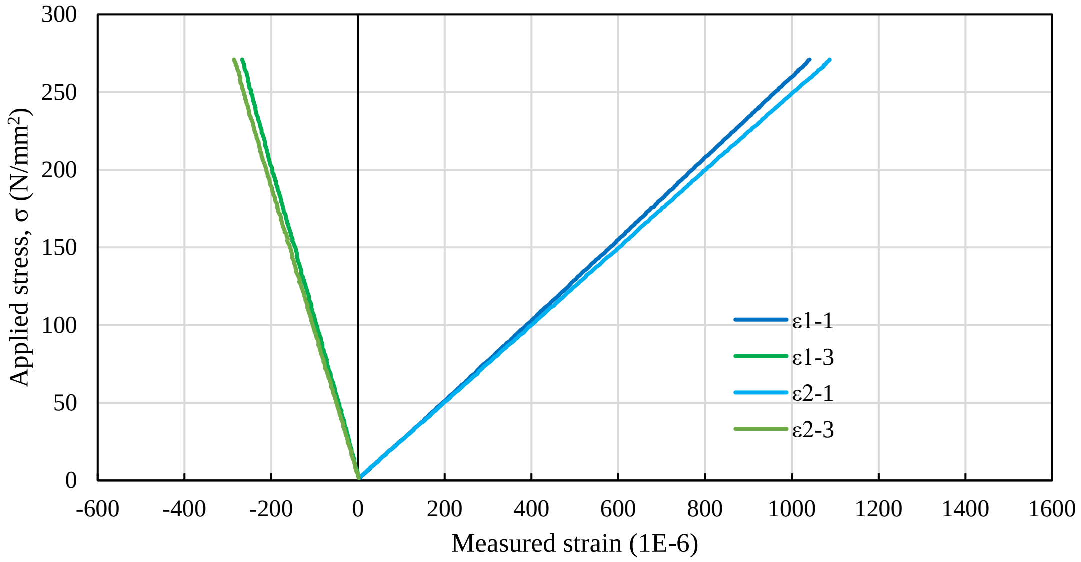

Figure 5.24 Stress-strain curves of Coupon S960-10c after drilling

All the measured strain values at different loading stages are summarized in Table 5-8, and the calibration coefficients are given by:

$$A = \frac{\varepsilon_1 + \varepsilon_3}{2\sigma}$$
$$B = \frac{\varepsilon_1 - \varepsilon_3}{2\sigma} \tag{5.4}$$

The calibration coefficients A, B of Coupon S960-10c at three loading levels are listed in Table 5-9. According to GB/T 31310, typical calculation is performed at a loading level at $0.3f_y$. If the loading level is close to $0.7f_y$ or $0.9f_y$, then the calibration coefficients A and B at the corresponding loading level should then be used.

Table 5-8 Measured strain of Coupon S960-10c under tension

Applied force F (kN)	Measured strains before drilling		Measured strains after drilling		Measured strain strains at the hole edge	
	$\bar{\varepsilon}_1/10^{-6}$	$\bar{\varepsilon}_3/10^{-6}$	$\bar{\varepsilon}_1/10^{-6}$	$\bar{\varepsilon}_3/10^{-6}$	$\bar{\varepsilon}_1/10^{-6}$	$\bar{\varepsilon}_3/10^{-6}$
120	1353	-364	1046	-321	-307	43
240	2748	-739	2101	-575	-647	164
360	4059	-1085	3056	-794	-1003	291

Table 5-9 Calibration coefficients for Coupon S960-10c

Applied force F (kN)	Applied stress σ (N/mm²)	Strains at the hole edge		Calibration coefficient	
		$\bar{\varepsilon}_1/10^{-6}$	$\bar{\varepsilon}_3/10^{-6}$	A	B
120	270	-307	43	-0.4884	-0.7475
240	540	-647	164	-0.4468	-0.7502
360	810	-1003	291	-0.4391	-0.7979

For Coupon S960-15c, the stress-strain curves before and after drilling are plotted in Figure 5.25 and Figure 5.26 for comparison.

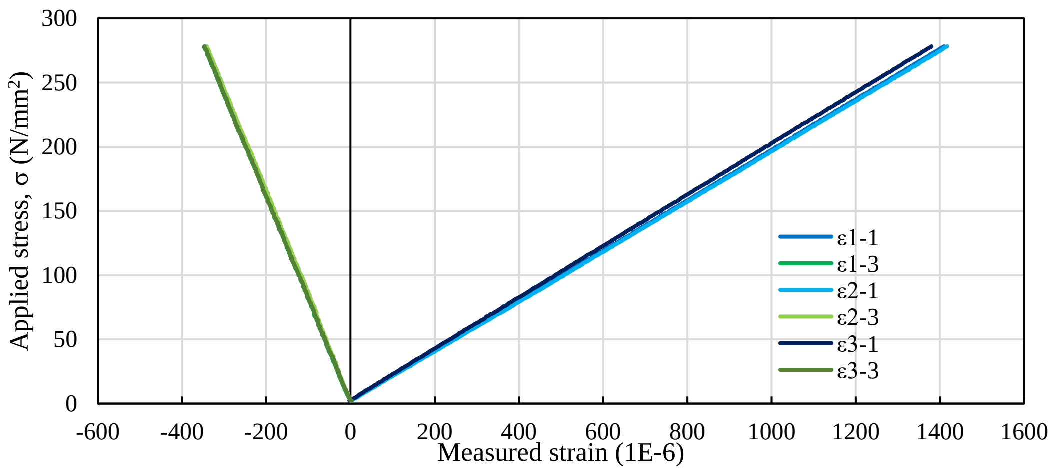

Figure 5.25 Stress-strain curves of Coupon S960-15c before drilling

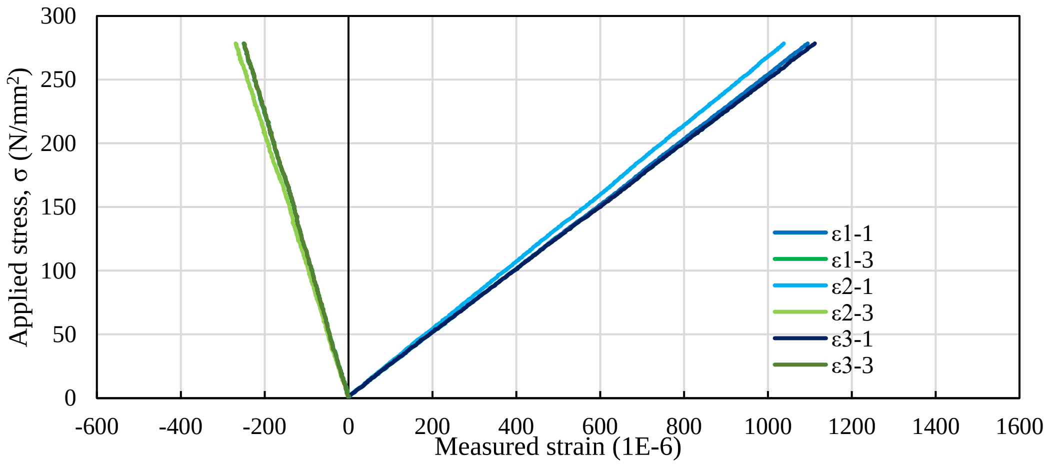

Figure 5.26 Stress-strain curves of Coupon S960-15c after drilling

Given the relatively small stress values which were close to $0.3f_y$, for Coupon S960-15c, only the strains under a loading level at $0.5f_y$ were measured. The calculated strains and both calibration coefficients A and B are presented in Table 5-11.

Table 5-10 Measured strain of Coupon S960-15c under tension

Applied force F (kN)	Measured strains before drilling		Measured strains after drilling		Measured strain strains at the hole edge	
	$\bar{\varepsilon}_1/10^{-6}$	$\bar{\varepsilon}_3/10^{-6}$	$\bar{\varepsilon}_1/10^{-6}$	$\bar{\varepsilon}_3/10^{-6}$	$\bar{\varepsilon}_1/10^{-6}$	$\bar{\varepsilon}_3/10^{-6}$
31	-87	248	-68	-86	19	-87
62	-176	555	-123	-179	53	-176
93	-267	792	-196	-269	71	-267
124	-355	1095	-257	-339	98	-355
155	-426	1363	-311	-426	115	-426

Table 5-11 Calibration coefficients for Coupon S960-15c

Applied force F (kN)	Applied stress σ (N/mm^2)	Strains at the hole edge		Calibration coefficient	
		$\bar{\varepsilon}_1/10^{-6}$	$\bar{\varepsilon}_3/10^{-6}$	A	B
31	70	-86	19	-0.4798	-0.7519
62	140	-179	53	-0.4512	-0.8307

93	209	-269	71	-0.4726	-0.8116
124	279	-339	98	-0.4315	-0.7824
155	349	-426	115	-0.4454	-0.7749

Therefore, calibration coefficient A and B presented in Table 5-9 and Table 5-11 should be used for t calculating the residual stresses of 10 mm and 15 mm thick S960 welded sections, respectively.

5.3.4. Residual stresses distributions across S960 welded sections

Measured data were processed according to Section 5.3.3 using the following equations to obtain the residual stresses at various measurement points:

$$\sigma_1 = C_1(\boldsymbol{\Delta}\varepsilon_1 + C_2\boldsymbol{\Delta}\varepsilon_3)$$
$$\sigma_3 = C_1(\boldsymbol{\Delta}\varepsilon_3 + C_2\boldsymbol{\Delta}\varepsilon_1) \quad (5.5)$$

where $C_1 = (A + B)\ /\ 4AB,\ C_2 = (B - A)\ /\ (A + B)$

Section S960-H1-R

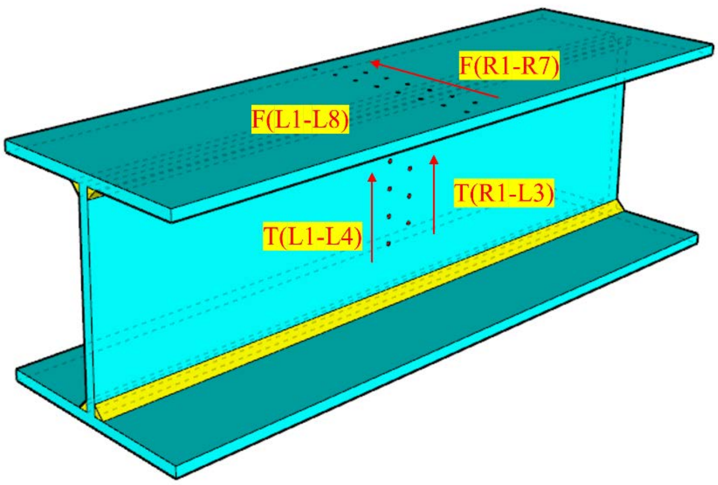

Figure 5.27 Schematic diagram on strain gauge arrangement for Section S960-H1-R

For Section S960-H1-R, a total of 15 measurement points were arranged on the flange while a total of 7 measurement points were arranged on the web, as shown in Figure 5.27. The measured relieved strains obtained with rosettes on the 22 measurement points are listed in Table 5-12.

Table 5-12 Measured relieved strains of Section S960-H1-R

Measurement points	ε_1 $\times 10^{-6}$	ε_2 $\times 10^{-6}$	ε_3 $\times 10^{-6}$
F-L1	10	1	7
F-L2	20	19	6
F-L3	44	21	-15
F-L4	31	-3	-11
F-L5	21	-12	-3
F-L6	-54	23	-21
F-L7	-172	-80	-162
F-L8	-156	-61	-32
F-R1	-176	-91	-45
F-R2	0	-1	-12
F-R3	6	6	-77
F-R4	13	1	-19
F-R5	36	-6	-9
F-R6	25	-9	-12
F-R7	7	-1	-11
T-L1	62	3	-116
T-L2	61	-10	-65
T-L3	72	-14	-142
T-L4	63	-1	-88
T-R1	63	16	-74
T-R2	68	5	-69
T-R3	57	-8	-76

The calculated residual stresses of these measurement points are listed in Table 5-13.

Table 5-13 Residual stresses of Section S960-H1-R

Measurement points	σ_1 (N/mm^2)	σ_3 (N/mm^2)
F-L1	-10	-8
F-R1	-18	-9
F-L2	-35	5
F-R2	-24	4
F-L3	-17	-1
F-R3	49	27
F-L4	174	168
F-R4	138	55
F-L5	157	69
F-R5	2	10
F-L6	9	64

F-R6	-8	14
F-L7	-29	1
F-R7	-19	6
F-L8	-4	8
T-L1	-32	87
T-R1	-40	44
T-L2	-36	107
T-R2	-38	63
T-L3	-40	51
T-R3	-45	46
T-L4	-35	54

Figure 5.28 plots the cross-sectional distribution of residual stresses on Section S960-H1-R, illustrating the variations and magnitudes of these residual stresses across the section. The results show that the tensile residual stresses are very high in the vicinity of the flange/web junctions, with a maximum value of 174 N/mm^2. The remaining parts of the top flange and the web have only small compressive residual stresses. In general, the residual stress distribution tends is considered to be essentially symmetrical despite some discrepancies.

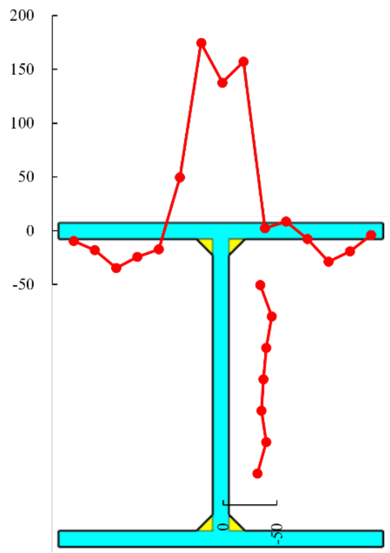

Figure 5.28 Measured residual stress distribution of Section S960-H1-R

It should be noted that the maximum residual stress given in ECCS for welded H-section are:

$$\sigma_{\gamma t} = \alpha f_y = 514 \ \text{N/mm}^2$$

$$\sigma_{rc} = \alpha f_y = 514 \ \text{N/mm}^2$$

Hence, the maximum residual stress of Section 960-H1-R is significantly smaller than these design values, indicating an urgent need to update existing standards to accommodate correct residual stress for S960 welded H-section.

Section S960-H2-R

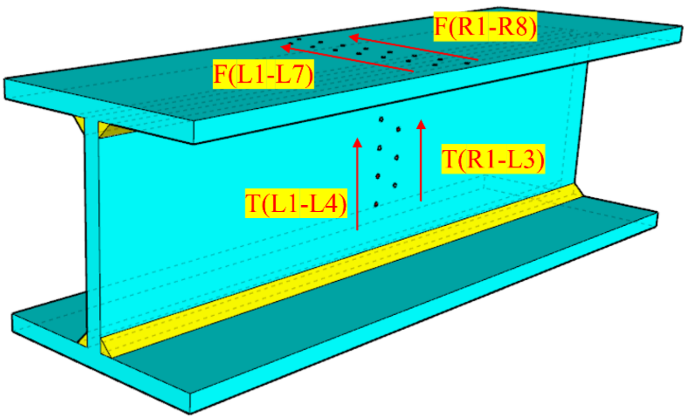

Figure 5.29 Schematic diagram on strain gauge arrangement for Section S960-H2-R

For section S960-H2-R, a total of 15 measurement points were arranged on the flange, while a total of 7 measurement points were arranged on the web, as shown in Figure 5.29. The measured relieved strains obtained with the rosettes on the 22 points are listed in Table 5-14.

Table 5-14 Measured relieved strains of Section S960-B1-R

Measurement points	ε_1 $\times 10^{-6}$	ε_2 $\times 10^{-6}$	ε_3 $\times 10^{-6}$
F-L1	41	62	-41
F-L2	55	24	15
F-L3	89	62	-8
F-L4	49	41	21
F-L5	38	79	-4
F-L6	59	32	-13
F-L7	-193	30	-39
F-R1	-158	40	-19
F-R2	-145	-6	-25
F-R3	82	42	-2
F-R4	114	63	-20
F-R5	111	57	-15
F-R6	107	116	-11
F-R7	72	36	3

F-R8	86	108	-1
T-L1	-58	-35	61
T-L2	-52	21	58
T-L3	-63	-24	72
T-L4	-68	-179	24
T-R1	-58	-130	28
T-R2	-64	7	66
T-R3	-70	42	66

The calculated residual stresses of these measurement points are listed in Table 5-15.

Table 5-15 Residual stresses of Section S960-B1-R

Measurement points	σ_1 (N/mm^2)	σ_3 (N/mm^2)
F-R1	-26	26
F-L1	-53	-28
F-R2	-78	-16
F-L2	-50	-32
F-R3	-33	-6
F-L3	-50	-4
F-R4	184	85
F-L4	147	58
F-R5	137	60
F-L5	-73	-20
F-R6	-97	-12
F-L6	-96	-15
F-R7	-93	-18
F-L7	-66	-21
F-R8	-77	-21
T-L1	-36	-40
T-R1	-32	-39
T-L2	-38	-48
T-R2	-55	-4
T-L3	-45	-10
T-R3	-40	-43
T-L4	-46	-41

Figure 5.30 plots the cross-sectional distribution of residual stresses on Section S960-H2-R, with a maximum value of 184 N/mm^2. The remaining parts of the top flange and the web have only small compressive residual stresses. In general, the residual stress distribution tends is considered to be essentially symmetrical despite some

discrepancies.

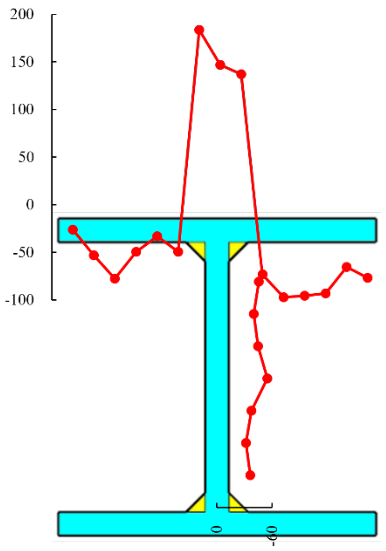

Figure 5.30 Measured residual stress distribution of Section S960-H2-R

It should be noted that the maximum residual stress given in ECCS for welded H-section are:

$$\sigma_{\gamma t} = \alpha f_y = 514 \ \text{N/mm}^2$$

$$\sigma_{rc} = \alpha f_y = 514 \ \text{N/mm}^2$$

Hence, the maximum residual stress of Section 960-H2-R is significantly smaller than these design values, indicating an urgent need to update existing standards to accommodate correct residual stress for S960 welded H-section.

Section S960-B1-R

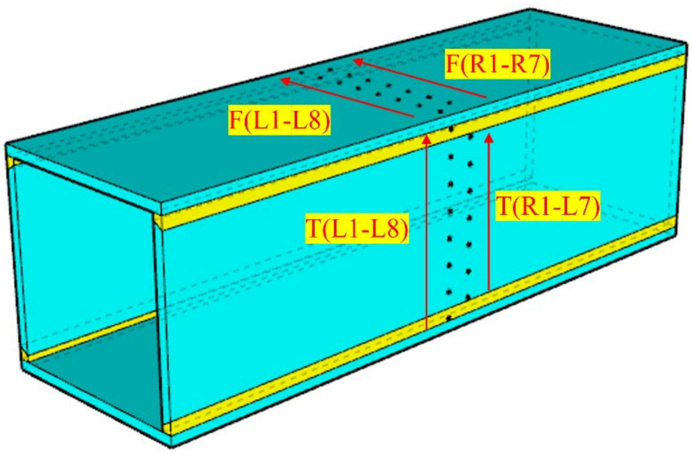

Figure 5.31 Schematic diagram on strain gauge arrangement for Section S960-B1-R

For Section S960-B1-R, a total of 30 measurement points were arranged on the flange and web. Numbering sequence of measurement points are shown in Figure 5.31. The relieved strains measured by rosette near the drilled hole of 30 points were listed in Table 5-16.

Table 5-16 Measured relieved strains of Section S960-B1-R

Measurement points	ε_1 $\times 10^{-6}$	ε_2 $\times 10^{-6}$	ε_3 $\times 10^{-6}$
F-L1	-169	-20	-32
F-L2	-51	-22	129
F-L3	61	49	11
F-L4	45	3	110
F-L5	60	5	4
F-L6	87	48	-35
F-L7	64	7	15
F-R1	25	-17	-14
F-R2	49	-25	-11
F-R3	38	-43	-36
F-R4	24	-22	-38
F-R5	78	9	-22
F-R6	21	-20	-25
F-R7	-193	125	-46
F-R8	-142	7	-129
T-L1	-80	-21	34
T-L2	10	-11	1
T-L3	34	1	1
T-L4	49	17	7
T-L5	30	9	20
T-L6	27	-5	137
T-L7	21	6	39
T-R1	33	-37	-9
T-R2	40	-5	46
T-R3	36	9	162
T-R4	14	14	73
T-R5	7	13	21
T-R6	-3	-20	-3
T-R7	-40	-5	46
T-R8	-110	-91	-86

The calculated residual stresses of those points could be found in Table 5-17.

Table 5-17 Residual stresses of Section S960-B1-R

Measurement points	σ_1 (N/mm^2)	σ_3 (N/mm^2)
F-R1	149	57
F-L1	20	-100
F-R2	-54	-20
F-L2	-58	-101
F-R3	-51	-14
F-L3	-67	14
F-R4	-57	-24
F-L4	-19	7
F-R5	-40	1
F-L5	-26	24
F-R6	-14	28
F-L6	-62	5
F-R7	-13	17
F-L7	172	73
F-R8	143	134
T-R1	62	-15
T-L1	-9	-3
T-R2	-29	-7
T-L2	-43	-15
T-R3	-29	-22
T-L3	-47	-121
T-R4	-25	-37
T-L4	-26	2
T-R5	-42	-46
T-L5	-59	-143
T-R6	-25	-64
T-L6	-10	-19
T-R7	3	3
T-L7	26	-32
T-R8	108	92

Plot the cross-sectional distribution of residual stresses on S960-B1-R in Figure 5.32. The results show that the tensile residual stresses are relatively high in the area near weld sections, the highest value is found at the measure point of the weld seam (172 N/mm^2), while the rest of the flange and web have small compressive residual stresses. Generally, the distribution of residual stresses tends to be essentially symmetrical, but the values are not completely symmetrical.

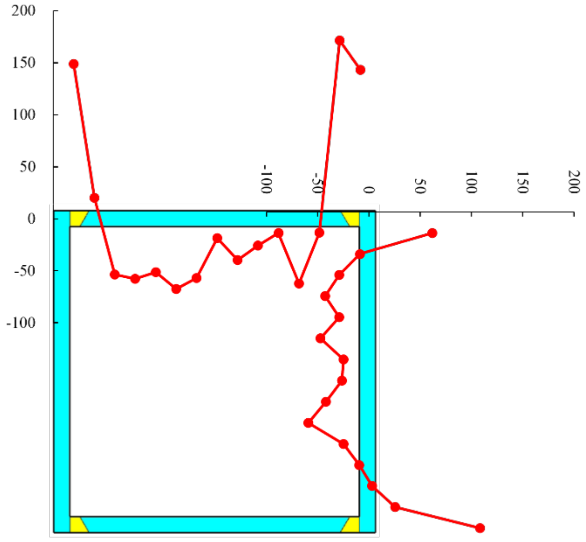

Figure 5.32 Measured residual stress distribution of Section S960-B1-R

It should be noted that the maximum residual stress given in ECCS for welded box section are:

$$\sigma_{\gamma t} = f_y = 1027 \text{ N/mm}^2$$

$$\sigma_{rc} = \frac{3d_t\sigma_{w,\gamma t}}{d-3d_t} = 440 \text{ N/mm}^2$$

Hence, the maximum residual stress of Section 960-B1-R is significantly smaller than these design values, indicating an urgent need to update existing standards to accommodate correct residual stress for S960 welded box section.

Section S960-B2-R

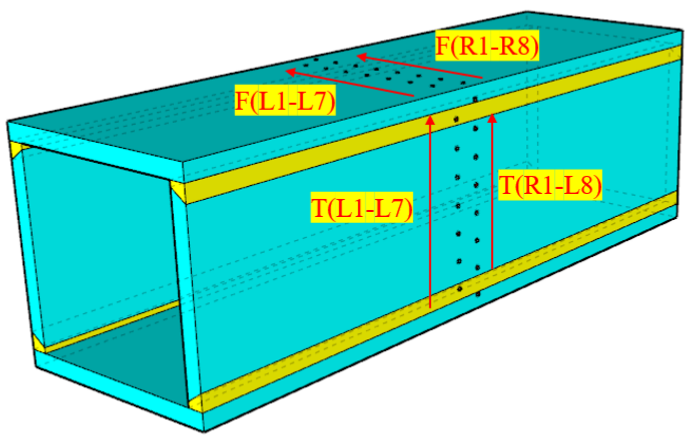

Figure 5.33 Schematic diagram on strain gauge arrangement for Section S960-B2-R

A total of 30 measurement points were arranged on the flange and web of S960-B2-R.

Numbering sequence of measurement points are shown in Figure 5.33. The relieved strains measured by rosette near the drilled hole of 30 points were listed in Table 5-18.

Table 5-18 Measured relieved strains of Section S960-B2-R

Measurement points	ε_1 $\times 10^{-6}$	ε_2 $\times 10^{-6}$	ε_3 $\times 10^{-6}$
F-L1	-113	27	-104
F-L2	-101	85	-27
F-L3	75	72	12
F-L4	66	85	4
F-L5	54	25	-5
F-L6	74	72	17
F-L7	57	86	51
F-R1	21	30	29
F-R2	46	69	69
F-R3	32	-32	45
F-R4	76	88	77
F-R5	45	44	72
F-R6	46	44	72
F-R7	-138	82	109
F-R8	-269	50	34
T-L1	-120	-40	-3
T-L2	-158	-56	137
T-L3	58	61	115
T-L4	64	73	62
T-L5	42	37	82
T-L6	58	53	54
T-L7	35	31	39
T-R1	37	47	59
T-R2	34	54	35
T-R3	62	47	37
T-R4	39	16	43
T-R5	42	73	87
T-R6	11	16	54
T-R7	-94	-10	-61
T-R8	-148	-1	79

The calculated residual stresses of those points could be found in Table 5-19.

Table 5-19 Residual stresses of Section S960-B2-R

Measurement points	σ_1 (N/mm^2)	σ_3 (N/mm^2)
F-R1	129	123
F-L1	98	51
F-R2	-71	-30
F-L2	-60	-21
F-R3	-47	-10
F-L3	-71	-35
F-R4	-64	-61
F-L4	-26	-32
F-R5	-59	-74
F-L5	-40	-49
F-R6	-88	-89
F-L6	-59	-76
F-R7	-60	-77
F-L7	96	-62
F-R8	233	39
T-R1	109	34
T-L1	106	-82
T-R2	-82	-118
T-L2	-74	-72
T-R3	-59	-85
T-L3	-66	-64
T-R4	-42	-44
T-L4	-49	-63
T-R5	-40	-40
T-L5	-65	-49
T-R6	-46	-49
T-L6	-60	-89
T-R7	-24	-51
T-L7	100	79
T-R8	113	-33

Plot the cross-sectional distribution of residual stresses on S960-B2-R in Figure 5.34. The results show that the tensile residual stresses are relatively high in the area near weld sections, the highest value 233 N/mm^2 is found at the measure point of the weld seam, while the rest of the flange and web have small compressive residual stresses. Generally, the distribution of residual stresses tends to be essentially symmetrical, but the values are not completely symmetrical.

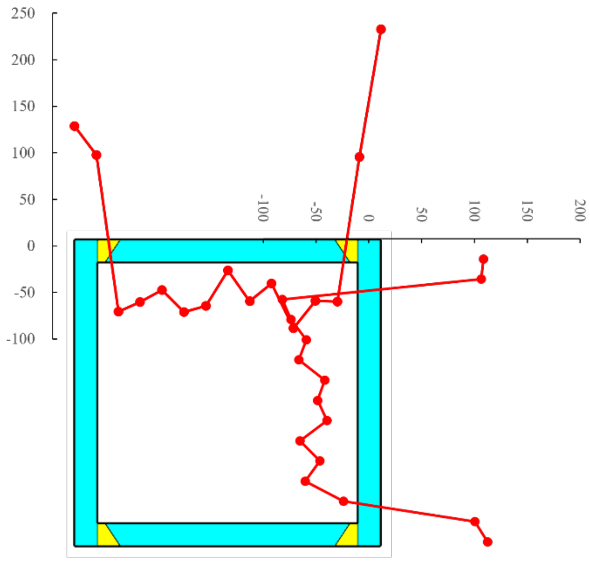

Figure 5.34 Measured residual stress distribution of Section S960-B2-R

C It should be noted that the maximum residual stress given in ECCS for welded box section are:

$$\sigma_{\gamma t} = f_y = 1028 \ \ \text{N/mm}^2$$

$$\sigma_{rc} = \frac{3d_t\sigma_{w,\gamma t}}{d-3d_t} = 841 \ \ \text{N/mm}^2$$

Hence, the maximum residual stress of Section 960-B2-R is significantly smaller than these design values, indicating an urgent need to update existing standards to accommodate correct residual stress for S960 welded box section.

From the measurement results of these four sections, the residual stresses along the longitudinal direction of the S960 welded section are higher than those in the transverse direction, therefore, in this part of investigation, only the longitudinal residual stresses (σ_1) are considered. For H-sections, during the welding process, high temperatures are concentrated in the area of the weld section and heat-affected zone. Consequently, high tensile residual stresses are formed at the back of weld sections, while there are compressive stresses in the central part of the flange and web due to the effect of force balance.

In the case of S960 box sections, it is important to acknowledge that the weld section's residual height was carefully polished to ensure a smooth surface for the subsequent hole drilling test. Although the polishing procedure might have influenced the residual stresses by relieving any pre-existing stresses, the measured residual stresses at the weld sections remain significantly higher compared to other areas. These data collected through experiments are compared with the results of numerical simulations in Chapter 6, to verify the accuracy of the S960 material model and the welding simulation method considering solid-state phase transformation.

CHAPTER SIX

NUMERICAL SIMULATION ON WELDING OF S960 STOCKY COLUMNSS CONSIDERING PHASE TRANSFORMATION

6.1. Introduction

Accuracy of finite element modelling of welding is highly dependent on the heat source model and the material properties of steel. Based on the measured continuous cooling transformation (CCT) curves, it is readily observed that high strength S690 and S960 steel undergo complex phase transformations during welding. Compared with ordinary low carbon steel, it is essential to consider the effect of phase transformation on post-weld deformations. Hence, it is important in the numerical simulations of welding of the S690 and the S960 steel to establish special material models to simulate the phase transformation during the heating and cooling process.

In this chapter, using an advanced finite element software SYSWELD, a series of welding models considering solid state phase transformation were established. Both the kinetics and the definitions of phase transformation, the double ellipsoidal heat source model, and the process of establishing finite element models are described. Finally, the temperature field, the residual stresses and the microstructural changes in the welding simulations are verified with the results from various experimental investigations. Furthermore, in Chapter 7, these thermo-mechanical-metallurgical models are exported into another general finite element package Abaqus, to further simulate the effects of welding on the structural performance of these high strength steel sections.

6.2. Kinetics of phase transformation in SYSWELD

ESI-SYSWELD is a commercial finite element software developed by the ESI Group in France. Nowadays, SYSWELD is a commonly employed tool in various fields including automotive, aerospace, energy, and mechanical industry for designing and analyzing welded components. Figure 6.1 shows the basic architecture of SYSWELD.

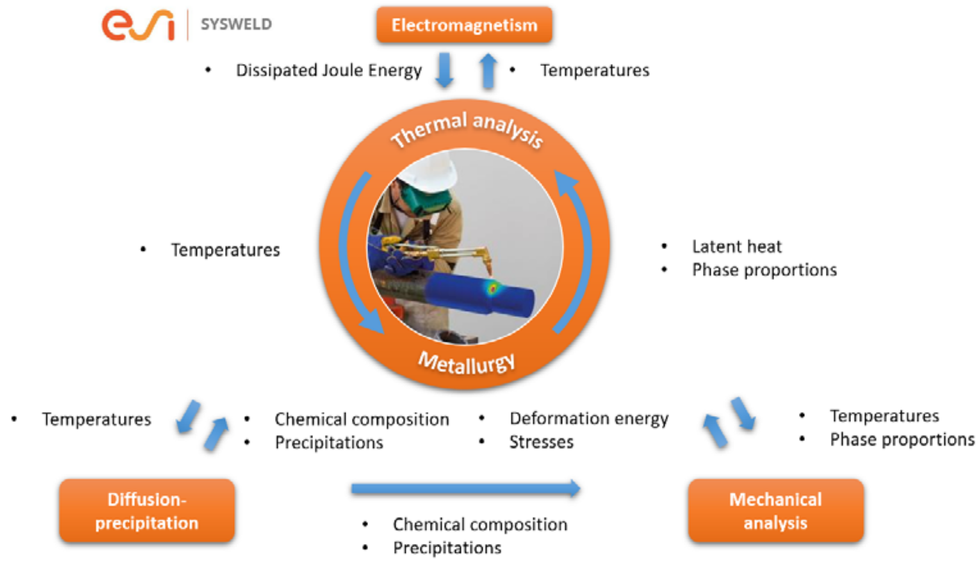

Figure 6.1 Architecture of SYSWELD

Compared with other finite element software such as Abaqus and Ansys, SYSWELD has a unique advantage on linking material microstructures into the simulation of the welding process through the following calculations and couplings:

- Thermal and metallurgical calculations that integrate temperatures and phase proportions. The information considered for each steel element encompasses not only its thermal history, but also its metallurgical history, such as the proportions of various phases.
- Thermal and mechanical calculations that involve the heat transfer and the resulting mechanical responses of the steel. This computational process constitutes an important step in the numerical simulation of welding.
- Mechanical plasticity calculations that depend not only on temperatures but also on metallurgical development history of the steel. Thus, this calculation considers both the phase-dependent thermomechanical variations and the transformation plasticity, which significantly influences residual stresses.

SYSWELD employs an integrated metallographic kinetic system to simulate the microstructural changes in the steel. This system provides essential kinetic for modelling solid-state phase transformations, and for computing formation and growth of various microstructures (ESI Group 2019). According to literature, solid-state phase transformations can be classified into two types: diffusional transformations and non-diffusional transformations. The specific definitions and characteristics of these transformation methods can be found in Chapter 2. In this section, the fundamental kinetics of phase transformation models used in subsequent numerical investigations are presented.

The computation of metallurgical transformations and grain sizes at GAUSS points involves utilizing the provided temperature and corresponding metallurgical transformation properties (Porter 2011). In metallurgy, the composition of a phase is characterized by the relative proportions P. All these kinetics and approaches are used for describing the metallurgical evolution of the steel, that is, to predict the changes in the proportions P over time. The basic approach of phase transformation in SYSWELD is generally written as:

$$\frac{dp}{dt} = \frac{\bar{P} - P}{TR} \tag{6.1}$$

P is the metallurgical phase proportion,

t: time,

$\bar{P}$: interpreted as the equilibrium value,

TR: equivalent to a “time delay”. If θ is varied in time, the above equation describes the fact that P follows $\bar{P}$ after time delay TR.

In the actual welding process, several phase transformations occur simultaneously. Equation 6.2 signifies that the transformation rate for phase *i* depends on the other metallurgical phases:

$$\frac{dP_i}{dt} = -\sum_{j \neq i} A_{ij} (j = 1,2, \dots, n) \tag{6.2}$$

where A_{ij} is the quantity of phase *i* transformed to phase *j* per time unit.

The expression of term A_{ij} is assumed to be independent of phase *k* ($k \neq i$ and $k \neq j$), and is given by the equation:

$$A_{ij} = \left(K_{i\to j} \cdot P_i\right) - (K'_{i\to j} \cdot P_j) \tag{6.3}$$

where $K_{i\to j}$ and $K'_{i\to j}$ are constants of reaction $i \to j$, which can depend on θ and $\dot{\theta}$ under:

$$\begin{aligned} K_{i\to j} &= K(\theta)F(\dot{\theta}) \\ K'_{i\to j} &= K'(\theta)F'(\dot{\theta}) \end{aligned} \tag{6.4}$$

To develop a clear understanding on these reaction constants, consider the case of a single 1→2 transformation, such as austenitization during a heating process. The equations 6.2 can then be written as:

$$\frac{dP_2}{dt} = K_{1\to 2}P_1 - K'_{1\to 2}P_2 \tag{6.5}$$

with $P_1 + P_2 = 1$,

$$\frac{dP_2}{dt} = K_{1\to 2} - (K_{1\to 2} - K'_{1\to 2})P_2 \tag{6.6}$$

By identification with Equation 6.1, the following equations are obtained:

$$\begin{aligned} K_{1\to 2} &- \frac{\overline{P_2}}{TR} \\ K'_{1\to 2} &- \frac{1-\overline{P_2}}{TR} \end{aligned} \tag{6.6}$$

After re-writing:

$$\begin{aligned} K_{1\to 2} &= K(\theta)F(\dot{\theta}) \\ K'_{1\to 2} &= K'(\theta)F'(\dot{\theta}) \end{aligned} \tag{6.7}$$

The following equations are obtained:

$$\begin{aligned} \bar{P} &= \frac{1}{1+\dfrac{F'\cdot K'}{F\cdot K}} \\ TR &= \frac{1}{KF + K'F} \end{aligned} \tag{6.8}$$

Two variables $Peq(\theta)$ and $Tau(\theta)$ can also be used, which identify with a proportion at equilibrium and time delay, both independent from:

$$K = \frac{Peq}{Tau} \text{ and } K' = \frac{1-Peq}{Tau} \tag{6.9}$$

Hence,

$$\bar{P} = \frac{Peq \cdot F}{Peq \cdot F + (1 - Peq)F'} \text{ and } TR = \frac{Tau}{Peq \cdot F + (1 - Peq)F'} \tag{6.10}$$

Knowledge of functions $Peq(\theta)$, $Tau(\theta)$, $F(\dot{\theta})$, and $F'(\dot{\theta})$ are therefore required for characterization of a metallurgical transformation, given $K(\theta) = \frac{Peq(\theta)}{Tau(\theta)}$, $K'(\theta) = \frac{1-Peq(\theta)}{Tau(\theta)}$, $F(\dot{\theta})$, $F'(\dot{\theta})$ and $n(\theta)$. In practice, the CCT diagram of the steel is required to obtain $Peq(\theta)$, $Tau(\theta)$, $F(\dot{\theta})$, and $F'(\dot{\theta})$.

6.2.1. Diffusional transformations

For diffusional transformations during welding, which occurs by nucleation and the growth of a new phase inside or at the inter-grain joints of the previous phase (Rheingans and Mittemeijer 2013), SYSWELD employs the Johnson-Mehl-Avrami model as the basic kinetic, and the following equation is adopted:

$$P_i(\theta, t) = \bar{P} \cdot [1 - \exp(-(t/TR)^n)] \tag{6.11}$$

When the temperature varies, consider P_i derivative with respect to time at constant temperature together, with temperature-dependent transformation parameters Peq, Tau and n:

$$\frac{dP_i}{dt} = n \cdot \left(\frac{\bar{P} - P_i}{TR}\right) \cdot \left(ln\left(\frac{\bar{P}}{\bar{P} - P_i}\right)\right)^{(n-1)/n} \tag{6.12}$$

$\bar{P}$: proportion obtained after an infinite time;

TR: delay time associated with the reaction;

N(θ): exponent illustrating the reaction rate.

It should be noted that when n=1, Equations 6.1 and 6.12 become identical. Considering an $i \rightarrow j$ transformation to illustrate this model, and introducing the previously defined reaction constants $K_{ij} = \frac{Peq(\theta)}{Tau(\theta)} \cdot F(\dot{\theta})$ and $K'_{ij} = \frac{1-Peq(\theta)}{Tau(\theta)} \cdot F(\dot{\theta})$, Equation 6.12 then becomes:

$$\frac{dP_i}{dt} = n_{ij} \cdot \left(\frac{K_{ij}P_i - K'_{ij}P_j}{TR}\right) \cdot \left(ln\left(\frac{K_{ij}(P_i + P_j)}{K_{ij}P_i - K'_{ij}P_j}\right)\right)^{(n-1)/n} \tag{6.13}$$

Knowledge of functions $Peq(\theta)$, $Tau(\theta)$, $F(\dot{\theta})$, $F'(\dot{\theta})$, and $n(\theta)$ is therefore required for characterization of a metallurgical transformation. In finite element model calculations, $Peq(\theta)$, $Tau(\theta)$, $F(\dot{\theta})$, $F'(\dot{\theta})$, and $n(\theta)$ can be obtained from the CCT diagram. By incorporating these factors into the simulation, SYSWELD can accurately predict the diffusional transformation of the steel during welding processes.

6.2.2. Martensitic transformation

Martensite is a specific microstructure in steel with an extremely hard crystalline structure and the martensitic transformation happens during cooling. When the temperature of the austenite reaches the martensite start temperature (M_s), the parent austenite becomes mechanically unstable. During welding, a large percentage of the austenite transforms into martensite until the lower transformation temperature M_f is reached, signifying the completion of transformation (I. Avramov 2015).

The martensitic transformation occurs at lower temperatures, where Fe-Carbon atoms exhibit limited mobility. As a result, atom migration mainly occurs to restructure crystal structures, leading to a non-diffusional transformation. In SYSWELD, the Koistinen-Marburger(K-M) equation has been specifically used in the calculation of martensite fraction (Koistinen and Marburger 1959), and it can be written as:

$$f_M = 1 - \exp\left(-\alpha(M_s - T)\right) \tag{6.14}$$

f_M : the martensite fraction,

M_s: the martensite start temperature,

α: the coefficient related to the martensitic transformation rate,

T: temperature.

In the simulation of both the S690 and the S960 steel, the coefficient α depends on the carbon content. The martensite start temperature will be determined according to dilatometry test results.

6.3. Definition of S690&S960 material properties

As the properties of high strength steel change with both temperature and phase transformations, it is evident that the S690 and the S960 have different properties at different phases. In the FEM simulation, the thermo-metallurgical properties that need to be defined including the thermal conductivity, the special heat, and the basic phase transformation reactions during various heating and cooling stages. Referring to the data of the S420 and the S460 embedded in SYSWELD, all these properties except the phase transformation reactions are quite similar, because low carbon high strength steel have similar metallurgical properties. In Appendix A, the definition of thermo-metallurgical properties of the S690 and the S960 steel are described in details and they are compared with the current simplified approach given in EN 1993-1-2 (CEN, 2005). Moreover, to accurately simulate the locked-in stresses after welding, the thermo-mechanical properties, including Young's modulus, Poisson ratio, the yield strength and the stress-strain relationships of different phases are defined according to relevant papers and experimental results. The definition of thermo- mechanical properties of the S690 and the S960 steel are also presented in Appendix A.

6.4. Heat source model of welding

6.4.1. Basic formulae of heat transfer during welding

According to Kim and Basu, an accurate observation of the heat transfer of GMAW is extremely difficult because of the presence of the arc over the weld surface (Kim and Basu 1998). Among the three fundamental modes of heat transfer, namely conduction, convection, and radiation, conduction is the most important process in welding. Fourier's Law is the basic formula for one-dimensional transient heat transfer analysis (Vollmer *et al*. 2010), and it is expressed as:

$$q = -\lambda \frac{dT}{dx} \tag{6.15}$$

where q is the heat flux in W/m^2;

dx is the material thickness in m;

dT is the temperature difference in K from a hot area to a cold area across thickness dx;

λ is the thermal conductivity in W/m/K.

In the specific case of GMAW, the equation for heat transfer from the welding arc to the parent steel could be summarized as:

$$\rho c_p \frac{\partial T}{\partial t} = \nabla(\lambda \nabla T) + \frac{\partial q_{arc}}{\partial t} \tag{6.16}$$

where ρ is the density of the welding electrode;

c_p is the specific heat capacity of the welding electrode;

λ is the thermal conductivity of the welding electrode;

∇ is Laplace-operaattori factor;

q_{arc} is the heat input energy.

The simulation of heat radiation includes two parts: convective heat transfer q_c between the steel and air, and radiative heat transfer q_r of the steel. Convective heat transfer is described according to Newton's law while radiative heat transfer is described using Stefan-Boltzmann's law, respectively as follows:

$$\begin{gathered} q_c = h_c(T - T_0) \\ q_r = \varepsilon_r \sigma_r (T^4 - T_0^4) \end{gathered} \tag{6.16}$$

where h_c is the convection heat transfer coefficient, determined by the heat transfer medium;

T_0 is the room temperature; $T_0 = 20°\text{C}$;

ε_r is the reduction factor; $\varepsilon_r = 0.8$;

σ_r is the Stefan-Boltzmann coefficient; $\sigma_r = 5.67 \times 10^{-8} W \cdot mm^{-2} \cdot K^{-4}$.

Before the modelling of welding process, the heat source model for gas metal arc welding (GMAW) needs to be carefully determined. According to the literature, the double ellipsoidal heat source model with appropriate parameters can accurately simulate the heat transfer during arc welding on the steel sections. Figure 6.2 shows the schematic diagram of typical double ellipsoid model.

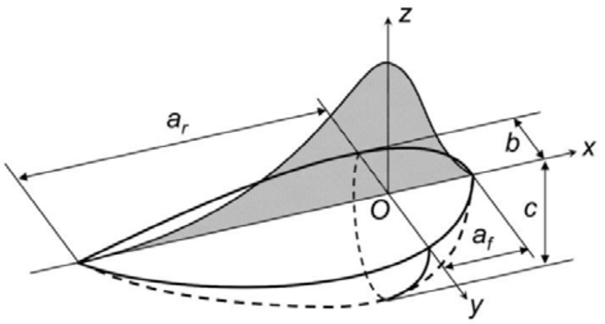

Figure 6.2 The schematic of the double ellipsoidal heat source model

The heat flow distribution function of the front quarter ellipsoid is given by:

$$Q_f(x, y, z) = \frac{6\sqrt{3}Q_o f_f}{abc\pi\sqrt{\pi}} * \exp\,[-3(\frac{x^2}{b^2} + \frac{y^2}{a_f^2} + \frac{z^2}{c^2})] \quad (6.17)$$

Similarly, the heat flow distribution function of the rear quarter ellipsoid is given by:

$$Q_r(x, y, z) = \frac{6\sqrt{3}Q_o f_r}{abc\pi\sqrt{\pi}} * \exp\,[-3(\frac{x^2}{b^2} + \frac{y^2}{a_r^2} + \frac{z^2}{c^2})] \quad (6.18)$$

where $Q_0 = \eta UI$, η is the arc thermal efficiency, U is voltage, and I is current. f_f and f_r are the heat flow density distribution coefficients, and they are used to express the proportional relationship between the rear and the back ellipsoidal heat input, i.e., $f_f + f_r = 1$. a_f, a_r, b and c are the parameters in defining the geometry of the melting pool.

6.4.2. Geometric modelling and meshing

To verify the double ellipsoidal heat source model, five butt welding models were established using Visual-Mesh, the visual interface provided by SYSWELD, as shown in Figure 6.3. To ensure convergence of these models during heat transfer, it is recommended to include a minimum of three layers of elements in the depth direction of each weld seam. Fine meshes are provided at locations close to the weld and heat-affected zone while coarse meshes are provided on those parts away from the weld seam, to ensure a balance between the numerical accuracy and computational efficiency.

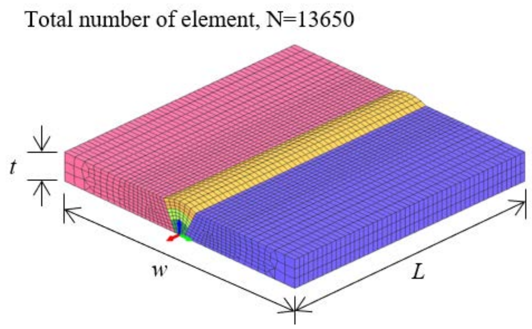

Section S690-10mm

$w \times t \times L = 100 \times 10 \times 100\ (mm)$

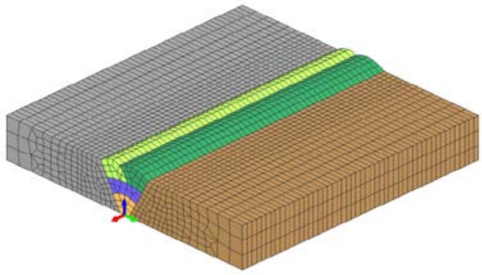

Section S690-16mm

$w \times t \times L = 100 \times 16 \times 100\ (mm)$

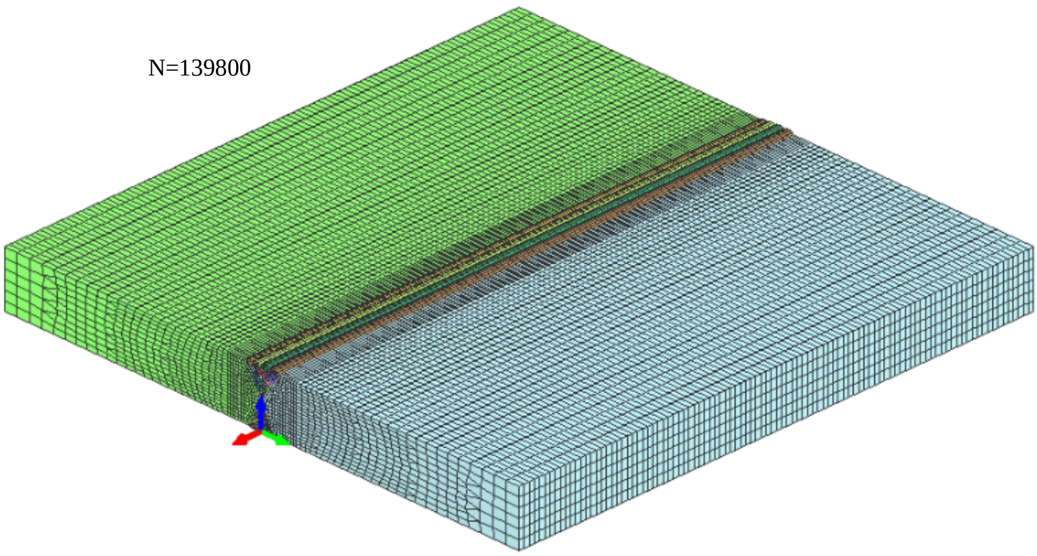

Section S690-30mm

$w \times t \times L = 300 \times 30 \times 300\ (mm)$

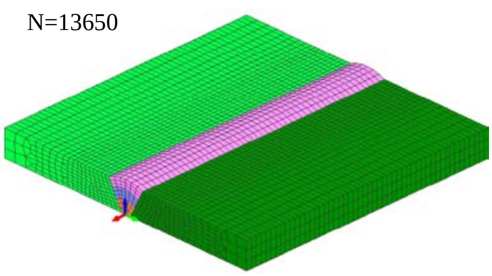

Section S960-10mm

$w \times t \times L = 100 \times 10 \times 100\ (mm)$

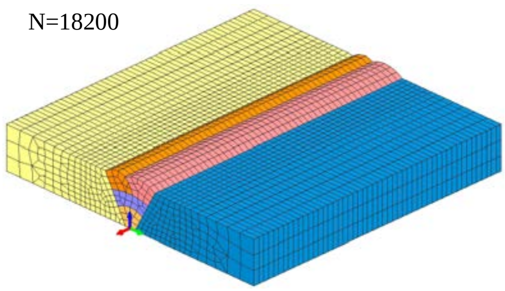

Section S960-15mm

$w \times t \times L = 100 \times 15 \times 100\ (mm)$

Figure 6.3 Demonstration of finite element models with graded mesh

According to the fabrication programme outlined in Chapter 4, the welded sections of the S690 steel consist of three plate thicknesses: 10, 16, and 30mm. The welded sections of the S960 steel include two plate thicknesses: 10 and 15mm. For these five models shown in Figure 6.3, the number of welding passes and the bevelling types are modelled according to the welding procedures in practical.

During welding simulation, the heat source moves along the welding groove and heats up the surrounding elements. Both the start and the end points of the welding line were placed at the center of each weld pass. Radiative heat transfer between the steel and the air has been considered according to the sequence of welding passes.

6.4.3. Heat source calibrations

During calibration of heat source models, the primary adjustment is to specify the dimensions of the melting pool. By altering the value of a_f, a_r, b and c in Equations 6.17 and 6.18, the double ellipsoidal heat source model could be modified to match with the various measured surface transient temperature of the welded sections. Therefore, referencing to the actual welding, the parameters of double ellipsoidal heat source models for these five butt weld joints are presented in Table 6-1. The schematic illustration the double ellipsoidal heat source model, which encompasses the weld section in both the transverse and the depth directions, is illustrated in Figure 6.2, to provide a visual representation of its application on the finite element model.

Table 6-1 Calibrated melting pool dimensions for various models of welded sections

Grade	Plate thickness (mm)	Welding pass	a_f (mm)	a_r (mm)	b (mm)	c (mm)
S690	10	3	5	10	3	3
	16	4	5	10	3	4
	30	20	6	12	4	4
S960	10	3	5	10	3	3
	15	4	5	10	3	4

It is interesting to compare the predicted metallurgical changes of these welded section with those boundaries of the heat-affected zones shown in corresponding welded sections after etching. A comparison between the numerical results of the welded sections and images of the etched section are illustrated in Figure 6.4. It is shown that the cases presented in Figure 6.4 all employed a heat input energy of 1.0 kJ/mm, with the same dimensions and numbers of welding passes as recorded in the actual welding.

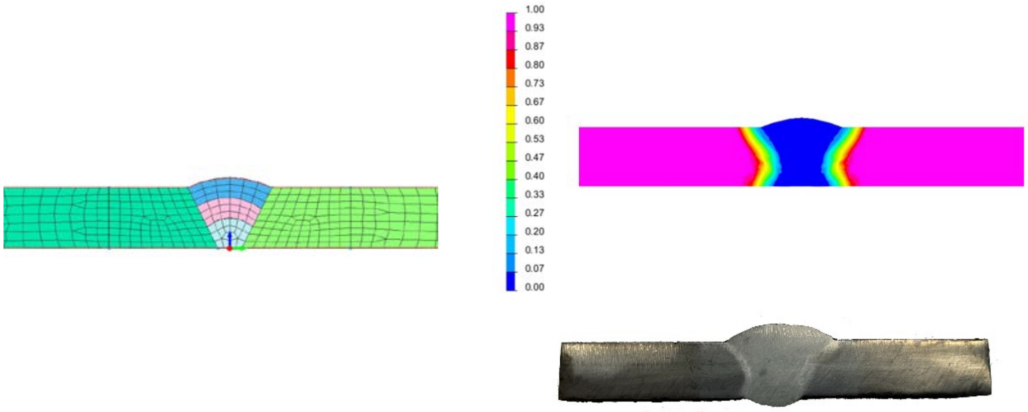

a) Section S690-10mm - Heat input energy at 1.0kJ/mm

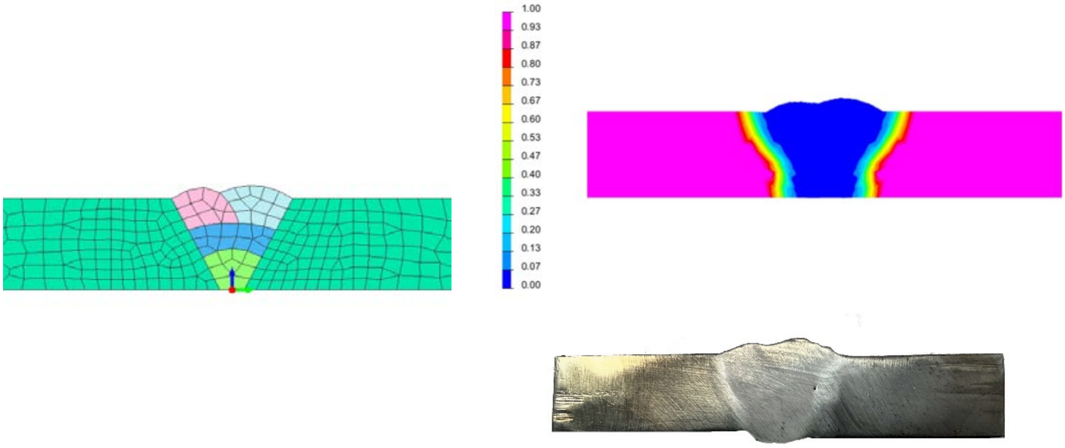

b) Section S690-16mm - Heat input energy at 1.0kJ/mm

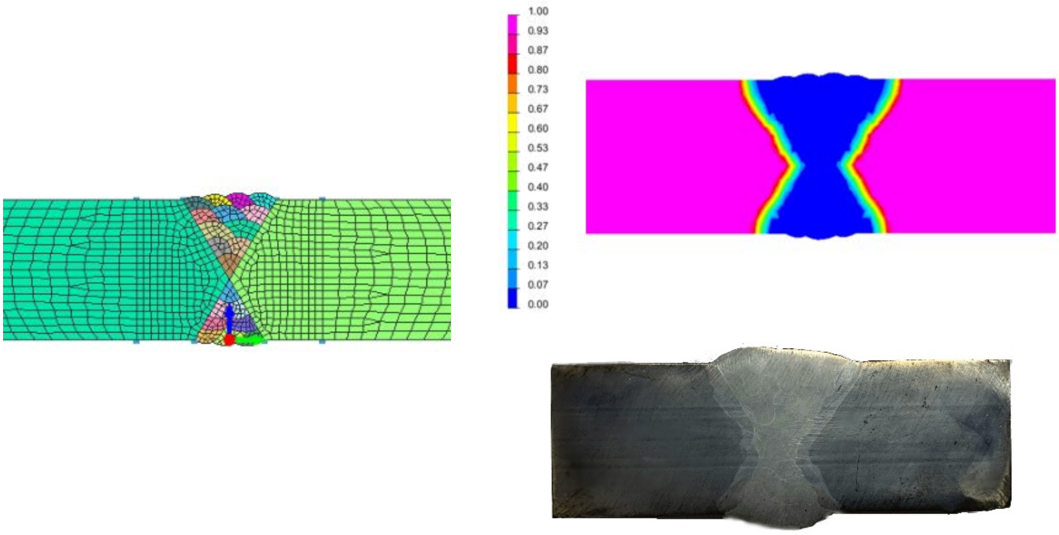

c) Section S690-30mm - Heat input energy at 1.0kJ/mm

Figure 6.4 Comparison on the predicted and observed boundaries of S690 welded sections

In the cloud graph, 0 to 1 on the left side represents "the degree of transition from the initial phase". It is shown that the predicted metallurgical plots extract of phase transformation which matches with the boundaries of the HAZ in various welded sections.

For the S960 steel, heat source calibration also completed using defined heat sources model and material data. The comparison of microstructure after welding and the actual weld sections are illustrated in Figure 6.5.

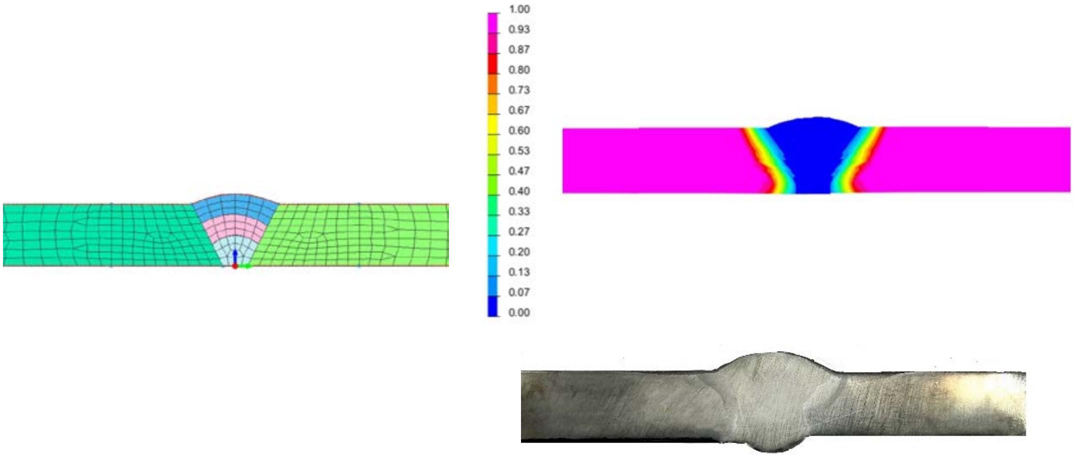

d) Section S960-10mm - Heat input energy at 1.0kJ/mm

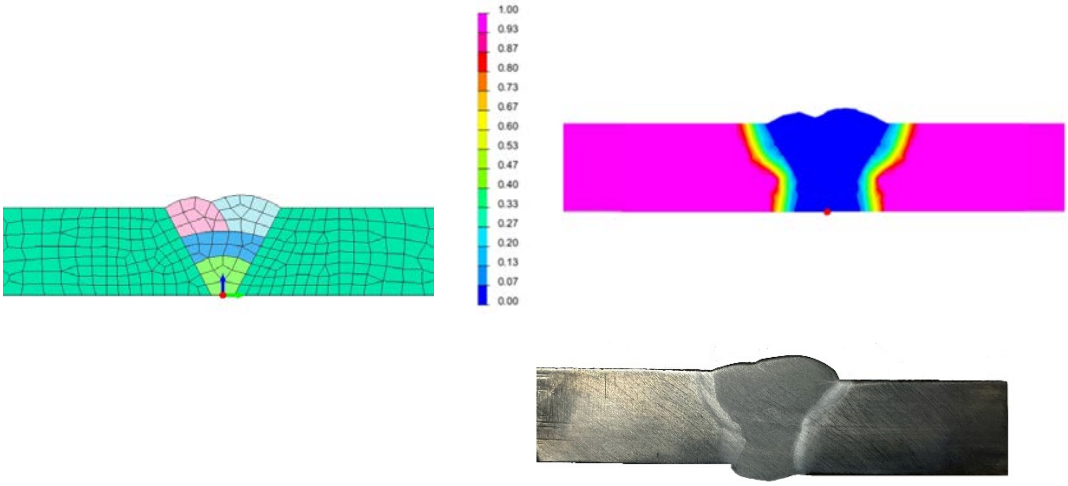

e) Section S960-15mm - Heat input energy at 1.0kJ/mm

Figure 6.5 Comparison on the predicted and observed boundaries of S960 welded sections

As a result, the double-ellipsoidal heat source models utilized in these simulations are considered to be sufficient, and they were adopted accordingly in the subsequent welding simulation of both the S690 and the S960 welded sections.

6.5. .Numerical simulation of S960 welded sections

6.5.1. Proposed finite element models

The thermo-metallurgical and thermo-mechanical properties of the high strength steel undergo nonlinear transformations during welding and there is an significant increase in the number of iterations required in those non-linear analyses. Hence, a large amount of computational resource is often needed. Therefore, the choice of mesh size is very important in these simulations. Owing to the page limitation, only models of the S960 welded sections are discussed and presented.

In order to investigate the effect of mesh sizes on these analyses, two meshes with different element sizes were established, and they are designed as Models 960-H1-1 and 960-H1-2. As the temperature variation is significant in regions close to the heat-affected zones during welding, therefore, a fine mesh is provided utilized in these regions, while a coarse meshing is provided at locations further away from the weld section, as shown in Figure 6.6. It should be noted that for Model 960-H1-1, the sizes of typical finest elements are 2.0×2.0×5.0 mm; for Model 960-H2-2, the sizes of typical finest elements are 1.0×1.0×2.5 mm.

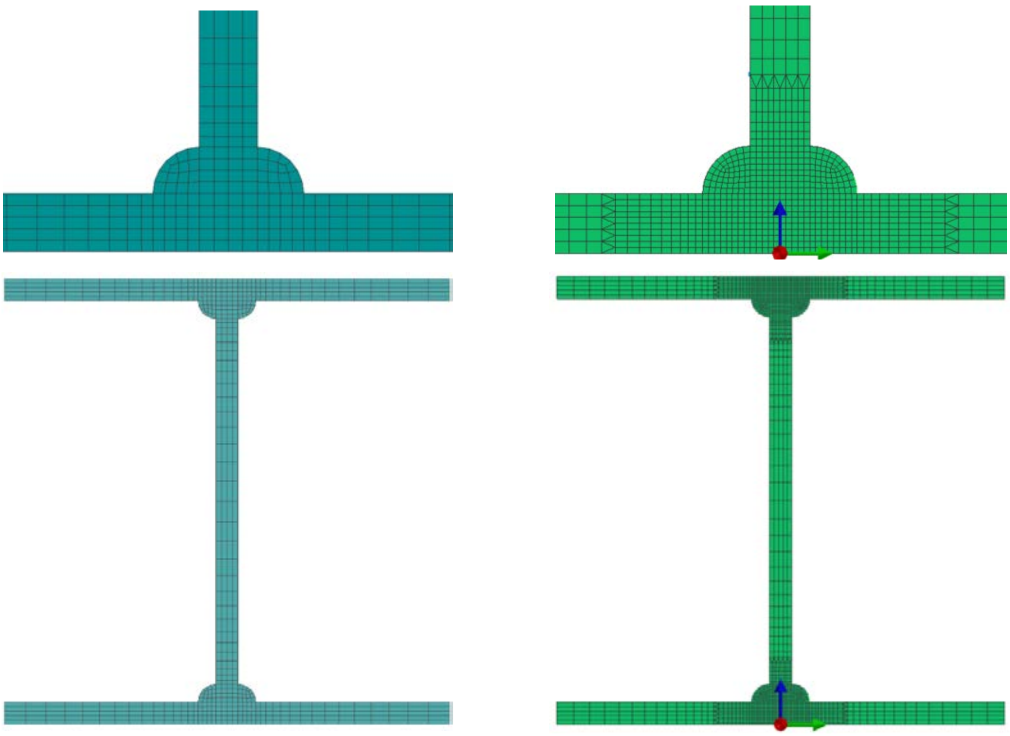

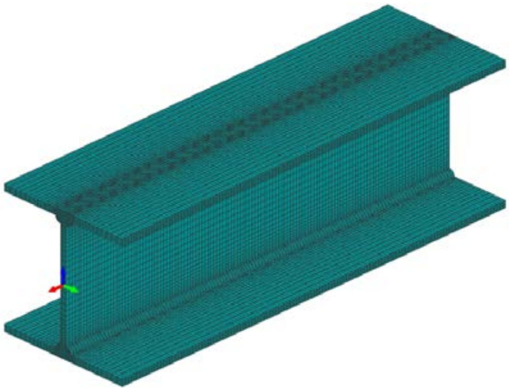

a) 960-H1-1

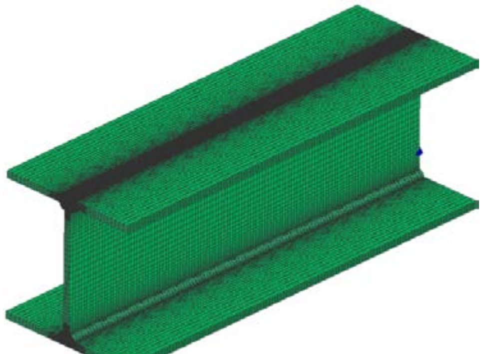

b) 960-H1-2

Figure 6.6 Meshing strategy in finite element models for S960 welded section

With reference to the physical welding procedure, the boundary conditions shown in Figure 6.7 are set identically for all these four models. It should be noted that the node groups at three edges are fixed as follows:

Node group	Boundary conditions
1	$U_x = U_y = U_Z = 0$
2	$U_x = U_Z = 0$
3	$U_Z = 0$

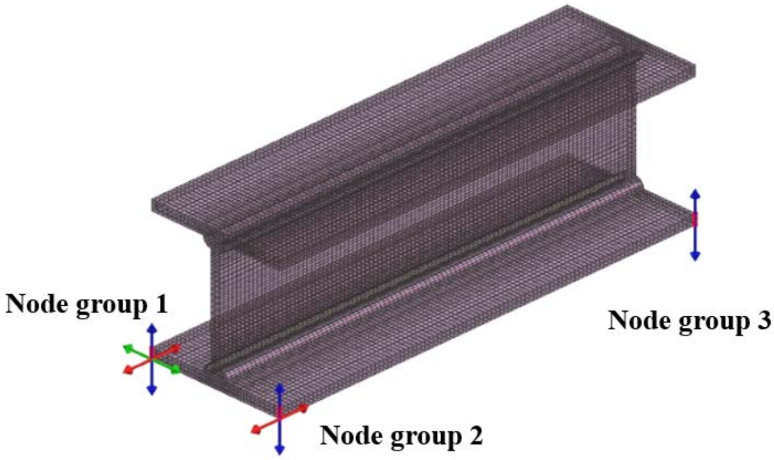

Figure 6.7 Boundary conditions of the proposed model

In SYSWELD, the thermo-metallurgical and the thermo-mechanical analyses are performed separately. When considering only the thermo-metallurgical results, the computational time for Model 960-H1-1 is 8.4 hours while for Model 960-H1-2, it takes 67.2 hours due to the use of a fine mesh. However, upon comparing the predicted temperature history curves at the same point in these two models as shown in Figure 6.8, the effect of mesh size on predicted the temperatures is found to be negligible.

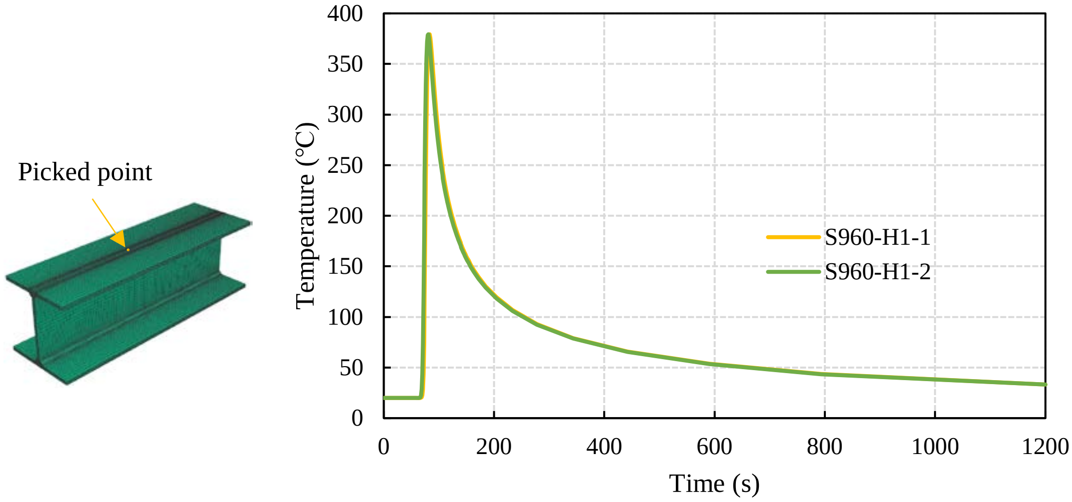

Figure 6.8 Comparison on temperature predicted with Models 960-H1-1 and 960-H2-2

When consider the stress field of these models, it was found that the calculation time for model 960-H1-1 was 24.8 hours, whereas for model 960-H1-2 it was 182.1 hours. Given the significantly prolonged computation time and high CPU occupancy, it appears that an excessive over-meshing of the area of weld section and heat-affected zone is not necessary. Therefore, Model 960-H1-1 was adopted in all subsequent numerical models. This meshing strategy is consistent with the movement of the heat source model, and it can effectively reduce computational time. The nominal cross-section dimensions of the proposed models for these four S960 welded sections are presented in Figure 6.10 and Table 6-2. The mesh sizes of those welded sections were established have at least four layers of elements in the direction of the plate thickness, and the minimum element size is 1mm. These meshes provides a good balance between computational efficiency and numerical accuracy. To ensure accuracy of the simulations, the shape of the welding seam was simplified according to the dimensions given in the Table 6-2, while preserving the residual heights of the welding seam. The welding passes and the air-cooling time were determined using measured data in Chapter 5. The boundary conditions of these four models are assigned to be the same as shown in Figure 6.7.

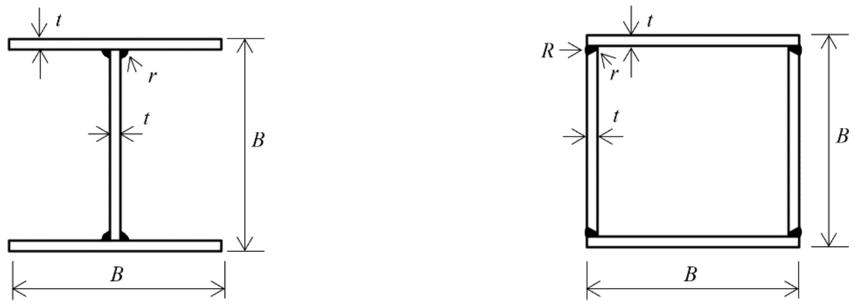

Figure 6.9 Nominal cross section dimensions of S960 welded sections

Table 6-2 Dimensions of finite element models S960 welded sections

Model	B (mm)	t (mm)	r (mm)	R (mm)	H (mm)
S960-H1	200	10	8	-	650
S960-H2	200	15	12	-	650
S960-B1	200	10	5	12	650
S960-B2	200	15	5	15	650

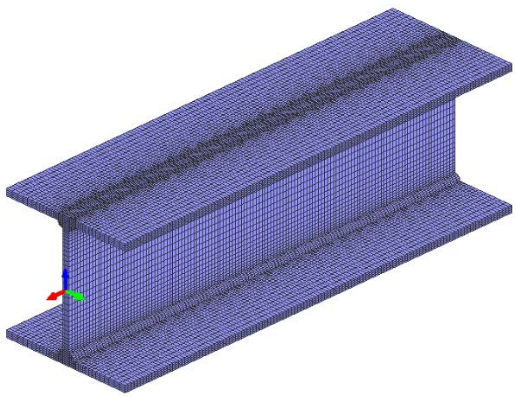

a) Model S960-H1

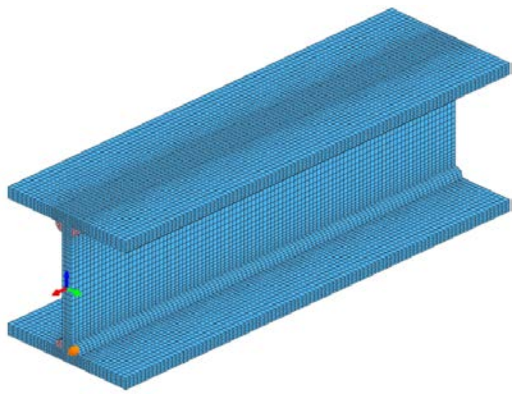

b) Model S960-H2

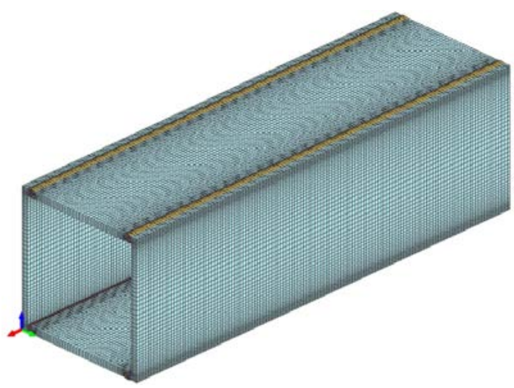

c) Model S960-B1

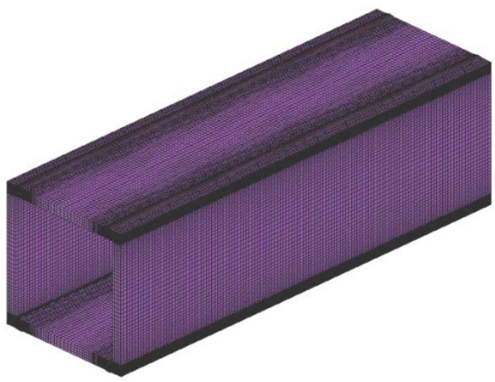

d) Model S960-B2

Figure 6.10 Finite element models of S960 welded sections with graded mesh

The double ellipsoidal heat source was adopted in these models. The heat input energy, the welding speed, the heat transfer coefficient, and the cooling time for each welding pass were assigned to take corresponding values measured in the welding process. All these parameters adopted in various models are shown in Tables 6-3 to 6-6.

Table 6-3 Summary of welding passes and welding time of Model S960-H1

Model	Pass	Weld speed (mm/s)	Heat input (kJ/mm)	Initial time (s)	End time (s)
S960-H1	1	4.38	1.00	0	149.7
	2	4.38	1.00	350	499.7
	3	4.92	0.87	700	833.3
	4	4.92	0.87	1050	1183.3

Table 6-4 Summary of welding passes and time of model S960-H2

Model	Pass	Weld speed (mm/s)	Heat input (kJ/mm)	Initial time (s)	End time (s)
S960-H2	1	4.17	1.75	0	155.8
	2	5.00	1.43	350	480.0
	3	5.00	1.43	700	830.0
	4	5.00	1.43	1050	1180.0

Table 6-5 Summary of welding passes and time of model S960-B1

Model	Pass	Weld speed (mm/s)	Heat input (kJ/mm)	Initial time (s)	End time (s)
S960-B1	1	4.51	0.88	0	144.1
	2	4.74	0.85	350	487.1
	3	4.58	0.89	700	841.9
	4	4.52	1.13	1050	1193.8
	5	4.39	1.05	1400	1548.0
	6	4.58	0.89	1750	1891.9
	7	4.52	1.13	2100	2243.8
	8	4.39	1.05	2450	2598.0
	9	4.74	1.01	2800	2937.1
	10	4.92	0.93	3150	3282.1
	11	4.64	1.03	3500	3640.0
	12	4.45	1.03	3850	3996.0

Table 6-6 Summary of welding passes and time of model S960-B2

Model	Pass	Weld speed (mm/s)	Heat input (kJ/mm)	Initial time (s)	End time (s)
S960-B2	1	5.00	0.94	0	130.0
	2	4.96	0.95	350	481.0
	3	4.97	0.91	700	830.7
	4	4.74	0.99	1050	1187.1
	5	4.68	1.06	1400	1538.8
	6	4.27	1.19	1750	1902.2
	7	4.27	1.19	2100	2252.2
	8	4.78	1.10	2450	2585.9
	9	4.70	0.96	2800	2938.3
	10	4.70	0.96	3150	3288.3
	11	4.85	1.13	3500	3634.0
	12	4.77	1.19	3850	3986.2
	13	4.77	1.19	4200	4336.2
	14	4.93	1.11	4550	4681.8
	15	4.87	1.16	4900	5033.4
	16	4.87	1.16	5250	5383.4

After completion of the simulation, the numerical results are subject to post-processed using an accompanying module, Visual-Viewer. In this module, the temperature contour plots for each time step of the welded sections, the temperature curves of specific nodes, the microstructural changes of the steel, and the distribution of residual stresses were extracted for visualization as discussed below.

6.5.2. Temperature results

1). Model S960-H1

For Model S960-H1, typical transient temperature contour plot during the first pass welding is shown in Figure 6.11. It should be noted that the temperature above the melting point of high strength steel, which is 1350°C, is indicated in purplish red. This region is also generally considered to be the melt pool in the welding simulation. Due to the use of the element birth and death technique in the simulation, the weldments are gradually formed as the heat source moves.

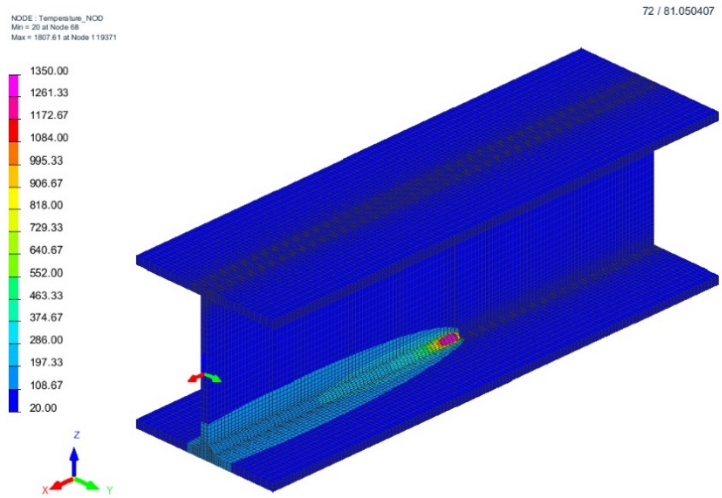

Figure 6.11 Transient temperature contour plot during welding in Model S960-H1

It is shown in Figure 6.11 that the elements along the welding groove are subsequently heated above the melting temperature as the heat source moves, forming a moving ellipsoidal thermo-distribution space. The temperatures of adjacent elements also increase due to transient heat transmission, and the temperature distribution behind the heat source forms a long elliptical trajectory. During the cooling stage, the temperatures of these elements in the heat-affected zones gradually decrease, and the temperatures of these elements decrease readily until the temperatures become uniform. As reported in Chapter 5 Section 5.2, six measurement points are selected on the top surface of the top flange of section S960-H1 are plotted in Figure 6.12. Points A, B, and C are located along the centreline of the flange, and they are 25mm apart. Points D, E, and F are located 20mm from Points A, B, and C, and they are also 25mm apart. The temperature-time curves of all these six points are shown in Figure 6.13. Depending on the actual weld width, the dimension of fillet weld section is set to be 8 mm. The temperature-time curves of the points indicate that these nodes undergo one welding heat cycle. Taking into account of the preheating process in the physical welding, the welding start temperature is set to 80°C.

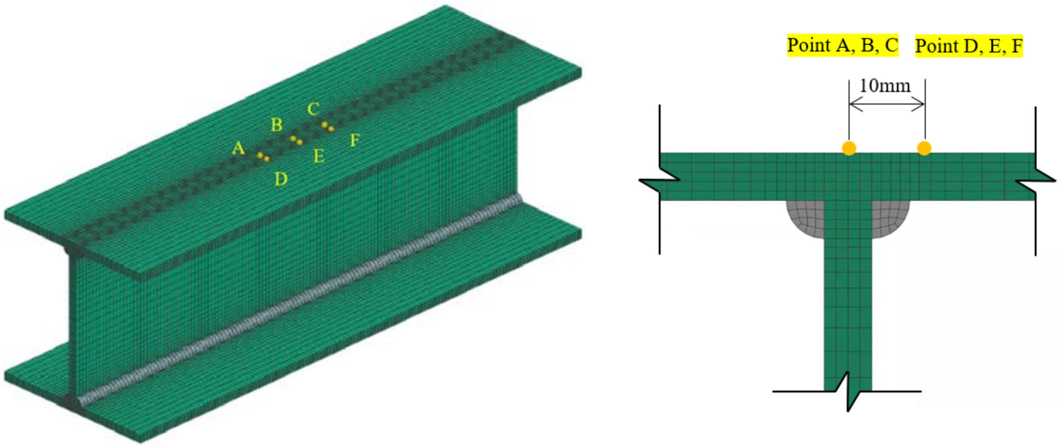

Figure 6.12 Locations of temperature measurement points in Model S960-H1

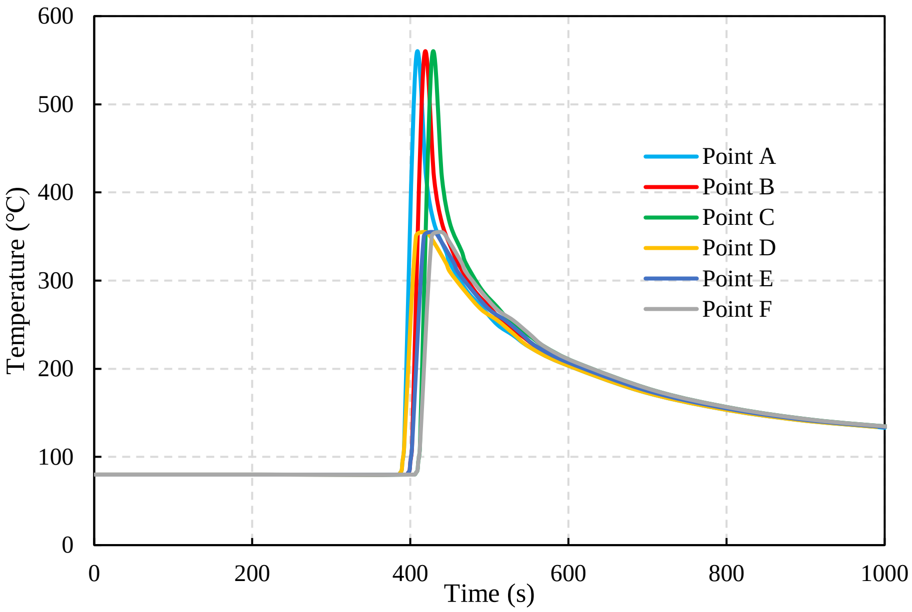

Figure 6.13 Temperature-time curves at various points of Model S960-H1

The data for Point B were selected for illustration. As illustrate in Figure 6.14, compared with the measured temperature curves at point B, the validated heat source model and material properties match well on FEM temperature results. As shown in Figure 6.14, a good agreement between the measured and the predicted temperature-time curves is achieved. Hence, the proposed model for Section S960-H1 is able to simulate the welding process effectively.

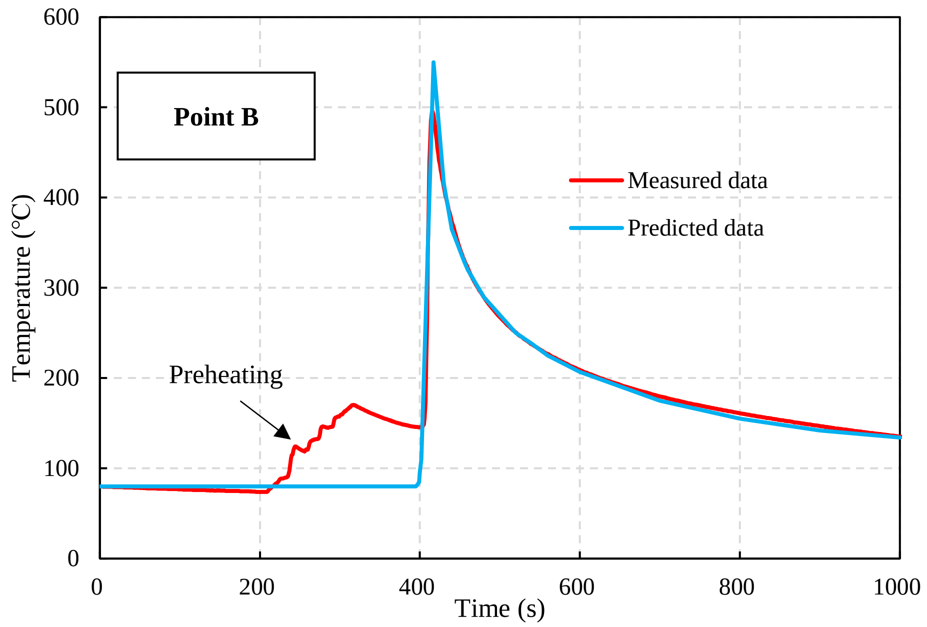

Figure 6.14 Comparison of predicted and measured temperatures-time curves of Point B in Section S960-H1

2) Model S960-H2

For Model S960-H2, typical transient temperature contour plot during the first pass welding is shown in Figure 6.15. Due to an increase in the plate thickness, the cross-sectional area of the weld joint is increased accordingly, when compared to that of Model S960-H1.

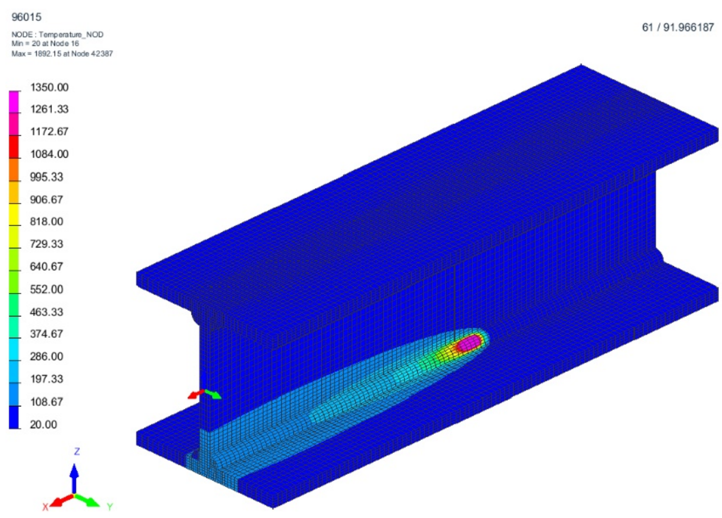

Figure 6.15 Transient temperature contour plot during welding of S960-H2

Similar to that in Model S960-H1, six points were selected on the top surface of the top flange of Model S960-H2 for temperature comparison, as shown in Figure 6.16. Depending on the actual weld width, the dimension of fillet weld section is set to be 10 mm.

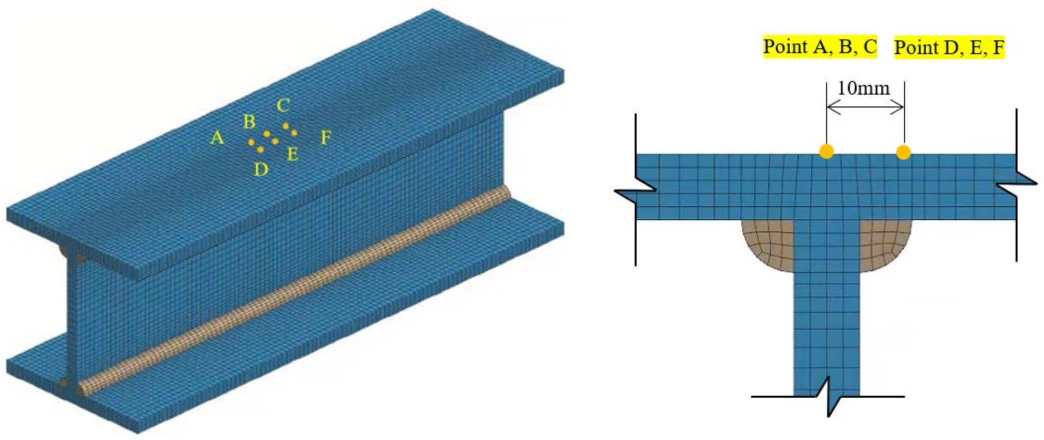

Figure 6.16 Locations of temperature measurement points in Model S960-H1

The temperature-time curves of these six points are shown in Figure 6.17. According to the measurement data, the welding start temperature is set to 38°C. The temperature curves of the measured points indicate that these nodes underwent one preheating and one welding heat cycle.

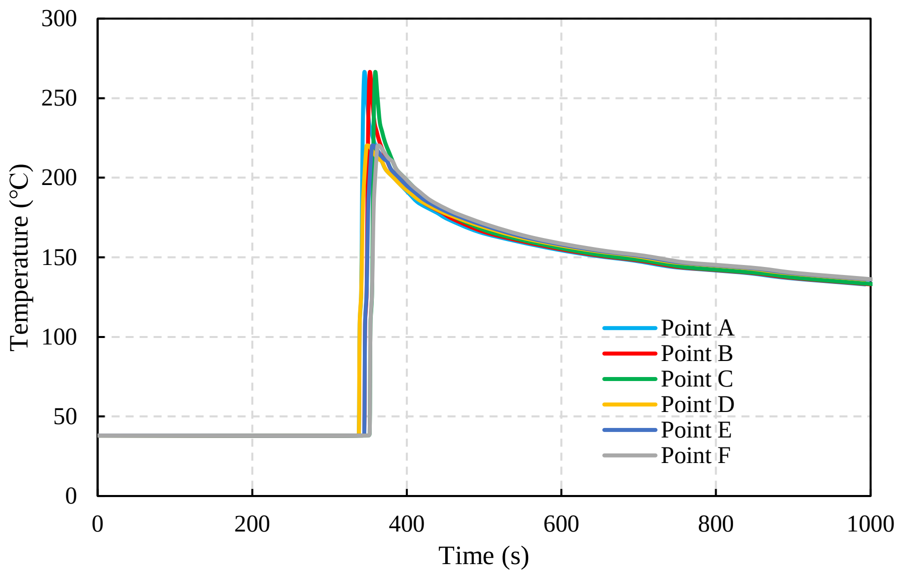

Figure 6.17 Temperature-time curves at various points of Model S960-H2

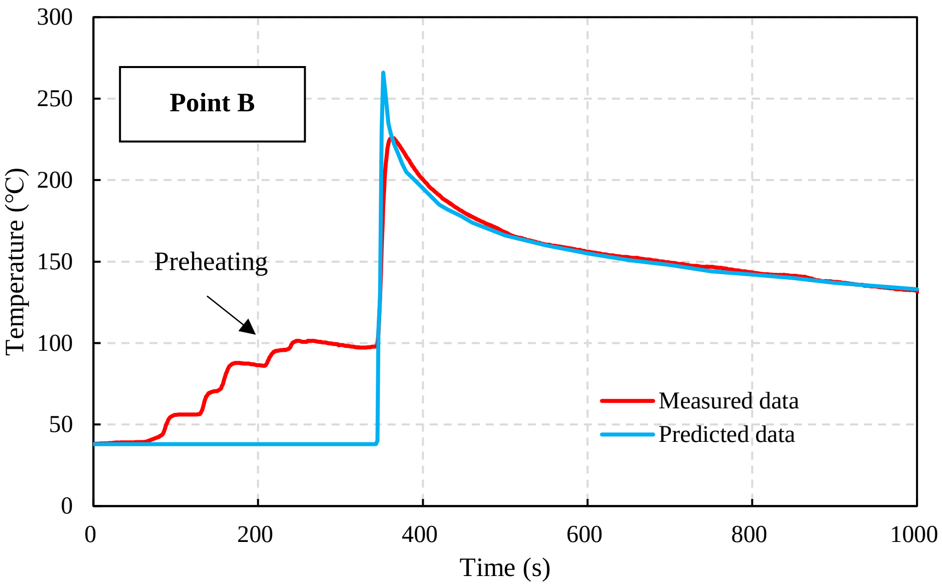

Figure 6.18 Comparison of predicted and measured temperature-time curves of point B in Section S960-H2

As shown in Figure 6.18, a good agreement between the measured and the predicted temperature-time curves is achieved. Hence, the proposed model for Section S960-H2 is able to simulate the welding process effectively.

3) Model S960-B1

For Model S960-B1 model, typical temperature contour plot during the third pass welding at one of the four corners is shown in Figure 6.19.

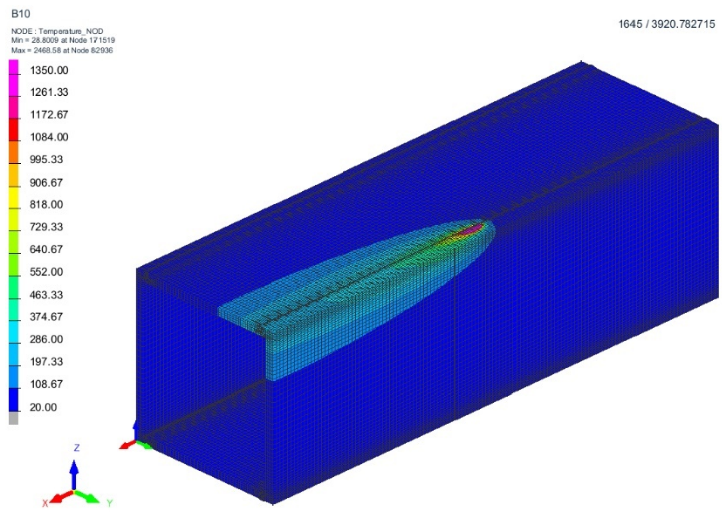

Figure 6.19 Transient temperature contour plot during welding of S960-B1

As shown in this figure, the sizes of the weld pool are found to cover the weld groove.

In each weld seam, selected welding passes are simulated in a bottom-to-top sequence. Six points were selected on the top surface of the top flange of Model S960-B1 for temperature comparisons, as shown in Figure 6.20. The corresponding temperature-time curves are shown in Figure 6.21. According to the measured data, the welding start temperature is set to 58°C.

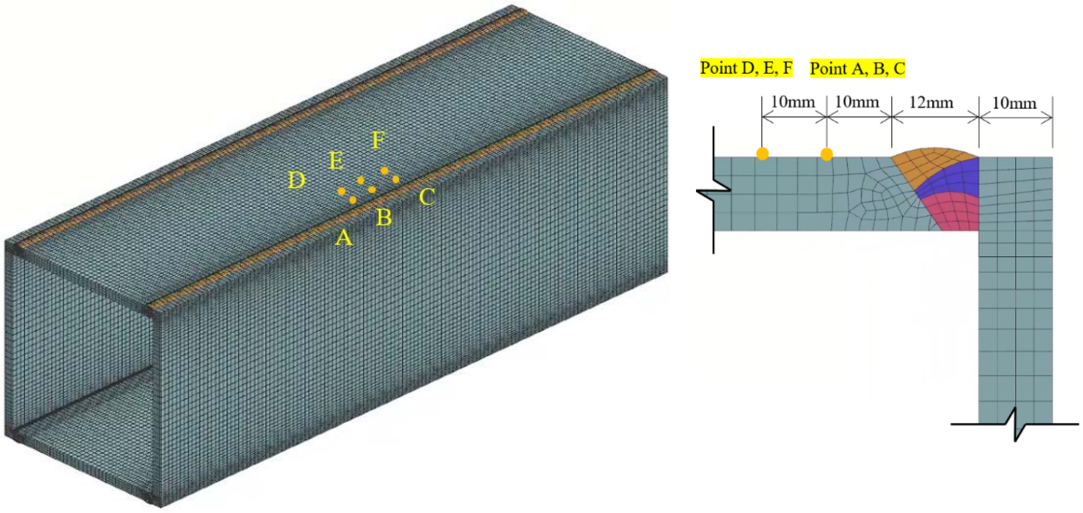

Figure 6.20 Locations of temperature measurement points in Model S960-B1

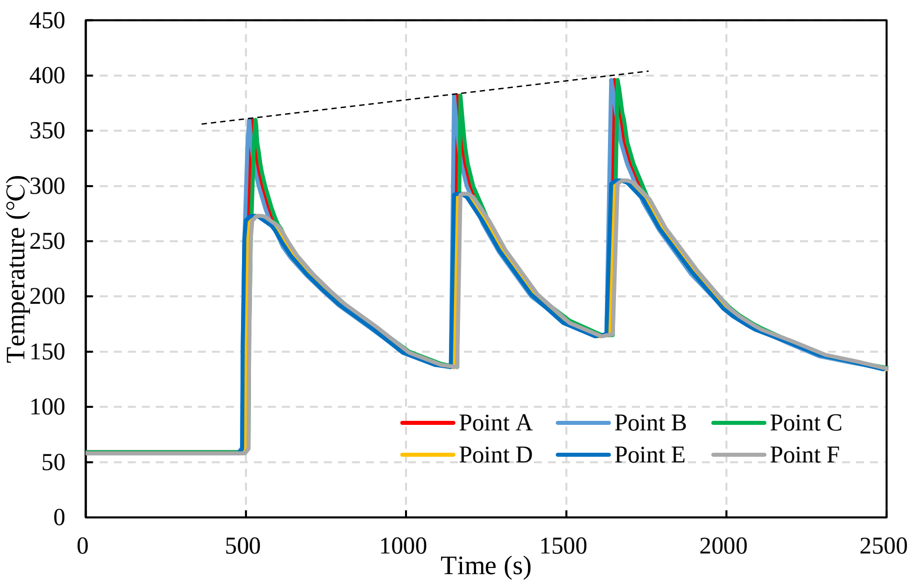

Figure 6.21 Temperature-time curves at various points of S960-B1

The temperature-time curves of these points indicate that these nodes undergo three welding heat cycles. It is evident that the peak temperature of each welding pass increases moderately among these welding heat cycles. It should be noted that the heat-affected zone is subjected to multiple welding heat cycles, leading to a relatively complex metallurgical transformation.

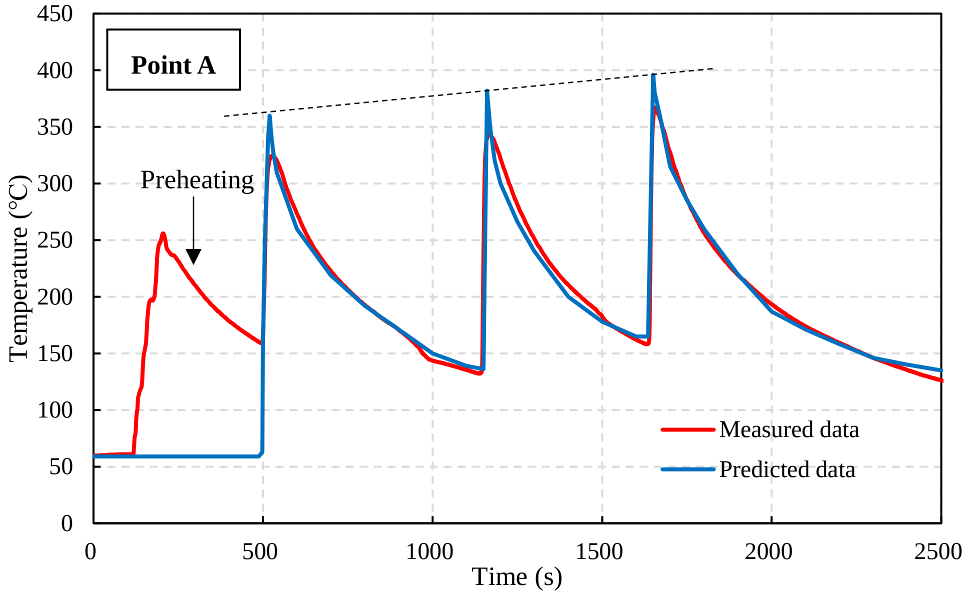

Figure 6.22 Comparison of predicted and measured temperature-time curves of point A in Section S960-B1

As shown in Figure 6.22, a good agreement between the measured and the predicted temperature-time curves is achieved. Hence, the proposed model for Section S960-B1 is able to simulate the welding process effectively.

4) Model S960-B2

For Model S960-B2, typical transient temperature contour plot during welding of the fourth pass at one corner of the four is shown in Figure 6.23.

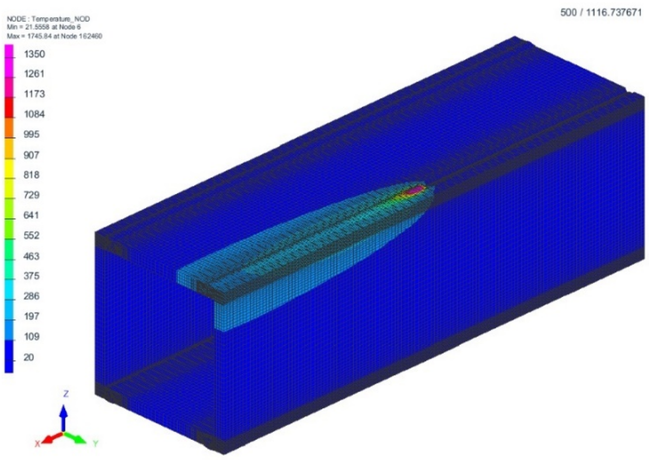

Figure 6.23 Transient temperature contour plot during welding of S960-B2

Similar to Model S960-B1, six selected points were selected on the top surface of the top flange for temperature comparison as shown in Figure 6.24. The temperature-time curves of these points indicate that these nodes undergo three welding heat cycles. It is evident that the peak temperature of each welding pass increases moderately among these welding heat cycles. It should be noted that the heat-affected zone is subjected to multiple welding heat cycles, leading to a relatively complex metallurgical transformation.

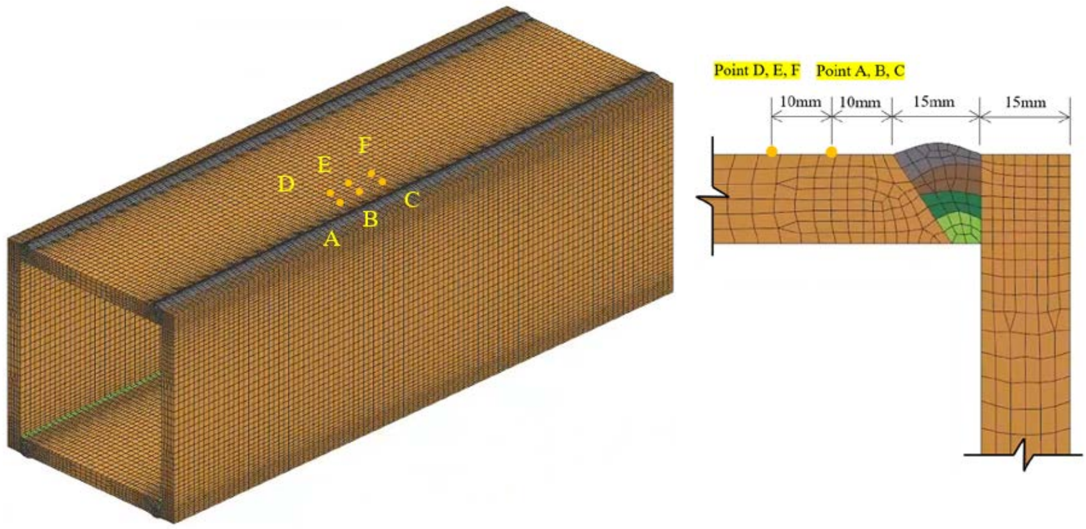

Figure 6.24 Locations of temperature measurement points in Model S960-B2

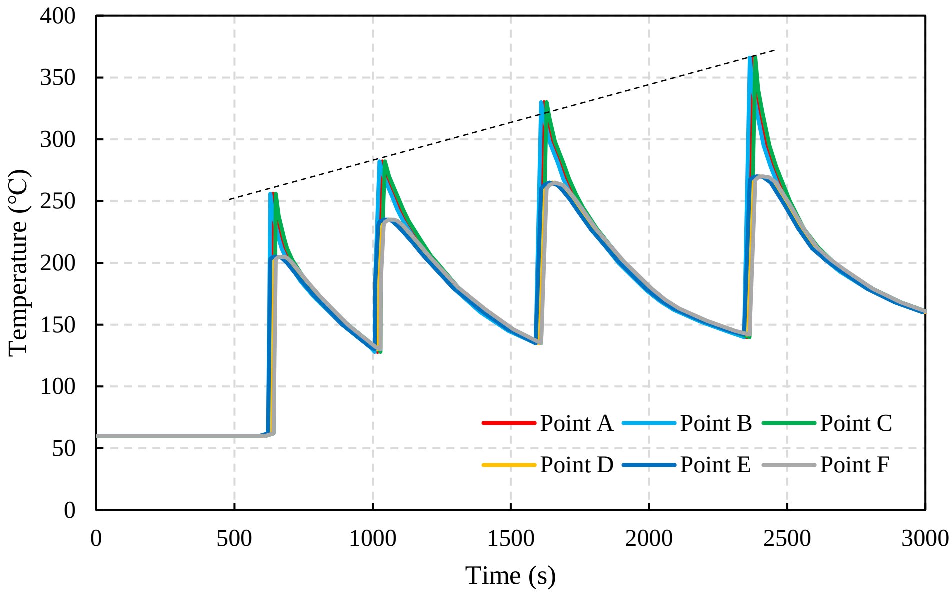

Figure 6.25 Temperature-time curves at various points of Model S960-B2

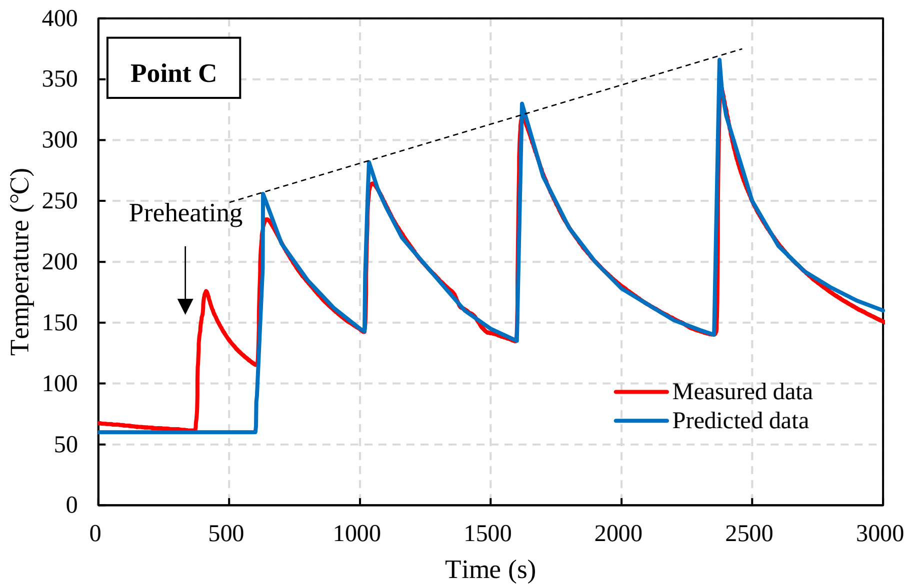

Figure 6.26 Comparison of predicted and measured temperature-time curves of point C in Section S960-B2

As shown in Figure 6.26, c a good agreement between the measured and the predicted temperature-time curves is achieved. Consequently, transient temperature distribution history, and the temperature-time curves of the proposed models confirmed that the S960 material model, the double ellipsoidal heat source model, and the heat transfer analyses together with various thermal parameters is able to simulate the welding processes effectively for both S960 H- and Box sections.

6.5.3. Residual stress result

1) Model S960-H1

For Model S960-H1, the Von Mises residual stress contour plot after welding is shown in Figure 6.27. The stresses illustrated in the figure are those of the final state, i.e., when both the welding and the cooling processes have been completed. To further illustrate the residual stresses, a cross-section view at the central part of Model S960-H1 is also shown.

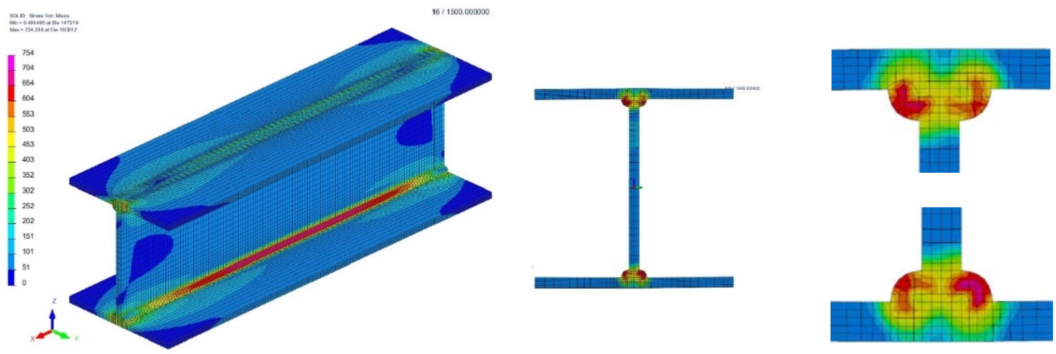

Figure 6.27 Contour plot of von mises residual stress after welding of Model S960-H1

The maximum residual stress is found to be located in the vicinity of the welding seams of the model, with a value of 754 MPa. Contour plots of the longitudinal residual stresses and transverse residual stresses are presented in Figure 6.28 and Figure 6.29, respectively.

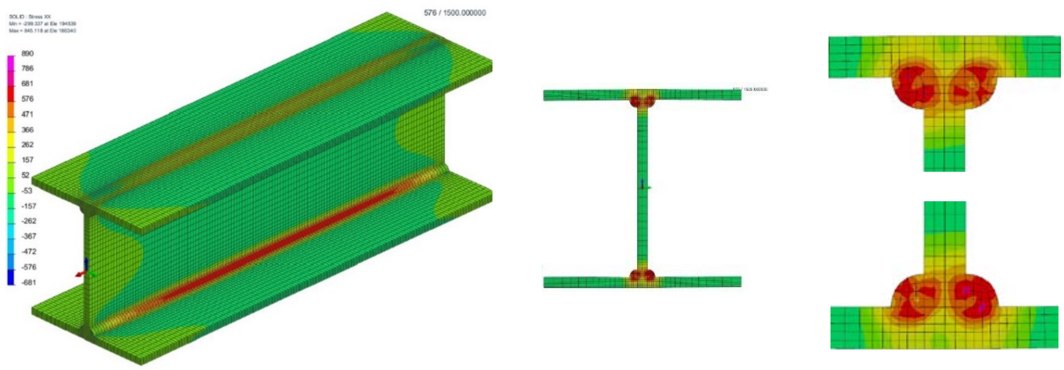

Figure 6.28 Contour plot of longitudinal residual stresses of Model S960-H1

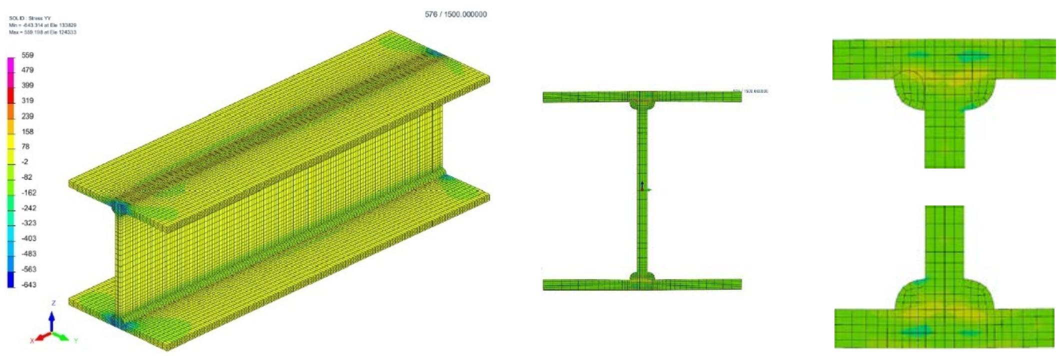

Figure 6.29 Contour plot of transverse residual stresses of Model S960-H1

The longitudinal residual stresses on the top surface of the top flange of Model S960-H1 are shown in Figure 6.28. The measured residual stresses presented in Chapter 5 are also plotted in the figure for a direct comparison, as shown in Figure 6.30. In the figure,

a_1, a_2, a_1', a_2' labels the location of the fillet welding and the web. A similar comparison on those measured and predict of longitudinal residual stresses in the web plate of S960-H1 is provide in Figure 6.31. In the figure, a_1, a_1' labels the location of the two farthest strain gauges rosettes.

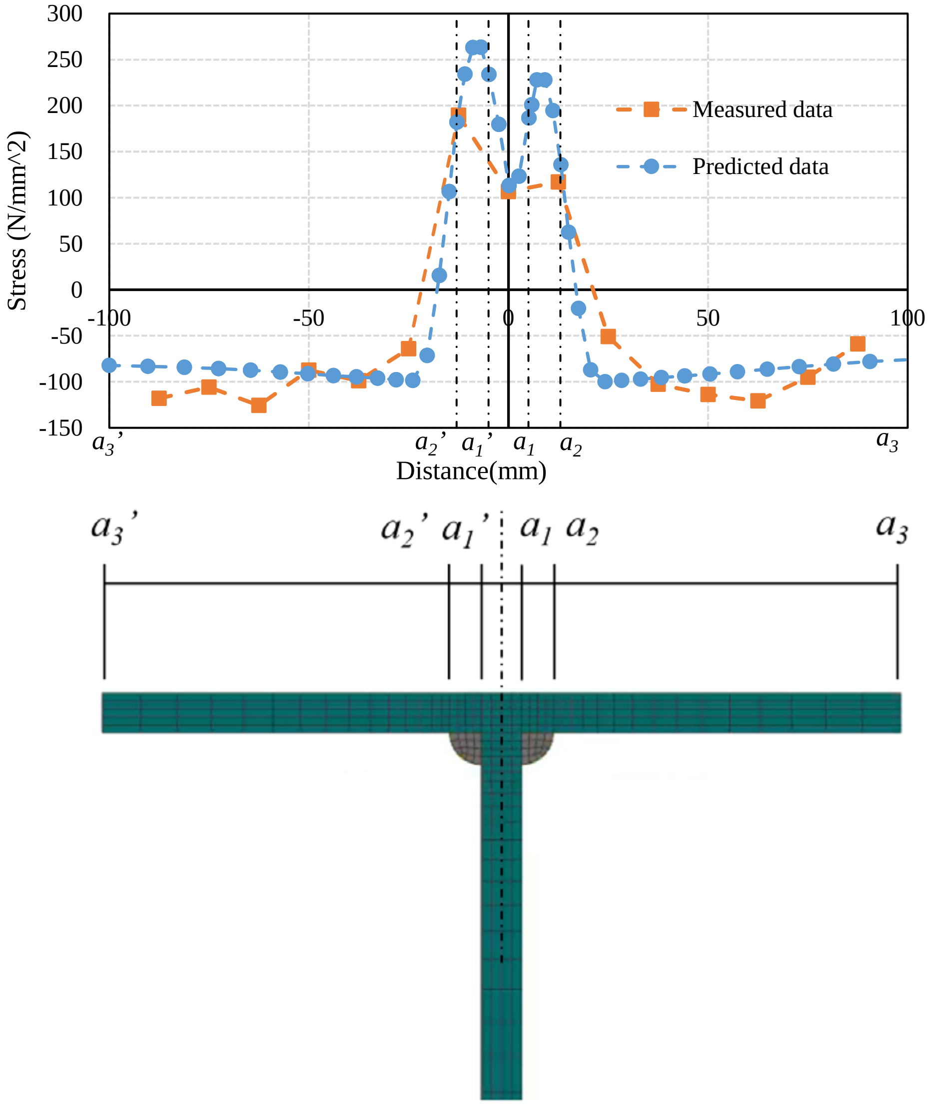

Figure 6.30 Comparison of predicted and measured residual stresses across the flange of Section S960-H1

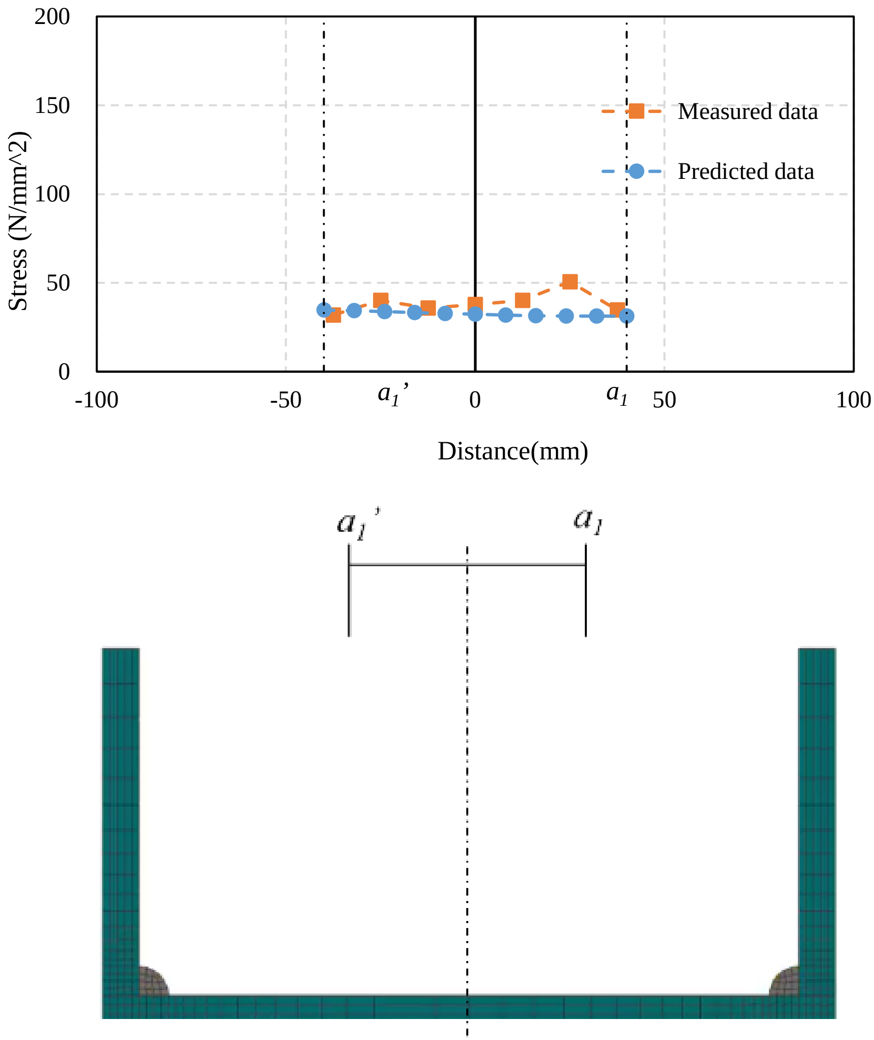

Figure 6.31 Comparison of predicted and measured residual stresses across the web of Section S960-H1

Therefore, a good comparison between the measured and the predicted longitudinal residual stresses in both the flanges and the web plate of Section S960-H1 is achieved.

2) Model S960-H2

For Model S960-H2, the Von Mises residual stress contour plot after welding is shown in Figure 6.32. The stresses illustrated in the figure are those of the final state, i.e., when both the welding and the cooling processes have been completed. To further illustrate the residual stresses, a cross-section view at the central part of Model S960-H2 is also shown.

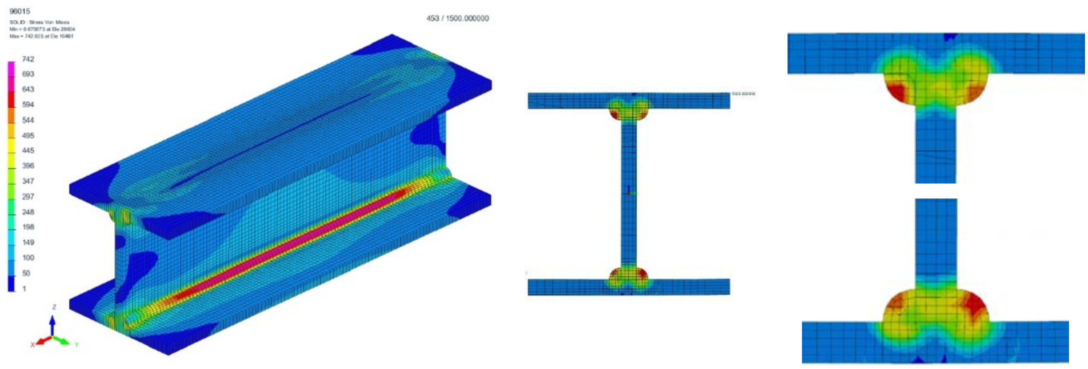

Figure 6.32 Contour plot of von mises residual stress after welding of Model S960-H2

The maximum residual stress is found to be located in the vicinity of the welding seams of the model, with a value of 742 MPa. Contour plots of the longitudinal residual stresses and transverse residual stresses are presented in Figure 6.26 and Figure 6.27, respectively.

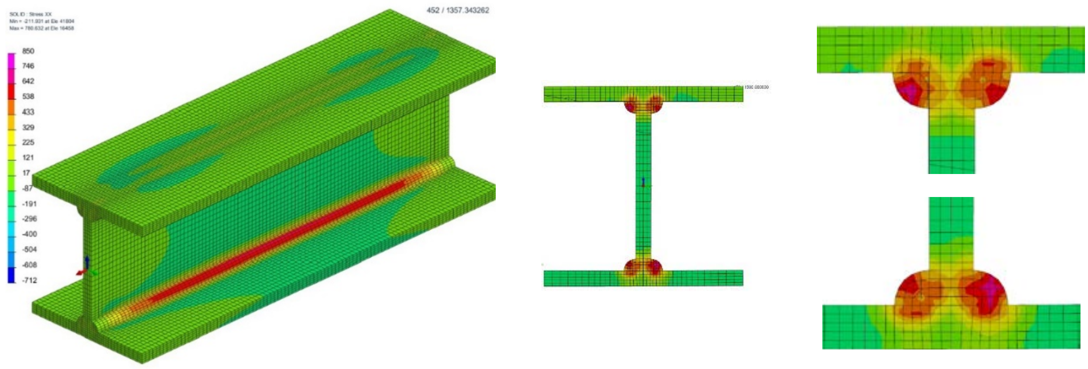

Figure 6.33 Contour plot of longitudinal residual stresses of Model S960-H2

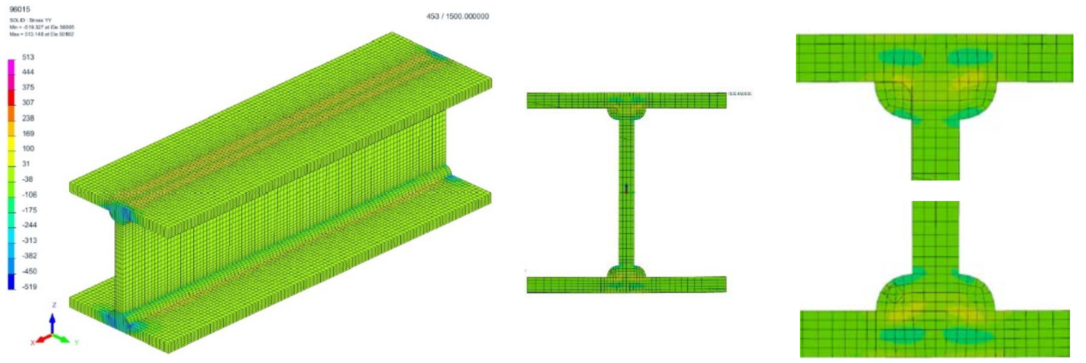

Figure 6.34 Contour plot of transverse residual stresses of Model S960-H2

The longitudinal residual stresses on the top surface of the top flange of Model S960-H2 are shown in Figure 6.33. The measured residual stresses presented in Chapter 5 are also plotted in the figure for a direct comparison, as shown in Figure 6.35. In the figure,

a_1, a_2, a_1', a_2' labels the location of the fillet welding and the web. A similar comparison on those measured and predict of longitudinal residual stresses in the web plate of S960-H2 is provide in Figure 6.36. In the figure, a_1, a_1' labels the location of the two farthest strain gauges rosettes.

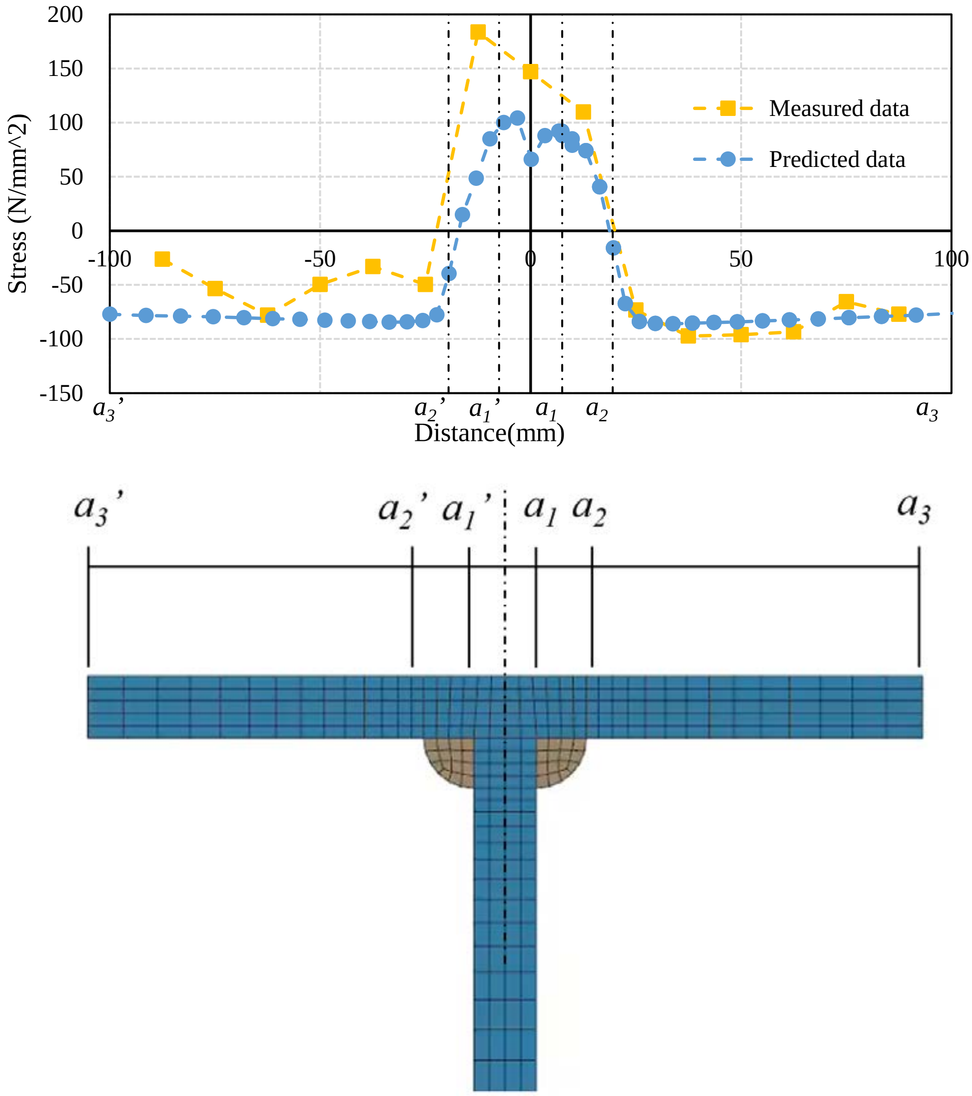

Figure 6.35 Comparison of predicted and measured residual stresses across the flange of Section S960-H2

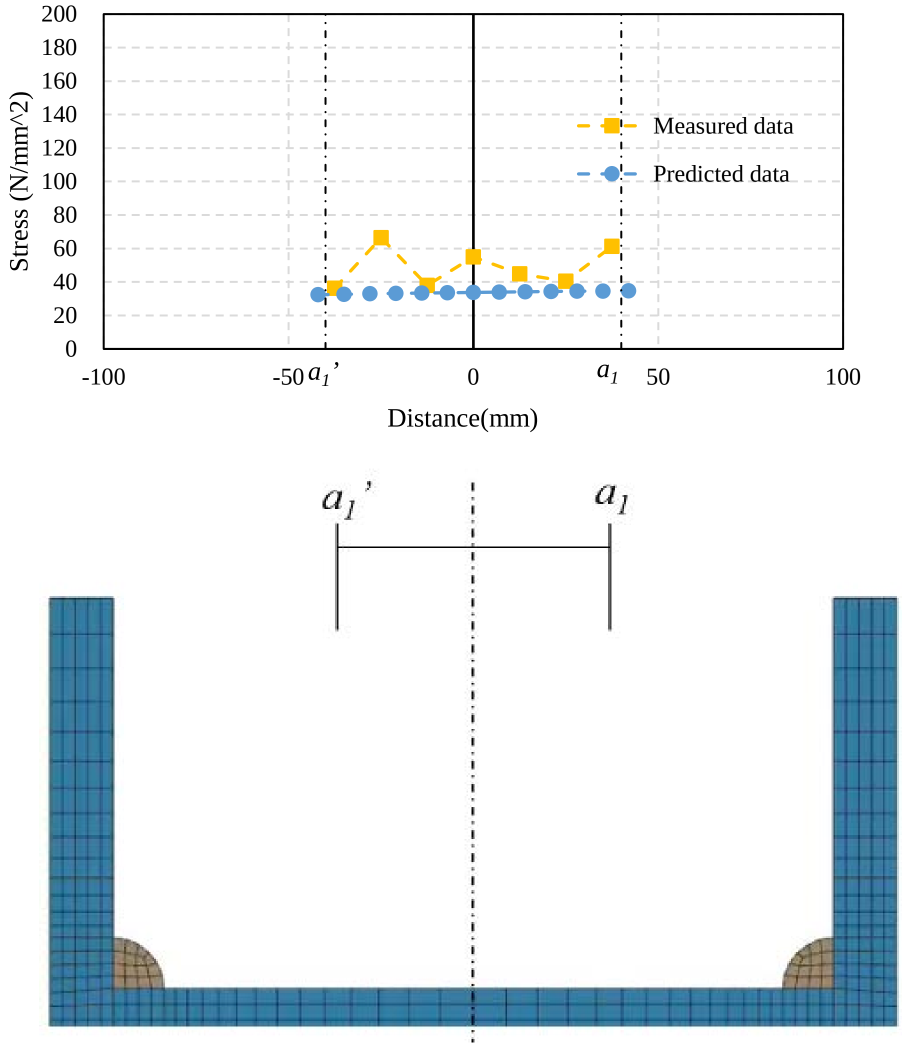

Figure 6.36 Comparison of predicted and measured residual stresses across the web of Section S960-H2

Therefore, a good comparison between the measured and the predicted longitudinal residual stresses in both the flanges and the web plate of Section S960-H2 is achieved.

3) S960-B1

For Model S960-B1, the Von Mises residual stress contour plot after welding is shown in Figure 6.37. The stresses illustrated in the figure are those of the final state, i.e., when both the welding and the cooling processes have been completed. To further illustrate the residual stresses, a cross-section view at the central part of Model S960-B1 is also shown.

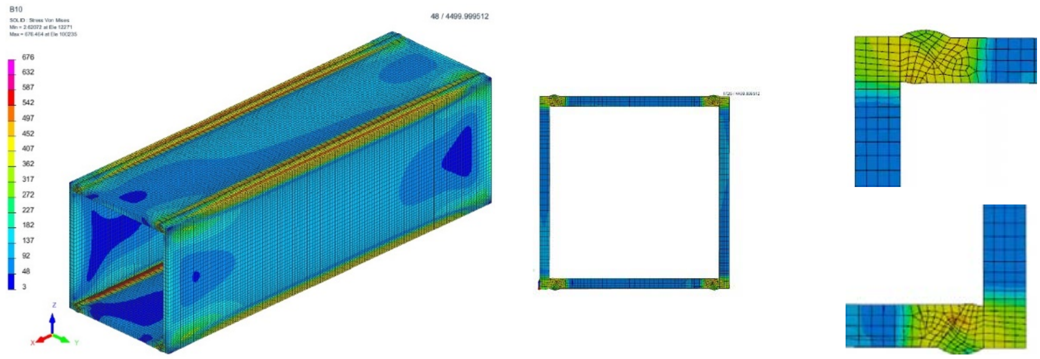

Figure 6.37 Contour plot of von mises residual stress after welding of Model S960-B1

The maximum residual stress is found to be located in the vicinity of the welding seams of the model, with a value of 676 MPa. Contour plots of the longitudinal residual stresses and transverse residual stresses are presented in Figure 6.38 and Figure 6.39, respectively.

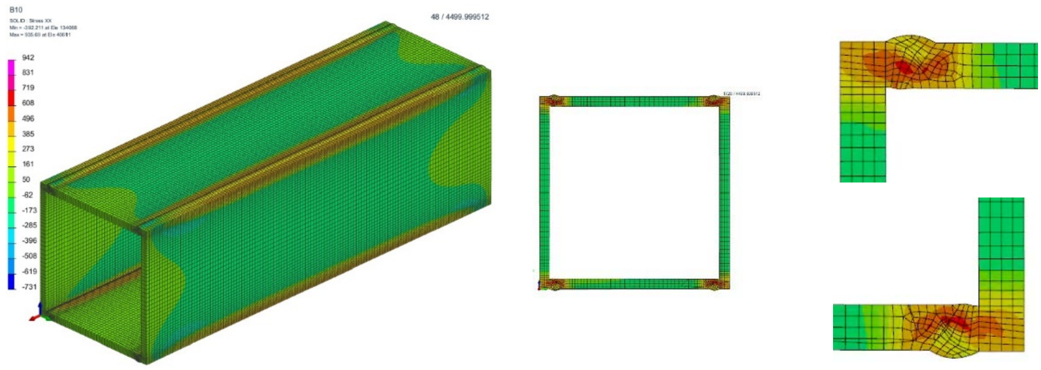

Figure 6.38 Contour plot of longitudinal residual stresses of Model S960-B1

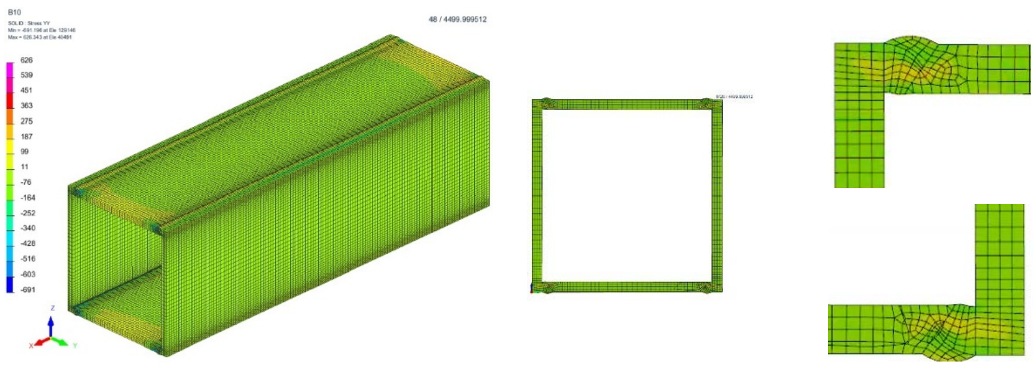

Figure 6.39 Contour plot of transverse residual stresses of Model S960-B1

The longitudinal residual stresses on the top surface of the top flange of Model S960-B1 are shown in Figure 6.38. The measured residual stresses presented in Chapter 5 are also plotted in the figure for a direct comparison, as shown in Figure 6.40. In the figure,

a_1, a_2, a_1', a_2' labels the location of the web plates. A similar comparison on those measured and predict of longitudinal residual stresses in the web plate of S960-B1 is provide in Figure 6.41. In the figure, a_1, a_2, a_3, a_1', a_2' , a_3' labels the location of the flange plates and butt welding sections.

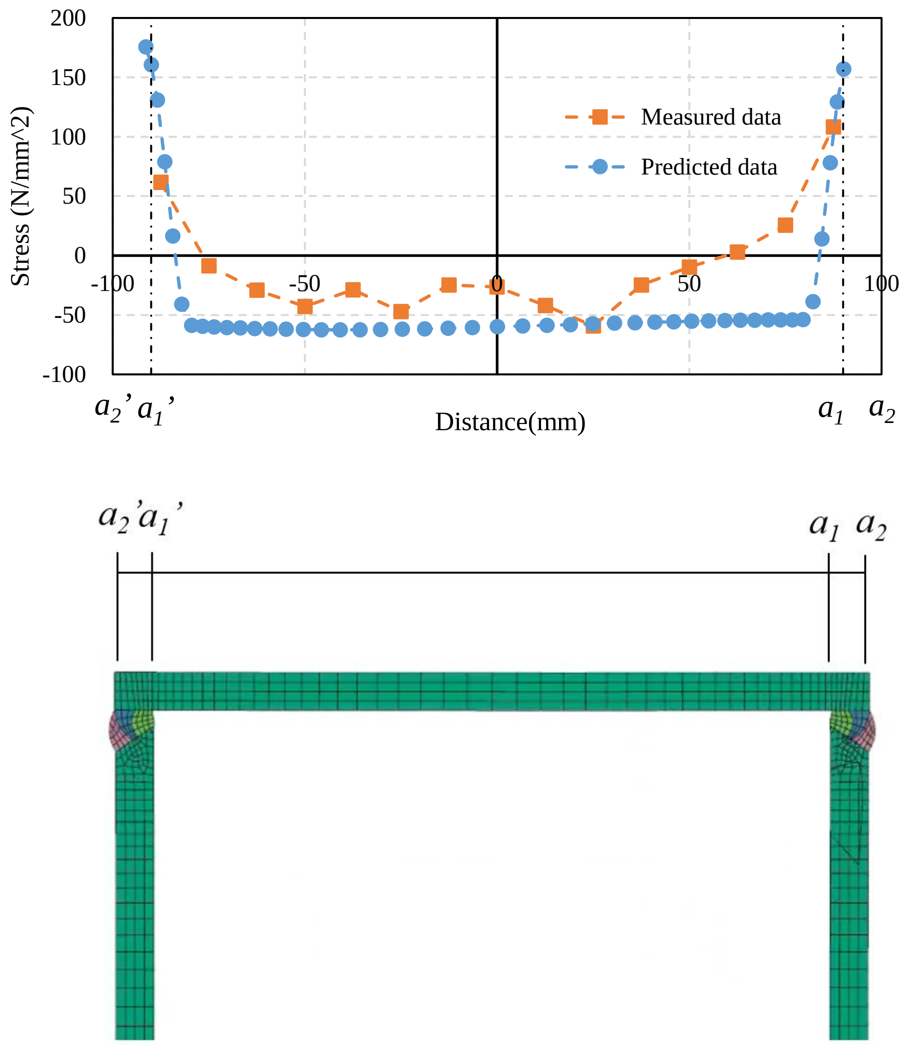

Figure 6.40 Comparison of predicted and measured residual stresses across the flange of Section S960-B1

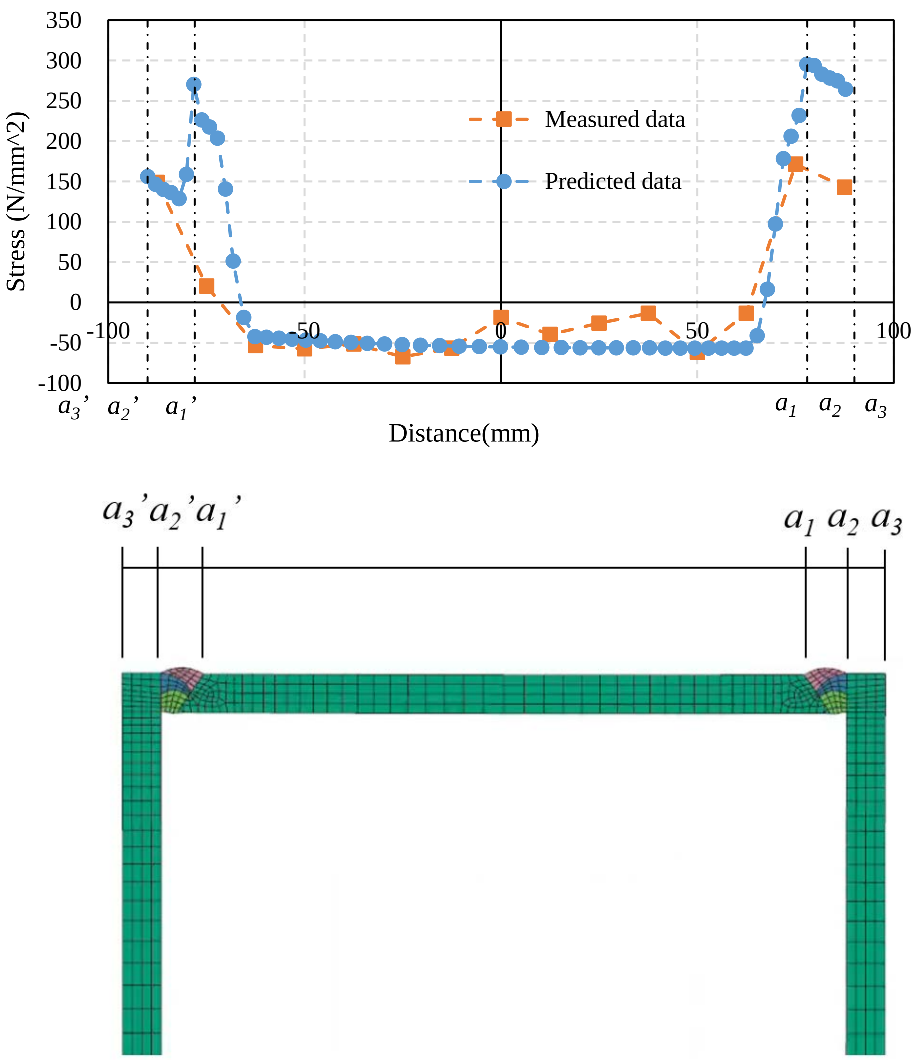

Figure 6.41 Comparison of predicted and measured residual stresses across the web of Section S960-B1

Therefore, a good comparison between the measured and the predicted longitudinal residual stresses in both the flanges and the web plate of Section S960-B1 is achieved.

4) Model S960-B2

For Model S960-B2, the Von Mises residual stress contour plot after welding is shown in Figure 6.42. The stresses illustrated in the figure are those of the final state, i.e., when both the welding and the cooling processes have been completed. To further illustrate the residual stresses, a cross-section view at the central part of Model S960-B2 is also shown.

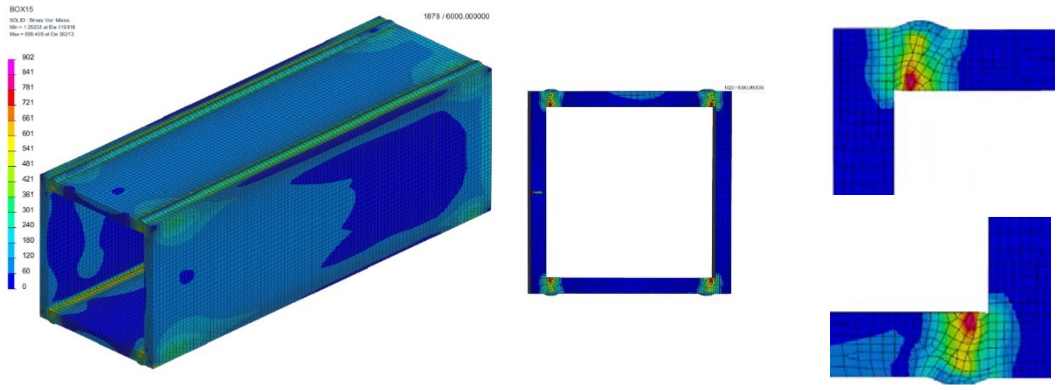

Figure 6.42 Contour plot of von mises residual stress after welding of Model S960-B2

The maximum residual stress is found to be located in the vicinity of the welding seams of the model, with a value of 902 MPa. Contour plots of the longitudinal residual stresses and transverse residual stresses are presented in Figure 6.43 and Figure 6.44, respectively.

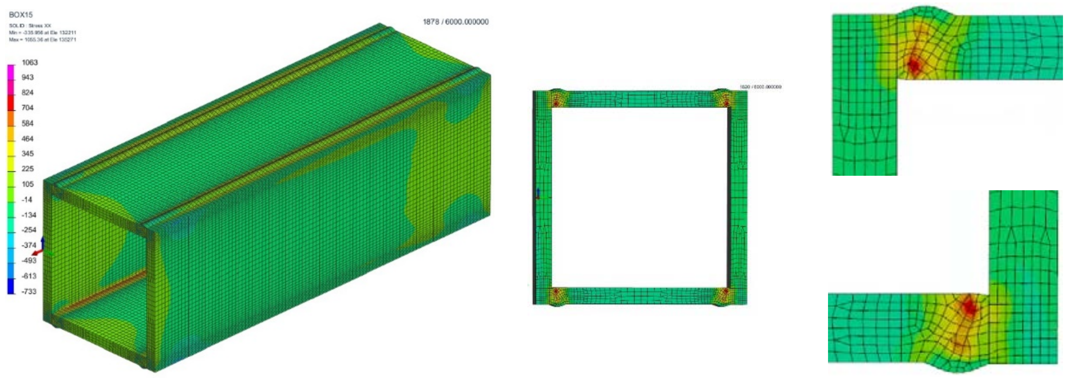

Figure 6.43 Contour plot of longitudinal residual stresses of Model S960-B2

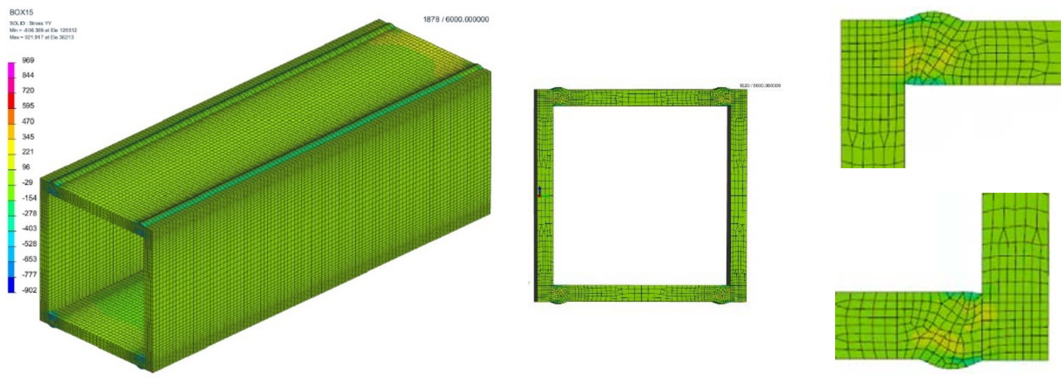

Figure 6.44 Contour plot of transverse residual stresses of Model S960-B2

The comparison of FEA results and measurement results on the midline of flange and web are shown in Figure 6.45 and Figure 6.46. In Figure 6.45, a_1, a_2, a_1', a_2' labels the location of the web plates. In Figure 6.46, a_1, a_2, a_3, a_1', a_2' , a_3' labels the location of the flange plates and butt welding sections. The residual stress distribution patten and values obtained from the finite element simulation are observed to be highly consistent with the experimental test results, both in the tensile and compressive stress regions.

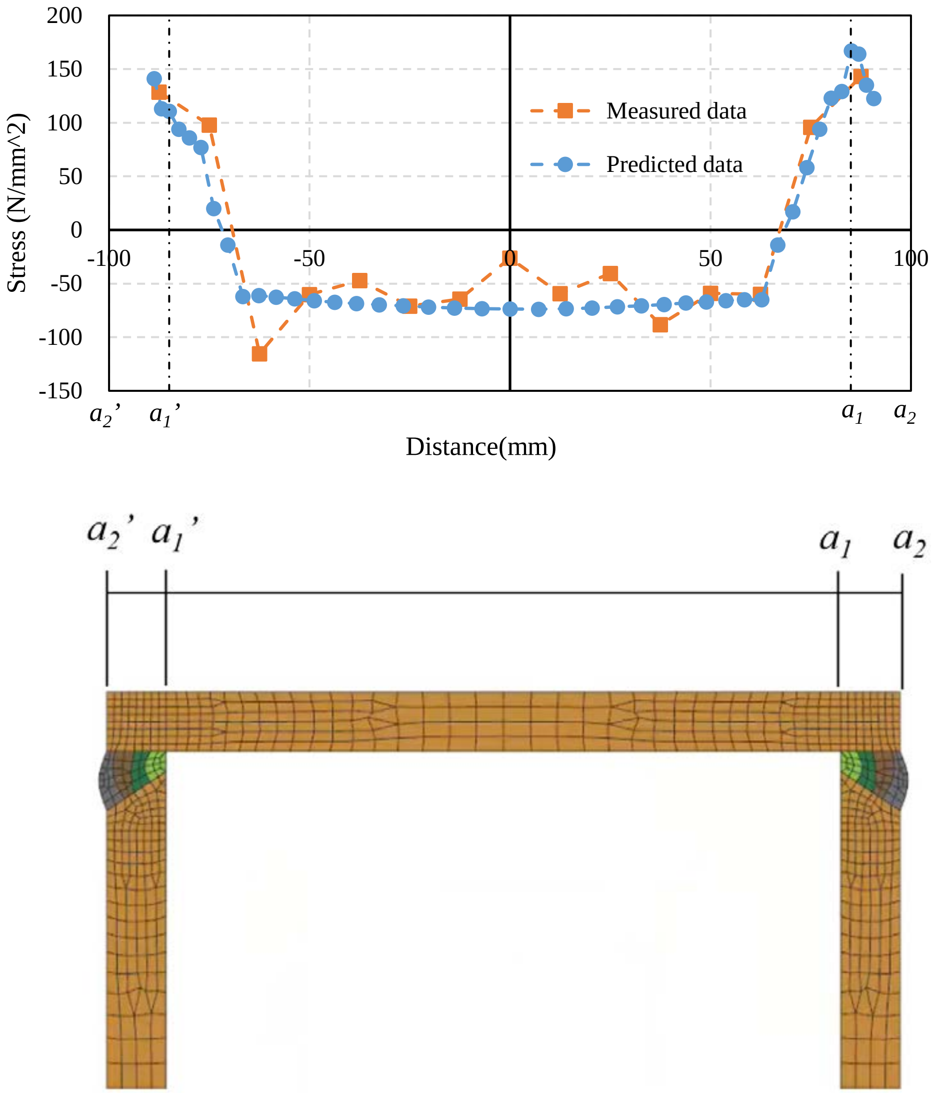

Figure 6.45 Comparison of predicted and measured residual stresses across the flange of Section S960-B2

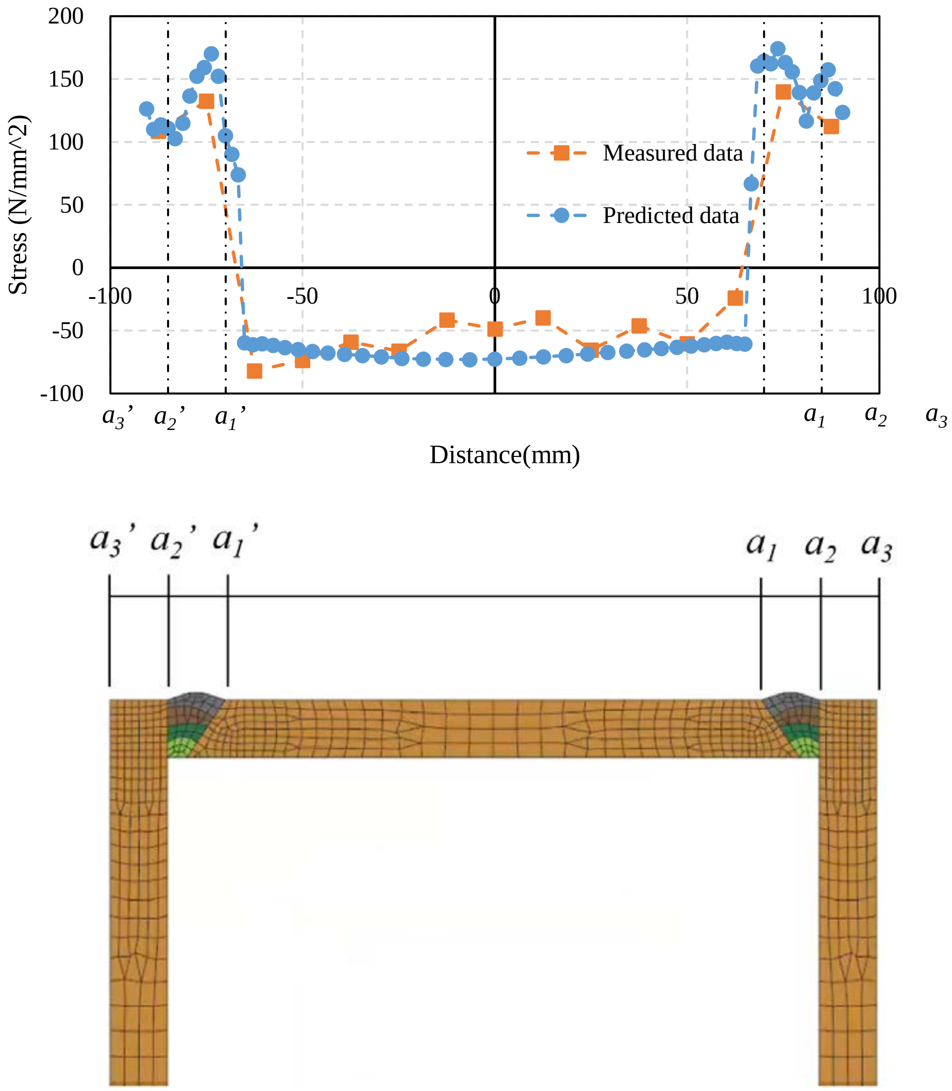

Figure 6.46 Comparison of predicted and measured residual stresses across the web of Section S960-B2

Therefore, a good comparison between the measured and the predicted longitudinal residual stresses in both the flanges and the web plate of Section S960-B2 is achieved. It should be noted that the welding simulations also consider the deformation of the cross-section in multi-pass welds, which is an important indicator in practical engineering applications.

6.5.4. Results of phase transformation

To validate the accuracy of the thermo-metallurgical analyses of the proposed welding model for S960 welded sections, an etching process was performed on these S960 welded sections. The specimens shown is the same one that was used to measure residual stresses reported in Chapter 5. In general, the images of the etched heat-affected zones provide valuable information, such as the boundaries of the heat-affected zones and the boundaries that differentiate the heat-affected zones from the weld metal and from the parent metal. Typical process for preparation of the heat-affected zone image of a welded section for etching is shown in Figure 6.47.

Figure 6.47 Cutting and etching of the heat-affected zones of a welded section

The process for preparation of images of etched heat-affected area involves the following steps:

1. Specimen preparation: A section of the welded section is cut by water jet, and then polished to obtain a smooth surface.
2. Etchant preparation: An appropriate etchant solution consisting of 4% nitric acid alcohol solution is prepared.
3. Etching: The polished specimen is immersed into the etchant solution for a specific duration between 10 and 20 seconds. It should be noted that the etchant solution attacks the microstructure of the specimen selectively, and thus reveals the different phases on the surface of the polished specimen.
4. Observation: The specimen is then rinsed with alcohol to stop the etching process and then dried with air. Considering possible corrosion of the specimen by air, the

etched surface of the specimen was immediately photographed.

It should be noted that the predicted phase transformation of the proposed welding simulation can be observed with the post-process Visual-Viewer. Figure 6.48 shows various degrees of phase transformation according to the thermo-metallurgical properties of those four models. From both the overall and the cross-sectional views of each model, it can be observed that after welding, the initial phase continues to exist in most parts of the S960 welded sections while all the heat-affected zones of the welded sections transform into various phases. As shown in the legends, the colour of various regions within the heat-affected zones vary from yellow, green, and blue. It should be noted that in the legend, the values vary from 1.00 to 0.00, indicate "the element retains the properties of the initial phase" to "the element is completely transformed into another phase".

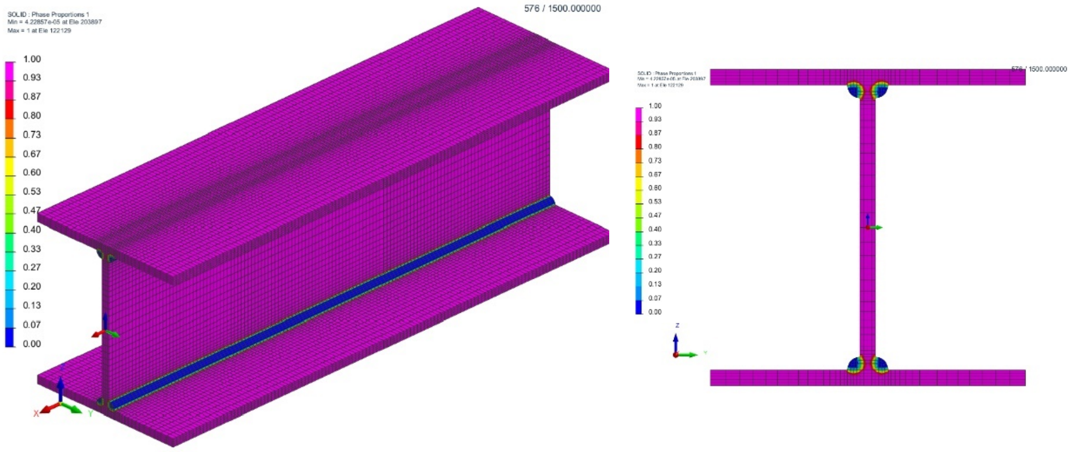

a) Model S960-H1

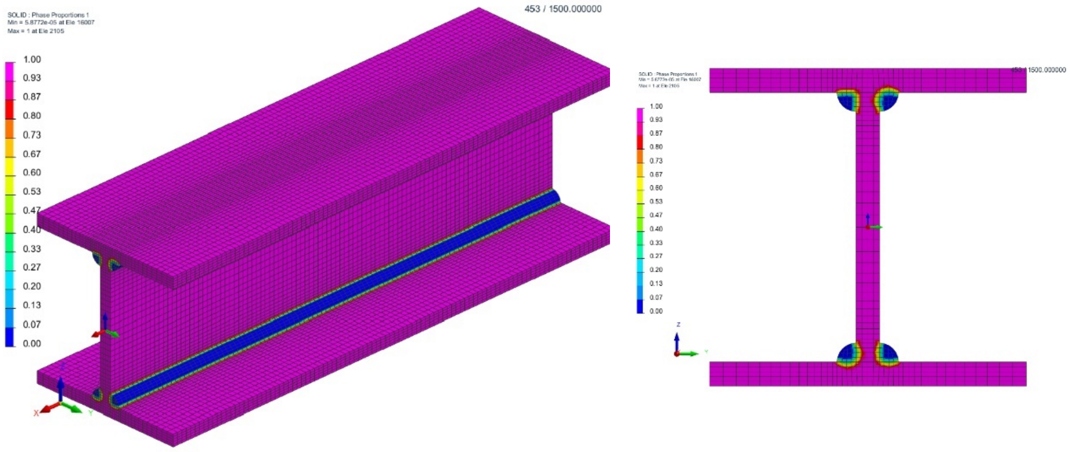

b) Model S960-H2

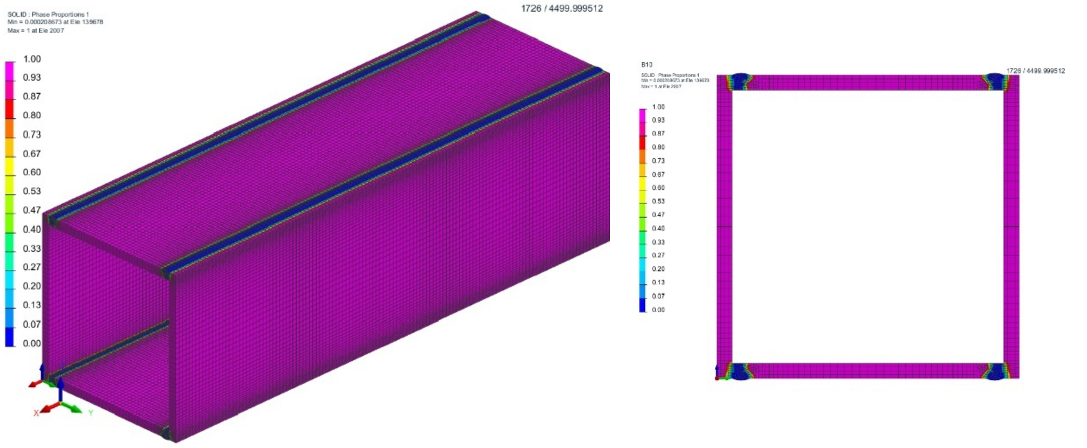

c) Model S960-B1

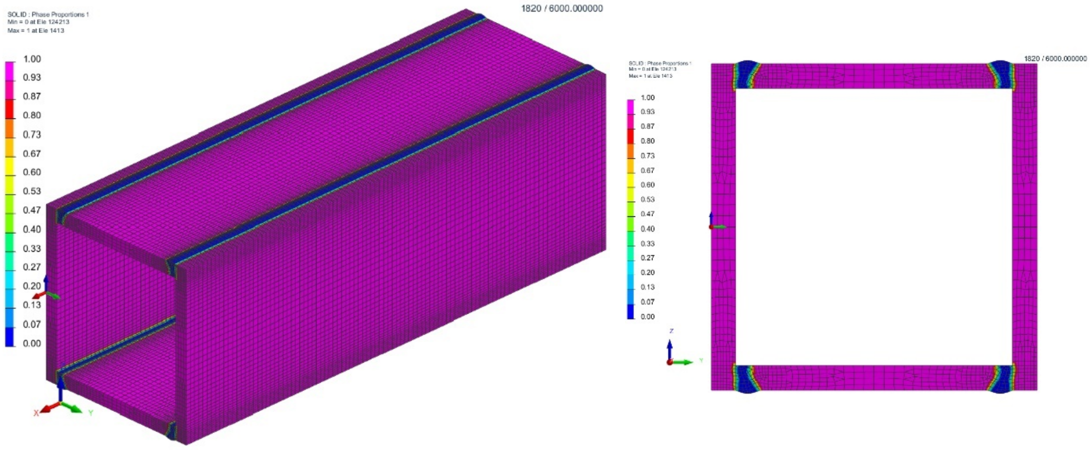

d) Model S960-B2

Figure 6.48 Phase transformation of S960 models

Comparison between the observed and the predicted images of microstructural changes of Section S960-H2 and S960-B2 is illustrated in Figure 6.49. Hence, whether in the single or the multi-pass welding, a good comparison on the pattern of the microstructural changes is evident.

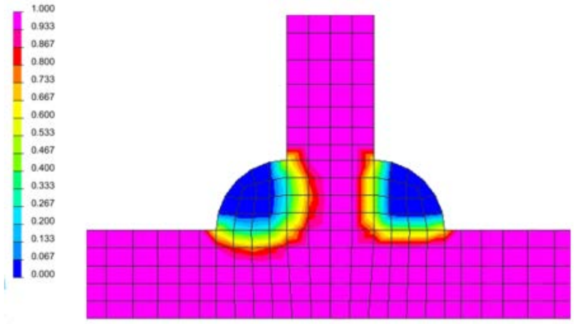

Section S960-H2
Observed heat-affected zone

Model S960-H2
Predicted heat-affected zone

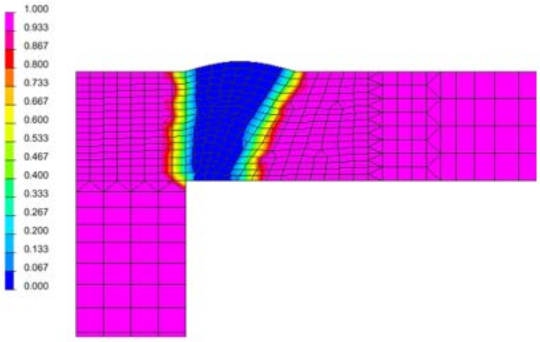

Section S960-B2
Observed heat-affected zone

Model S960-B2
Predicted heat-affected zone

Figure 6.49 Comparison on observed and predicted image of microstructural changes in heat-affected zones

It should be noted that since the HAZ of the welded corners are subjected to multiple cycles of heating and cooling, a number of phase transformations have taken place within the HAZ, leading to the formation of a relatively complex heterogeneous microstructure. A detailed illustration on typical phase transformation kinetic in the HAZ of Model S960-B1 is presented in Figure 6.50, and the development of various changes in phase proportions over time in a specific location near the fusion line are plotted together with the temperature changes over three weld passes. In the first and the second weld passes, the heat source moves along the weld seam which causes the temperature at this point to increase quickly, and then to decrease gradually. No significant phase transformation takes place in the steel as the heat source is far away, and its peak temperature does not exceed the critical temperature A_{c1}, i.e. 717°C.

However, in the third weld pass, the temperature at this point is found to be more than 1,000°C, exceeding the critical temperature A_{c3}, i.e. 875°C. Hence, phase change of the steel is initialized, transforming martensite to austenite. With a gradual decrease in temperature, the austenite proportion (or fraction) of the steel decreases, and then, it transforms into bainite. Hence, a complex heterogeneous microstructure with a total of 5 phases, including ferrite, bainite, austenite, tempered martensite, martensite, each with various proportions (or volumetric fractions), is formed within the HAZ after welding.

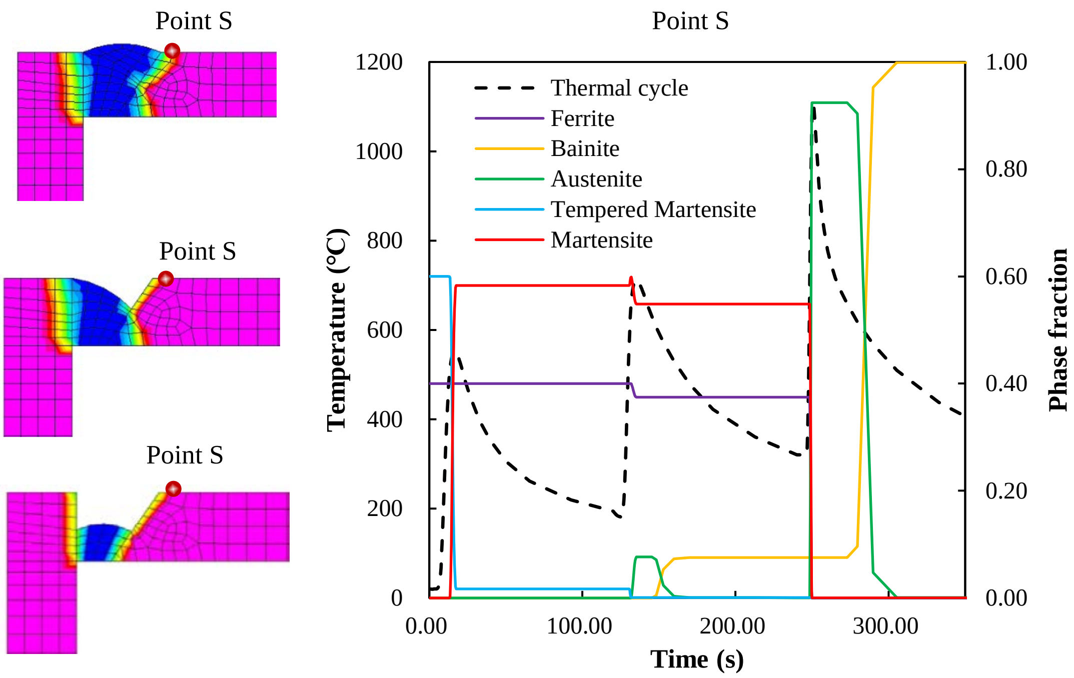

Figure 6.50 Temperature cycle and volume fractions of various phases during welding

The thermo-mechanical-metallurgical model presented in this chapter shown to be able to simulate the welding process of these high strength steel effectively. The results presented a) the transient temperature fields predicted by the models match the measured data very well; b) the residual stress distributions on both the flange and web plates of the welded section also match the measured data; c) various degrees of phase transformation predicted by the model match the observed images of etched heat-affected zones well. Consequently, the proposed finite element modelling approach is successfully demonstrated to have a high accuracy in predicting the thermo-mechanical-metallurgical behaviour of these high strength steel during welding.

In Chapter 7, the above validated models are employed to simulate the structural performance of various welded sections of these high strength steel under axial compression.

CHAPTER SEVEN

NUMERICAL MODELLING ON STRUCTURAL BEHAVIOUR OF S690 AND S960 STOCKY COLUMNS UNDER COMPRESSION CONSIDERING PHASE TRANSFORMATION

7.1. Introduction

In this chapter, an advanced numerical simulation approach, namely, the "***Thermal-Metallurgical-Mechanical-Structural***' approach, or the TMMS approach, is presented which is able to simulate the effects of welding on the structural behaviour of the S690 and the S960 welded sections considering phase transformation. The approach is an extension of the *integrated and coordinated advanced numerical simulation* approach, or the ICANS approach, which is developed collectively by Liu *et al.* (Liu 2018), Hu *et al.* (Hu 2019), and Xiao *et al.* (Xiao 2021) at CNERC. It should be noted that no phase transformation is considered in the ICANS approach as it is developed primarily for those high strength S690 welded sections with a proper control of the heat input energy during welding.

The TMMS approach is adopted to model the structural behaviour of two S690 and S960 welded sections under compression. Detailed descriptions on both the finite element modelling technique and the material definitions are provided, and comparisons on the predicted and the measured data are presented in a comprehensive manner.

7.2. Integrated and coordinated numerical simulations approach

In recent years, significant advancement has been made in advanced numerical simulations of two main fabrication processes for steel structures, i.e., i) welding, and

ii) cold-forming through the development of integrated and coordinated advanced numerical simulation approach. According to Liu *et al.* (Liu 2018), Hu *et al.* (Hu 2019), and Xiao *et al.* (Xiao 2021), an overview of the ICANS approach is illustrated in Figure 7.1. The ICANS approach is able to simulate the entire fabrication process of welded steel sections through i) *heat transfer analysis* to determine transient temperature history, ii) *thermomechanical analysis* to determine "locked-in" or residual stresses and strains, and iii) *structural analysis* to determine deformation characteristic under specific loading and support conditions.

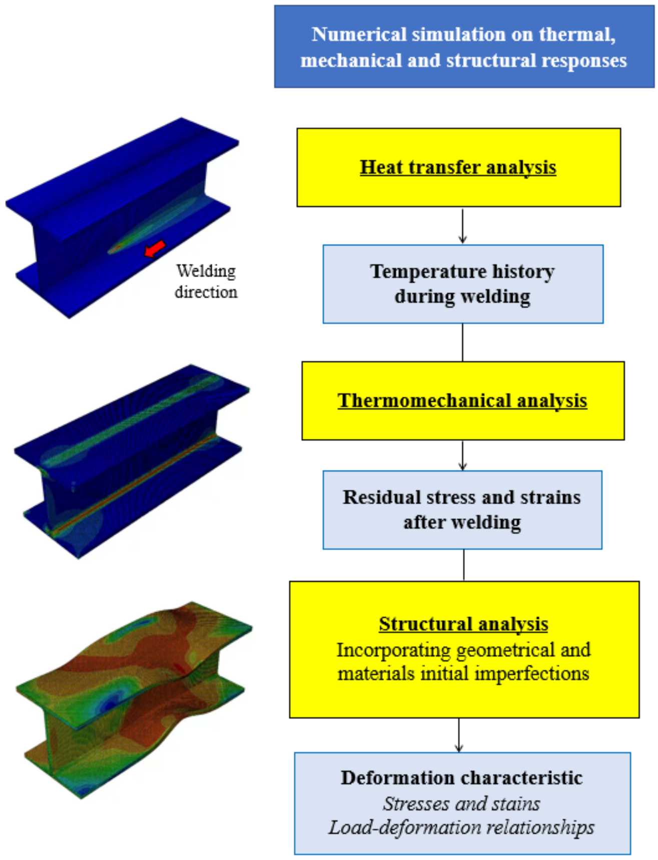

Figure 7.1 An overview on integrated and coordinated numerical simulation approach

Based on the experimental data on compression tests on the S690 and S960 welded steel sections presented in Chapter 4, the following two welded H-sections were selected for demonstration of the proposed approach, as shown in Figure 7.2 and Table 7-1.

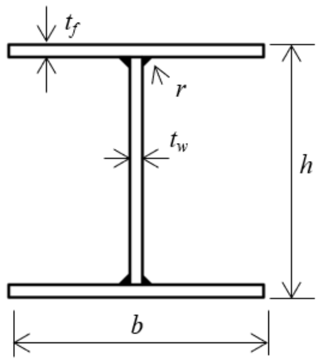

Figure 7.2 Dimensions of welded H-sections

Table 7-1 Measured dimensions of welded H-sections

Model	b (mm)	h (mm)	t_f (mm)	t_w (mm)	r (mm)
S690-A	199.7	200.8	9.93	15.98	9.8
S960-A	198.1	200.4	15.01	15.10	8.0

Hence, two advanced finite element models were established accordingly, and they are referred as Models S690 and S960 in order to demonstrate the effects of welding onto the structural performance of these high strength steel welded sections under compression.

7.3. Modelling to ICANS approach

Three-dimensional solid elements were employed in both the flanges and the web plates of these Models. In order to ensure high numerical accuracy and computational efficiency, a total of four solid elements were provided across the thicknesses of both the flanges and the web plates in the vicinity of the flange/web junctions with local mesh refinement. Hence, the finite element meshes of these two models are shown in Figure 7.3.

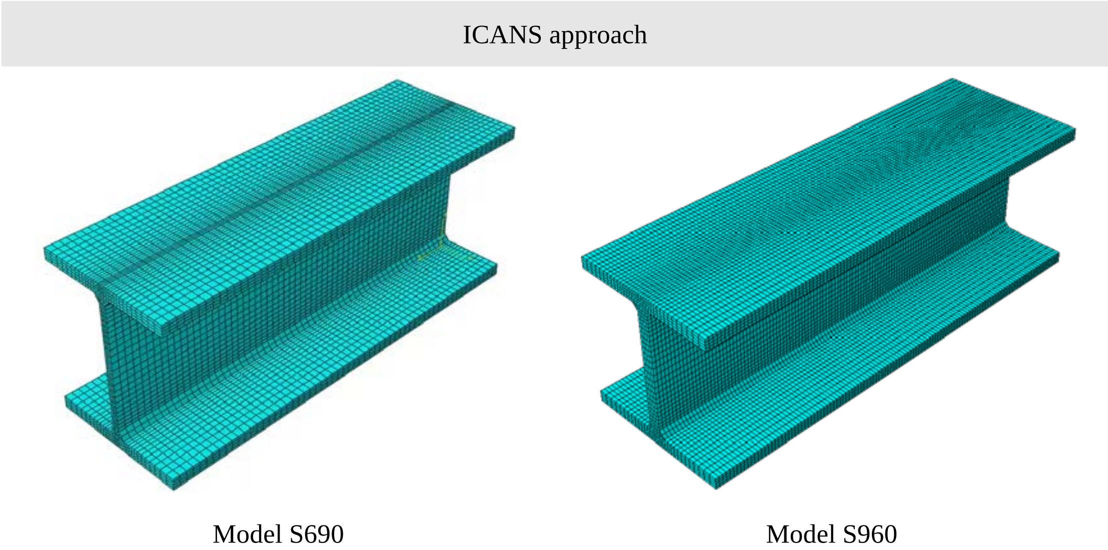

Figure 7.3 Finite element meshes of Models S690 and S960 with local mesh refinement

It should be noted that solid elements with a triangular cross-section are adopted as fillet welds along the flange/web junctions as these two sections were fabricated with single-pass fillet welding.

7.3.1. Simulation of heat transfer

In these Models, the double ellipsoidal model presented by Goldak *et al.* (Goldak *et al.*, 1984) as the heat source as shown in Figure 7.4.

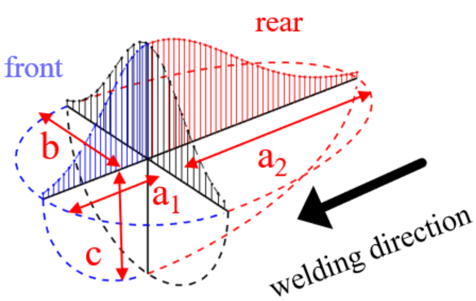

Figure 7.4 The double ellipsoidal model as a moving heat source

It should be noted that the values of various parameters are dependent on the welding methods and the corresponding heat input energy during welding, which in turn define the dimensions of the weld pool. After a careful calibration against measured data, the parameters of the heat source model are summarized in Table 7-2.

Table 7-2 Typical parameters of double ellipsoidal model

Model	a_1 (mm)	a_2 (mm)	b (mm)	c (mm)	U (V)	I (A)
S690-A	8	10	5	10	25	300
S960-A	7.5	10	4	10	25	300

The predicted transient temperature history of these thermal analyses are presented in Section 7.5. Boundary conditions of these thermal analyses are simplified based on actual welding boundary conditions, as presented in Figure 6.7.

7.3.2. Simulation of thermomechanical responses

Another sets of three dimensional models were established to simulate thermomechanical responses of the sections during welding, i.e., the heating up stage, and then after welding, i.e. the cooling down stage. Based on the predicted transient temperature history obtained above, these temperature history are incorporated into the newly developed Models so that both expansion and contraction throughout the Models are predicted accordingly. Owing to differential cooling, there are differential contraction within these Models, leading to the presence of "locked-in" strains as well stresses after welding.

The thermo-mechanical properties of both the S690 and the S960 steel, i.e., the thermal conductivity, the specific heat capacity, and the coefficient of thermal expansion, given in EN1993-1-2 are adopted in these Models, and their variations against temperature up to 1,800°C are plotted in Figure 7.5. It should be noted that the convective stirring effect of fluid flow in the molten zone is modelled with a simplistic method, i.e., the use of an amplified thermal conductivity when the temperature exceeds the melting point of the steel. This method adopts the use of an effective heat conductivity due to thermo-capillary flow, which commonly known as the Marangoni effect (Lee and Chang 2011). Therefore, during the simulation of the S690 and the S960 steel at their melting point and above, the value of the thermal conductivity is increased with a factor of 5 from its at room temperature after calibration between predicted and measured temperatures.

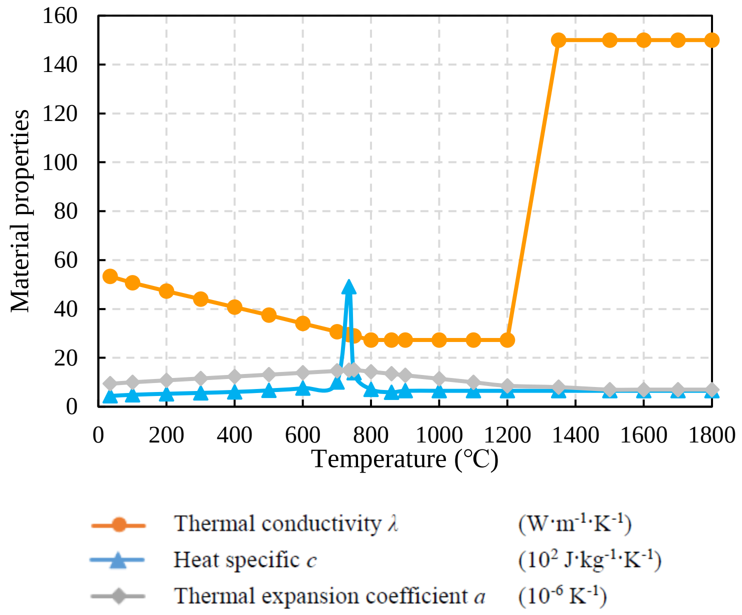

Figure 7.5 Temperature depended thermal material properties of S690 and S960

In addition, a true stress-strain curve for each of the S690 and the S960 steel, derived from test data of standard tensile tests, is plotted in Figure 7.6, and these two curves are adopted as the respective constitutive models of the steel.

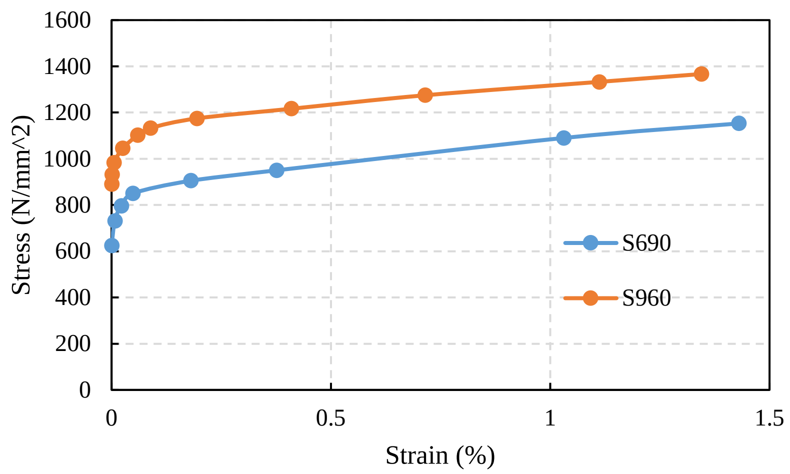

Figure 7.6 True stress-strain curves of S690 and S960 steel derived from test data

It is also important to consider the reductions in mechanical properties of both the S690 and the S960 steel at elevated temperatures, such as yield strength and Young's modulus. Reduction factors for various mechanical properties of the steel are given in EN1993-1-2, and these reduction factors for both the yield strength and the Young's modulus are plotted in Figure 7.7.

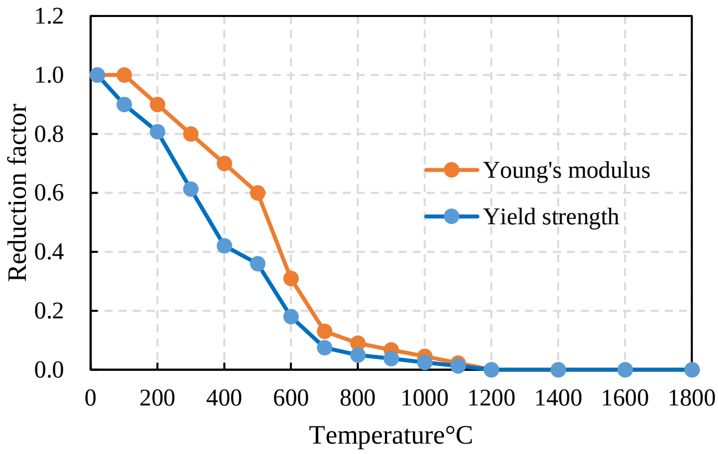

Figure 7.7 Reduction factors to mechanical properties at elevated temperatures in EC3:1-2

For simplicity, both Figure 7.6 and Figure 7.7 are assumed to be applicable to the weld metal in these analyses. Hence, the residual stresses and strains are determined with the reduced mechanical properties at various temperatures in an accumulative manner during cooling.

The predicted residual stresses of these thermomechanical analyses are presented in Section 7.5.

7.3.3. Simulation of structural responses

In order to simulate the structural responses of these welded H-sections, the third sets of three-dimensional models were established to perform material and geometrical non-linear analyses to determine their deformation characteristics with a full incorporation of welding-induced residual stresses and strains. Hence, all the residual stresses and strains obtained from the thermomechanical analyses mentioned above are included in the models as initial material imperfections. In addition, linear eigenvalue analyses are conducted under relevant loading and support condition, and the eigenmode corresponding to the lowest eigenvalue is selected to be the initial geometrical imperfection of the Models. The magnitude of the maximum out-of-straightness of the initial geometrical imperfection of the Models are assigned to be 1/500 of the nominal flange widths of these welded H-sections, i.e., 0.4 mm in both Models.

The support conditions of the models are implemented as follows:

- At the bottom end of the Models, all the translational displacements u_x, u_y, u_z and all the rotational displacements θ_x, θ_y, θ_z of the elements are assigned to be zero.
- At the top end of the Models, the translational displacements u_y, u_z, and the rotational displacements θ_x, θ_y, θ_z are assigned to be zero while the translational displacement u_x is selected as the control for load application during the non-linear analyses.

Figure 7.8 illustrates typical support condition of the Models. It should be noted that for ease of modelling, two reference points, namely, Points RP-1 and RP-2, are established so that all degrees of freedom of all the nodes at both the top and the bottom ends of the models are linked up together to satisfy the support conditions mentioned above.

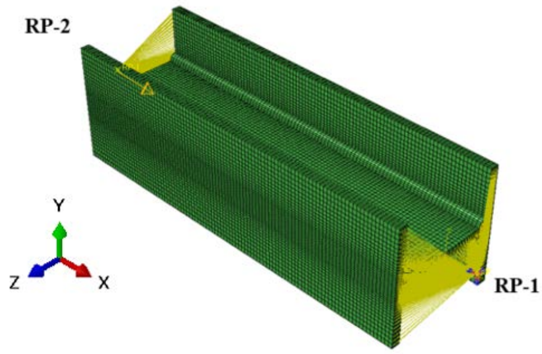

Figure 7.8 Support condition of the Models

The predicted residual stresses of these thermomechanical analyses are presented in Section 7.5.

7.4. Thermo-Mechanical-Metallurgical-Structural approach

The TMMS approach is an advanced numerical simulation method based on the ICANS approach with an important additional capability – phase transformation. Owing to the exposure of high transient temperatures caused by welding, *phase transformation*, *recrystallization* and *grain growth* may take place within the heat affected zones of the welded sections of both the S690 and the S960 steel. Refer to Chapter 6 for detailed description on the microstructural evolution within the heat affected zones. It should be noted that an additional procedure on metallurgical responses is incorporated as shown in Figure 7.9, that the thermos-metallurgical analyses should be performed straight after completion of the thermal analyses, i.e. once the transient temperature history within the heat affected zones of the welded sections is known..

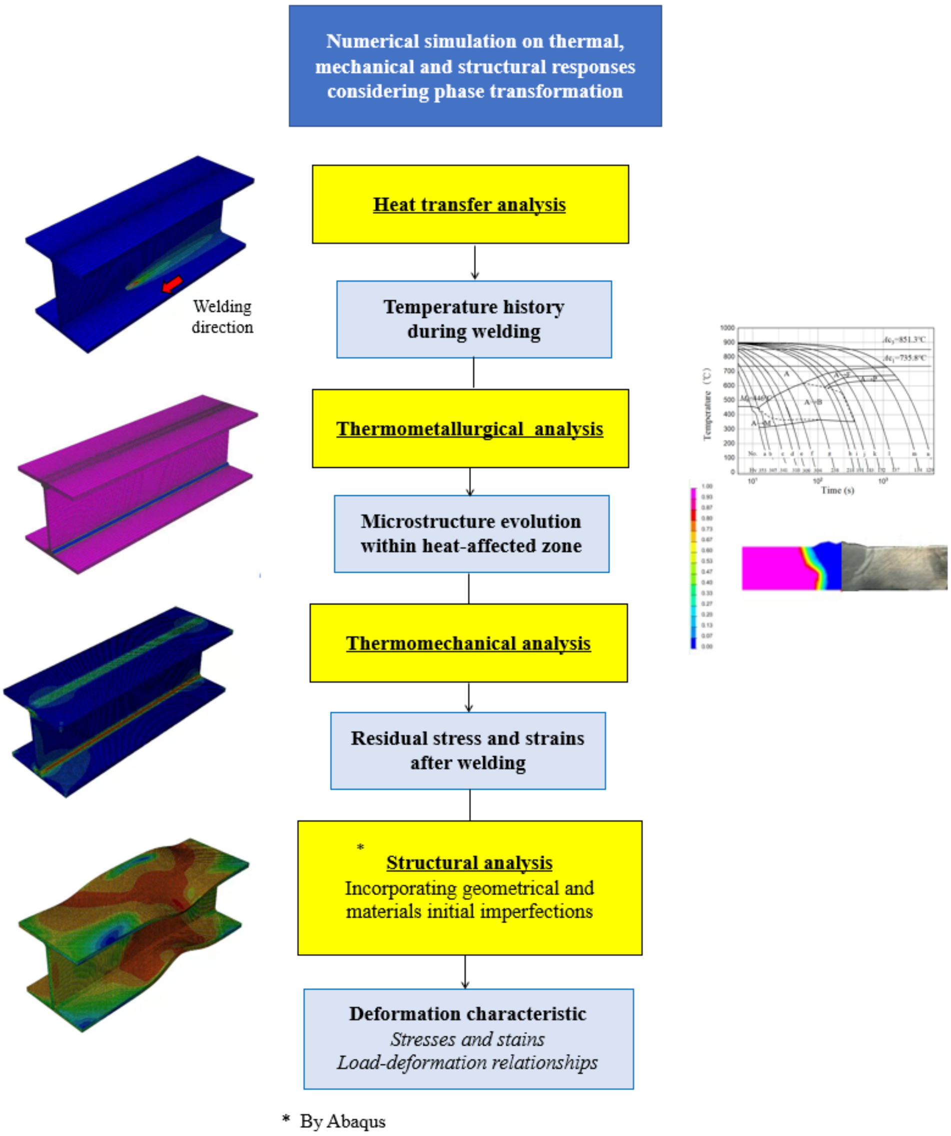

Figure 7.9 An overview on TMMS simulation approach

Based on the transient temperature history, phase transformation is determined to predict occurrence of microstructural changes within the heat affected zones, if any, and hence, provide the modified mechanical properties of these elements through generation of different material sets. Hence, based on the modified mechanical properties of those elements within the heat affected zones, thermomechanical analyses are then performed to determine the welding-induced residual stresses within the welded sections accordingly. All of these numerical results are then transferred into another structural models to determine their structural responses.

For details of the metallurgical analyses of the S690 and S960 steel under the effects of welding, refer to Chapter 6. For detailed formulation of the continuous cooling transformation curves of the S690 and the S960 steel, refer to Appendix A.

7.4.1. Finite element meshes

Figure 7.10 illustrates the finite element meshes of both models. It should be noted that these two models were established according to the section dimensions given in Table 7-1. These meshes are similar to those illustrated in Figure 7.3.

TMMS approach

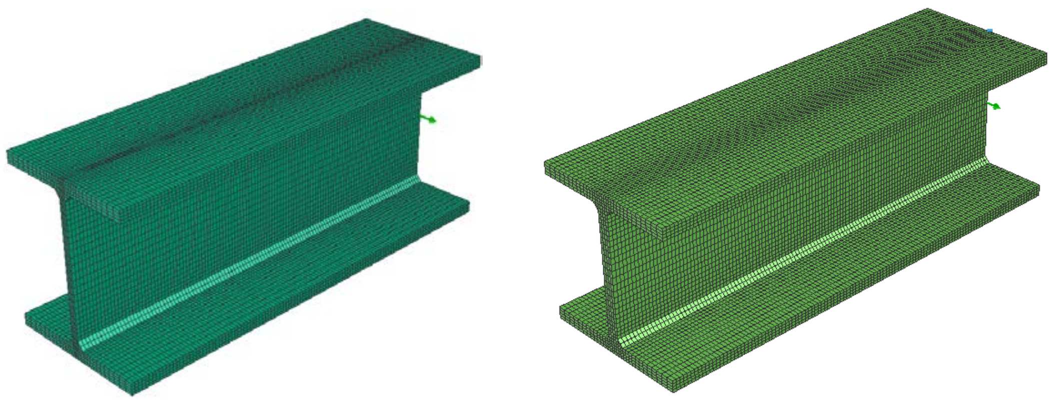

Model S690 Model S960

Figure 7.10 Finite element models of both Sections in SYSWELD

7.4.2. Modified mechanical properties

Based on the transient temperature history of the two models predicted by the thermal analyses, the thermo-metallurgical analyses on these Models were performed in SYSWELD. It should be noted that owing to possible phase transformation within the heat affected zones, the mechanical properties of some of those elements within the heat affected zones should be modified accordingly. Hence, new material definitions are created, and the corresponding mechanical properties are assigned to these elements according to the results of the thermo-metallurgical analyses. Figure 7.11 illustrates typical predicted distribution of various phases of the steel in the vicinity of the flange/web junctions of the two Models. It should be noted that the spectrum of colour illustrates the extent of phase transformation after welding.

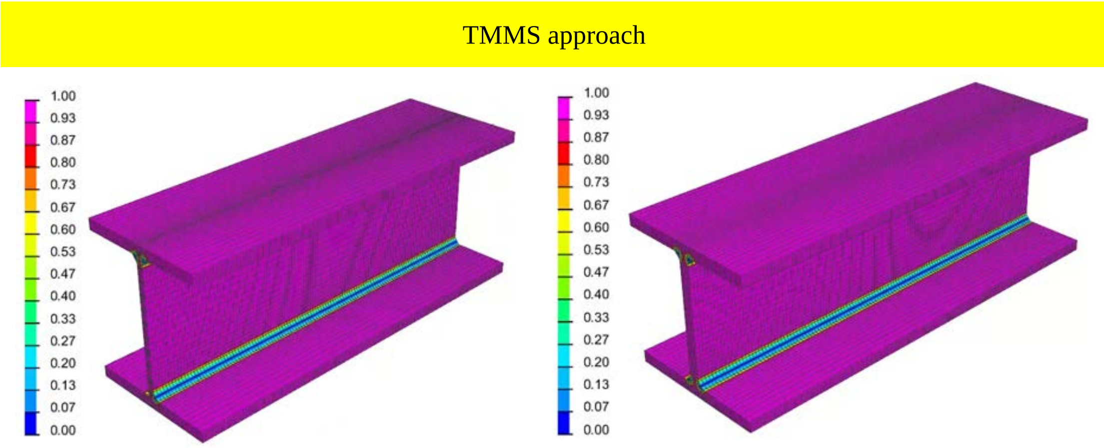

Model S690 Model S960

Figure 7.11 Extent of phase transformation in the vicinity of the heat affected zones of both Sections in SYSWELD

Owing to the occurrence of phase transformation, a total of 10 to 20 different material sets will be established according to the thermo-metallurgical analyses. All of these data will then be transferred into another Models for subsequent structural analyses.

It should be noted that owing to phase transformation and reduction of mechanical properties in the vicinity of the heat affected zones of the welded sections, large locked-in strains, i.e., residual plastic strains, are induced. Through the modified mechanical properties, the residual stresses are readily obtained. In those regions where large residual stresses are present, they will contribute to initiation and propagation of plastic deformations. These plastic strains will also affect the distributions of residual stresses, and hence, the sizes and shapes of “yield zones”. Hence, it is essential to transfer these plastic strains obtained in SYSWELD to Abaqus as initial material imperfection for subsequent analyses.

7.5. Numerical simulation results of H-sections

This section presents the results of the proposed TMMS through modelling the structural behaviour of both Sections S690 and S960, and the thermal, the metallurgical, the mechanical and the structural responses of these two welded sections are presented in detail. It should be noted that comparisons with those results obtained with the ICANS approach are also provided, whenever available, in order to demonstrate the importance of considering phase transformation in these advanced numerical simulations.

7.5.1. Maximum transient temperatures

Figure 7.12 illustrates the maximum transient temperature distributions at the flange / web junctions of Models S690 and S960 obtained with both approaches for comparison.

TMMS approach with SYSWELD

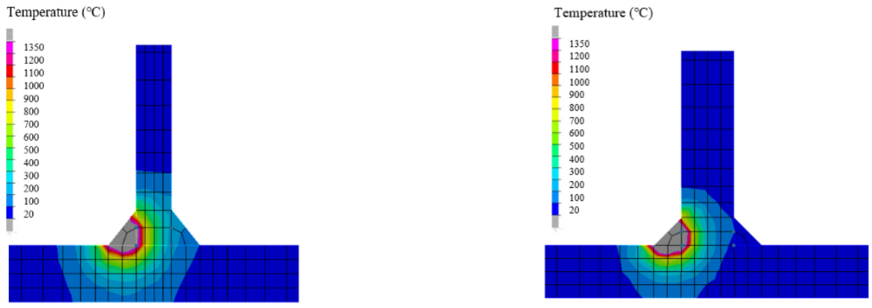

Model S690 | Model S960

ICANS approach with Abaqus

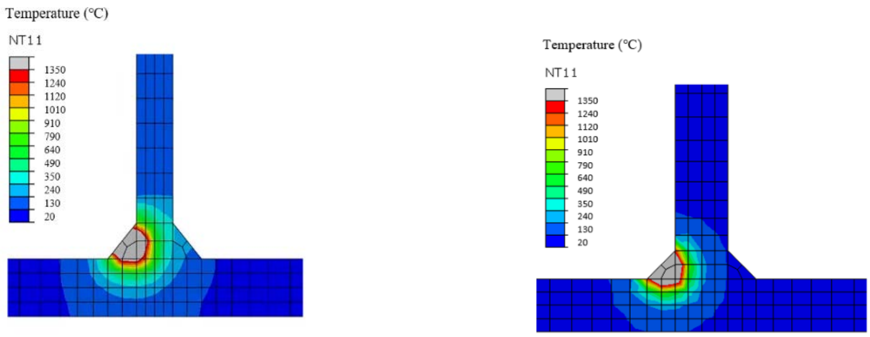

Model S690 | Model S960

Figure 7.12 Transient temperature distributions at flange-web junctions of both Models

As the same heat source model is adopted in both approaches, a notable similarity is observed in these distributions. It should be noted that compatibility of the sizes of the welding pool in all four models with the actual welding conditions is found to validate accuracy of the heat source model.

In order to examine transient temperatures predicted by the proposed approach, a specific monitoring point at the central position of the top flange at the mid-length of the Models is selected, and the predicted temperatures at this point of these Models are plotted in Figure 7.13 and 7.14.

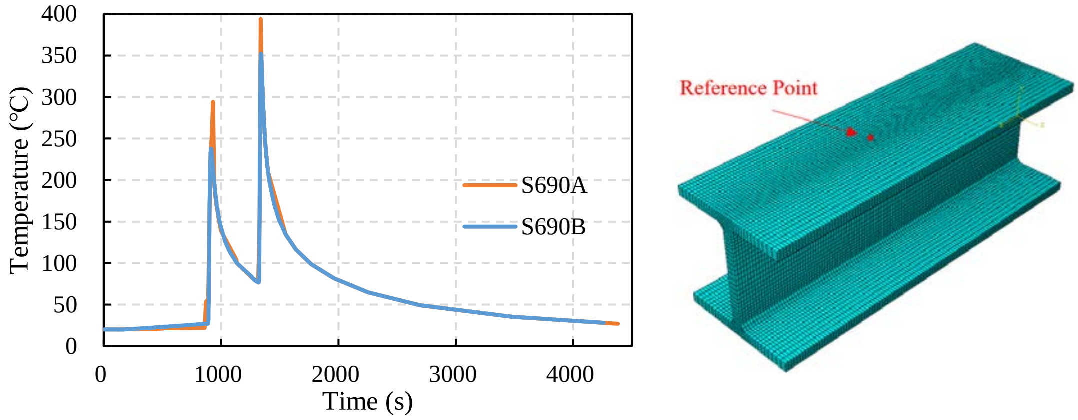

Figure 7.13 Transient temperature history at a reference point of Model S690

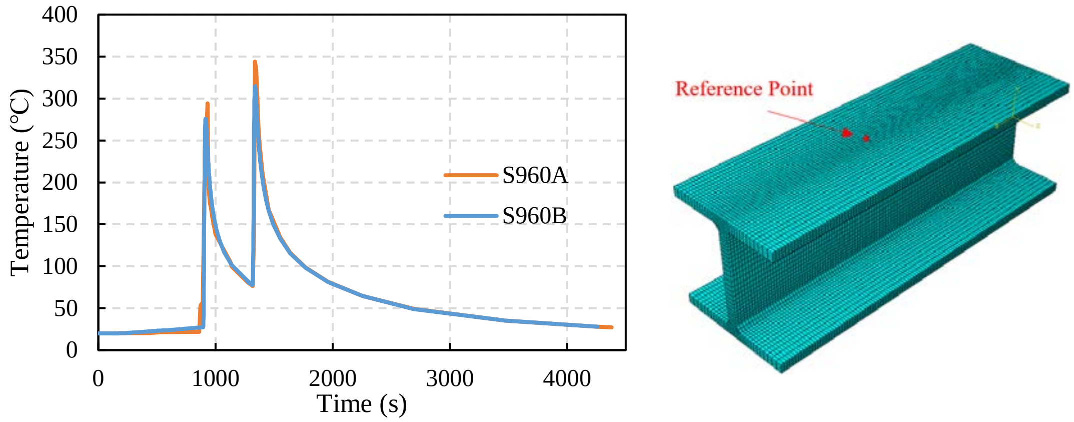

Figure 7.14 Transient temperature history at a reference point of Model S960

Regardless of considering phase transformation or not, the transient temperature history at the monitoring point for both Models S690 and S960 are shown to agree with each other closely along the entire time range. These are due to the use of the same heat source model as well as the same set of material properties of the steel at elevated temperatures.

7.5.2. Phase transformation after welding

Figure 7.15 illustrates the modified distribution of phases in the flange/web junctions of Models S690 and S960 obtained with the TMMS approach. As shown in the legends, the colour of various regions within the heat-affected zones vary from yellow, green, and blue. It should be noted that in the legend, the values vary from 1.00 to 0.00, indicate "the element retains the properties of the phase of parent metal" to "the element is completely transformed into another phase".

TMMS approach with SYSWELD

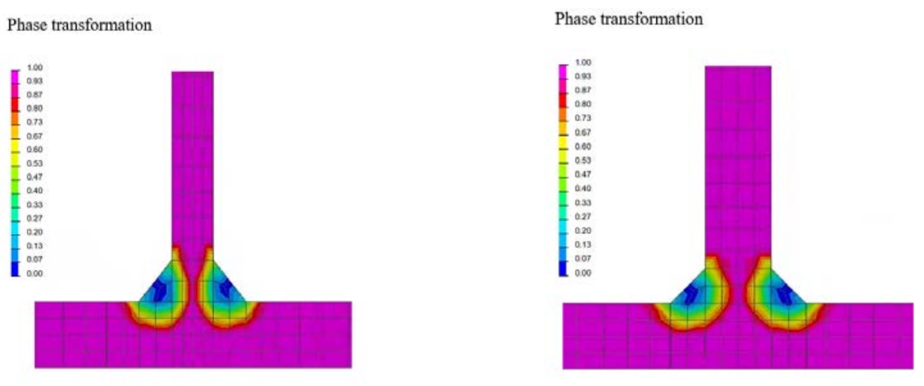

Model S690 Model S960

Figure 7.15 Modified distribution of phases in the flange/web junctions of both Models after transformation due to welding

It is shown that significant phase transformation occurs within the heat affected zones of the flange/web junctions of these Models. Owing to the limited areas with modified mechanical properties, the effect of phase transformation is expected to have only minimal impact onto the structural behaviour of these welded sections.

7.5.3. Residual stresses after welding

Figure 7.16 illustrates the contour plots of the predicted residual stresses in the format of von Mises stresses at the flange/web junctions of the models obtained with both the TMMS and the ICANS approaches for comparison.

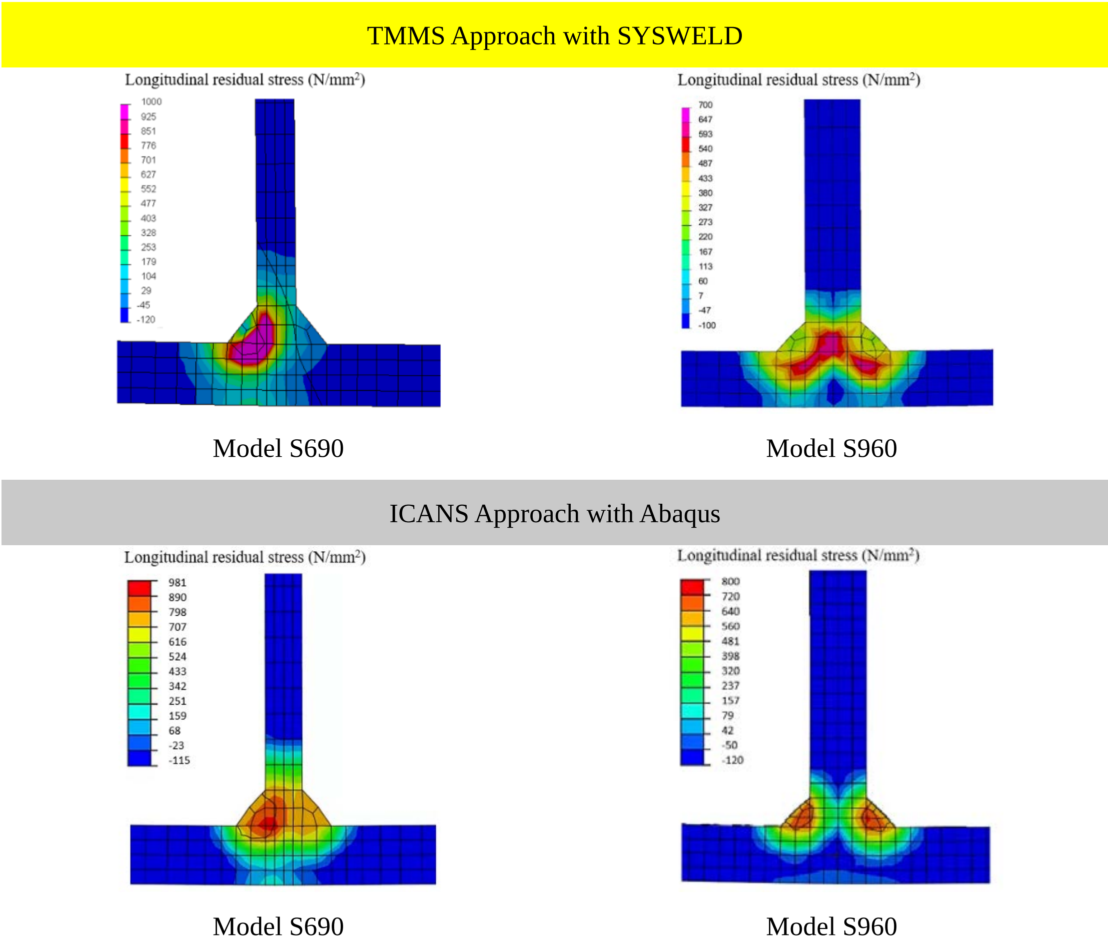

Figure 7.16　Typical residual stress distributions at flange/web junctions of both Models

It is shown that the residual stress distributions obtained with SYSWELD are smaller in both magnitude and size when compared with those obtained with Abaqus.

In order to examine the residual stresses predicted by the proposed approach, the surface residual stresses along the width of the top flange at the mid-length of the Models are plotted in Figure 7.17 and 7.18.

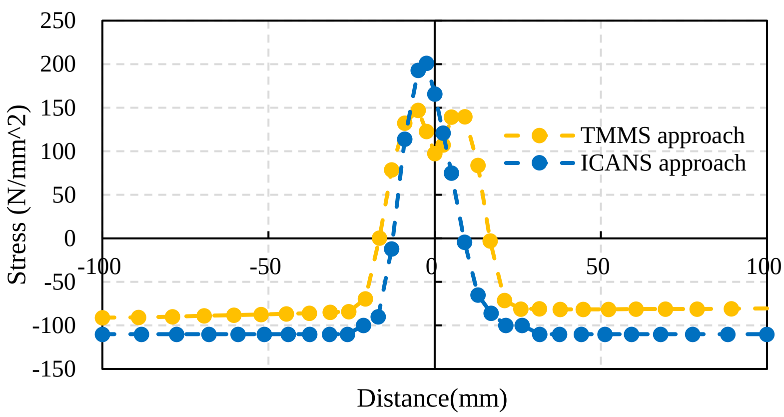

Figure 7.17　Comparison of surface residual stress distributions of Model S690

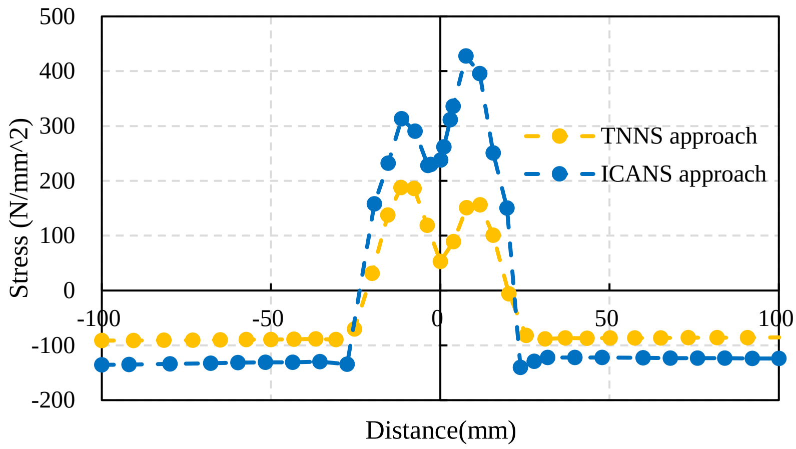

Figure 7.18 Comparison of surface residual stress distributions of Model S960

It is shown that the surface residual stresses obtained with SYSWELD are significantly smaller than those obtained with Abaqus. For Model S690, the tensile residual stresses near the flange/web junction calculated through TMMS is 25% smaller than the value calculated through ICANS, while the compression residual stresses at the top surface of flange is 26% smaller than the value calculated through ICANS. For Model S960, the tensile residual stresses near the flange/web junction calculated through TMMS is 56% smaller than the value calculated through ICANS, while the compression residual stresses at the top surface of flange is 31% smaller than the value calculated through ICANS.

Hence, the incorporation of phase transformation in these advanced numerical simulations is able to provide accurate prediction to the effects of welding onto the structural behaviour of these S690 and S960 welded H-sections.

7.5.4. Structural responses

Figure 7.19 illustrates the deformed meshes of the Models at large deformations for comparison.

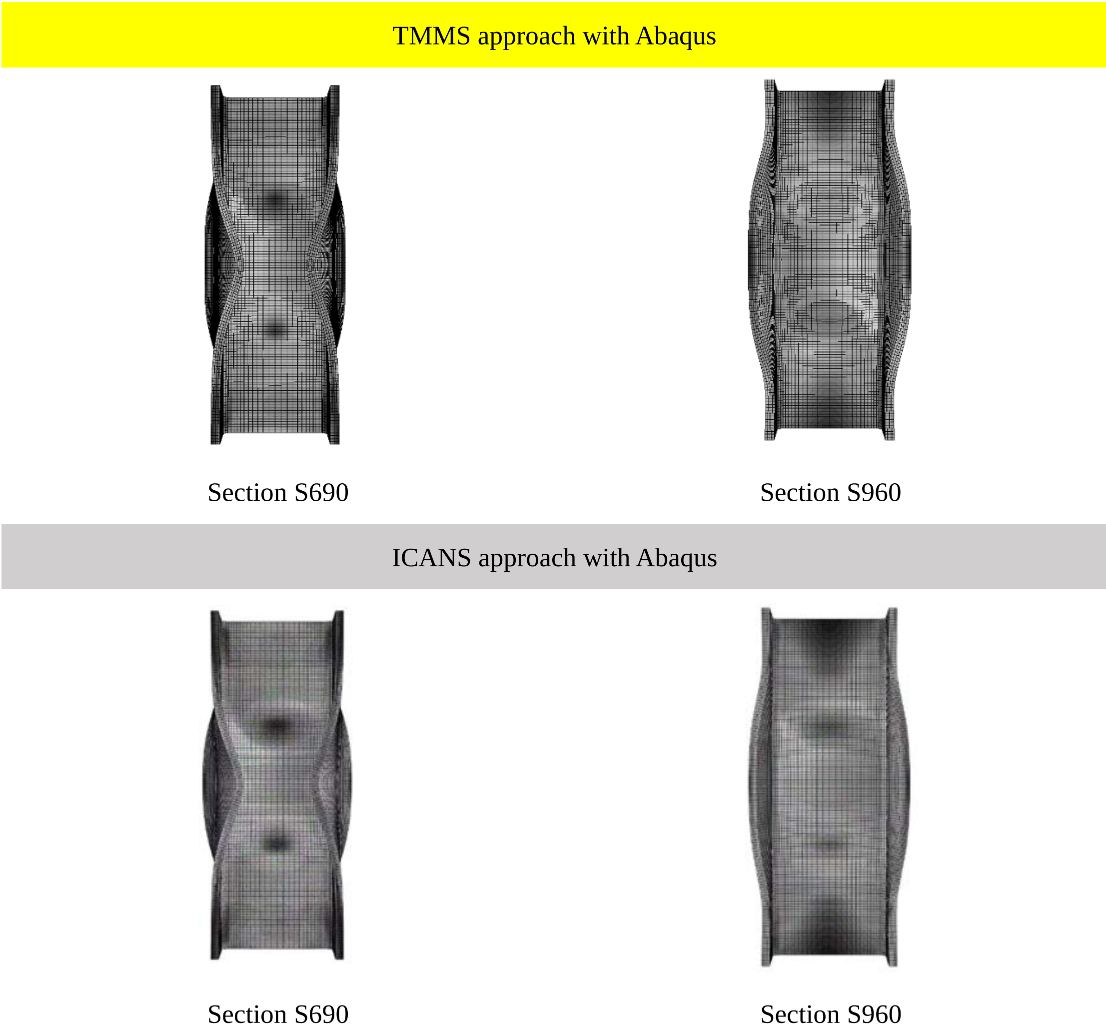

Figure 7.19 Deformed meshes of both Models at large deformations

It is shown that the deformed meshes of the Models obtained with SYSWELD are fairly similar to those obtained with Abaqus.

Figure 7.20 plots the applied load-axial shortening curves of these models for comparison.

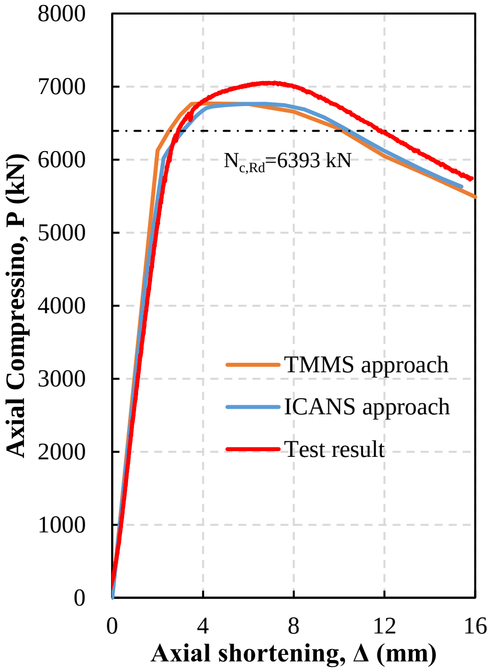

S690

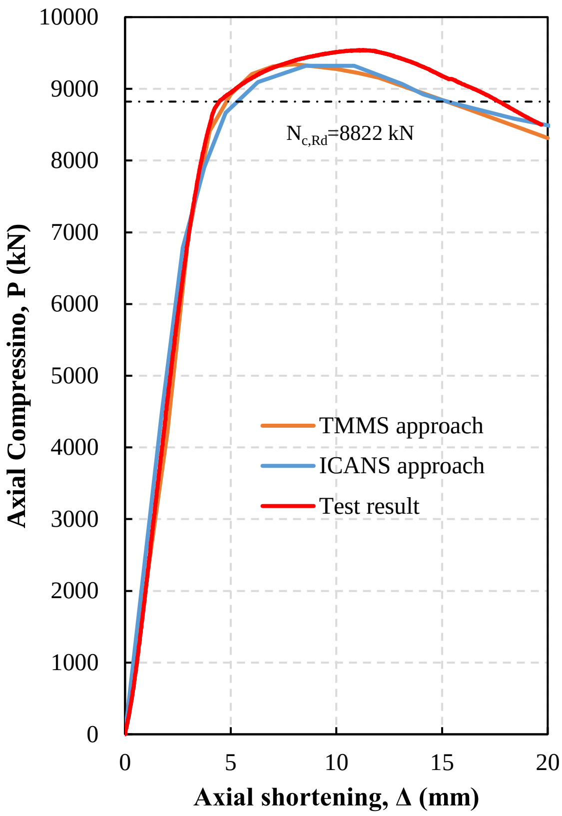

S960

Figure 7.20 Load-displacement curves of HSS welded H-sections

Regardless of considering phase transformation or not, the predicted load-shortening curves of both Models S690 and S960 are shown to follow each other closely along the entire deformation range. These curves are also found to be in good agreement, and yet conservative, when compared with the measured results.

It is considered to be worthy to compare the computational resources with the TMMS approach and the ICANS approach, and Table 7-3 summarizes the running times for these Models.

Table 7-3 Comparison of computation time

Model	Approach	Number of 3D elements	Computation time (hours)
S690	TMMS	21,380	12.2
S960		45,600	17.4
S690	ICANS	21,380	96.5
S960		45,600	114.8

It is shown that the TMMS approach is highly effective in term of computational time, and it takes very short time, i.e., 12 to 15%, to complete complex non-linear thermal as well as thermal-mechanical analyses in SYSWELD, when compared with those in Abaqus. Therefore, the TMMS approach is readily extended to deal with complex welded structures, such as T-joints with curved welding seams between circular hollow sections.

7.6. Specific modelling technique and data transfer

Despite both SYSWELD and Abaqus are commercial finite element packages which are developed for different usage and engineering disciplines over a couple of decades, it is possible to transfer data between these two software through compatible data interface. For example, SYSWELD is employed to simulate the welding process of the S690 welded sections according to practical welding processes and procedures to obtain the residual stress distributions of the welded sections. Then, the predicted residual stress data are readily imported into Abaqus as the initial stress field of the corresponding structural models. Hence, this allows an integrated and coordinated simulation of the structural behaviour of the S690 welded sections fully incorporating the effects of welding. A flow chart of the modelling technique is illustrated in Figure 7.21.

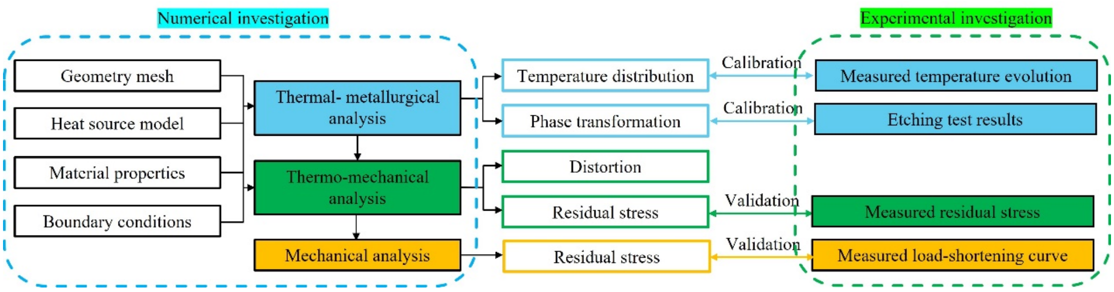

Figure 7.21 Flow chart of FEM and experiments comparison of this study

Following the welding simulation in SYSWELD, the post-processing module in Visual-Viewer was employed to export the deformation data, residual stress data, plastic strain data, and phase-dependent material properties data via the File-Export function. The exported data was then saved in the form of nodal components, which were identified by Abaqus as the initial data loaded on the model. Thus, the compatibility of

SYSWELD and Abaqus software was established through a comprehensive data interface, facilitating the efficient transfer of element and stress data.

Figure 7.22 shows the primary layout of the "Sysweld2Abaqus" interface, which functions as a subroutine in the Visual-Viewer. It helps to transform data produced by SYSWELD into a format that satisfies the requirements of the Abaqus program. The subroutine is comprised of three main components, namely material properties transformation, collector elements transformation, and stress results transformation.

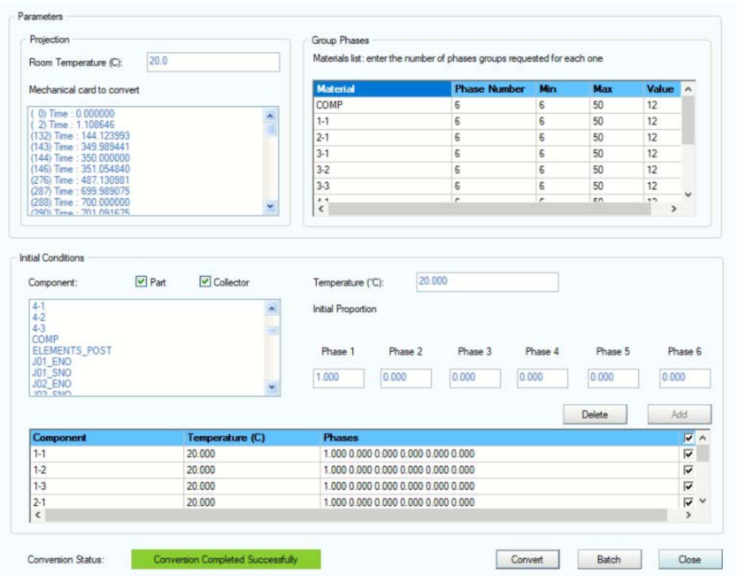

Figure 7.22 User Interface for Sysweld to Abaqus

In SYSWELD, the material properties of each elements contained its thermal-metallurgical performance, but in Abaqus, the characteristics of this part are not recorded in the material properties. Therefore, it is necessary to transform appropriate parameters in the material model input file. After this step, several different input files are obtained, including the material-dependent materials, the model dimensions, the mesh statement, the boundary conditions, the residual stress, and the plastic strain. All output files should be saved in the same working directory.

To ensure that those input files are compatible with Abaqus for the subsequent analysis, it is necessary to perform some additional steps to modify the numerical model, such as updating the element formulations and node name list to match the requirements of the Abaqus command solver. It must be ensured that the units of the same variable in

SYSWELD and Abaqus are the same. To use these input files simultaneously, a Fortran coding file is used to implement this procedure.

Figure 7.23a) illustrates a modified HAZ region of the welded corner in Model S960-B1 in Abaqus, while Figure 24d) shows the version of S960-B1-q2. Those elements which have underwent phase transformations, and hence, have modified mechanical properties are shown in different colours, as illustrated in Figure 7.23 b), c), e) and f). The corresponding true stress-true strain curves of these elements are plotted in Figure 7.23g).

a) Typical box section

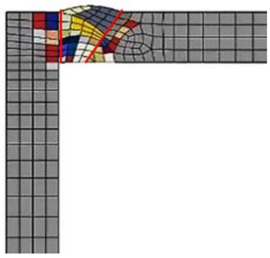

b) Section S960-B1

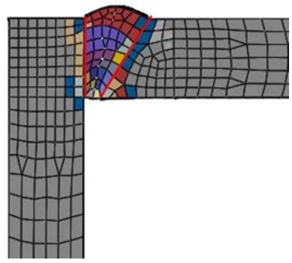

c) Section S960-B2

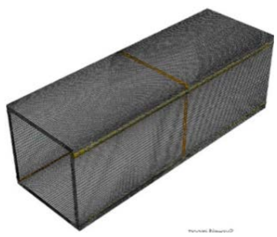

e) Typical box section with weld splices

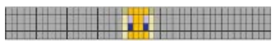

d) weld splice: S960-B1

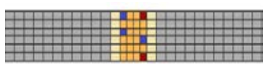

f) weld splice: S960-B2

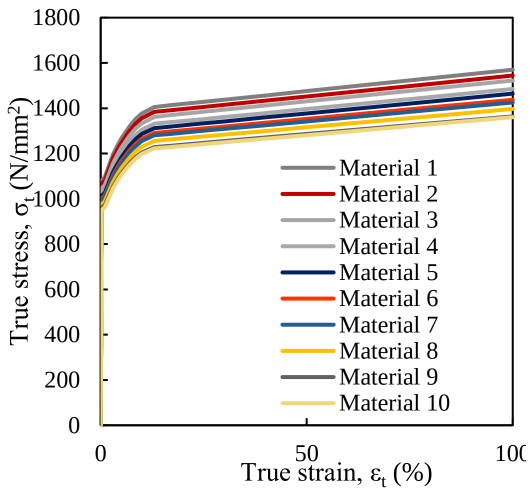

g) Stress-strain curves of various steel phases

Figure 7.23 Details of heat affected zones of Model S960-B1

After incorporating these SYSWELD results into the structural models of the high strength steel welded sections in the finite element software Abaqus, the structural behaviour of these box sections under compression was obtained. Consequently, the proposed *TMMS* approach is demonstrated to be able to predict "*thermo-metallurgical-mechanical-structural*" responses of these high strength S960 steel welded box sections effectively.

CHAPTER EIGHT

CONCLUSTION AND FUTURE WORK

8.1. Introduction

This thesis presents a comprehensive examination into the structural behaviour of the high strength S690 and S960 welded sections under axial loads, and both experimental and numerical investigations have been conducted to provide scientific data for development of structural understanding. It should be noted that the effects of welding onto these S690 and S960 steel have been studied systematically while metallurgical changes within the heat-affected zones of these welded sections is simulated through coupled thermomechanical-metallurgical analyses using an advanced numerical simulation package SYSWELD. Key findings of both experimental and numerical investigations are presented in the following sections while a plan for future work is also provided.

8.2. Experimental investigations

In this project, a series of experimental investigations was successfully carried out, and they include:

a) monotonic tensile tests on the coupons of both the base plates and their welded sections of the S690 and the S960 steel;

b) dilatometry tests on both the S690 and the S960 steel;

c) measurements on transient temperature history during welding and residual stresses after welding on the S960 welded H-sections and box sections;

d) compression tests on both the S690 and the S960 stocky columns.

Through these experimental investigations, scientific understanding to thermal, mechanical, metallurgical, and structural responses of these high strength steel welded sections is achieved. A large amount of test data is obtained for subsequent calibration of various finite element models for numerical simulations of these responses.

Key findings of these experimental investigations are summarized as follows:

a) Mechanical properties of S690 and S960 welded sections

A total of 16 monotonic tensile tests on standard coupons of the S690 steel and their welded sections were carried out to obtain detailed deformation characteristics as reference data for subsequent analyses. Similarly, for those of the S960 steel, a total of 16 monotonic tensile tests on standard coupons of the S690 steel and their welded sections were also carried out. Based on the test results of these monotonic tensile tests, both the yield and the tensile strengths, and the elongations at fracture of both the S690 and the S960 steel are obtained. It should be noted that:

- For both the S690 and the S960 steel, the mechanical properties of their welded sections are demonstrated to exhibit various degrees of reduction, and such a reduction may become significant when the welding is not properly controlled.
- For the S690 and the S960 steel, when a heat input energy at 2.0 kJ/mm is adopted during welding, the reductions in the yield strengths of these coupons of the welded sections are found to be 14% and 11% respectively. For the tensile strengths, this reduction are found to be only 8% and 4%.
- For the S690 steel, a reduction of 30% in the yield strengths of the coupons of the welded sections are achieved when a heat input energy at 5.0 kJ/mm is adopted during welding.
- When the heat input energy is kept to be equal to or smaller than 1.0 kJ/mm, reduction in the strengths of these S690 and S960 welded sections becomes very small, and it is generally considered to be negligible.

Hence, the heat input energy is always an important factor to the mechanical properties of the S690 and the S960 welded sections. It should be noted that the nominal plate thicknesses of the S690 and the S960 steel are 16 and 15 mm respectively. In general, for those S690 steel plates with thicknesses larger than 30 mm, there is experimental evidence that the reductions in their mechanical properties become less pronounced, i.e., ⩽2 to 5%, depending on the joint types, the welding methods and the heat input energy during welding.

b) Continuous cooling transformation (CCT) phase diagram of high strength S690 and S960 steel

A continuous cooling transformation (CCT) phase diagram for each of the S690 and the S960 steel is essential to understand changes in their microstructures, i.e., phase change, when they are cooled at different rates, for example, different cooling rates within the heat affected zones of welded sections after welding with different heat input energy. These changes are readily registered with their changes in linear expansion which is commonly measured with dilatometry tests. It should be noted that the initial phases at room temperature of the S690 steel are primarily tempered martensite and bainite. For the S960 steel, its initial phase at room temperature is primarily tempered martensite.

For the S690 steel, a total of 14 dilatometry tests were carried out at different cooling rates. Similarly, a total of 16 dilatometry tests were also carried out at different cooling rates for the S960 steel. Based on the dilatometric curves and microstructure results of different cooling rates, a set of CCT curves for each of the S690 and the S960 steel have been plotted. These curves are parts of the essential data for simulating phase transformation within the heat-affected zones of these steel during welding. The critical phase transformation temperatures of the S690 and the S960 steel were also identified.

c) Residual stresses of S960 welded H-sections and box sections

By applying the hole-drilling method on a total of four S960 welded H-sections and box sections, surface residual stresses of those welded sections were obtained. According to the measured data, the tensile residual stresses were found to be large, i.e., $0.25f_y$, in the locations in the vicinity of the welding seams while small compressive surface residual stresses, i.e., $0.08f_y$, were found in the rest of the flange plates and the webs. In general, the magnitudes of these residual stresses are found to be proportionally smaller than those of the S355 welded sections, i.e., $0.75f_y$. It should be noted that a set of carefully executed calibration exercises were carried out on a specially devised specimen of a S960 steel section to determine the values of calibration factors for use in the rosettes of the same batch.

d) Structural behaviour of S690 and S960 spliced stocky columns under axial compression

A total of 39 S690 and S960 stocky columns were tested under axial compression. The failure modes, section resistances and deformation characteristics of all welded H-sections and box sections were clearly presented. It was found that S690 and S960 sections with or without butt welded splices have the same failure modes, while the measured compressive resistances of all these sections are larger than the design values calculated according to EN 1993-1-1. The experiments also demonstrate that the current provisions for Class 4 sections in EC3 are relatively conservative for the S690 and the S960 steel.

8.3. Numerical investigations

a) The coupled thermo-mechanical-metallurgical-structural approach for high strength S690 and S960 steel

Using finite element modelling package SYSWELD and Abaqus, a new coupled thermo-mechanical-metallurgical-structural approach for the S690 and S960 has been developed. By introducing phase transformations determined by measured CCT curves, this approach considers the volumetric fraction changes of different metallurgical phases in high strength steel at variable temperatures. Finite element models of these steel plates with uniform metallurgical properties (homogeneous microstructures) are transformed under a direct exposure to transient temperature distribution history according to the maximum temperatures and the amount of heat input energy experienced during welding. By introducing the double ellipsoid model in thermal simulation, changes the parameters a_f, a_r, b and c to simulate the specific melt pool shape with different heat input energy. Hence, finite element meshes with non-uniform metallurgical properties (heterogeneous microstructures) are obtained. Transient temperature distribution history and surface residual stresses of these sections were employed to calibrate these finite element models, and good comparisons on both the temperatures and the residual stresses were achieved.

After welding simulation, the structural behaviour of these stocky columns with welded splices was also successfully simulated with the proposed TMMS approach, and good comparisons among the predicted and the measured deformation characteristics of these columns over the entire deformation ranges were successfully achieved. Compared to another FEM approach, this approach requires fewer computational resources and is more efficient in the simulation of structural performance. Thus, the welding process and subsequent structural performance of high strength S690 and S960 steel can be simulated accurately.

8.4. Future plans

The recommendations for future research work are proposed as follows:

1. Based on the thermo-mechanical-metallurgical coupled approach presented in this thesis, further development will be conducted in two aspects: one involves the application of this simulation approach to different materials, such as high strength S1100 steel, composite steel, galvanized steel, etc.; the other pertains to its application on more complex structures, including T-joints of RHS or CHS, multi-layer and multi-pass welded joints, etc.
2. High strength S690 and S960 steel stocky columns have been tested under axial compression in this study. Another test programme on S960 welded slender columns compression test has also been processed. Numerical studies on slender columns of S960 welded H-sections and box sections buckling about major and minor axis will also be carried out, including the parametric studies on the *c/t* ratio, to provide evidence for the design of the S690 and S960 steel.
3. In present study, the surface residual stresses of S960 H-sections and box sections

have been measured by hole drilling method, and stress values near weld sections are rather low. Considering the difference between experimental results and numerical simulation values, other measurement methods such as sectioning method and X-ray diffraction method were prepared for residual stress measurement test on the same S960 welded sections.

4. Since the performance of welding joints of high strength steel has an important influence on the safety, reliability and economy of construction projects, it is necessary to investigate the performance of welding joints on high strength steel under different welding conditions, especially for electrode arc welding which has less environmental requirements and suitable for construction projects. In future research, a comparative investigation of S690 and S960 electrode arc welding with different heat input energy will be conducted to determine the structural safety under this welding method.

Appendix A

DEFINITIONS OF MATERIAL PROPERTIES OF S690 AND S960 IN SYSWELD

A.1 Definitions of thermo-metallurgical properties

In numerical simulation of welding, it is common to assume that the steel is an isotropic, homogeneous, and plastic material. However, these assumptions are over simplistic for an accurate representation of the material characteristics of steel at elevated temperatures, particularly for low carbon high strength steel. As discussed in Chapter 6, the thermo-mechanical and thermo-metallurgical characteristics of different phases of the steel should defined separately, to achieve a high level of accuracy of welding simulations, and to analyse microstructural changes induced by welding. Therefore, this Appendix describes a full set of definitions of the thermo-metallurgical properties of the S690 and the S960 steel, including their phase transformations during welding, densities, specific heat capacities, and coefficients of thermal conductivity. Moreover, the thermo-mechanical properties such as Young's modulus, Poisson ratio, yield strengths and thermal strains of various phases of the steel are also defined, to capture the effects of welding onto the mechanical properties and the structural behaviour of these high strength steel. These material models incorporating the coupling of multiple properties were then employed in the simulation of welding, to predict effects of the heating and cooling stages onto the microstructure of steel, and also the distribution of residual stresses within the S690 and the S960 welded sections.

As the thermo-metallurgical properties are highly nonlinear and dependent on both temperatures and phases, the process of defining various sets of thermo-metallurgical properties, and subsequently calculations in SYSWELD are depicted in Figure A1.1.

Upon establishing the CCT curves through experimental investigations in Chapter 3, six primary phases are identified for these S690 and S960 steel.

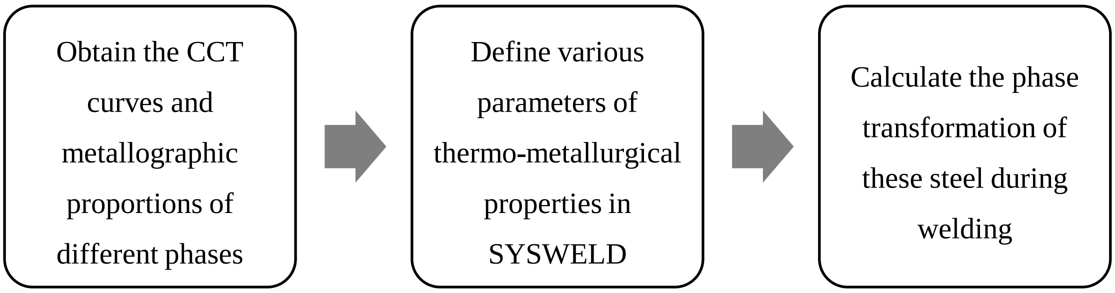

Figure A1.1 Flow chart of defining thermal properties for phase transformation

To facilitate the programming process, all these input information were converted into a .mat file using Excel VBA programming. The material data file comprises a large amount of information pertaining to the thermo-metallurgical properties of the steel. This includes fundamental phase transformations represented by simplified CCT curves, together with parameters such as densities, specific heat capacities, and coefficients of thermal conductivity. Table A1-1 presents the units of these properties to be defined. Those properties are important in the precise predictions of phase distribution and surface temperature distributions during the welding process.

Table A1-1 Units of thermo-metallurgical properties

Properties	Units
Temperature	$^{\circ}$C
Density	kg/mm^3
Specific heat capacity	J/kg/K
Thermal conductivity	W/m/K

A1.1 Phase transformation

The phase transformation information of both the S690 and the S960 steel are written into the material file according to the metallurgical percentage at different cooling rates. For the S690 steel, referring to CCT curves obtained by dilatometry tests as reported in

Chapter 3, there are a number of main phases formed within the heat-affected zones in welding: tempered martensite, austenite, martensite, bainite, pearlite, and ferrite. However, owing to the presence of only a small proportion of pearlite in the overall transformation process, pearlite was combined with ferrite in the metallurgical simulation. Meanwhile, the initial phases of both the S690 and the S960 are set to tempered martensite. The definition file was populated with the aforementioned information via Fortran. These phases are numbered as follows:

Phase 1: Initial phase (Tempered martensite)

Phase 2: Fictive phase (for case of numerical analyses)

Phase 3: Martensite

Phase 4: Bainite

Phase 5: Ferrite

Phase 6: Austenite

Through this numbering, phase transformation that may occur during the welding process is readily described as transformation from Phase 1 to Phase 2, followed by transformation to Phase 6 during the heating process. After austenitization is completed, the contents of Phases 3, 4, and 5 in the microstructure of the heat-affected zone of the steel are determined according to different cooling rates. Table A1-2 lists various phase proportions and their corresponding cooling rates for phase transformation of the S690 steel.

Table A1-2 Phase proportions and their corresponding cooling rates of the S690 steel

Cycle number	Start time (s)	End time (s)	Rate	Phase1 (%)	Phase2 (%)	Phase3 (%)	Phase4 (%)	Phase5 (%)	Phase6 (%)
1	0.00	10.00	-70	0	0	100	0	0	0
2	0.00	14.00	-50	0	0	100	0	0	0
3	0.00	23.33	-30	0	0	90	10	0	0
4	0.00	35.00	-20	0	0	50	50	0	0
5	0.00	46.67	-15	0	0	45	55	0	0
6	0.00	70.00	-10	0	0	30	70	0	0
7	0.00	140.00	-5	0	0	0	100	0	0
8	0.00	280.00	-2.5	0	0	0	70	30	0

9	0.00	350.00	-2	0	0	0	60	40	0
10	0.00	466.67	-1.5	0	0	0	53	47	0
11	0.00	700.00	-1	0	0	0	0	100	0
12	0.00	1166.67	-0.6	0	0	0	0	100	0
13	0.00	2800.00	-0.25	0	0	0	0	100	0
14	0.00	4666.67	-0.15	0	0	0	0	100	0

For these 14 different cooling rates, the phase proportions for Martensite (3), Bainite (4) and Ferrite (5) are determined directly according to the CCT curves. Using the material tool interface of SYSWELD, it is possible to calculate differences between various proportions according to different cooling curves, and then complete entire simulation curves numerically through intermediate interpolation. Thereby, Figure A1.2 presents the S690 CCT curves in SYSWLED.

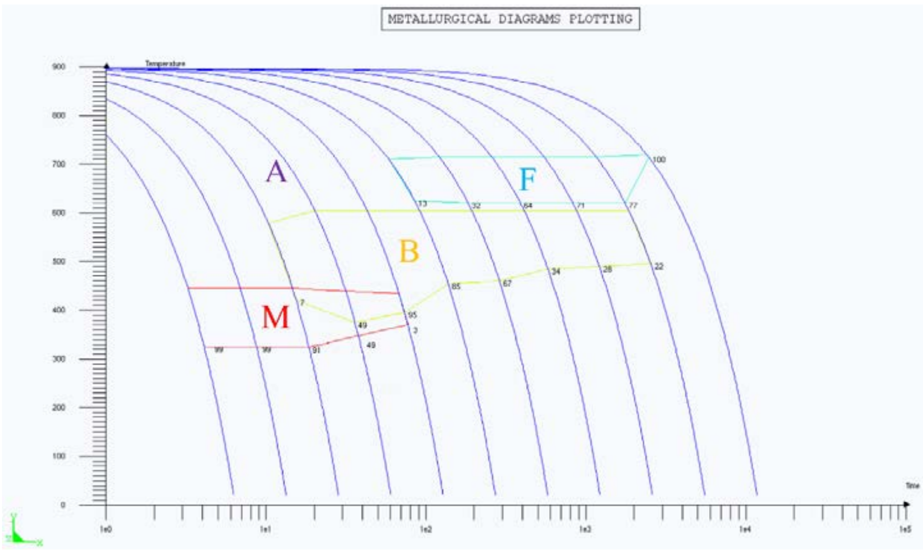

Figure A1.2　CCT curves of the S690 in SYSWELD

In this figure, “A” denotes austenite, “M” denotes martensite, “B” denotes bainite, “F” denotes ferrite. These phase of the steel will change according to the different cooling rates. For example, when the cooling rate is 70°C/s, after completion of the cooling, 100% martensite is obtained; when the cooling rate is 2.5°C/s, after cooling, 30% ferrite and 70% bainite are obtained. All these properties are defined and saved in the METALLURGY.DAT file.

For the S960 steel, referring to the CCT curve described in Chapter 3, there are also a number of main phases formed within the heat-affected zones after welding. Compared with the CCT curves of S690 steel, due to differences in chemical compositions and heat treatments, S960 steel does not contain pearlite. Table A1-3 lists various phase proportions and their corresponding cooling rates for phase transformation of the S960 steel.

Table A1-3　Phase proportions and their corresponding cooling rates of the S960 steel

Cycle number	Start time (s)	End time (s)	Rate	Phase1 (%)	Phase2 (%)	Phase3 (%)	Phase4 (%)	Phase5 (%)	Phase6 (%)
1	0.00	7.00	-100	0	0	100	0	0	0
2	0.00	10.00	-70	0	0	100	0	0	0
3	0.00	14.00	-50	0	0	100	0	0	0
4	0.00	23.33	-30	0	0	100	0	0	0
5	0.00	35.00	-20	0	0	100	0	0	0
6	0.00	70.00	-10	0	0	100	0	0	0
7	0.00	140.00	-5	0	0	90	10	0	0
8	0.00	233.33	-3	0	0	80	20	0	0
9	0.00	350.00	-2	0	0	30	70	0	0
10	0.00	700.00	-1	0	0	20	80	0	0
11	0.00	1400.00	-0.5	0	0	0	100	0	0
12	0.00	2333.33	-0.3	0	0	0	100	0	0
13	0.00	4666.67	-0.15	0	0	0	90	10	0
14	0.00	7000.00	-0.1	0	0	0	80	20	0

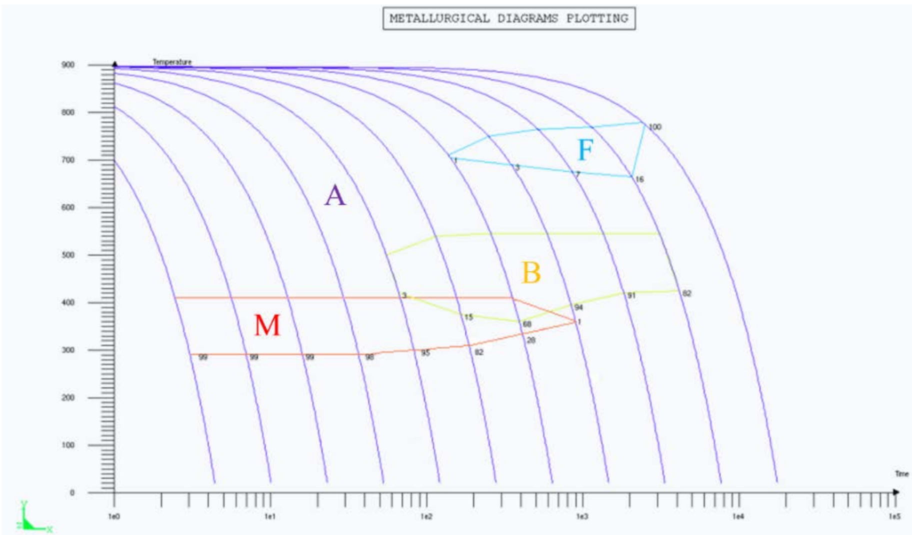

Figure A1.3　CCT curves in SYSWELD of the S960

Figure A1.3 presents the re-presented S960 CCT curves in SYSWLED. In this diagram, “A” denotes austenite, “M” denotes martensite, “B” denotes bainite, “F” denotes ferrite.

Therefore, when the cooling rate is 100°C/s, after completion of the cooling, 100% martensite is obtained; when the cooling rate is 0.5/s, after cooling, 100% bainite are obtained. The METALLURGY.DAT file provide a comprehensive description of the transformation kinetics for each constituent phase of the steel.

A1.2 Density

Within the temperature range pertinent to welding, the initial density of steel is typically assumed to be the ambient value of 7.85E-06kg/mm^3. However, the density of austenite in low carbon steel is generally larger than other phases such as ferrite and pearlite, due to its more closely packed crystal structures (Avrami 1941). Therefore, to accurately account for variation in density with a wide range of temperature for both the S690 and the S960 steel, their densities are assigned to be the same to the density setting of the S460 in SYSWELD. Table A1-4 and Figure A1.4 present the density definitions of the S690 and the S960 steel for different metallurgical phases at various temperatures. The melting temperature is set to be 1350°C.

Table A1-4 Densities of the S690 and the S960 with different phases

Phase	Temperature (˚C)	Density (kg/mm^3)
Initial phase, fictive phase, martensite, bainite, ferrite	20	7.82E-06
	1350	7.29E-06
Austenite	20	7.99E-06
	1350	7.29E-06

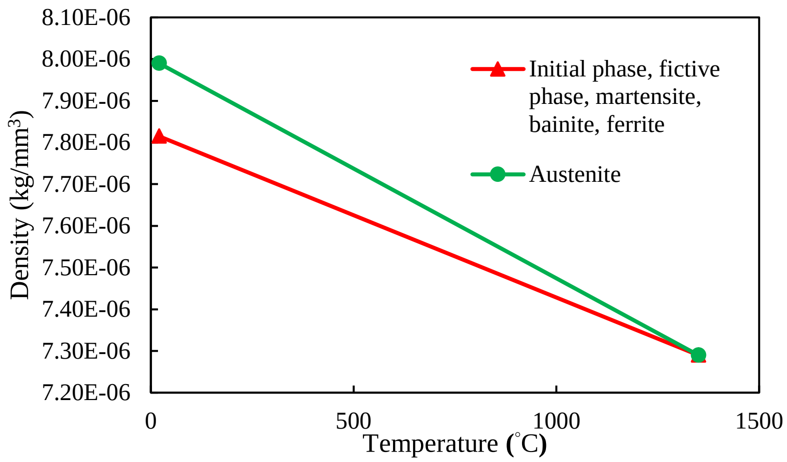

Figure A1.4 Density of the S690 and the S960

For both the S690 and the S960 steel, the density of austenite is marginally larger than that of other phases at room temperature, i.e., 20°C. As the temperature increases, the densities of all phases decrease linearly to 7.29E-06 kg/mm^3 at 1350°C.

A1.3 Thermal conductivity

Thermal conductivity is a measure of the amount of heat required to raise the temperature of a unit mass of a substance by a unit degree. It is very important for accurate determination of the temperature distribution in the steel during welding. The increase in temperature within a welded section can be mathematically expressed in terms of the thermal conductivity of the steel (Choi, Chung, and Kim 2014).

The thermal conductivity of steel, λ_a, can be determined as:

$$\lambda_a = \alpha \cdot c_p \cdot \rho \tag{A1.1}$$

where α is the thermal diffusivity;

c_p is the specific heat capacity of the steel;

ρ is the density of the steel.

Since measurement of thermal diffusivity is quite complex, a simplified coefficient is generally adopted to represent the thermal conductivity. In EN1993-1-2 (CEN, 2005), the variation of the thermal conductivity of the steel with temperature is presented in Figure A1.5

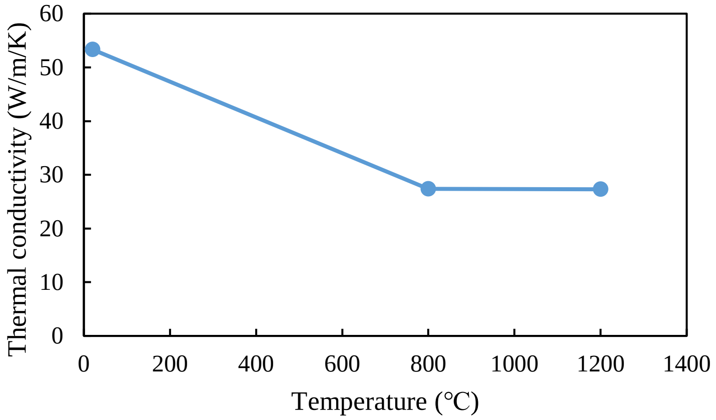

Figure A1.5 Thermal conductivity of carbon steel given in EN1993-1-2

That is, for 20°C≤ θ_a ≤800°C, $\lambda_a = 54 - 3.33 \times 10^{-2}\theta_a$ W/mk;

for 800°C≤ θ_a ≤1200°C, $\lambda_a = 27.3\ \mathrm{W/mk}$

where θ_a is the temperature of steel.

Similar to other thermal-metallurgical properties, the thermal conductivity of each phase of the steel can vary significantly due to differences in their microstructures and crystal structures. Table A1-5 and Figure A1.6 present the thermal conductivity definitions of both the S690 and the S960 steel for different metallurgical phases with various temperatures.

Table A1-5 Thermal conductivity of S690 and S960 steel with different phases of the steel

Phase	Temperature (°C)	Thermal conductivity (W/mK)
Initial phase, fictive phase, martensite, bainite, ferrite	0	46
	100	46
	200	45
	300	43
	400	41
	500	38
	600	35
	700	29
	800	24
	1350	32
	2200	32
	2500	32
Austenite	0	15
	800	24
	1350	32
	2200	32
	2500	32

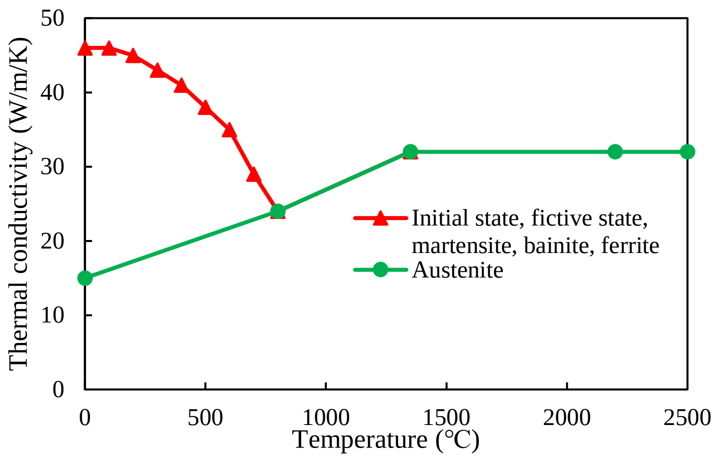

Figure A1.6 Definitions of thermal conductivity of S690 and S960 steel

These values are determined according to the data of the S460 steel in SYSWELD. In summary, austenite exhibits a slightly lower thermal conductivity, when compared to other phases below 800°C, and this conductivity gradually increases with higher temperatures. After 800°C, the thermal conductivity of all phases becomes the same.

A1.4 Specific heat capacity

The specific heat capacity relates to the amount of heat energy that can be stored in a material. Typically, specific heat increases with rising temperatures, with a significant peak value between 700°C to 800°C. This increase in specific heat capacity is attributed to the phase changes in the steel, specifically the atomic transition from a face centered cubic (FCC) structure to a body centered cubic (BCC) structure that requires significant energy (Wang *et al*.). Similarly, considering various difficulty of experimental testing, simplified models are commonly used to describe these specific heat capacity. In EN1993-1-2, for low carbon steel such as S355 steel, the simplified model of the specific heat capacity at elevated temperatures are presented in Figure A1.7.

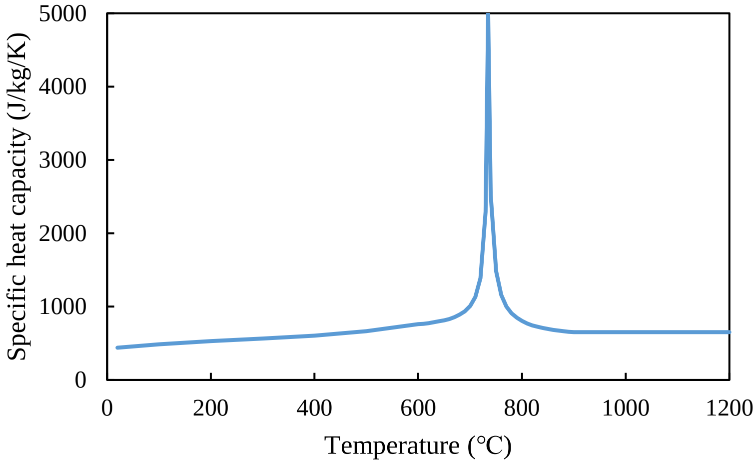

Figure A1.7 Specific heat capacity of carbon steel in EN1993-1-2

That is, for 20°C≤ θ_a ≤600°C,

$$c_a = 425 + 0.773\theta_a - 1.69 \times 10^{-3}\theta_a^2 + 2.22 \times 10^{-6}\theta_a^3 \ \text{J/kgK}$$

For 600°C≤ θ_a ≤735°C, $c_a = 666 + \frac{13002}{738-\theta_a}$ J/kgK

For 735°C≤ θ_a ≤900°C, $c_a = 545 + \frac{17820}{\theta_a - 731}$ J/kgK (A1.2)

For 900°C≤ θ_a ≤1200°C, $c_a = 650$ J/kgK

In these high strength steel, specific heat capacity for different phases need to be defined separately due to differences in their thermal properties. Table A1-6 and Figure A1.8 present the specific heat capacity of both the S690 and the S960 steel for different phases with various temperatures. These values are defined according to various definitions of other low carbon high strength steel in SYSWELD.

Table A1-6 Specific heat capacities of S690 and S960 steel with different phases

Phase	Temperature (°C)	Thermal conductivity (W/kg/K)
Initial state, fictive state, martensite, bainite, ferrite	0	430
	100	500
	200	550
	300	580
	400	610
	500	650
	600	710

	700	790
	800	865
	900	565
	1350	630
	2500	707
Austenite	0	450
	100	473
	200	495
	300	512
	400	523
	500	533
	600	541
	700	548
	800	556
	900	565
	1350	630
	2500	707

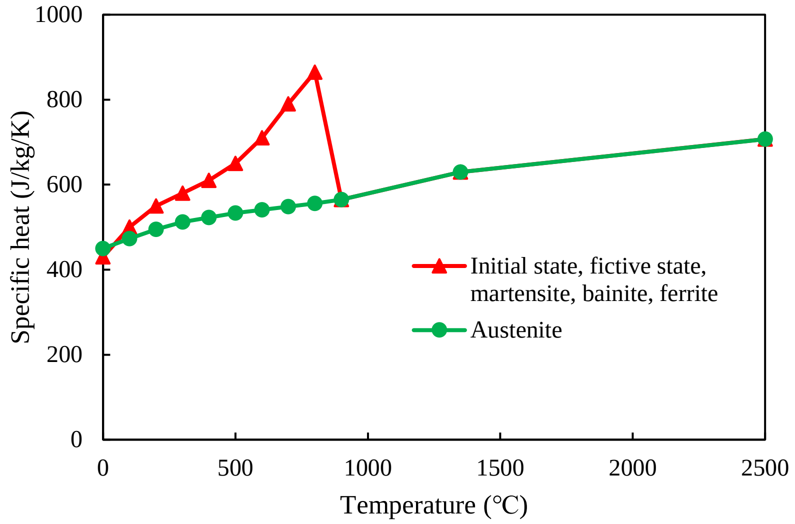

Figure A1.8 Definition of specific heat capacities of S690 and S960 steel

In addition to thermal conduction, the analysis also accounts for heat loss resulting from convection and radiation. The convective heat transfer coefficient for the S690 and the S960 steel was assumed to be 25 $\mathrm{W/(m^2 \cdot K)}$ while the emissivity was set to be 0.8 (Li *et al*. 2017). Such information consider the variation of material properties with temperatures and phase transformations. All these thermo-metallurgical properties data are then readily used to predict the temperature distribution and the microstructural evolution during heating and cooling processes.

A.2 Definitions of thermo-mechanical properties

During welding, any change in the mechanical properties of the heat affected zones of the steel sections is closely related to the phase transformations in the steel. Therefore, the thermo-mechanical properties of the steel should be accurately defined and characterized. In this section, the defined thermo-mechanical properties of both the S690 and the S960 steel, including Young's modulus, Poisson's ratio, stress-strain curves of each phase, and thermal strain are defined accordingly.

Table A2-1 lists the units of all thermo-mechanical properties of the steel considered in this section.

Table A2-1 Units of thermo-mechanical properties

Properties	Units
Temperature	˚C
Stress	N/mm^2
Strain	%
Thermal strain	%
Youngs Modulus	N/mm^2

A2.1 Young's modulus

The Young's modulus of the S690 and the S960 steel generally decreases with increasing temperatures, and this is similar to that of normal strength steel. Such a decrease in the values of Young's modulus is due to a thermal expansion of the steel, as it causes atomic bonds to be loosened when and the steel expands. Derived from previous research on fire resistance of steel, after considering the collective effects of all phases, the Young's modulus of the S690 steel in SYSWLED are shown in Table A2-2 (Huang *et al.* 2022).

Table A2-2 Young's modulus of S690 steel at elevated temperatures

T (°C)	20	300	400	500	600	700	800
E (N/mm^2)	209,000	197,000	182,000	180,000	155,000	103,000	52,000

Similarly, the Young's modulus of the S960 steel defined in SYSWLED are shown in Table A2-3 (Wang *et al*. 2020).

Table A2-3 Young's modulus of S960 steel at elevated temperatures

T (°C)	20	300	400	500	600	700	800
E (N/mm^2)	210,000	204,000	193,000	177,000	160,000	93,000	53,000

It should be noted that the experimentally determined values for both the Young's modulus and the yield strength are directly correspondent to the composite phases. Due to measurement conditions, only data up to 800°C are obtained. Hence, it is necessary to complete data for the temperature range between 800°C and1350°C with data from other low carbon steel such as the S460. Therefore, in SYSWELD, the definition of Young's modulus on both the S690 and the S960 steel are shown in Figure A2.1 and Figure A2.2, correspondingly.

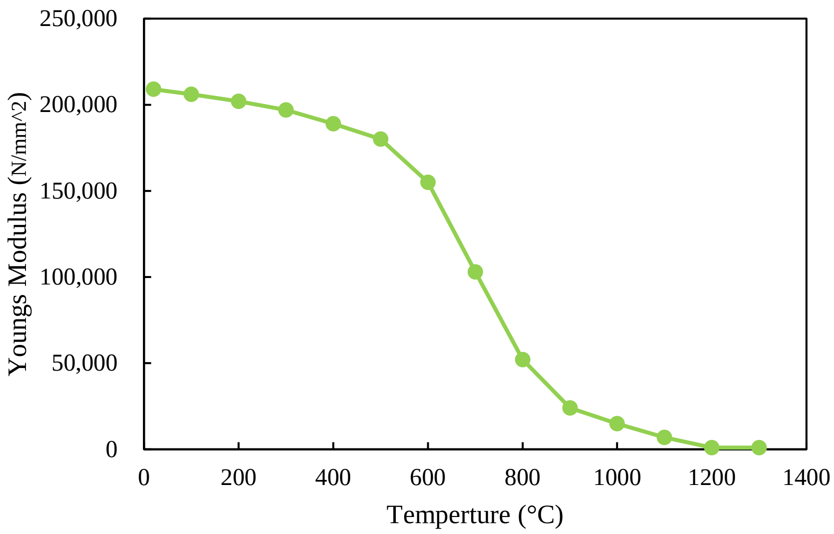

Figure A2.1 Definition of Young's modulus of the S690 steel

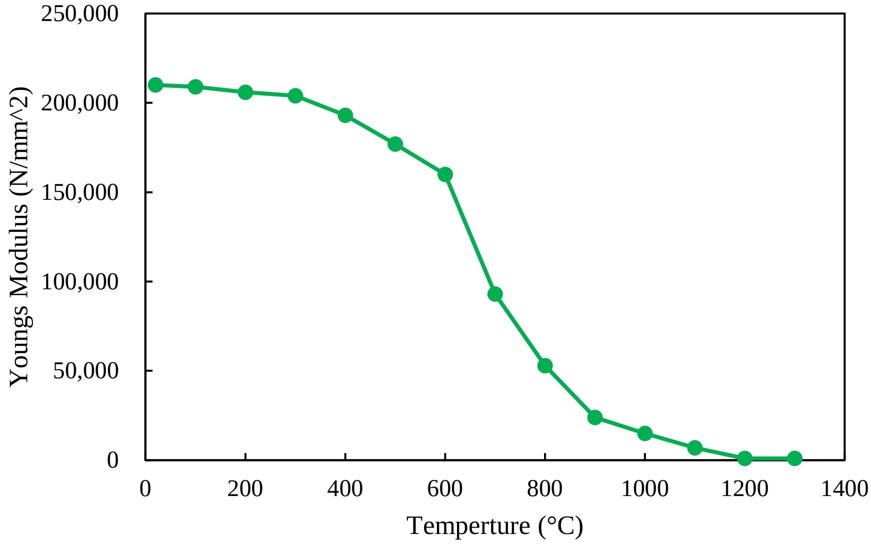

Figure A2.2 Definition of Young's modulus of` the S960 steel

A2.2 Poisson's ratio

Poisson's ratio is defined as the negative ratio of a lateral strain (a strain perpendicular to an applied stress) to the longitudinal strain (a strain parallel to the applied stress). In other words, Poisson's ratio describes how much a steel will be contracted laterally when being stretched in the longitudinal direction. In general, the Poisson's ratio of the steel tends to decrease slightly with increasing temperatures, but the magnitude of this change is usually small, and it is readily negligible for low carbon steel.

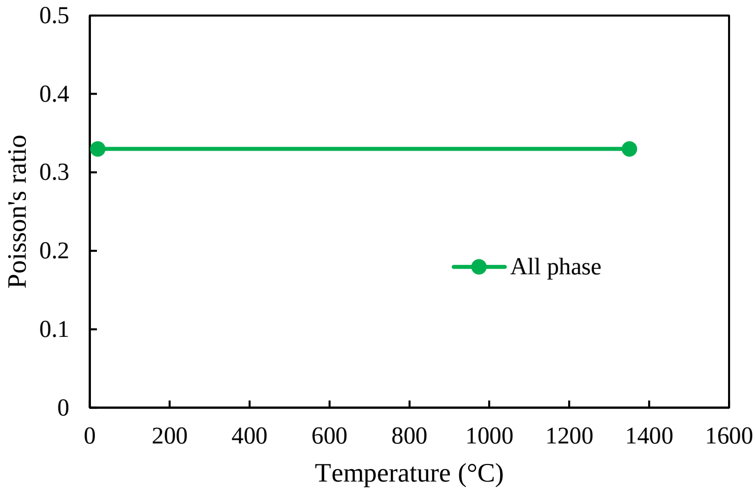

Figure A2.3 Definition of Poisson's ratio of S690 and S960 steel

As commonly presented in the literature, the Poisson's ratio of low carbon steel is relatively similar. Referring to data of the S460 steel, Figure A2.3 shows the typical definition of Poisson's ratio of the S690 and the S960 steel. This value is set to 0.33 in the temperature range pertinent in the welding simulation for all phases.

A2.3 Yield strength

A stress-strain curve is a relationship between the stress and the strain of the steel. As the temperature increases, the strength of low carbon steel decreases due to unstable grain structures, reduced crystallinity, and multiple phase transformations. EN1993-1-2 gives a non-linear stress-strain curve of the steel at elevated temperatures, the reduction factors for yield strength, proportional limited slope of linear elastic range of the steel over a wide range of temperatures are shown in Figure A2.4 and Figure A2.5.

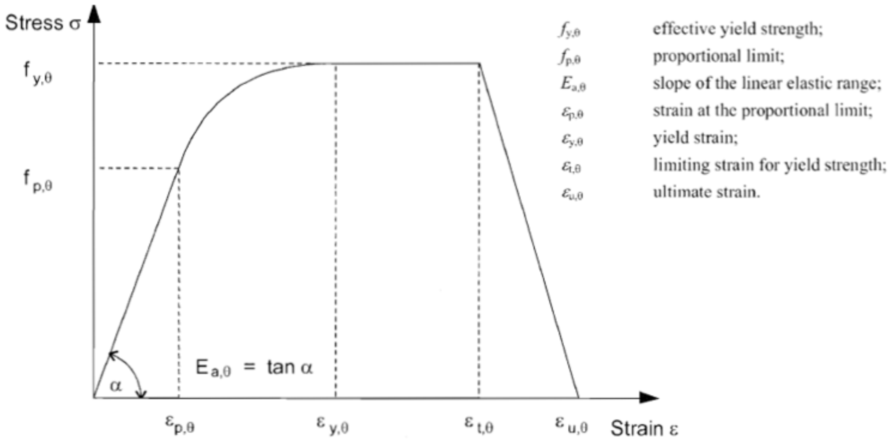

Figure A2.4 Stress-strain relationship for carbon steel at elevated temperatures

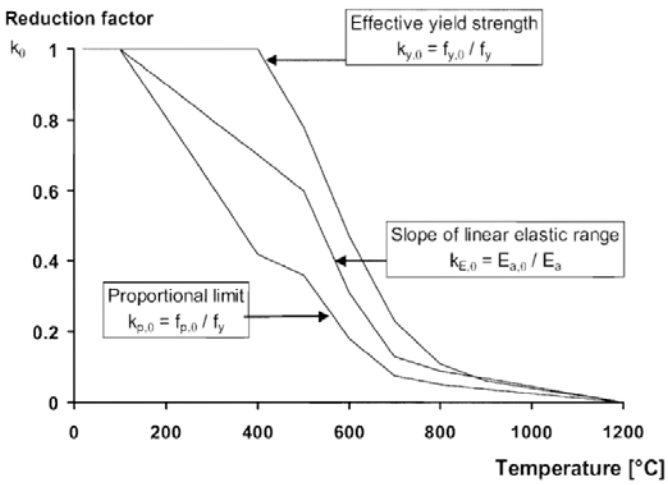

Figure A2.5 Reduction factors for the stress-strain relationship of carbon steel at elevated

temperatures

In this section, the stress-strain curves of the S690 and the S960 steel are defined using test data from heat treated coupons, and then processed with the use of SYSWELD Toolbox, taking into account of both the phase transformation and increased temperatures. Just as the phase transformation defined in Section A1.1, six phases of the S690 and the S960 defined in SYSWELD are described as follows:

1. *Initial phase (tempered martensite)*: a modified form of martensite that has improved toughness due to partial transformation of hard martensite into more ductile phases. It should noted that it is the basic metallurgy at room temperature for both the S690 and the S960 steel.
2. *Fictive phase*: a state of the steel during the heating and cooling stages of welding simulations, where the steel is assumed to be in a hypothetical state for the use of numerical simulation.
3. *Martensite*: a hard and brittle phase that formed under high cooling rates. It has a rather high yield strength, but a low ductility.
4. *Ferrite*: a soft and ductile phase that formed under low cooling rates. It has a low yield strength but a high ductility.
5. *Bainite*: a mixture of ferrite and carbides that forms at intermediate cooling rates. It has a lower yield strength, but a higher ductility when compared to martensite.
6. *Austenite*: a face-centered cubic structure formed only at high temperatures. It has an excellent ductility and toughness, but a poor hardness and strength.

In general, the yield strengths of all phases decrease with increasing temperatures. As it is impractical to experimentally determine the yield strength for each phase at different temperatures, these data are established with reference data from the S460 steel, the temperature-dependent variations of Young's modulus, and the overall yield strengths. According to Loose (Loose, 2008), for the low carbon steel S355, the yield strengths of bainite, martensite are readily expressed as follows:

$$\begin{cases} \sigma_y(bainite) = 1.39\sigma y(ferrite) \\ \sigma_y(martensite) = 1.97\sigma_y(ferrite) \end{cases} \tag{A2.1}$$

Considering that both the S690 and the S960 steel are low carbon steel, these expressions are readily applied to the strength data for various phases. Therefore, these curves for the modified yield strengths of various phases of the S690 and the S960 steel are shown in Figures A2.6 and A2.7. Both the fictive phase and the austenite data are also obtained from those of the S460 in SYSWELD.

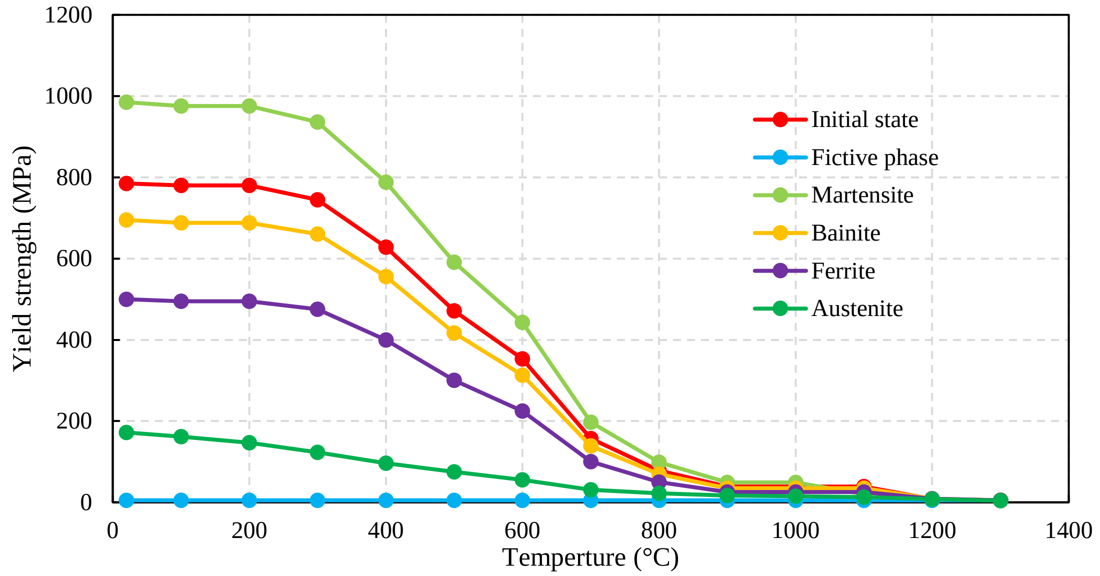

Figure A2.6 Relationship between yield strengths of various phases and temperatures of S690 steel

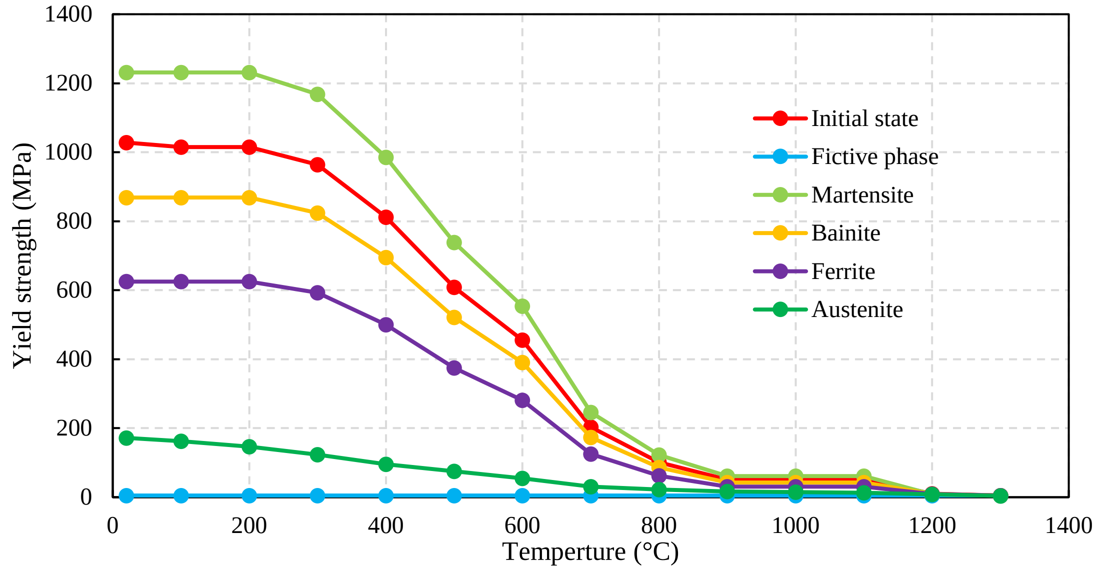

Figure A2.7 Relationship between yield strengths of various phases and temperatures of

S960 steel

It is also important to establish the thermo-mechanical module for strain hardening during phase transformation through the use of strain hardening tools. As shown in Figures A2.8 and A2.9, a simplified constitutive model was used in stress-strain relationships of various phases of the steel. Due to space limitations, only representative stress-strain curves for the initial state (tempered martensite), martensite, and austenite at different temperatures are shown here.

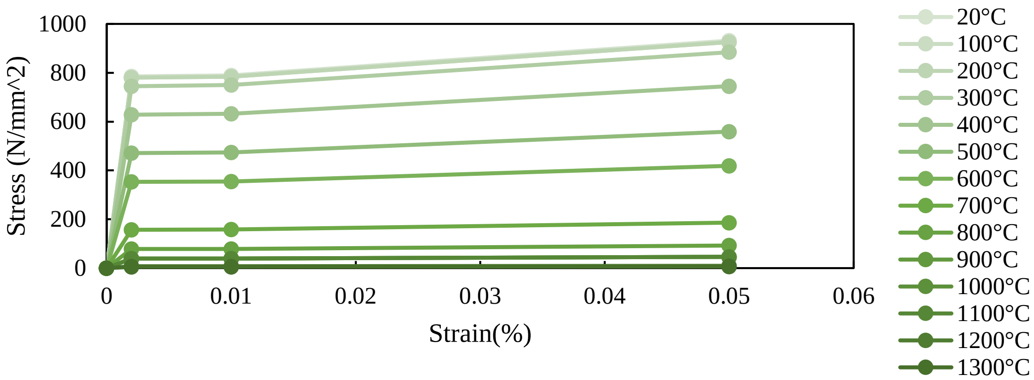

Initial state (tempered martensite)

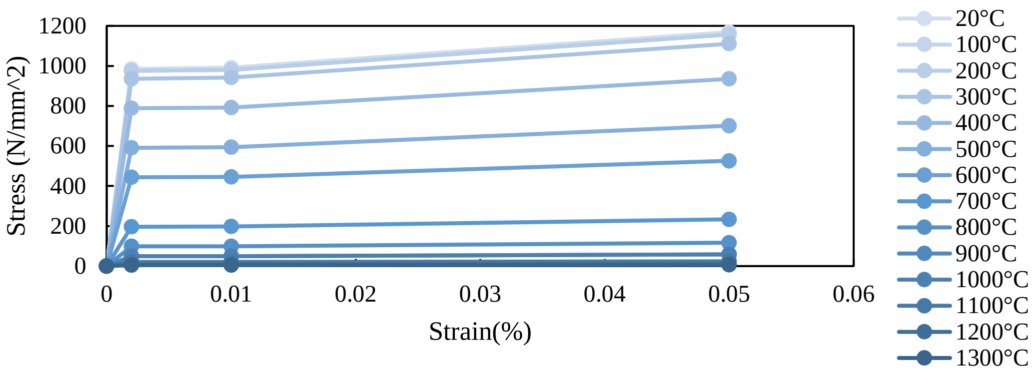

Martensite

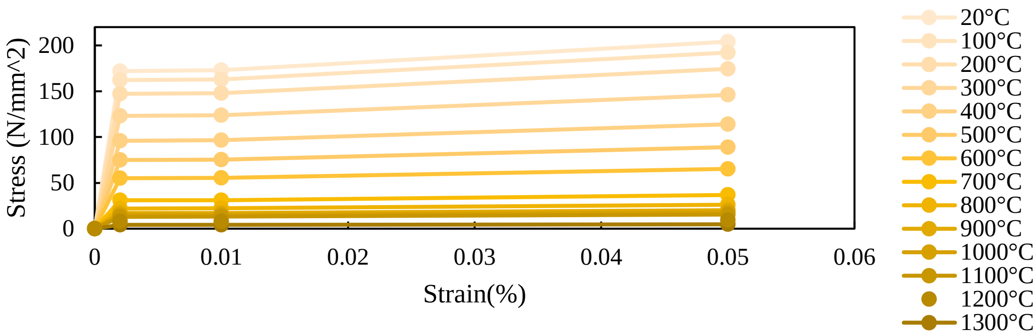

Austenite

Figure A2.8 Stress-strain relationships of various phases of the S690 steel

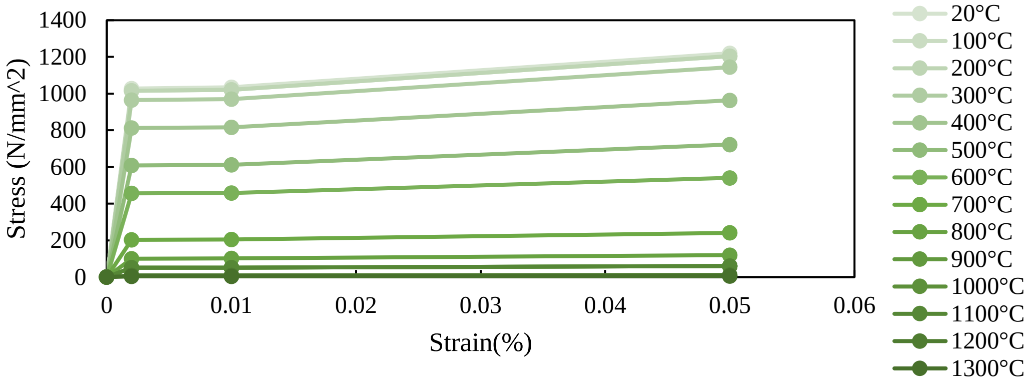

Initial state

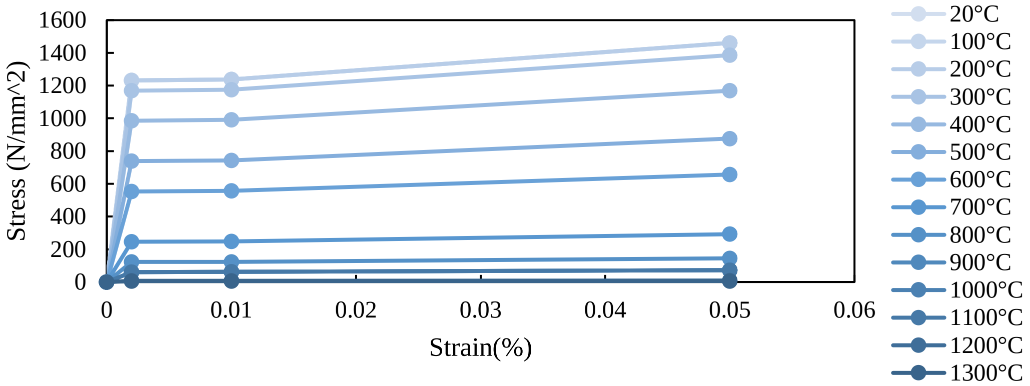

Martensite

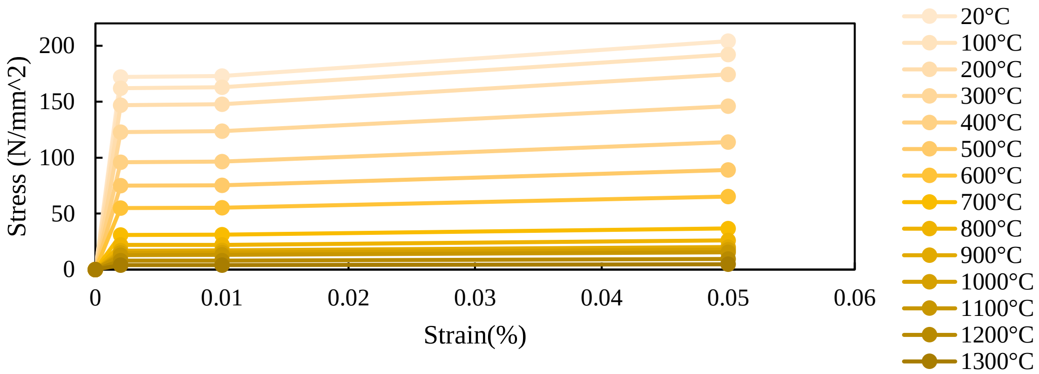

Austenite

Figure A2.9 Stress-strain relationships of various phases of the S960 steel

All these data are generated and saved in a set of mechanical definition files. Therefore, by determining the compositional variations during phase transformation of the steel based on temperature changes, different mechanical properties of these phases at various temperatures are obtained accordingly.

A2.4 Thermal strains

The total strain increment during welding process is readily expressed as follows:

$$\Delta\varepsilon_{total} = \Delta\varepsilon_e + \Delta\varepsilon_p + \Delta\varepsilon_{th} + \Delta\varepsilon_{trip} \tag{A2.2}$$

where $\Delta\varepsilon_e$ is the increment of elastic strain;

$\Delta\varepsilon_p$ is the increment of plastic strain;

$\Delta\varepsilon_{th}$ is the increment of thermal strain;

$\Delta\varepsilon_{trip}$ is the increment of transformation induced plasticity (TRIP) strain.

It should be noted that a thermal strain refers to a dimensional changes that occurs in the steel due to a temperature variation. Phase transformation often results in significant alterations to its thermal and mechanical properties. Therefore, in SYSWELD, a thermal strain is used to register an expansion or a contraction of the steel under various temperatures. This approach is employed instead of using the conventional thermal expansion coefficient to incorporate thermal effects in the analysis. With reference to other low carbon steel, such as the S355 and the S460 steel in SYSWELD, the thermal strains of various phase of the S690 and the S960 steel are shown in Figure A2.10 and Figure A2.11, respectively.

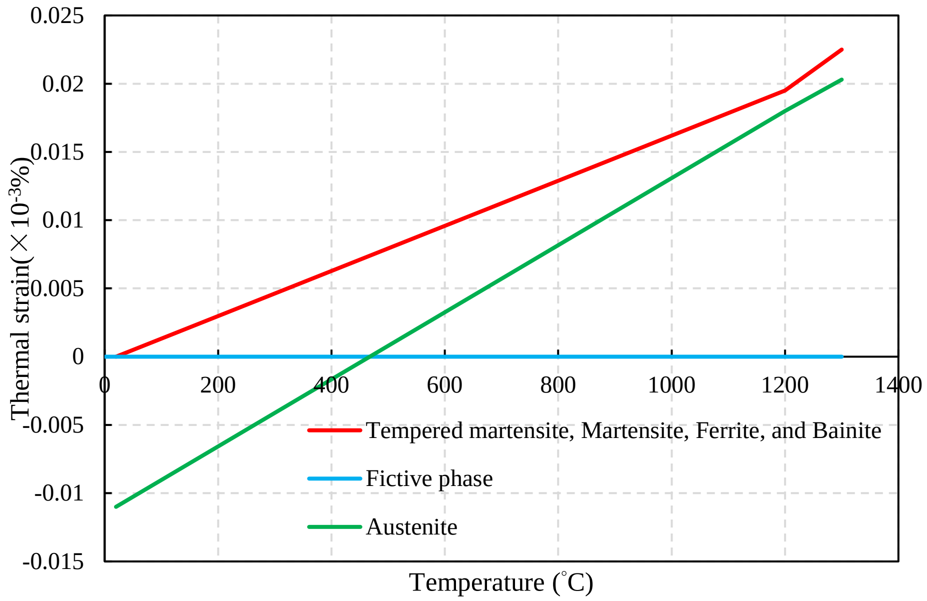

Figure A2.10 Thermal strain of the S690 steel

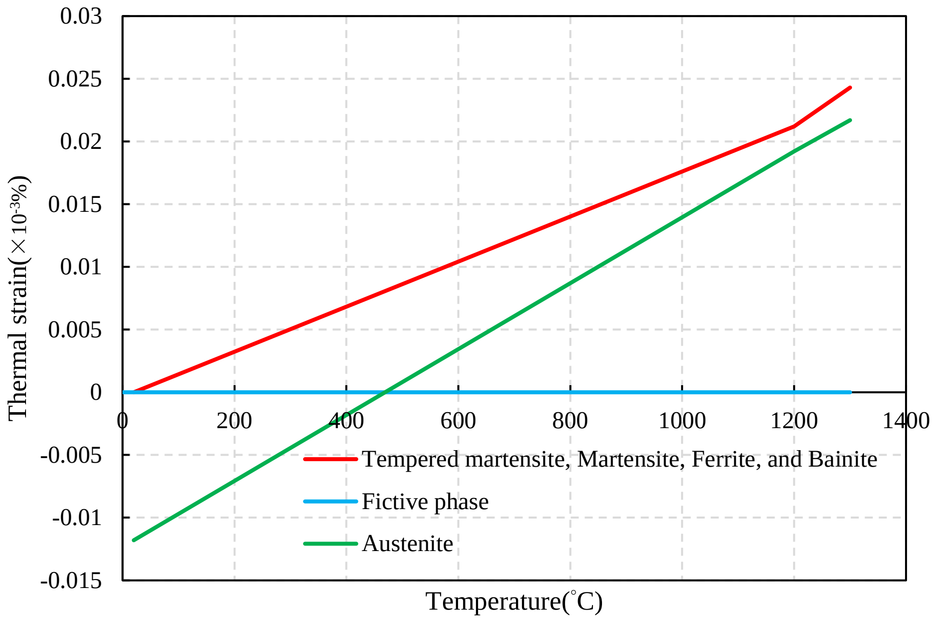

Figure A1.20 Thermal strain of the S960 steel

In summary, all the aforementioned thermo-mechanical properties are compiled into the material data file together with the thermo-metallurgical properties described in Section A1. They form the complete sets of material models for the S690 and the S960 steel in SYSWELD. The proposed thermo-mechanical-metallurgical model, accounting for various nonlinear relationships, has demonstrated successful application in the numerical simulations. A comparison between the numerical and measured data reveals good agreements, confirming its effectiveness in simulating the effects of welding onto mechanical properties of the heat-affected zones of the welded sections on high strength S690 and S960 steel.

Reference

ABAQUS User’s Manual. Version 6.13. Dassault Systemes Simulia Corp., Providence, USA; 2013

Abraham C. Hole-drilling residual stress measurement in an intermediate thickness specimen[D]. University of British Columbia, 2011.

ASTM_E837-13. 2008. “Standard Test Method for Determining Residual Stresses by the Hole-Drilling Strain-Gage Method.”

Avrami M. Kinetics of phase change. I General theory[J]. The Journal of chemical physics, 1939, 7(12): 1103-1112..

Avrami M. Granulation, phase change, and microstructure kinetics of phase change. III[J]. The Journal of chemical physics, 1941, 9(2): 177-184.

Avramov I, Šesták J. Generalized kinetics of overall phase transition in terms of logistic equation[J]. arXiv preprint arXiv:1510.02250, 2015.

Azar A S, Ås S K, Akselsen O M. Determination of welding heat source parameters from actual bead shape[J]. Computational materials science, 2012, 54: 176-182.

Ban H. Y, Shi G, Shi Y. J. Experimental and unified model investigations on residual stress within high strength steel welded I-sections[J]. 工程力学, 2014, 31(8): 83-91.

Ban H. Y, Shi G, Shi Y. J, *et al*. Experimental investigation of the overall buckling behaviour of 960 MPa high strength steel columns[J]. Journal of Constructional Steel Research, 2013, 88: 256-266.

Beg D, Hladnik L. Slenderness limit of class 3 I cross-sections made of high strength steel[J]. Journal of Constructional Steel Research, 1996, 38(3): 201-217.

Beg D, Kuhlmann U, Davaine L, *et al.* Design of plated structures: Eurocode 3: Design of steel structures, part 1-5: Design of plated structures[M]. John Wiley & Sons, 2012.

Celin R, Burja J. Effect of cooling rates on the weld heat-affected zone coarse grain microstructure[J]. Metallurgical and Materials Engineering, 2018, 24(1): 37-44.

CEN. (1992). BS-EN10002-5. Tensile testing of metallic materials - Part 5: Method of test at elevated temperatures. British Standard Institute (BSI); 1992.

CEN. (2001). BS EN 1011-2, Welding - Recommendations for welding of metallic materials - Part 2: Arc welding of ferritic steel. European Committee for Standardization.

CEN. (2005). BS EN 1993-1-1, Eurocode 3: Design of steel structures Part 1-1: General rules and rules for buildings. European Committee for Standardization.

CEN. (2005). BS EN 1993-1-2, Eurocode 3: Design of Steel Structures, Part 1-2: General rules — Structural fire design. European Committee for Standardization.

CEN. (2007). BS EN 1993-1-12, Eurocode 3: Design of Steel Structures Part 1-2: Additional rules for the extension of EN 1993 up to steel grades S 700. European Committee for Standardization.

CEN. (2009). BS EN ISO 6892-1, Metallic materials – Tensile testing, Part 1: Method of test at ambient temperature. European Committee for Standardization.

Chung K F, Ho H C, Hu Y F, *et al*. Experimental evidence on structural adequacy of high strength S690 steel welded joints with different heat input energy[J]. Engineering Structures, 2020, 204: 110051.

Chung K F, Hu Y F, Xiao M, *et al*. Structural behaviour of welded H-sections made of high-strength S690 steel plates and their applications in construction[M]//Analysis and Design of Plated Structures. Woodhead Publishing, 2022: 539-591.

Collin P, Johansson B. Eurocode for high strength steel and applications in construction[C]//International Conference Super-High Strength Steel: 02/11/2005-04/11/2005. Associazione Italiana di Metallurgia, 2005.

Cui Q, Jiang S, Lin X, *et al*. High-pressure quenching effect on martensitic transformation characteristics and mechanical properties of low-alloy medium-carbon steel[J]. Journal of Materials Research and Technology, 2023, 23: 765-777.

Deng D, Murakawa H. Prediction of welding residual stress in multi-pass butt-welded modified 9Cr–1Mo steel pipe considering phase transformation effects[J]. Computational Materials Science, 2006, 37(3): 209-219.

Deshpande A A, Tanner D W J, Sun W, *et al*. Combined butt joint welding and post weld heat treatment simulation using SYSWELD and ABAQUS[J]. Proceedings of the Institution of Mechanical Engineers, Part L: Journal of Materials: Design and Applications, 2011, 225(1): 1-10.

Deng Y, Zhou S, Li J, *et al*. Buckling behaviour of Q460GJ welded H-section columns subjected to minor axis under axial compression[C]//Structures. Elsevier, 2021, 34: 1416-1428.

Fanfoni M, Tomellini M. The Johnson-Mehl-Avrami-Kohnogorov model: a brief review[J]. Il Nuovo Cimento D, 1998, 20: 1171-1182.

Fisher C R, Nahshon K, NAVAL SURFACE WARFARE CENTER CARDEROCK DIV BETHESDA MD WEST BETHESDA United States. Simulation of Weld Mechanical Behaviour to Include Welding-Induced Residual Stress and Distortion: Coupling of SYSWELD and Abaqus Codes[R]. Report No. NSWCCD-61-TR-2015/31.–Text: electronic, 2015.

Fortunier R, Leblond J B, Bergheau J M. A numerical model for multiple phase transformations in steel during thermal processes[J]. JOURNAL-SHANGHAI JIAOTONG UNIVERSITY-ENGLISH EDITION-, 2000, 5(1): 213-220.

Gáspár M, Balogh A. GMAW experiments for advanced (Q+T) high strength steel[J]. Production Processes and Systems, 2013, 6(1): 9-24.

Goldak J, Chakravarti A, Bibby M. A new finite element model for welding heat sources[J]. Metallurgical transactions B, 1984, 15: 299-305.

Guo J, Pan B, *et al*. Recent progress of residual stress measurement methods: A review[J]. Chinese Journal of Aeronautics, 2021, 34(2): 54-78.

Grajcar A, Zalecki W, Skrzypczyk P, *et al*. Dilatometric study of phase transformations in advanced high-strength bainitic steel[J]. Journal of Thermal Analysis and

Calorimetry, 2014, 118: 739-748.

Halabuk D, Návrat T. Determination of Residual Stresses in Cylindrical Components by the Hole-drilling Method[J]. Experimental Mechanics, 2022, 62(1): 87-99.

Hsu T Y, Xu Z Y. Design of structure, composition and heat treatment process for high strength steel[C]//Materials science forum. Trans Tech Publications Ltd, 2007, 561: 2283-2286.

Hu Y. F. Structural behaviour of high strength S690 steel cold-formed circular hollow sections[D]. The Hong Kong Polytechnic University. 2019.

Hu Y. F, Chung K. F, Ban H.Y, *et al*. Investigations into residual stresses in S690 cold-formed circular hollow sections due to transverse bending and longitudinal welding[J]. Engineering Structures, 2020, 219: 110911.

Huang D, Zhang L, Wang W, *et al*. Test on post-fire residual mechanical properties of high strength Q690 steel considering tensile stress in fire[J]. Journal of Constructional Steel Research, 2022, 194: 107340.

Inoue T, Tanaka K. An elastic-plastic stress analysis of quenching when considering a transformation[J]. International Journal of Mechanical Sciences, 1975, 17(5): 361-367.

ISO 15607:2019. 2019. Specification and Qualification of Welding Procedures for Metallic Materials-General Rules(E) Ii.

ISO 16834. 2012. Welding Consumables - Wire Electrodes, Wires, Rods and Deposits for Gas Shielded Arc Welding of High Strength Steel.

http://d.g.wanfangdata.com.cn/Standard_EN ISO 11885-2009.aspx.

Jia X, Xu J, Liu Z, *et al*. A new method to estimate heat source parameters in gas metal arc welding simulation process[J]. Fusion Engineering and Design, 2014, 89(1): 40-48.\.

Jiang J, Bao W, Peng Z Y, *et al*. Experimental investigation on mechanical behaviours of TMCP high strength steel[J]. Construction and Building Materials, 2019, 200: 664-680.

J Jiang J, Chiew S P, Lee C K, *et al*. An experimental study on residual stresses of high strength steel box columns[J]. Journal of Constructional Steel Research, 2017, 130: 12-21.

Jung M, Kang M, Lee Y K. Finite-element simulation of quenching incorporating improved transformation kinetics in a plain medium-carbon steel[J]. Acta Materialia, 2012, 60(2): 525-536.

Khan M, Paradowska A, Uy B, *et al*. Residual stresses in high strength steel welded box sections[J]. Journal of Constructional Steel Research, 2016, 116: 55-64.

Koistinen, D. P., and R. E. Marburger. 1959. “A General Equation Prescribing the Extent of the Austenite-Martensite Transformation in Pure Iron-Carbon Alloys and Plain Carbon Steel.” Acta Metallurgica 7(1): 59–60.

Kuhlmann U, Schmidt‐Rasche C, Jörg F, *et al*. Update on the revision of Eurocode 3: Evolution by improvement and harmonization[J]. Steel Construction, 2021, 14(1): 2-13.

Kumar N. Experimental Investigation of Submerged ARC Welding on High Strength Low Alloy Steel (HSLA)[J].

Lee C. H, Chang K. H. Prediction of residual stresses in high strength carbon steel pipe weld considering solid-state phase transformation effects[J]. Computers & Structures, 2011, 89(1-2): 256-265.

Li T J, Li G Q, Wang Y B. Residual stress tests of welded Q690 high-strength steel box- and H-sections[J]. Journal of Constructional Steel Research, 2015, 115: 283-289..

Li, P. L, and Hao L. 2011. Sensitivity Analysis and Prediction of Double Ellipsoid Heat Source Parameters[J]. TRANSACTIONS OF THE CHINA WELDING INSTITUTION 32(11): 89–92.

Li T. J, Li G. Q, Chan S L, *et al*. Behaviour of Q690 high-strength steel columns: Part 1: Experimental investigation[J]. Journal of Constructional Steel Research, 2016, 123: 18-30.

Li X. Study on Local Stability of High-Strength Q960 Steel Compression Member at Elevated Temperature[D]. Chongqing University, 2021.

Lin, C. C. Local Buckling and Design Method of High Strength Steel Welded-Section Members under Axial Compression[D]. Tsinghua University, 2014.

Liu, X. Structural Effects of Welding onto High Strength S690 Steel Plates And Weld Sections[D]. The Hong Kong Polytechnic University. 2017.

Liu X, Chung K F, Ho H C, *et al*. Mechanical behaviour of high strength S690-QT steel welded sections with various heat input energy[J]. Engineering Structures, 2018, 175: 245-256.

Liu Q. M, Xu X. P, and Zou J. H. 2017. Welding Test Research on High Strength Q960E Steel[J]. Welding Technology 46: 27–31.

Lundbäck A. Finite element modelling and simulation of welding of aerospace components[D]. Luleå tekniska universitet, 2003.

Marques E S V, Silva F J G, Pereira A B. Comparison of finite element methods in fusion welding processes - a review[J]. Metals, 2020, 10(1): 75.

Mathar J. Determination of initial stresses by measuring the deformations around drilled holes[J]. Transactions of the American Society of Mechanical Engineers, 1934, 56(3): 249-254.

Mičian M, Harmaniak D, Nový F, *et al*. Effect of the $t_{8/5}$ Cooling Time on the Properties of S960MC Steel in the HAZ of Welded Joints Evaluated by Thermal Physical Simulation[J]. Metals, 2020, 10(2): 229.

Moradi Eshkafti M. Influence of various welding sequence schemes on the load bearing capacity of square hollow section T-joint[D]. BTU Cottbus-Senftenberg, 2017.

Nishino F, Tall L, Ueda Y. Experimental investigation of the buckling of plates with residual stresses[M]. ASTM International, 1967.

Olson G B, Tsuzaki K, Cohen M. Statistical aspects of martensitic nucleation[J]. MRS Online Proceedings Library (OPL), 1985, 57: 129.

Owens A. In - situ stress determination used in structural assessment of concrete structures[J]. Strain, 1993, 29(4): 115-124.

Peng Y, Zhao J, Chen L, *et al*. DIC-hole drilling method for in-situ residual stress measurement[C]//MATEC Web of Conferences. EDP Sciences, 2019, 275: 02004.

Porter D A, Easterling K E, Sherif M Y. Phase transformations in metals and alloys[M]. CRC press, 2021.

Rasmussen K J R, Hancock G J. Plate slenderness limits for high strength steel sections[J]. Journal of Constructional Steel Research, 1992, 23(1-3): 73-96.

Rasmussen K J R, Hancock G J. Tests of high strength steel columns[J]. Journal of Constructional Steel Research, 1995, 34(1): 27-52.

Raoul J. Use and application of high-performance steel for steel structures[M]. Iabse, 2005. Rheingans B, Mittemeijer E. J. Phase transformation kinetics: advanced modelling strategies[J]. Jom, 2013, 65: 1145-1154.

Rossini N. S, Dassisti M, Benyounis K. Y, *et al*. Methods of measuring residual stresses in components[J]. Materials & Design, 2012, 35: 572-588.

Schajer G S. Hole-drilling residual stress profiling with automated smoothing[J]. 2007.

Schaupp T, Ernst W, Spindler H, *et al*. Hydrogen-assisted cracking of GMA welded 960 MPa grade high-strength steel[J]. International journal of hydrogen energy, 2020, 45(38): 20080-20093.

Shen Y, Chen B, Wang C. In situ observation of phase transformations in the coarse-grained heat-affected zone of P91 heat-resistant steel during simulated welding process[J]. Metallurgical and Materials Transactions A, 2020, 51: 3371-3376.

Shome M, Tumuluru M. Introduction to welding and joining of advanced high-strength steel (AHSS)[M]//Welding and joining of advanced high strength steel (AHSS). Woodhead Publishing, 2015: 1-8.

Slováček M, Diviš V, Junek L, *et al*. Numerical simulation of the welding process—distortion and residual stress prediction, heat source model determination[J]. Welding in the World, 2005, 49: 15-29.

STANDARD, BRITISH. "Welding - Recommendations for welding of metallic materials." Change 13981 (2002): 30.

Standard, China. 2014. GB/T 31310-2014: Metallic Materials - Determination of Residual Stress -Hole Drilling Strain-Gage Method.

Standard, European. 2005. “ENV 1993-1-1: 2005, Design of Steel Structures-Part 1-1.” General Rules and Rules for Buildings, CEN.

Standardization, European Committee for. 2018. BS EN ISO 15607[2], Specification and Qualification of Welding Procedures for Metallic Materials.

Stoschka M, Loose T, Barsoum Z. Distortion analysis of a welded corner stiffening frame considering manufacturing restraining conditions[J]. Computers & Structures, 2013.

Taljat B, Radhakrishnan B, Zacharia T. Numerical analysis of GTA welding process with emphasis on post-solidification phase transformation effects on residual stresses[J]. Materials Science and Engineering: A, 1998, 246(1-2): 45-54.

Tian X. H, Liao J, Cheng P, *et al*. Element Simulation of Welding Residual Stresses and Distortion in 5083 Incorporating Metallurgical Phase Transformation[C]//2017 International Conference on Applied Mathematics, Modelling and Simulation (AMMS 2017). Atlantis Press, 2017: 164-168.

Tong M W. Development of 550/690MPa high strength-toughness construction steel with low yield ratio and research of its anti-fracture performance [D]. Wuhan University of Science and Technology, 2016

Toyoda M, Mochizuki M. Control of mechanical properties in structural steel welds by numerical simulation of coupling among temperature, microstructure, and macro-mechanics[J]. Science and technology of advanced materials, 2004, 5(1-2): 255.

Tsai C L, Han M S, Jung G H. Investigating the bifurcation phenomenon in plate welding[J]. welding journal, 2006, 85(7): 151-162.

Ueda Y, Yamakawa T. Analysis of thermal elastic-plastic stress and strain during welding by finite element method[J]. Japan Welding Society Transactions, 1971, 2(2).

USAMI T, FUKUMOTO Y, AOKI T. Tests on the interaction strength between local and overall buckling of welded box columns[C]//Proceedings of the Japan Society of Civil Engineers. Japan Society of Civil Engineers, 1981, 1981(308): 47-58.

W, Soete, and Vancrombrugge R. 1950. An Industrial Method for the Determination of

Residual Stresses[C]// Proc. SESA 8(Report MATC(A)04): 17–18.

Wang F, Lui E M. Experimental investigation of post-fire residual stresses in Q690 welded I-sections[J]. Thin-Walled Structures, 2021, 163: 107631.

Wang M, Xu G, Yang H L, *et al*. Research on CCT curve of 12Cr2Mo1R pressure vessel steel[J]. Applied Mechanics and Materials, 2014, 556: 468-471.

Wang W, Zhang Y, Xu L, *et al*. Mechanical properties of high-strength Q960 steel at elevated temperature[J]. Fire Safety Journal, 2020, 114: 103010.

Weisz-Patrault D. Multiphase model for transformation induced plasticity. Extended Leblond's model[J]. Journal of the Mechanics and Physics of Solids, 2017, 106: 152-175.

Willms R. High strength steel for steel constructions[C]//Nordic Steel Construction Conference, Malmo, Sweden. 2009.

Worldsteel association. 2022. 1 World Steel in Figures. http://www.worldsteel.org/wsif.php.

Yue, Ma. Study on Numerical Simulation of General Expression of Double Ellipsoidal Heat Source Model[D]. Hebei University of Technology, 2015

Xiao M. Structural Behaviour of High Strength S690 Cold-Formed Square Hollow Sections under Compression[D]. The Hong Kong Polytechnic University. 2021.

Xiao M, Hu Y F, Jin H, *et al*. Prediction of residual stresses in high-strength S690 cold-formed square hollow sections using integrated numerical simulations[J]. Engineering Structures, 2022, 253: 113682.

Zrilic M, Grabulov V, Burzic Z, *et al*. Static and impact crack properties of a high-strength steel welded joint[J]. International journal of pressure vessels and piping, 2007, 84(3): 139-150.

Zuo S, Wang Z, Wang D, *et al*. Numerical simulation and experimental research on temperature distribution of fillet welds[J]. Materials, 2020, 13(5): 1222.